University of Alberta

Three-Dimensional Kinematic Model of a Task Specific Motion Based on Instantaneous Screw Axis Theory Developed for Golf Motion Analysis

by

Alessandro Stéphane Vena

A thesis submitted to the Faculty of Graduate Studies and Research
in partial fulfillment of the requirements for the degree of

Master of Science

Mechanical Engineering

Fall 2009
Edmonton, Alberta

Examining Committee

Dr. Jason Carey, Department of Mechanical Engineering, University of Alberta

Dr. Pierre Baudin, Faculty of Physical Education & Recreation, University of Alberta

Dr. Farbod Fahimi, Department of Mechanical Engineering, University of Alberta

Dr. Adrian Liggins, Department of Cell Biology, University of Alberta

Abstract

A large number of studies have concentrated on golf swing biomechanics, ranging from planar rigid-link models to 3D kinematic analysis. A promising technique, instantaneous screw axis (ISA) theory, has not been covered in the literature and could provide a better true segment rotation approximation. The objectives of this study are to identify ISA location and orientation, as well as segment angular velocity, of the major body segments involved in the golf swing. For all subjects, it was found that the magnitude of maximum angular velocities increased from the most proximal segment (the pelvis) to the most distal segment (the left arm), in accordance with the summation of speeds principle. Furthermore, most subjects achieved their maximum angular velocities in the desired kinematic sequence, where the first maxima was achieved by the most proximal segment and followed by the more distal segments in the kinematic chain.

Table of Contents

List of Tables

List of Figures

List of Abbreviations

CCD	Charged coupled device
CMM	Coordinate measuring machine, used for calibration of the rotational apparatus and translational apparatus
IS	Indeterminate system, where marker occlusion does not allow for ISA computation
ISA	Instantaneous screw axis
ISA_A	ISA computed from the complete motion of the left arm
ISA_C	ISA computed from the complete motion of the golf club
ISA_L	ISA computed from the complete motion of the left leg
ISA_P	ISA computed from the complete motion of the pelvis
$ISAr_A$	ISA computed from the motion of the left arm relative to the shoulders
$ISAr_C$	ISA computed from the motion of the golf club relative to the left arm
$ISAr_P$	ISA computed from the motion of the pelvis relative to the left leg
$ISAr_S$	ISA computed from the motion of the shoulders relative to the pelvis
ISA_S	ISA computed from the complete motion of the shoulders
LASIS	Left anterior superior iliac crest
LHJC	Left hip joint center
LPSIS	Left posterior superior iliac crest
PSD	Power spectral density of a given signal, obtained by Fast Fourier Transform [Kreyszig (1999b)]
RASIS	Right anterior superior iliac crest
RB	Rigid body
RHJC	Right hip joint center
RMSE	Root mean squared [Taylor (1982a)] error

$RMSE_{velocity}$	Root mean squared [Taylor (1982a)] error between Computed and Measured marker velocity
RPSIS	Right posterior iliac crest

List of Nomenclature

Bias	Bias refers to the systematic difference between an accepted reference value and a set of measurement values [ASTM International]
Computed marker velocity	Marker velocity computed from motion about the segment's ISA
Distal segment	Segment situated farthest to the origin of the kinematic chain, ie the feet
Global coordinate frame	Coordinate frame of the stereophotogrammetric system (photogrammetric frame of Cappozzo et al. [Cappozzo et al. (2005)])
Left Leg Axis	Vector connecting the left hip joint center to the centroid of the left ankle
Local coordinate frame	Coordinate frame of a given segment constructed from the position of three or more features on that segment (marker cluster technical frame of Cappozzo et al. [Cappozzo et al. (2005)])
Measured marker velocity	Marker velocity from numerical differentiation of measured marker position
Percent mean velocity	Ratio of RMSE on marker velocity, from ISA computation, divided by mean marker velocity and expressed in percent
Percent mean relative velocity	Ratio of RMSE on relative marker velocity, from ISAr computation, divided by mean relative marker velocity and expressed in percent
Percent occluded frames	Ratio of occluded frames by the total number of frames of the downswing, used in the Marker Occlusion Study

Precision	Precision relates to the closeness of measurement values to each other under similar experimental conditions [ASTM International]
Proximal segment	Segment situated closest to the origin of the kinematic chain, ie the feet
Supination axis	Vector connecting the wrist centroid to the elbow centroid
Random instrument error	Sources of random instrument error in stereophotogrammetric systems include: electronic noise, marker flickering, the digitization process and marker image shape distortion [Chiari et al. (2005)]
Soft tissue artifact	Soft tissue artifact originates from the relative motion between skin-mounted markers and the underlying bone structure [Leardini et al. (2005)].
Spine axis	Vector connecting the pelvic centroid to the shoulder centroid
Stationary marker	Stationary marker of the translational apparatus
Stereophotogrammetry	Principle whereby the three-dimensional coordinates of a given point can be computed from two or more two-dimensional images taken from different planes [Adams and Spirakis (1997)].
Systematic instrument error	Systematic instrument errors in stereophotogrammetric systems include: photogrammetric calibration inaccuracies or any non-linearities that the model could not remove [Chiari et al. (2005)].
Translating marker	Translating marker, actuated by the micrometer, of the translational apparatus

List of Symbols

ε_F	Error between measured marker velocity (stereophotogrammetric data) and computed marker velocity (motion about ISA)
ε_o	Error in instantaneous screw axis orientation (angle between ISA_{clean} and ISA_{noisy})
ε_P	Error in instantaneous screw axis position (distance between Int_{clean} and Int_{noisy})
ε_v	Error in the magnitude of segment parallel velocity in ISA direction
ε_ω	Error in the magnitude of segment angular velocity in ISA direction
$\theta_1, \theta_2, \theta_3$	Phase angles of the analytical model of markers M1, M2 and M3, respectively
$\varphi_x, \varphi_y, \varphi_z$	Phase angles of the x-, y- and z-components of the continuous noise model (adapted from Chèze et al. [Chèze et al. (1998)])
$\vec{\omega}$	Applied angular velocity vector to the analytical model
$\overrightarrow{\omega_{clean}}$	Angular velocity about the ISA computed from analytical rigid body motion
ω_C	Frequency of golf club head displacement
ω_{max}	Maximum angular velocity from motion about ISA
$\overrightarrow{\omega_{noisy}}$	Angular velocity about the ISA computed from disturbed analytical motion
ω_N	Frequency of the continuous noise model (adapted from Chèze et al. [Chèze et al. (1998)])
ω_{Ny}	Nyquist Frequency from sampling frequency theorem [Leigh (1992)]
ω_S	Sampling frequency [Leigh (1992)]

a_{1s}, a_{2s}, a_{3s}	Imposed position of the rigid geometry with the solidification procedure [Chèze et al. (1995)]
$\left\|\vec{A}\right\|$	Total magnitude of the continuous noise model (adapted from Chèze et al. [Chèze et al. (1998)])
A_x, A_y, A_z	Amplitude of the x-, y- and z-components of the continuous noise model (adapted from Chèze et al. [Chèze et al. (1998)])
A, B, C	Matrices (3x3) of the least-squares technique of Söderkvist and Wedin [Söderkvist and Wedin (1993)]
b	Highest frequency in the sampled power spectrum, from sampling frequency theorem [Leigh (1992)]
b_1, b_2, b_3	Measured position of three non-collinear markers on a given segment used in the solidification procedure [Chèze et al. (1995)]
b_{1s}, b_{2s}, b_{3s}	Solidified position of three non-collinear markers on a given segment resulting from the solidification procedure [Chèze et al. (1995)]
C_1, C_2	Plane constant from the vector equation of a plane [Nicholson (2003)]
$Disp_i$	Displacement *i*, where *i*= [1:5], of the translational apparatus
$Distance_I$	Inter-marker distance of the translational apparatus
Int_{clean}	Intersection of ISA, computed from analytical rigid body motion, with the plane formed by marker M1, M2 and M3 of the analytical model
Int_{noisy}	Intersection of ISA, computed from disturbed analytical motion, with the plane formed by marker M1, M2 and M3 of the analytical model
ISA_{clean}	ISA computed from analytical rigid body motion
$ISA_{Diagnostic\ 1}$	Computational diagnostic used to determine ISA direction
$ISA_{Diagnostic\ 2}$	Computational diagnostic used to determine if ISA direction cannot be defined

$ISA_{Diagnostic\ 3}$	Computational diagnostic used to determine if ISA position cannot be defined
ISA_{noisy}	ISA computed from disturbed analytical motion
$\overrightarrow{ISA_o}$	Unit vector parallel to the ISA of a given segment
$\overrightarrow{ISA_p}$	Coordinates of the ISA intersection with the xy-plane of the global coordinate frame
Length 1, 2	Reference lengths of the rotational apparatus
M1, M2, M3	Three non-collinear markers of the analytical model
n	Specific data point, or time frame, of the analytical model
n_C	Number of computations of the ISA of a given segment
n_{Cycles}	Number of measurement cycles from the Measurement Accuracy Study
n_f	Number of data frames of the downswing
n_{LT}	Number of lost trials form the Measurement Accuracy Study
n_m	Number of markers affixed to a given segment used in ISA computation
n_o	Number of occluded data frames from the Marker Occlusion Study
n_{trials}	Number of measurement trials from the Marker Occlusion Study
n_T	Total number of measurements from Measurement Accuracy Study
$\vec{N}$	Continuous noise model for adding systematic instrument error or soft tissue artifact to an analytical signal (adapted from Chèze et al. [Chèze et al. (1998)])
N_1	Number of adjacent data points removed from positional signal to simulate marker occlusion
N_2	Number of adjacent impulses added to the positional signal to simulate random instrument error
$N_{outliers}$	Number of outliers determined from Chauvenet's criterion

P	Probability density function of a Gaussian distribution [Kreyszig (1999a)]
P_{1S}, P_{2S}, P_{3S}	Vertices of the unit isosceles triangle, computed from a_{1s}, a_{2s} and a_{3s}, of the solidification procedure [Chèze et al. (1995)]
P, Q, Γ	Matrices (3x3) from singular value decomposition of matrix C of the least-squares minimization problem of Söderkvist and Wedin [Söderkvist and (1993)]
Q_1, Q_2, Q_3	Vertices of the unit isosceles triangle, computed from b_1, b_2 and b_3, of the solidification procedure [Chèze et al. (1995)]
r	Radius of the analytical model (cylinder radius)
r_S	Radius of standard deviation, computed as the magnitude of the x- and y-components of standard deviation, of ISA intersection with the xy-plane
R	Rotational matrix (3x3) from the Solidification procedure [Chèze et al. (1995)]
S	Standard deviation
t	Translation vector (3x1) from the Solidification procedure [Chèze et al. (1995)]
t_i	Given time frame *i* of the downswing
t_{iN}	Normalized time frame *i* of the downswing, in percent downswing
t_I	Time frame coinciding with impact, the final time frame of the downswing
t_0	Time frame marker the beginning of the downswing
t_S	Number of standard deviations away from mean error used with Chauvenet's criterion
var_1	First variable of the minimization problem of the golf swing model, represents the number of possible combinations of three markers from a given number of affixed markers placed on a segment

var_2	Second variable of the minimization problem of the golf swing model, represents the number of computations of ISA position
var_3	Third variable of the minimization problem of the golf swing model, represents the number of computations of motion about the ISA
$\overrightarrow{v_{ISA}}$	Marker velocity from motion about ISA
$\overrightarrow{v_{i/ISA}}$	Velocity of marker *i* relative to the preceding ISA
$\overrightarrow{v_{//}}$	Parallel component of marker velocity, from segment translation along ISA
$\overrightarrow{v_{\perp}}$	Perpendicular component of marker velocity, from segment angular velocity in ISA direction

Chapter 1 Introduction

In 1968, the Golf Society of Great Britain undertook the lofty challenge of trying to identify the characteristics of the perfect golf swing and in the process put forth the most comprehensive study on the physics of the golf swing [Cochran and Stobbs (1968)]. This marked the first of many studies to apply scientific principles to the analysis of golf in the effort to achieve a better understanding and improve the performance of golfers and their equipment [Penner (2003)]. The main areas of research have been the physics of the golf ball, with regards to energy transfer with the golf club and aerodynamics, the physics of golf clubs, with regards to optimal design of the club head and shaft, and the physics of the golf swing. This last area of research has been the source of much attention in the scientific community and has the potential to offer golfers significant insight into proper swing technique.

A large number of studies have concentrated on the physics of the golf swing, ranging from planar rigid-link models to three-dimensional kinematic analysis. Most of these studies share a common objective: to study the effect of body segment rotation, or the applied torques generating segment rotation, on the performance of the golf swing, which has been primarily characterized by club head velocity at impact. Recent studies have measured the angular velocity of body segments, and the sequence at which segments achieve their maximum angular velocities, and their relation to club head velocity. These studies have determined segment angular velocity from the displacement of an imposed reference frame on that segment and expressed segment rotation in terms of sequence dependant Euler/Cardan angles convention. Although this is a proven analysis technique, the choice of a segment's coordinate system can affect the magnitude and orientation of angular velocity and in the process may not provide the best representation of segment rotation. This is especially important if segment rotation does not occur about a fixed point, for example segments that may rotate about multiple joints such as the pelvis. One analysis technique that

has not been covered in the literature of golf swing analysis, and that could provide a better approximation of a segment's true rotation, is instantaneous screw axis theory. The main advantage of instantaneous screw axis theory, when compared to an Euler/Cardan angles convention, is that an instantaneous screw axis can change position and orientation during the motion. This provides an indication of the magnitude and orientation of a segment's gross rotation as a function of time, which is of particular interest when analyzing segments that do not rotate about a fixed point. Furthermore, the angular velocity about a segment's instantaneous screw axis would provide an accurate description of segment rotation. When applied over multiple segments involved in the golf swing motion, this provides valuable insight into the kinematic sequence of events.

Study Objectives

There are three main objectives of the current study to achieve a better understanding of the rotational components of the golf swing. First, to identify the location and orientation of the instantaneous screw axis of the major body segments involved in the golf swing. Second, to compute the amplitude of segment angular velocity relative to the corresponding instantaneous screw axis of that segment. Third, to verify if the amplitude and sequence of the maximum angular velocity of body segments follows the expected proximal to distal sequence brought forth by Cochran and Stobbs [Cochran and Stobbs (1968)].

Thesis outline

This thesis is divided into 6 chapters: literature review, experimental apparatus, methods, results, discussion and conclusion and future work. The literature review chapter consists of a summary of previous studies on golf swing analysis, instantaneous screw axis theory and stereophotogrammetry theory. In the experimental apparatus chapter, the experimental setup of a stereophotogrammetric system is discussed for the purpose of golf swing measurement. Instantaneous screw axis computation from rigid-body displacements and from stereophotogrammetric measurements of segment

displacement, as well as the golf swing model of this study is discussed in the methods chapter. The following two chapters include results and discussion, where the results and validation of the golf swing model are presented. In the final chapter, conclusions and future work are discussed.

Chapter 2 Literature Review

The following section provides a literature review on the topics of golf swing analysis, though the use of kinematic models and three-dimensional analysis of body rotation, instantaneous screw axis theory, as a methodology to compute the rotation of body segments, and stereophotogrammetry theory, as a technology to measure the displacement of body features.

2.1 Golf Swing Analysis

Scientific principles have been applied in the analysis of the golf swing to improve the performance of golfers of all skill levels. The following review of literature focuses on planar kinematic models and three-dimensional kinematic measurements of the golf swing.

2.1.1 Kinematic Models

The beginning of golf swing scientific investigation began with Cochran and Stobbs [Cochran and Stobbs (1968)], with their book entitled *The search for the perfect golf swing*. This was the first publication to present the double pendulum model of the golf swing, which constitutes the primary model used to analyze golf swing kinematics. The double-pendulum model consists of two rigid links: the upper link, which represents the shoulders and left arm, and the lower link, which represents the golf club. The upper link, spanning from the mid-point of the shoulders to the center of the wrists, rotates about a central hub following the application of a shoulder couple, while the lower link, spanning the center of the wrists and the golf club head, rotates about the pivot point connecting the two links following the application of a wrist couple. The motion of the two links is maintained within a single two-dimensional plane, consistent with an approximation of the plane formed by the left arm and golf club, and is controlled by the magnitude and sequence of the applied shoulder and wrist torques.

From the stroboscopic images of an experienced golfer, Jorgensen [Jorgensen (1970, 1994)] constructed a planer double-pendulum model and studied the influence of hand and shoulder torques. Jorgensen determined that applying a lateral shift to the central hub produced better agreement with experimental club head velocities. This lateral shift consisted of applying a positive acceleration for the first 160 ms of the downswing and then applying a negative acceleration until impact. The lateral shift could increase club head velocity by up to 17 percent. Furthermore, Jorgensen studied the energy transfer during the downswing, from the applied torques and lateral shift of the central hub. It was determined that the kinetic energy of the top link increased at the start of the downswing and decreased before impact, similar to a bell shaped curve, while the kinetic energy of the bottom link increased to impact. This confirmed the transfer of energy from the top link to the bottom link. Pickering and Vickers [Pickering and Vickers (1999)] conducted a numerical study of a planar double pendulum model, studying the effect of ball position relative to the central hub and determined that placing the ball forward of the central hub resulted in a slight increase in horizontal club head speed (1.3 percent); larger increases could be achieved when delaying the golf club release (1.6 percent). Miura [Miura (2001)] conducted a numerical study on a planar double-pendulum model to determine the effect of inward pull on the central hub, which had been observed for some experienced golfers. Applying a constant vertical acceleration to the central hub, for the last 40 ms of the downswing, resulted in good agreement between the measured and computed position of the hands. Furthermore, several authors [Cochran and Stobbs (1968), Jorgensen (1970, 1994), Pickering and Vickers (1999)] have used the double-pendulum model to study the effect of delaying the release of the golf club, by maintaining at constant angle between the upper and lower links, on club head velocity. It was found that delaying the release of the club head could result in higher club head velocities, although proper timing between the two links had to be maintained to ensure proper contact with the ball.

Triple-link models have also been used to study the kinematics of the golf swing. These models consist of three rigid links: a link from the central hub to the left shoulder joint, a link from the shoulder joint to the center of the wrists and a third link to represent the golf club. These models apply a series of three couples, located at the central hub, left shoulder joint and wrists to generate motion of the three links. Turner and Hills [Turner and Hills (1999)] applied two sets of couples to a planar triple-link model: one set for the motion of the backswing and a second set for the downswing. It was found that the time of the golf swing became sensitive to the relative magnitudes between the two sets of couples. Kaneko and Sato [Kaneko and Sato (2000)] established a criterion based on the minimization of total power expenditure to determine the value of time varying couples applied to a planar triple-link model. It was found that the torques that minimized the criterion had good agreement with experimental data, and that the torque applied to the central hub and shoulders decreased before impact. This confirmed that the upper links imparted their energy to the system before impact, and that the constant torques of other studies represents a rough estimation. Sprigings and Neal [Sprigings and Neal (2000)] applied couples according to the velocity properties of muscle tissue, using a linearized Hill model, to drive the three links of a planar triple-link model. It was determined that an optimally timed wrist torques on the golf club link could increase club head speed by up to 9 percent and confirmed that optimal club head speed can be achieved when torques are engaged in a proximal to distal sequence.

2.1.2 Three-Dimensional Kinematic Measurement of Body Rotation During the Golf Swing

Many authors have measured the extent and sequence of pelvis, torso and left arm rotation during the golf swing providing insight into the sequence of the downswing and attempting to establish the relation between body rotation and club head velocity. McTeigue et al. [McTeigue et al. (1994)] measured spine and hip rotation by placing gyroscopes and potentiometers on professional and

amateur golfers. It was determined that the swing of professional golfers conformed to the summation of speeds principle as the hips initiated the downswing followed by the shoulders and the upper body rotated faster than the hips. Furthermore, the upper body decelerated just prior to impact, while the hips decelerate substantially before impact. Robinson [Robinson (1994)] conducted a study to establish a correlation between the swing characteristics and club head velocity of professional and amateur golfers. The most significant variables were the angular velocity between left arm and the shoulders at impact, measuring 7.93 rad/s for amateurs and 9.44 rad/s for professionals, and the angular velocity of the hips at the midpoint of the downswing, measuring 4.18 rad/s for amateurs and 5.37 rad/s for professionals. McLaughlin and Best [McLaughlin and Best (1994)] conducted a three-dimensional kinematic study to determine statistically significant differences in the swing variables between three groups of golfers. The most significant variable was club head velocity, as expected, while the second most significant variable was the rotation angle of the hips at mid-downswing. Burden et al. [Burden et al. (1998)] measured hip and shoulder rotation to determine if the sequence of these rotations satisfies the summation of speed principle. It was determined that, for three quarters of the golfers analyzed, hip rotation initiates the downswing and that the shoulders follow the motion of the hips and therefore satisfies the proximal to distal sequence. Teu et al. [Teu et al. (2006)] analyzed the golf swing as a kinematic chain using dual Euler angles and studied the contribution of upper extremity segment rotation on club head velocity. It was determined that torso rotation, upper arm rotation, forearm rotation and hand rotation accounted for 33.8 percent, 24.1 percent, 18.6 percent and 23.4 percent of club head velocity at impact, respectively. Myers et al. [Myers et al. (2008)] determined statistically significant differences between torso and pelvis rotations between three categories of golfers. The biggest significant difference between groups was the differential angle between the torso and the hips, where an increase in this separation between the pelvis and shoulders could lead to an increase in club head speed. Cheetham et al. [Cheetham et al. (2008)] studied the kinematic sequence of the golf swing by determining the angular

velocity of segments expressed relative to their local coordinate frame. For professional golfers, both the maximum angular velocity of each segment and the order in which these maximum values were achieved followed a proximal to distal sequence. Both of these results support the summation of speed principle.

2.1.3 Kinematic Model Limitations

Studies based on double-pendulum and triple-link models have shown high agreement with experimental data. However, the position and movement of the central hub have not been well established in these models. Studies have shown [Jorgensen (1970, 1994), Pickering and Vickers (1999)] that the position of the central hub should not be kept fixed during the downswing. However, the displacement of the central hub has not been properly characterized and no attempts have been made to relate its displacement with the more proximal segments of the golf swing, such as the pelvis. Furthermore, these planar rigid-linked models assume that the location of the central hub lies approximately at the mid-point between the shoulders. However, no studies have attempted to confirm the center of the shoulders as the true center of rotation of the upper link.

Three-dimensional kinematic studies have attempted to quantify the extent and sequence of rotations of the major body segments involved in the golf swing. Some authors [Robinson (1994), Burden et al. (1998), Myers et al. (2008)] have constructed two-dimensional lines to represent the position of the pelvis and shoulders, and have determined the time-derivative of the relative angle between these two-dimensional lines and the line of play. These represent only one component of segment rotation and do not represent true segment rotation. Recent studies [Teu et al. (2006), Cheetham et al. (2008)] have computed the angular velocity of body segments relative to a local coordinate frame imposed on that segment. Although these studies have determined full segment rotation, angular velocities have been expressed relative to an assumed reference that best describes these motions. Although this methodology, along with an Euler/Cardan angles

convention, can be an effective analysis technique, it may not provide the best representation of segment rotation, especially if the rotation does not occur about a fixed point. That being said, it would be of interest to determine segment angular velocity about an instantaneous axis of rotation, analogous to a two-dimensional instantaneous centre of rotation. This would not only provide the best approximation of a segment's true rotation, but it would also allow for this instantaneous axis to change position and orientation during the motion. Furthermore, if a segment's angular velocity was computed relative to an instantaneous axis of rotation, this would represent the magnitude of a segment's gross rotation as a function of time. When repeated over the major segments involved in the motion, this methodology would provide valuable insight into the kinematic sequence of the golf swing.

2.2 Instantaneous Screw Axis Theory

A number of methods have been used to identify and describe of the motion of a joint coordinate system, including sequence dependant Euler/Cardan angles and an instantaneous screw axis [Woltring (1994a)]. This last method is of particular interest in describing the motion of a segment that does not rotate about a fixed point.

2.2.1 Instantaneous Screw Axis Computation

The three-dimensional analogue to a two-dimensional instantaneous center of rotation is an instantaneous screw axis (ISA). This represents the closest kinematic representation to an instantaneous axis of rotation for a three-dimensional motion. At any give time, the motion of a rigid body can be expressed as a single translation and rotation about an ISA [Woltring et al. (1985)]. The motion of any feature on that rigid body can be decomposed into a translational velocity, in the ISA direction, and a rotational velocity, from a rotation in the ISA orientation [Woltring et al. (1985)]. ISA computation has been

studied by many others [Panjabi (1979), Bryant et al. (1984), Eberharter and Ravani (2006)], which have based their computations on the two-dimensional Reuleaux method [Reuleaux (1963)]. The Reuleaux method identifies a two-dimensional instantaneous center of rotation from the displacement of two analogous features on a body, as long as the displacements are not parallel [Eberharter and Ravani (2006)]. The three-dimensional ISA computation identifies ISA orientation from the displacement of three analogous features on a body, as long as relative displacement between features is present [Eberharter and Ravani (2006)]. From ISA orientation, feature displacements are decomposed into translational and rotational components and ISA position can be solved from the two-dimensional Reuleaux method [Eberharter and Ravani (2006)].

2.2.2 Application of ISA in Biomechanical Analysis

ISA theory can be of particular interest in biomechanical analysis, particularly to determine the location and orientation of anatomical joints. In vivo and in vitro knee joint kinematics have been studied using ISA theory [Blankevoort et al. (1990), Reinschmidt et al. (1999)], while comparisons between normal and abnormal knee pathologies have also been conducted with ISA theory [Lewis and Lew (1978), Jonsson and Kärrholm (1994)]. The international society of biomechanics recommended the use of ISA theory to locate the position of the glenohumeral joint of the shoulders [Wu et al. (2005)], a methodology used by other authors to analyze motion about the shoulder joint [Veeger et al. (1996), Stokdijk et al. (2000)]. Furthermore, ISA theory has also been applied to study the location and motion of the elbow joint [Stokdijk et al. (1999)], as well as motion about the cervical joints in whiplash diagnostics [Woltring et al. (1994b)]. Therefore, literature has shown that ISA theory is an effective methodology to identify joint position and study segment rotation. In order to compute the ISA of a given segment, the displacement of three features must be known and can be computed using stereophotogrammetry.

2.3 Stereophotogrammetry Measurements

Video based optoelectronic stereophotogrammetry is a common measurement tool in biomechanical analysis, allowing for the accurate measurement of body features without imposing mechanical constraints [Everaert et al. (1999)]. The following section described the theory behind stereophotogrammetric systems, as well discuss system limitations and measurement error.

2.3.1 Stereophotogrammetry Theory

Stereophotogrammetric systems are based on the principle of stereophotogrammetry, whereby the three-dimensional coordinates of a given point can be computed from two or more two-dimensional images taken from different planes [Adams and Spirakis (1996)]. Stereophotogrammetric systems consist of a series charged-coupled device (CCD) cameras fitted with infrared lenses [Adams and Spirakis (1996)], where their image sensor operates on an intensity scale [Gill et al. (1996)]. Spherical retroflective makers are placed on relative anatomical landmarks of the body, and when placed in the calibrated volume of a stereophotogrammetry system, reflect infrared light back to the camera image sensors [Gill et al. (1996)]. If the reflective marker is in sight of two or more cameras, each camera constructs a one-dimensional line (or ray) from its nodal point, through the markers position on its sensor to the marker itself by direct linear transformation [Gill et al. (1996)]. When two or more camera rays intersect, the three-dimensional coordinates of the given marker are computed [Gill et al. (1996)]. Therefore, the three-dimensional displacements of relevant body features are computed by placing retroflective spherical markers on the skin and ensuring that these markers are in sight of a minimum of two cameras during motion.

2.3.2 System Limitations and Measurement Error

As with all measurement systems, stereophotogrammetric systems are not free of measurement error. The main sources of measurement error and corresponding compensation techniques are discussed below. The following section of this literature review has largely been based off the four part review series *Human Movement Analysis using Stereophotogrammetry*, written by Cappozzo, Chiari, Leardini and Croce [Cappozzo et al. (2005), Chiari et al. (2005), Leardini et al. (2005), Croce et al. (2005)]. This represents one of the most comprehensive studies of stereophotogrammetric systems for use in biomechanics analysis, and has provided ample technique background for the purposes of this current study. Although measurement uncertainty is the proper term to describe differences between measurements and actual values, where the sources of uncertainty are intrinsic to the process of measurement [Taylor (1982b)], this will be referred to as measurement error to be consisted with literature terminology [Chiari et al. (2005)].

2.3.2.1 Marker Occlusion

In order to compute three-dimensional position of a given marker, it needs to be in sight of two or more cameras at all times. However, when a marker is occluded from the field of view of the cameras by a body segment or foreign object in the measurement volume [Chiari et al. (2005)], the cameras loose sight of the marker and three-dimensional position cannot be determined. Marker occlusion causes loss of positional data, resulting in an incomplete positional signal. Various methods have been devised to replace instances of marker occlusion and complete the positional signal. These include methods based on the rigid-body assumption [Veldpaus et al. (1988), Herda et al. (2001)], and methods based on temporal interpolation [Muijtjens et al. (1997)]. Computations relying on the rigid body assumption construct an orthogonal reference frame for a given segment, and the missing marker is replaced by knowing its position with the orthogonal reference frame from previous frames [Desjardins et al. (2002)]. However, this

methodology requires a minimum of three non-occluded data points at all times [Desjardins et al. (2002)]. Temporal interpolation techniques, which use time-dependant algorithms, have proven effective in some cases [Chiari et al. (2005)]. In its simplest form, temporal interpolation can be carried out by applying interpolating cubic splines to a marker's positional signal [Motion Analysis (2006)]. The main disadvantage of temporal interpolation is that a minimum distance between markers belonging to the same segment is not maintained, and in the process can violate the rigid body assumption [Desjardins et al. (2002)]. Therefore, applying temporal interpolation to replaced occluded markers may require that the rigid body assumption be verified.

2.3.2.2 Systematic and Random Instrument Error

Instrument measurement error can be divided into two categories: systematic instrument error and random instrument error [Chiari et al. (2005)]. Systematic instrument errors are caused by photogrammetric calibration inaccuracies or any non-linearities that the model could not remove [Chiari et al. (2005)]. The magnitude of systematic instrument error is a function of the size of the calibration volume and the position of the marker within the volume [Gazzani (1993)]. Sources of random instrument error include electronic noise, marker flickering, the digitization process (of converting image coordinates into digital values) and marker image shape distortion brought on by velocity effects, partial marker occlusion and the merging of markers in close proximity to one another [Chiari et al. (2005)]. There are two methods to quantify measurement error from stereophotogrammetric systems [Chiari et al. (2005)]: inter-marker distance measurement [Klein and DeHaven (1995), Ehara et al. (1997), Richards (1999), Maletski et al. (2007)] and marker displacement measurement [Richards (1999), Everaert et al. (1999)]. Among these studies, Richards [Richards (1999)] conducted an extensive evaluation of 7 commercially available optical systems relative to the following four variables: the ability to measure the distance between two constantly visible markers, the ability to measure the motion

associated with a static marker, to reconstruct the motion of a marker visible to alternating sets of cameras and the ability to measure the position of two markers moving in close proximity to one another. Five of seven systems produced less than 2.0mm root mean squared error (RMSE) when measuring fully visible moving markers and less than 1.0mm RMSE when measuring a stationary marker [Richards (1999)].

Stereophotogrammetric signals of human movement have a high signal-to-noise ratio, where the base signal has a low-frequency content with additive high frequency noise [Chiari et al. (2005), Alonso et al. (2005)]. It is important to compensate for these measurement errors as high-frequency noise has a deleterious effect on the estimates of signal derivatives, such as marker velocity and acceleration [Chiari et al. (2005)]. Many compensation techniques have been developed to reduce the effects of instrument noise [Woltring (1995)], including: graphical methods, finite difference techniques, spline functions and digital filtering [Chiari et al. (2005)]. Due to the high-frequency content of instrumental noise [Alonso et al. (2005)], low-pass digital filters have shown to be effective in attenuating unwanted high-frequency noise [Winter (2004)]. The major assumption with using low-pass digital filters is that the signal is stationary [Chiari et al. (2005)], and therefore a constant cut-off frequency can be used. Recent alternative methods have been developed with adaptive time-frequency filtering [Giakas et al. (2000)].

2.3.2.3 Soft Tissue Artifact

The largest source of measurement error in stereophotogrammetric systems originates from the relative motion between skin-mounted markers and the underlying bone structure, called skin motion artifact [Leardini et al. (2005)]. Inertial effects, skin deformation and sliding, and deformation caused by muscle contractions all contribute to soft tissue artifact [Leardini et al. (2005)]. Several studies have quantified the extent of soft tissue artifact on the lower extremity

using the following techniques: intra-cortical pins [Fuller et al. (1997)], external fixators [Cappozzo et al. (1996)], percutaneous trackers [Holden et al. (1997)] and roentgen photogrammetry [Sati et al. (1996)]. Fuller et al. [Fuller et al. (1997)] placed reflective markers on the leg using intra-cortical pins and measured displacements of up to 20 mm for the thigh and shank. Cappozzo et al. [Cappozzo et al. (1996)] scattered markers along the leg using an external fixator during walking and cycling tasks and measured positional errors of up to 40 mm. Holden et al. [Holden et al. (1997)] used percutaneous trackers to study the movement of the thigh during walking and measured absolute displacement of a segment's reference frame to 6.5 mm (transverse plane) and 10.5 mm (longitudinally). Sati et al. [Sati et al. (1996)] used standard fluoroscopy to measure the aspect distal of the thigh, measuring errors from 16.8 mm to 17.1mm for the lateral and medial regions, respectively.

As the frequency content of soft tissue artifact is similar to that of body motion, it becomes difficult to apply filtering techniques to compensate for these errors [Leardini et al. (2005)]. That being said, some compensation techniques have been developed to reduce the effects of soft tissue artifact, such as the calibrated anatomical system technique [Cappozzo et al. (1995)], the dynamic calibration technique [Lucchetti et al. (1998)], the point cluster technique [Andriacchi et al. (1998)] and the solidification procedure [Chèze et al. (1995)]. The techniques proposed by Cappozzo et al. [Cappozzo et al. (1995)] and Lucchetti et al. [Lucchetti et al. (1998)] make use of static and dynamic calibrations using maker clusters fitted onto rigid structures. The positions of skin mounted anatomical markers are determined relative to the coordinate frame constructed from the rigid cluster position and, depending on the static or dynamic relationship between the anatomical markers and rigid coordinate frame, the position of the anatomical markers is modified to minimize the changes in position relative to the rigid cluster [Leardini et al. (2005)]. The point cluster technique [Andriacchi et al. (1998)] consists of scattering a number of markers uniformly over a given segment and assigning a mass for each marker. The center of mass and inertia

tensor of the sum of all markers are computed at each time step, leading to the computation of the principle axes and moments of inertia of that segment [Andriacchi et al. (1998)]. At each time step, the magnitudes of each assigned mass (one for each marker) are modified in an attempt to minimize the changes in the segment's principle axes and moments of inertia [Andriacchi et al. (1998)]. This procedure leads to the position and orientation of the segment's local coordinate frame at each time step. In the solidification procedure proposed by Chèze et al. [Chèze et al. (1995)], a best-fit rigid triangle is determined from the displacement of three non-collinear skin-mounted markers. This rigid triangle is imposed at each time step using the single value decomposition algorithm of Söderkvist and Wedin's least squares method [Söderkvist and Wedin (1993)], which eliminates the relative motion between markers. This method generates a rigid-body motion and allows for the unambiguous use of rigid-body theory while maintaining the kinematic accuracy of the least-squares method [Leardini et al. (2005)].

Summary of Literature Review

Upon reviewing the double-pendulum and triple link kinematic models used to analyze the kinematics of the golf swing, the major limitation is the displacement of the central hub, as it has not been related to the more proximal segments of the golf swing and no attempts have been made to confirm the center of rotation of the upper link. More recent studies have examined the three-dimensional kinematics of the golf swing to determine the effect of segment rotation on club head velocity. These studies have expressed segment rotation relative to an imposed reference system, which might not provide the best representation of segment rotation, especially if the rotation does not occur about a fixed point. ISA theory has been successfully used to identify joint position and study segment rotation and could therefore be used in golf swing analysis to determine segment angular velocity about an instantaneous axis of rotation. This would not only provide the best approximation of segment true rotation, but it would also allow for ISA to change position and orientation during the motion. As discussed,

stereophotogrammetric systems are effective measurement tools in biomechanical analysis, as they provide accurate displacement of body features without imposing mechanical constraints. By measuring the position of at least three spherical markers on a given segment, the ISA can be computed to study segment kinematics. Therefore, the following study will use stereophotogrammetric measurements to compute a segment's ISA. By applying this method to the primary segments of body motion, the golf swing will be analyzed as a system of ISA.

Chapter 3 Methods

The following section outlines the methodology followed to study the kinematic sequence of the golf swing by applying ISA theory. This includes the experimental apparatus, consisting of an optimal stereophotogrammetric system, used to measure the displacement of body landmarks. The methodology used to compute the ISA is described for both rigid body displacements and stereophotogrammetric displacements. Finally, the golf swing model employed to study golf swing kinematics is presented.

3.1 Experimental Apparatus

Positional measurements of body landmarks were obtained by stereophotogrammetry, as this provides three-dimensional displacements of body segments without imposing mechanical constraints [Everaert et al. (1999)]. Data collection was carried out at the Syncrude Centre for Motion and Balance at the Glenrose Rehabilitation Hospital, in Edmonton, Alberta, Canada. The facilities are equipped with a Motion Analysis HiRes (Motion Analysis, Santa Rosa, California, USA) passive-marker optical system. A total of eight cameras (Eagle Digital; Motion Analysis, Santa Rosa, California, USA) are positioned within the laboratory as shown in Figure 3-1. The system utilized EVaRT v.4.2 software (Motion Analysis, Santa Rosa, California, USA) to compute reflective markers position. System calibration is conducted as per manufacturer's procedures [Motion Analysis (2006)], where the short form is outlined in Appendix 1.

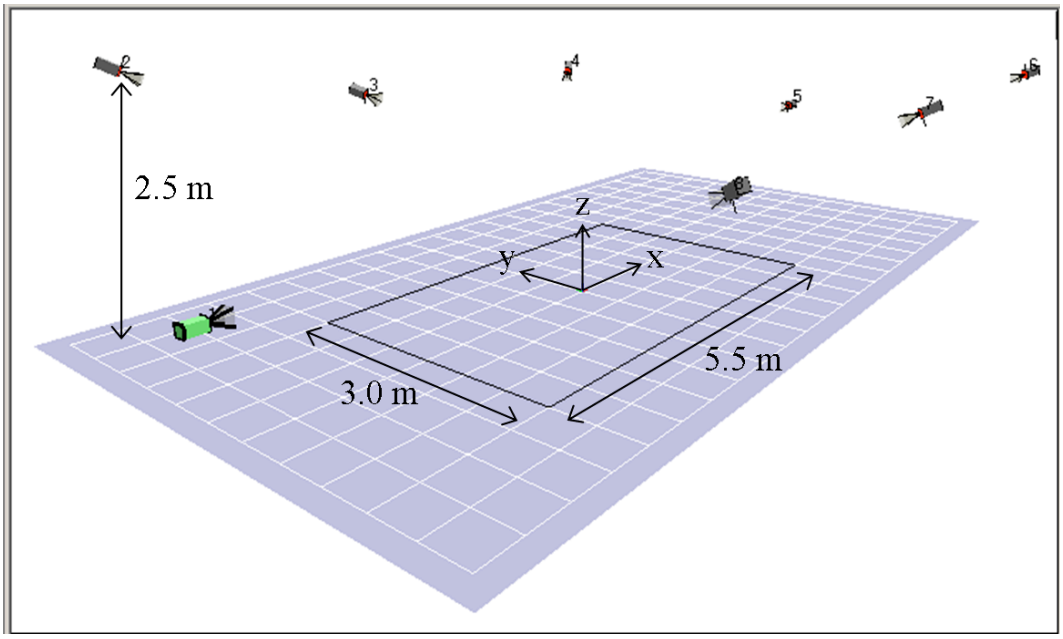

Figure 3-1: Stereophotogrammetric system, Syncrude Centre for Motion and Balance; gait specific camera configuration. Measurement dimensions are 5.5m in length (along x-axis), 3.0m in width (along y-axis) and 2.0m in height (along z-axis).

The stereophotogrammetric system shown in Figure 3-1 is used for gait analysis in patients suffering from movement disorders. The cameras are operated at a sampling rate of 60 Hz, an established standard for gait analysis, and are positioned to create a large measurement volume, the dimensions of which are shown in Figure 3-1. More specifically, the majority of cameras (6 out of 8) are positioned above the measurement volume with a field of vision directed to the floor of the lab (xy-plane). This camera setup is suited for the low-frequency motions involved in gait analysis and the limited occurrence of marker occlusion, where body segments or external objects obscure the field of view of multiple cameras. When attempting to measure the displacement of body segments during the golf swing with such an experimental setup, two issues arise. First, a sampling rate of 60 Hz is too low for golf swing analysis and does not satisfy Shannon's Sampling theory when applied to the displacement of the golf club [Leigh (1992)]. Second is marker occlusion, as the motion of the arms during the golf swing can occlude other markers placed on the body from the camera field of view. These two issues will be investigated in the Measurement Accuracy and Marker Occlusion Studies, respectively.

3.1.1 Measurement Accuracy Study

As the displacement of the golf club head is non-cyclical, a distinct frequency cannot be associated with its motion. However, for the purpose of verifying Shannon's sampling theory, the following assumptions are made. Assuming the displacement of the golf club head just prior to impact can be modeled as a rotation of 90 degrees, 0.25 rotations, occurring within 50 milliseconds, as the duration of club head release during the downswing has been found to last approximately 50 to 100 milliseconds [Penner (2003)], the frequency of golf club head motion, ω_c, can be approximated as

$$\omega_C = \frac{0.25\ rotations}{50m\sec} = \frac{0.25\ cycles}{50\times10^{-3}\sec} = \frac{5\ cycles}{\sec} = 5\ Hz \qquad \textbf{(3-1)}$$

According to Shannon's sampling theory, also referred to as the sampling theory, a function is uniquely determined by a discrete set of sampling values provided that the sampling frequency, ω_S, is twice the largest frequency in the sampled power spectrum [Leigh (1992)]. The limiting sampling frequency, the Nyquist Frequency (ω_{Ny}), is given by $\omega_{Ny}= 2b$, where b is the highest frequency in the sampled power spectrum. In practice, the sampling frequency should be 5 to 10 times the highest frequency thought to be present [Leigh (1992)]. Therefore, the sampling frequency required to capture the displacement of the golf club head is as follows:

$$\omega_S = 10\times\omega_{Ny} = 10\times\left(2\times\omega_{Ny}\right) = 10\times\left(2\times5\ Hz\right) = 100\ Hz \qquad \textbf{(3-2)}$$

Therefore, a sampling frequency of 60 Hz is not sufficient to avoid aliasing of the displacement signal and a higher sampling frequency is required. Furthermore, if the position of the clubface at impact is to be measured, than a larger sampling frequency would be required as the effect of impact on clubface orientation is a high frequency event [Watanabe and Hokari (2006)]. That being said, if the cameras are operated a higher frequencies, to avoid aliasing of high frequency maker displacements, does this have a significant effect on measurement

accuracy? Furthermore, does the high velocity movement of the club head experienced in the golf swing also have an effect on measurement accuracy? Although researchers have studied the effects of many variables on the accuracy characteristics of stereophotogrammetric systems, as discussed in Section 2.3.2, it appears as though few have studied the effects of sampling rate [Polk et al. (2005)] and no studies have been carried out for high velocity movements.

The objectives of the current study are to determine the effects of sampling rate on the accuracy of measuring (1) high-speed rotational motions and (2) to determine the effects of sampling rate on measurement noise, for measuring the position of a static marker, and to relate these effects to the measurement of small linear displacements between markers. Both high-speed rotational motions and small linear displacements were studied to best represent all possible motions involved in stereophotogrammetry.

Although the resolution of the cameras decreases when a maximum sampling rate is met, this simply reduces the field of view of the cameras. Therefore, if the cameras are positioned to form the required capture volume, the measurement accuracy should not be affected. It is hypothesized that the cameras' accuracy characteristics, described with the terms precision and bias, are independent of sampling rate.

3.1.1.1 Experimental Apparatus

The experimental apparatuses were controlled mechanical devices generating accurate and repeatable motions and once calibrated served as references to establish the accuracy characteristics of the stereophotogrammetric system.

Rotational Apparatus

The device shown in Figure 3-2 (a), which consists of a slender rotating disk fitted with four reflective spherical markers (Markers 1 to 4) and one non-reflective spherical marker (Ghost marker), was developed and fabricated at the University

of Alberta's Mechanical Engineering Machine Shop (University of Alberta, Edmonton) to study the effects of sampling rate on the accuracy of measuring high speed rotational motions. This apparatus was developed based on the Gait and Clinical Movement Analysis Society proposal for Standards Assessment of Motion System Accuracy [Piazza et al. (2007)]. The proposed standard device, developed by Richards [Richards (1999)], consists of a beam rotating at an angular velocity of 60 rpm, producing marker velocities of approximately 3.14 m/s. As this device does not produce marker velocities consistent with club head motion, typically ranging from 39-52 m/s [Nesbit (2005)], the current device was developed.

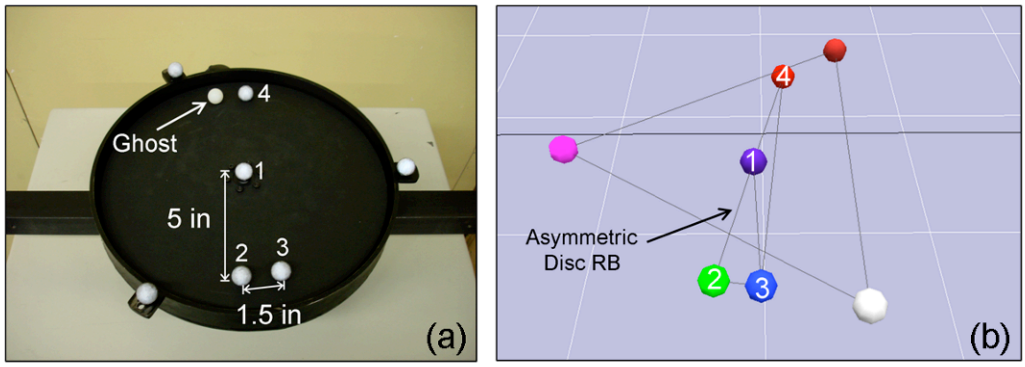

Figure 3-2: Rotational apparatus; (a) Reference lengths 1 and 2, (b) Asymmetric disc RB

Two constant reference lengths of 5 inches and 1.5 inches served as standards to evaluate the measurements of the optical system. Dynamic balancing of the rotating disk was achieved using two spherical markers placed at the polar opposites of the orbiting reflective markers (Marker 4 and Ghost marker). When linked together, Markers 1, 2, 3 and 4 create an asymmetric rigid body (RB), which can be more easily identified by the stereophotogrammetric system when compared to a symmetric rigid body (Figure 3-2 (b)). The slender disk is driven by a hand grinder (Bosch Tool Corporation, Farmington Hills, Michigan, USA) controlled by a Variac Autotransformer (120 V, Type W10 MT3, General Radio Company, Concord, Massachusetts, USA). Angular velocities ranged from 0 to 11000 RPM and were calibrated with a Strobotac stroboscope (General Radio

Company, Concord, Massachusetts, USA). The entire apparatus is mounted on a variable height table (disk height range of 35 to 53 inches from the floor).

Translational Apparatus

To study the effects of sampling rate on the accuracy of measuring small linear displacements, the apparatus shown in Figure 3-3 was developed. It consists of a Thorlabs MT1 1/2" translation Stage (Thorlabs, Newton, New Jersey, USA) fitted with two reflective spherical markers. The first marker is placed on a stationary portion of the device, *Stationary Marker*, while the second marker is placed in the center of the translating surface, *Translating Marker*, thus creating a linear relative motion between markers (see Figure 3-3). The translating surface is actuated by a screw micrometer with a maximum travel of 0.5" and a resolution of 0.001" per graduation. The reference displacements are given by the micrometer, which will serve as standards to evaluate the measurements of the optical system. This apparatus provides a high level of accuracy for the reference system since it controls the displacement of the markers, as opposed to controlling the distance between markers, which can result in faulty measurement due to skewed marker attachments or imperfect spherical markers [Everaert et al. (1999)]. The translation stage is mounted on Manfrotto 128RC tripod (Manfrotto, Bassano del Grappa, Italy).

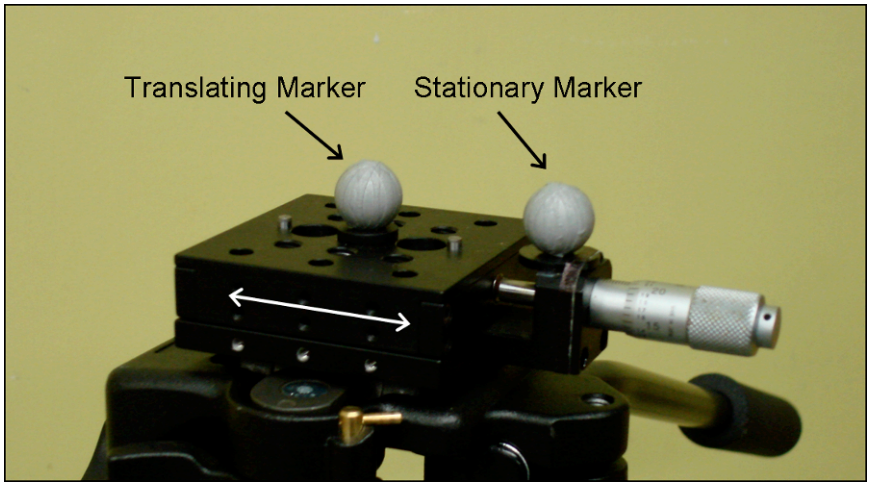

Figure 3-3: Thorlabs MT1 ½" translation stage; Translating and stationary markers

Calibration of experimental apparatus

In order to correctly assess the accuracy characteristics of the system, it was essential to calibrate the experimental apparatus. This ensures that the reference system provides an accurate "gold standard" for establishing measurement error. A coordinate-measuring machine, CMM (MicroVal, Brown & Sharp, Rhode Island, USA), was used to establish the distances between the centroids of spherical markers. In the case of the rotational apparatus, the coordinates of *Markers 1, 2 and 3* were measured and reference distances of 5.01322" and 1.49665" were calculated. These distances represent the mean measurements of the CMM from three trials, where the complete results are shown in Table A2-1 and Table A2-2 of Appendix 2. In the case of the translational apparatus, the coordinates of the stationary and translating markers were measured for all micrometer positions and the resulting displacements were calculated. Although the translational apparatus is actuated by a micrometer of fine tolerance, measuring the displacements with the CMM was necessary to account for any misalignment of the two markers. Results are shown in Table A2-3 of Appendix 2. Furthermore, the stereophotogrammetric system was calibrated as per manufacture's procedures, outlined in Appendix 1.

3.1.1.2 Experimental Methods

Once calibrated, the stereophotogrammetric system was successively set for 4 sampling rates: 60 Hz, 125 Hz, 250 Hz and 500 Hz. The lowest sampling rate, 60 Hz, is an established standard for gait analysis, while 500Hz exceeds the maximum setting for which the cameras can operate with a full field of view. The experimental procedures outlined below were repeated for the 4 sampling rates.

Rotational Accuracy

The rotational apparatus was successively set for 5 speeds: 750 RPM, 1500 RPM, 2250 RPM, 2800 RPM and 3500 RPM. For each setting, three displacement cycles were performed using the following procedure. The rotational apparatus

was positioned in three different locations relative to the calibration volume (Figure 3-4). Positions 1 and 3 covered the outer extremities of the volume, while Position 2 was situated in the center, which coincides with the origin of the captured volume. For each position, the displacements were carried out at two different heights: where the rotating disk was set to 35 inches (Height 1) and then raised to 53 inches (Height 2). For each of the 6 settings (3 positions X 2 heights), the testing device was sequentially set to each of its 5 speeds, where each speed corresponds to a displacement. Taken together, the five displacements made up one displacement cycle. Each displacement was captured for a period of 10 seconds, where a total of 90 displacements were performed (5 speeds X 6 settings X 3 cycles).

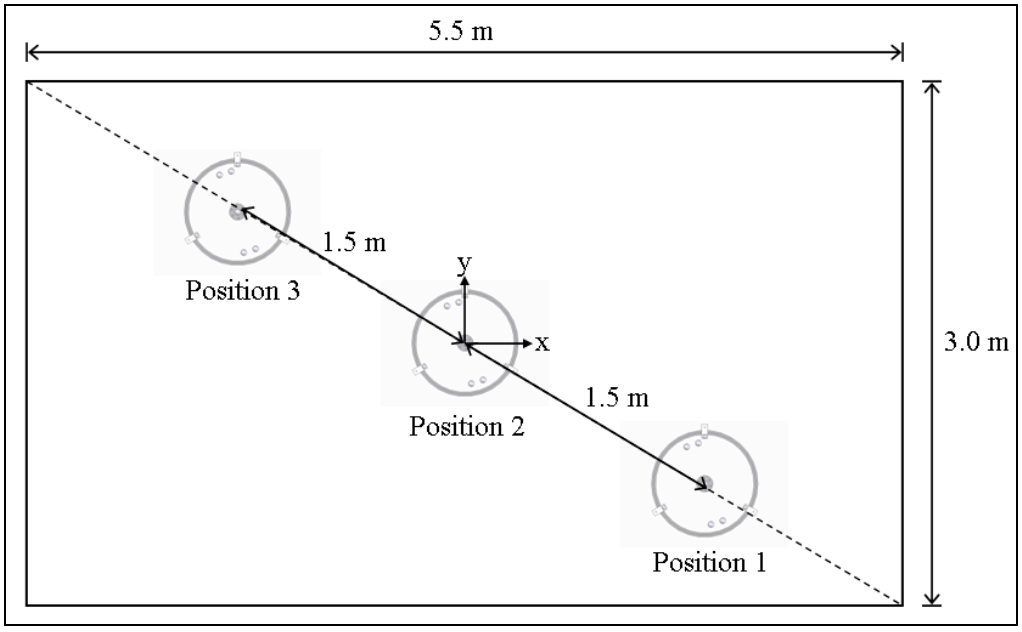

Figure 3-4: Diagram of the positioning of the rotating device in the volume of capture

Translational Accuracy

The translation stage was successively set for 5 displacements: 0.025 inches, 0.050 inches, 0.100 inches, 0.250 inches and 0.400 inches. For each setting, three displacement cycles were performed, using the following procedure. The translational apparatus was placed in three positions relative to the calibration

volume, as described in Figure 3-4. For each position, the displacements were performed at a height of 35 inches, which coincides with the height of the rotating disk when positioned at Height 1. Furthermore, for each position, the displacements were carried out in three orientations: 0 degrees (along the length of the volume, x direction), 90 degrees (along the width of the volume, negative y direction) and 45 degrees (Figure 3-5). For each of the 9 settings (3 positions X 3 orientations), the testing device was sequentially set to each of its 5 displacements, where the five displacements make up one displacement cycle. Each displacement was captured for a period of 5 seconds, where a total of 135 displacements are performed (5 displacements X 9 setting X 3 cycles).

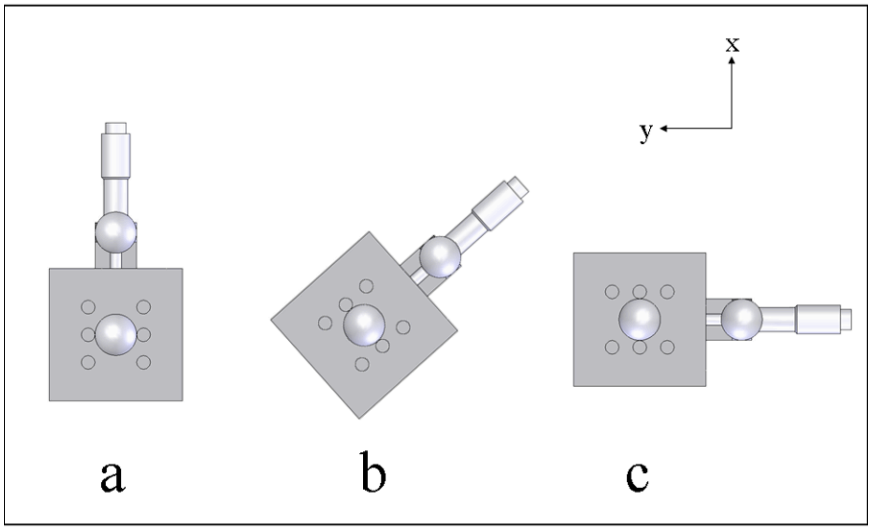

Figure 3-5: Translation stage orientation; a) 0 degrees, b) 45 degrees, c) 90 degrees

3.1.1.3 Analysis

Post-Processing

Post-processing in EVaRT involves generating three-dimensional trajectories of Markers 1 to 4 of the rotating apparatus and the Stationary and Translating Markers of the translational apparatus. Rigid body definition procedures were followed to improve identification of markers that undergo large displacements; Markers 1 to 4 from the rotating disk rigid body (Figure 3-2 (b)). For all sampling rates and settings, 60 frames of data were analyzed. This results in a minimum of

1.5 rotations for all combinations of sampling rate and rotational speed. The translational apparatus consists of two markers of variable distance between them, and are thus not a rigid body. However, since the displacements were conducted on a small scale, there is no need to aid the system in identifying the markers from one frame to another. For all sampling rates, 300 frames of data were analyzed, which represents the maximum number of frames collected at the lowest sampling rate (60 Hz x 5 sec).

Data Analysis

Rotational Accuracy

The accuracy characteristics of the rotational apparatus were determined by the system's ability to measure two reference lengths. *Length 1* is measured from *Marker 1* to *Marker 2*, which is 127.336 mm (5.01322in), while *Length 2* is measured from *Marker 2* to *Marker 3*, which is 38.015mm (1.49665in), where both reference lengths were determined by the CMM. For each data frame, these reference lengths were calculated from the three-dimensional trajectories generated by the motion capture system. For each setting, speed and displacement cycle, 60 frames of data were processed, which could result in a total of 60 separate measurement values. However, each time the system lost sight of a marker, due to marker occlusion, a measurement was also lost. Therefore, the total number of measurement, n_T, is given by

$$n_T = 60 - n_{LT} \quad \textbf{(3-3)}$$

where n_{LT} is the total number of lost measurements. For each setting and speed, the measurements from these frames are averaged and the results from the three cycles (n_{cycles}) are also averaged, which gives one reference measurement for each setting (position and height) and speed. The average reference *Length 1* is given by

$$Length\,1 = \frac{\sum_{i=1}^{n_{cycles}} \left(\frac{\sum_{j=1}^{n_T} \left\| \overrightarrow{v_{1-2}} \right\|_j}{n_T} \right)_i}{n_{cycles}} = \frac{\sum_{i=1}^{n_{cycles}} \left(\frac{\sum_{j=1}^{n_T} \left(\sqrt{(x_1 - x_2)^2 + (y_1 - y_2)^2 + (z_1 - z_2)^2} \right)_j}{n_T} \right)_i}{n_{cycles}} \quad \textbf{(3-4)}$$

where x_1, y_1 and z_1 are the coordinates of *Marker 1*, x_2, y_2 and z_2 are the coordinates of *Marker 2* and n_{cycles} is equal to 3 (three measurement cycles). The average reference *Length 2* is given by

$$Length\,2 = \frac{\sum_{i=1}^{n_{cycles}} \left(\frac{\sum_{j=1}^{n_T} \left\| \overrightarrow{v_{2-3}} \right\|_j}{n_T} \right)_i}{n_{cycles}} = \frac{\sum_{i=1}^{n_{cycles}} \left(\frac{\sum_{j=1}^{n_T} \left(\sqrt{(x_2 - x_3)^2 + (y_2 - y_3)^2 + (z_2 - z_3)^2} \right)_j}{n_T} \right)_i}{n_{cycles}} \quad \textbf{(3-5)}$$

where x_3, y_3 and z_3 are the coordinates of *Marker 3*.

To quantify the accuracy of the Motion Analysis system, experimental measurement values are compared to CMM measurements using the terms precision and bias as described by ASTM International [ASTM International (2008)]. Bias refers to the systematic difference between an accepted reference value (CMM) and a set of measurement values (stereophotogrammetric system).

Precision relates to the closeness of measurements values to each other under similar experimental conditions. In the present case, bias is given by

$$Bias\ i = abs\left((Length\ i)_{CMM} - Length\ i\right) \qquad where\ i = 1,2 \tag{3-6}$$

while the precision is given by the standard deviation (S) of the measured population.

Translational Accuracy

The accuracy characteristics of the translational apparatus are determined by the system's ability to measure the displacements of the micrometer. Five displacements were carried out with the translational apparatus: 0.02543 in, 0.04949 in, 0.10122 in, 0.25002 in, 0.39831 in (as measured by the CMM). For each frame of the data, these displacements were calculated from the three-dimensional trajectories generated by the motion capture system. For each setting, displacement and displacement cycle, 300 frames of data were processed, which results in a total of 300 separate measurement values. For each setting and displacement, the measurements from these 300 frames are averaged and the results from the three orientations and three cycles are also averaged, which gives one reference measurement for each position and displacement. For each micrometer displacement, the measurement value from the optical system is given by the displacement of the *Translating Marker* from the zero position, on the micrometer scale, to the displaced position, also on the micrometer scale. For example, the first displacement (*Disp 1*) is given by

$$Disp\,1 = \frac{\sum_{i=1}^{n_{cycles}} \left(\frac{\sum_{j=1}^{300} \left\| \overrightarrow{v_{0-0.025}} \right\|_j}{300} \right)_i}{n_{cycles}}$$

$$= \frac{\sum_{i=1}^{n_{cycles}} \left(\frac{\sum_{j=1}^{300} \left(\sqrt{(x_0 - x_{0.025})^2 + (y_0 - y_{0.025})^2 + (z_0 - z_{0.025})^2} \right)_j}{300} \right)_i}{n_{cycles}} \quad \textbf{(3-7)}$$

where x_0, y_0 and z_0 are the coordinates of the *Translating Marker* at the zero position, $x_{0.025}$, $y_{0.025}$ and $z_{0.025}$ are the coordinates of the *Translating Marker* at the 0.025" micrometer position and n_{cycles} is equal to 9 (3 orientations x 3 measurement cycles).

To quantify the translational accuracy of the stereophotogrammetric system, the experimental measurement values are compared to the CMM measurements using the terms precision and bias, as was the case for the Rotational apparatus.

Statistical Analysis

Statistically significant differences between samples were evaluated and comparison of standard deviations was also performed to assess difference between population variance.

For rotational measurements, three cycles were performed for each sampling rate, setting (position and height) and speed. Therefore, each setting and speed has 4 populations of data, one for each sampling rate, each consisting of 3 separate measurements. To determine if statistical significance can be found between sampling rates, these 4 populations were compared by way of a student t-test using a 5 percent significance level (p-value = 0.05). The student t-test evaluated the null hypothesis (h_0) that data in *population x* and *population y* are independent random samples from normal distributions with equal means and equal but unknown variances, against the alternative (h_1) that the means are not equal.

For translational measurements, three cycles were performed for each orientation, sampling rate and setting (position and displacement). Therefore, each setting (position and displacement) has 4 populations of data, one for each sampling rate, each consisting of 9 separate measurements. To determine if statistical significance can be found between sampling rates, these 4 populations were compared by way of the student t-test described above.

To verify the assumption of equal but unknown population variances, the standard deviations of each population, from the same setting (4 populations), were compared. If the ratio of the maximum to minimum standard deviation was less than two, the populations were said to have equal variances

3.1.1.4 Results

For rotational accuracy, measurement bias and precision of reference *Length 1* are shown for all settings (position, height) and for all 5 rotational speeds, in Table A2-4 and Table A2-5 and statistical analysis of variance between measurement populations are given in Table A2-6 and Table A2-7, all in Appendix 2. Measurement bias and precision of reference *Length 2* are shown for all settings (position, height) and for all 5 rotational speeds, in Table A2-8 and Table A2-9 and statistical analysis of variance between measurement populations are given in Table A2-10 and Table A2-11, all in Appendix 2. For translational accuracy, statistical analysis of variance is given in Table A2-14 and Table A2-15 of Appendix 2.

Rotational Accuracy

Measurement bias and precision of reference *Length 1* and *Length 2* are given in Table 3-1. Results are provided for each measurement position, height and have been averaged for all 5 rotational speeds.

Table 3-1: Rotational Accuracy- Lengths 1 and 2-Measurement Bias and Precision (S: Standard Deviation) at 3 different positions and 2 different Heights at 4 different sampling rates

Position	Height	Sampling Rate [Hz]	Length 1 Bias [mm]	Length 1 Precision (S) [mm]	Length 2 Bias [mm]	Length 2 Precision (S) [mm]
1	1	60	0.187	0.222	0.343	0.318
		125	0.087	0.124	0.368	0.228
		250	0.280	0.180	0.188	0.178
		500	0.321	0.096	0.082	0.064
	2	60	0.971	0.267	0.531	0.360
		125	1.017	0.275	0.461	0.224
		250	0.732	0.402	0.329	0.525
		500	0.313	0.206	0.135	0.181
2	1	60	0.094	0.056	0.083	0.046
		125	0.109	0.055	0.110	0.043
		250	0.197	0.088	0.062	0.049
		500	0.174	0.096	0.082	0.071
	2	60	0.781	0.133	0.198	0.162
		125	0.823	0.176	0.234	0.199
		250	0.911	0.233	0.226	0.152
		500	0.736	0.356	0.254	0.179
3	1	60	0.116	0.152	0.136	0.136
		125	0.079	0.214	0.096	0.194
		250	0.153	0.225	0.186	0.232
		500	0.283	0.248	0.130	0.176
	2	60	0.248	0.105	0.203	0.104
		125	0.235	0.164	0.286	0.141
		250	0.401	0.111	0.238	0.072
		500	0.460	0.071	0.201	0.111

Translational Accuracy

Measurement bias and precision of reference displacements 1 through 5 are given in Table 3-2 and Table 3-3, respectively. Results are provided for each measurement position and sampling rate, and have been averaged over the three trials.

Table 3-2: Translational Accuracy- Displacement Bias for 3 positions at 4 sampling rates for 5 displacement measurements.

Position	Sampling Rate [Hz]	Displacement Bias Disp. 1 [mm]	Disp. 2 [mm]	Disp. 3 [mm]	Disp. 4 [mm]	Disp. 5 [mm]
1	60	0.242	0.358	0.255	0.160	0.203
	125	0.145	0.232	0.294	0.119	0.190
	250	0.148	0.387	0.212	0.170	0.066
	500	0.127	0.219	0.086	0.363	0.090
2	60	0.135	0.226	0.153	0.165	0.179
	125	0.085	0.095	0.077	0.059	0.104
	250	0.148	0.146	0.137	0.120	0.197
	500	0.097	0.134	0.096	0.090	0.166
3	60	0.139	0.242	0.188	0.274	0.478
	125	0.179	0.235	0.226	0.503	0.704
	250	0.132	0.228	0.264	0.237	0.529
	500	0.106	0.336	0.308	0.326	0.499

Table 3-3: Translational Accuracy- Displacement Precision (S: Standard deviation) for 3 positions at 4 sampling rates for 5 displacement measurements.

Position	Sampling Rate [Hz]	Displacement Precision (S) Disp. 1 [mm]	Disp. 2 [mm]	Disp. 3 [mm]	Disp. 4 [mm]	Disp. 5 [mm]
1	60	0.372	0.592	0.311	0.244	0.323
	125	0.122	0.257	0.311	0.133	0.276
	250	0.137	0.415	0.224	0.212	0.075
	500	0.188	0.232	0.099	0.477	0.128
2	60	0.172	0.322	0.216	0.229	0.264
	125	0.101	0.138	0.099	0.074	0.103
	250	0.193	0.184	0.156	0.133	0.204
	500	0.128	0.164	0.119	0.133	0.220
3	60	0.181	0.290	0.232	0.350	0.363
	125	0.217	0.280	0.298	0.801	1.007
	250	0.184	0.267	0.412	0.369	0.598
	500	0.150	0.379	0.366	0.362	0.448

3.1.1.5 Discussion

Rotational Accuracy

Average results of the rotational displacements are shown in Table 3-1. Measurement bias for *Lengths 1* and *2* are shown for all settings, position and height. Results have been averaged for all 5 rotational speeds. For both measurements the bias was significantly smaller in the center of the captured volume when compared to the outer extremities, by an average factor of 5.65 and 2.20 for *Lengths 1* and *2*, respectively. The same can be said for the standard deviation. The maximum bias for measurement of *Length 1* was 0.302mm in the center of the volume (Position 2, Height 1) and 1.289mm in the extremities of the volume (Position 1, Height 2). The maximum bias for measurement of *Length 2* was 0.197mm in the center of the volume (Position 2, Height 1) and 0.9036 in the extremities of the volume (Position 1, Height 2). It can be seen that the bias on a given measurement is nearly unaffected by distance between markers.

A statistical variance test was conducted to verify the null hypothesis of equal but unknown variance between sampling rate populations. The null hypothesis was rejected if the ratio of standard deviations was larger than 2. For the measurements of *Lengths 1* and *2*, 55 percent and 49 percent of the tests conducted could not reject the null hypothesis, respectively. As the majority could not reject the null hypothesis, student t-tests for populations of equal but unknown variance were carried out for all settings to produce a standard test. Of the 180 t-tests conducted for *Lengths 1* and *2*, 29 and 26 rejected the null hypothesis at a 5 percent significance level, respectively. Therefore, 84 percent of measurements of *Length 1* and 86 percent of measurements of *Length 2* taken within the same setting but at different sampling rates have the same mean value at a 5 percent significance level. Therefore, the results indicate that a camera's sampling rate has no statistically significant effect on the accuracy of measuring high-speed marker displacements. However, markers placement within the measurement volume has

an important effect, as measurement bias and standard deviation increase in the extremities of the measurement volume.

Translational Accuracy

Results of linear translations measurements are shown in Table 3-2 and Table 3-3, which show average of the measurement bias and average measurement standard deviation, respectively, for the 5 linear displacements for each of the 4 sampling rates and 3 positions. Bias and standard deviation were both noticeably smaller, by an approximate ratio of 2.5, in the center of the capture volume when compared to the outer extremities. The average bias for measurements in the center of the volume was 0.137mm while the average standard deviation was 0.176mm. This bias would result in a 5 percent measurement error on a displacement of approximately 2.750mm, while the standard deviation of 5 percent would be achieved on a displacement of approximately 3.500mm. The statistical variance test, as described above, was conducted to verify the null hypothesis of equal but unknown variance between sampling rate populations. Of the 90 variance tests conducted, 23 rejected the null hypothesis of equal variance. As the majority (75 percent) could not reject the null hypothesis, student t-tests for populations of equal but unknown variance were carried out for all settings to produce a standard test. All t-test performed could not rejected the null hypothesis at a 5 percent significance level. Therefore, all measurements taken within the same setting but at different sampling rates have the same mean value at a 5 percent significance level. Therefore, the results indicate that a camera's sampling rate has no statistically significant effect on the accuracy of measuring small linear displacement.

3.1.1.6 Conclusion

The current study investigated the effects of sampling rate on the accuracy characteristics of a stereophotogrammetric system for measuring high-speed rotational motions and small linear displacements. Statistical analysis showed, for

a majority of rotational accuracy tests and all translational accuracy tests, that measurements taken within the same setting but at different sampling rates had the same mean at a 5 percent significance level. For both high-speed rotational measurements and small-linear displacements, measurement bias and standard deviation is highly dependent on the position within the capture volume. Measurements taken within the center of the volume have smaller bias, and standard deviation when compared to measurements taken within the extremities. Camera positioning has an important influence on these results, as it dictates the calibrated volume. Therefore, the main conclusion of this study is that a camera's sampling rate has no statistically significant effect on measurement accuracy, while the position of the markers within the measurement volume has an important effect. Therefore, the position of the cameras must be carefully selected, as this dictates the calibrated volume and can affect marker occlusion, which will be investigated in the following study.

3.1.2 Marker Occlusion Study

The second issue encountered when applying a gait analysis setup to measure the displacement of the body during the golf swing is marker occlusion. During the golf swing, the motion of the arms can occlude other markers placed on the body from the field of view of the cameras. Although this issue cannot be completely avoided, it is possible to reduce the occurrence of marker occlusion by positioning the cameras in an optimal configuration.

The objective of the current study is to determine optimal camera positioning to (1) decrease the occurrence of marker occlusion when measuring the displacement of the body during the golf swing, (2) while maintaining measurement accuracy (as described in the Measurement Accuracy Study). Static measurements of two markers, placed at a known distance from one another, were used to determine measurement accuracy.

Camera configuration is a function of the movement being captured. Therefore, the position of the cameras can be altered to reduce marker occlusion and increase measurement accuracy, as smaller measurement volumes can reduce measurement error [Everaert et al. (1999)]. Consequently, it is hypothesized that marker occlusion can be reduced and measurement accuracy maintained by changing the positions of the cameras to form a "golf swing specific" measurement volume.

3.1.2.1 Experimental Apparatus

Camera Configurations

Two camera configurations were investigated: a "gait specific" configuration, used to measure the displacements experienced in gait analysis, and a "golf swing specific" configuration, used to measure the displacements of the body during the golf swing. The two camera configurations were calibrated by following the procedure outlined in Appendix 1.

Gait Specific Configuration

A standard camera configuration used in gait analysis is illustrated in Figure 3-1, where the coordinates of each camera are listed in Table 3-4. The camera positions produce a large measurement volume (dimensions listed Figure 3-1), allowing several gait cycles to be measured. The length and width of the measurement volume exceed what is required in golf swing analysis, as the motion of the golf swing is contained within a smaller and stationary working envelope. However, the height of the measurement volume is insufficient to measure the position of the golf club head throughout the golf swing. From preliminary data of Subject 1, the displacement of the club head reached heights (z component) of approximately 2.15 m, exceeding the height of the measurement volume.

Table 3-4: Gait specific camera configuration; camera position and orientation with respect to the global reference frame. Camera orientation given by elevation, azimuth and roll angles. Azimuth angle measured from the positive y axis (positive from y axis to x axis), elevation angle measured from the x-y plane (positive from the x-y plane to the z axis) and roll angle measured clockwise from position vector (vector from the origin to the camera position).

Camera	Position			Orientation		
	x [mm]	y [mm]	z [mm]	Elevation [deg]	Azimuth [deg]	Roll [deg]
1	-4739.578	-234.193	1167.973	1.45	-87.16	88.98
2	-3674.930	2677.346	2581.763	-25.93	-128.50	4.17
3	-454.524	3099.465	2031.327	.18.23	-152.94	161.52
4	3720.744	3151.017	1986.138	.25.46	124.46	-171.72
5	6234.114	477.214	1415.190	-3.34	91.44	90.44
6	6135.946	-2923.424	2142.139	-15.76	61.38	-0.17
7	1924.090	-2856.664	2089.799	-22.70	40.71	162.25
8	-2219.376	-2885.878	2026.466	-25.80	-38.34	-169.91

Golf Swing Configuration

In an effort to produce a golf swing specific setup, the camera configuration in Figure 3-6 was developed as a result of the following modifications to the gait specific camera configuration. First, the 4 cameras placed in the corners of the measurement volume, cameras 2, 4, 6 and 8, were placed higher and closer to the origin of the global reference frame. This reduced the footprint of the measurement volume, by decreasing the length (x-component) and width (y-component), while increasing its height (z-component) (see Table 3-5 for camera coordinates). The resulting measurement volume is concentrated about the origin of the global reference frame, where the fixed working envelop of the golf swing is located, and is better suited to measure the position of markers placed on the shoulders and to measure the displacement of the club head throughout the swing. Second, the 2 cameras perpendicular to the line of play, cameras 3 and 7, were lowered (decrease in z-coordinate) and their elevation was decreases, pointing away from the xy- plane of the measurement volume. The placement and orientation of cameras 3 and 7 aimed to decrease occlusion of markers placed on the shoulders and to aid in the measurement of markers placed on the club head. Third, the camera placed along the line of play, camera 1 , was placed closer to

the origin of the global reference frame, further concentrating the working envelop of the golf swing.

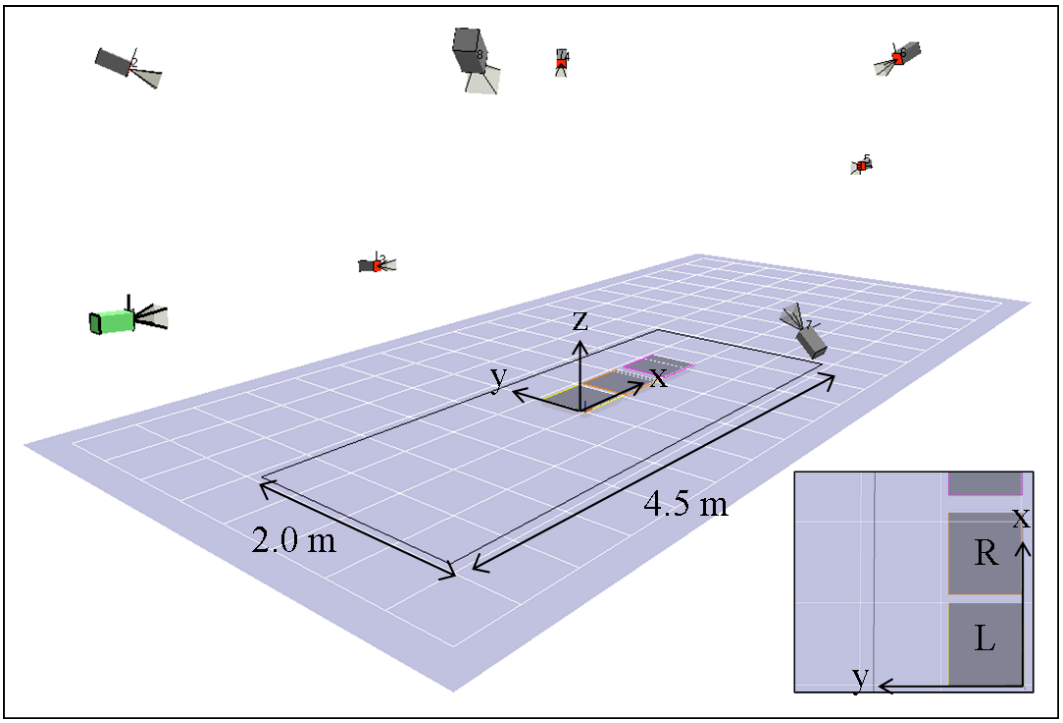

Figure 3-6: Stereophotogrammetric system, Syncrude Centre for Motion and Balance; golf specific camera configuration. Measurement dimensions are 4.5m in length (along x-axis), 2.0m in width (along y-axis) and 2.5m in height (along z-axis). Right platform (R) and left platform (L) denote foot placement for the stance of subject.

Table 3-5: Golf specific camera configuration; camera position and orientation with respect to the global reference frame. Camera orientation given by elevation, azimuth and roll angles. Azimuth angle measured from the positive y axis (positive from y axis to x axis), elevation angle measured from the x-y plane (positive from the x-y plane to the z axis) and roll angle measured clockwise from position vector (vector from the origin to the camera position).

Camera	Position			Orientation		
	x [mm]	y [mm]	z [mm]	Elevation [deg]	Azimuth [deg]	Roll [deg]
1	-3241.852	871.633	1283.026	-5.56	-88.72	-0.40
2	-2435.305	2055.388	2657.399	-24.95	-121.65	-1.28
3	302.033	2843.101	760.807	6.56	-174.29	6.13
4	2815.318	2551.156	2662.983	-30.34	127.47	2.33
5	6252.344	443.981	1415.127	-3.24	91.45	90.17
6	2756.122	-1191.825	2715.627	-27.20	62.52	0.64
7	558.878	-1551.489	838.813	37.94	-14.03	-64.29
8	-2636.209	-1366.787	2719.124	-26.33	-57.73	-4.04

Marker Occlusion of Golfer with Reflective Markers

To assess the effect of camera positioning on the occurrence of marker occlusion, reflective markers were placed on anatomical landmarks of the body and a series of golf swings were performed in each camera configuration. The position of reflective markers on the body are listed in Table 3-6, with their respective labels, and shown in Figure 3-7. A total of 4 markers were placed on the club head, as shown in Figure 3-8 and listed in Table 3-6. Markers affixed to the body were secured to the skin using hypoallergenic tape, while markers were screwed to the club head.

Table 3-6: Marker Placement- Marker occlusion study [Moore and Dalley (2006)]

Segment	Number of marker	Marker Placement	Marker Label
Pelvis	4	Right anterior superior iliac crest (RASIS)	P1
		Left anterior superior iliac crest (LASIS)	P2
		Right anterior posterior iliac crest (RPSIS)	P3
		Left anterior posterior iliac crest (LPSIS)	P4
Torso	3	Jugular notch	T1
		Right xiphoid	T2
		Left xiphoid	T3
Shoulders	4	Jugular notch	S1
		C7 cervical vertebra	S2
		Right acromion	S3
		Left acromion	S4
Left Arm	4	Left elbow, humerus lateral epicondyle	A1
		Left elbow, humerus medial epicondyle	A2
		Left wrist, radius styloid process	A3
		Left wrist, ulna styloid process	A4
Golf Club	4	Marker 1 of the club head	C1
		Marker 2 of the club head	C2
		Marker 3 of the club head	C3
		Marker 4 of the club head	C4

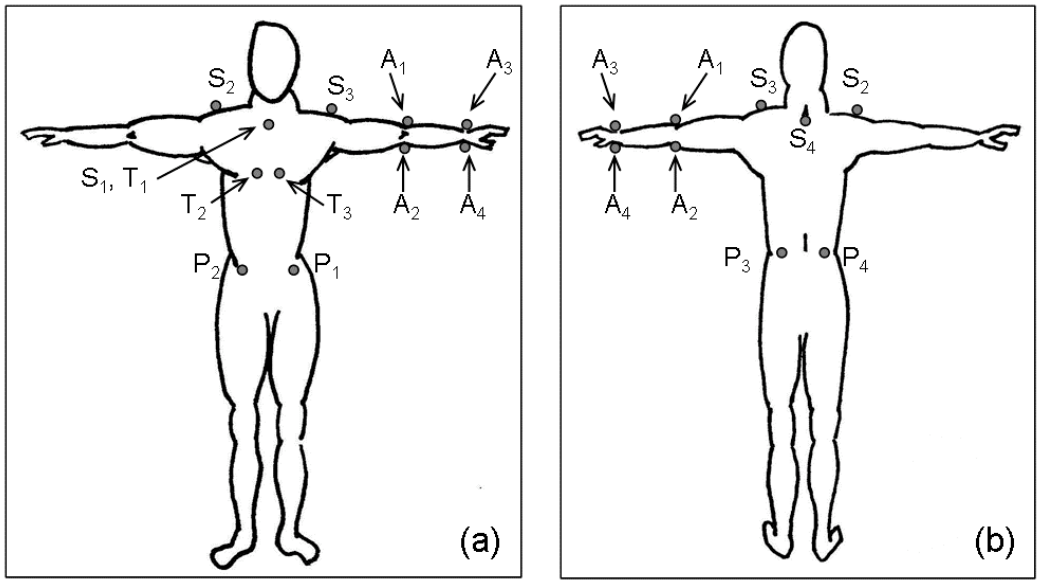

Figure 3-7: Marker Placement Guide-Marker occlusion study (a) Front view, (b) Rear view. Individual marker labels listed in Table 3-1

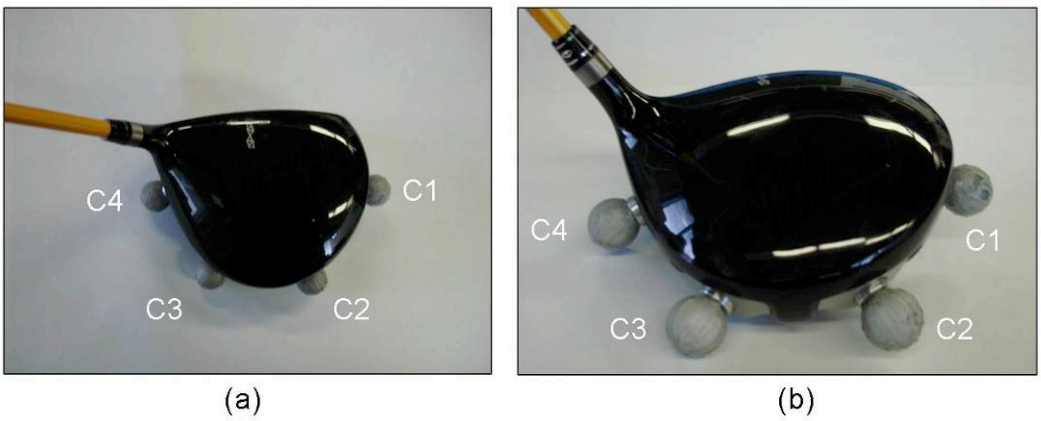

Figure 3-8: Reflective markers affixed to the club head; (a) Top view (b) Back view

Measurement of Inter-Marker Distance Accuracy

To assess the effect of camera positioning on measurement accuracy within the working envelop of the golf swing, the inter-marker distance between two reflective markers was measured in each camera configuration. The two reflective markers were placed on the translational apparatus of the Measurement Accuracy Study (see Figure 3-3), in a fixed micrometer position. As was the case in the Measurement Accuracy Study, a CMM was used to establish the distance between

the two makers, providing a reference length. The distance between the two reflective markers was 49.000 mm, where the *Translating marker* was placed in the 0.000 micrometer position. Inter-marker distance was calculated from the mean length of the *Position vector (relative to Stationary marker)* in Table A2-3 of Appendix 2.

3.1.2.2 Experimental Procedure

For each of the two camera configurations, the following experimental procedures were followed. Once calibrated, the stereophotogrammetric system was set to a sampling rate of 400 Hz. This sampling rate corresponds to the maximum sampling rate at which the cameras can operate at full field of view.

Marker Occlusion of Golfer with Reflective Markers

Once fitted with the reflective markers shown in Figure 3-7, Subject 1 performed three golf swings, corresponding to three trials. Subject 1 was situated near the origin of the global reference frame, with their right and left feet placed at the center of the right and left platform shown in Figure 3-6, respectively, and facing in the direction of the positive y axis. The position of all reflective markers was measured for the complete duration of each trial.

Measurement of Inter-Marker Distance Accuracy

To measure inter-marker distance, the translational apparatus was placed in 5 positions within the measurement volume, as shown in Figure 3-9. Assuming the working envelop of the golf swing can be characterized as a stationary sphere, defined by the motion of the club head, positions 1, 2 and 3 represent the position of the golfer while positions 4 and 5 denote the outer edge of the sphere. The coordinates of the midpoint between the *Translating* and *Stationary* markers are listed in Table 3-7. For each of the 5 positions, the static position of the markers was measured for a period of 10 seconds.

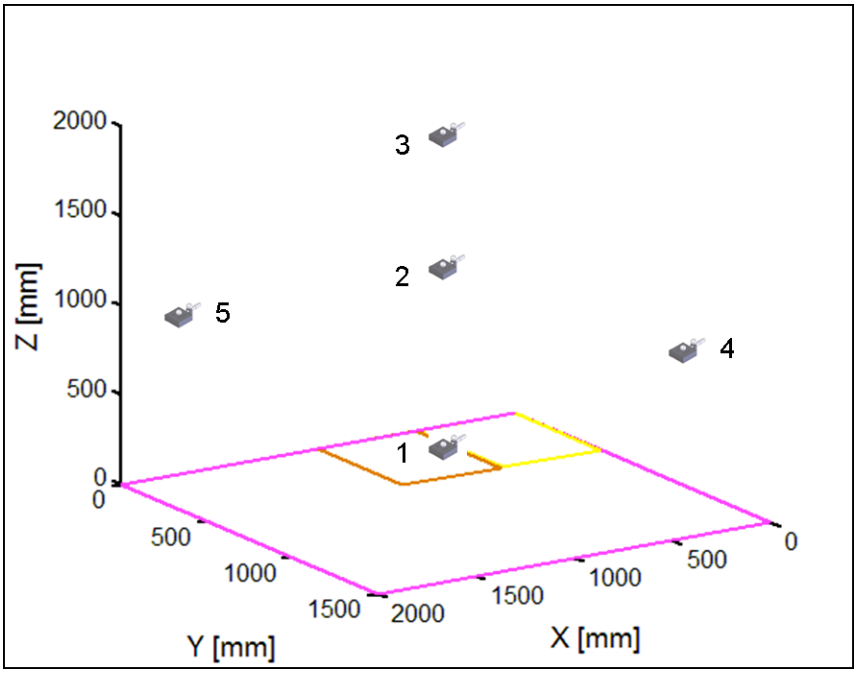

Figure 3-9: Positions 1 to 5 of the translating apparatus

Table 3-7: Position of the translational apparatus; coordinates of the midpoint between the translating and stationary markers

Position	Midpoint Coordinates		
	X [mm]	Y [mm]	Z [mm]
1	546.737	218.205	30.695
2	546.766	229.035	992.867
3	562.501	217.587	1732.338
4	353.453	1449.878	991.601
5	1865.573	242.883	993.671

3.1.2.3 Analysis

Marker Occlusion of Golfer with Reflective Markers

To quantify marker occlusion, the number of data frames where a reflective marker is lost during the downswing was identified. The start of the downswing is marked by the transition between the backswing arc and downswing arc of the club head, while the end of the downswing coincides with impact. The limits of the downswing will be further discussed in a following section (see Golf Swing

Model). For the purpose of this study, the data frames marking the limits of the downswing were identified by visual inspection. As swing duration was not constant, trials were normalized by the duration of the downswing. For each trial and reflective marker, the number of occluded data frames, n_o, was divided by the total number of data frames of the downswing, n_f, and expressed in percent occluded frames, calculated as follows:

$$Percent\ occluded\ frames = \frac{n_o}{n_f} \times 100\% \tag{3-8}$$

The percent occluded frames of each reflective marker were averaged for all 3 trials. Furthermore, to quantify the effect of marker occlusion on the computation of rigid body kinematics, the percent of frames where the position of a minimum of 3 markers is not known (three dimensional rigid body kinematics cannot be computed) are identified and normalized. Theses instance produce an indeterminate system and are labeled accordingly as *IS*.

Measurement of Inter-Marker Distance Accuracy

For each of the 5 positions of the translational apparatus within the measurement volume, the inter-marker distance, $Distance_I$, between the *Translating* and *Stationary* markers is given by

$$\text{Distance}_1 = \frac{\sum_{i=1}^{n_{trials}} \left(\frac{\sum_{j=1}^{n_f} \left(\sqrt{(x_S - x_T)^2 + (y_S - y_T)^2 + (z_S - z_T)^2} \right)_j}{n_f} \right)}{n_{trials}} \tag{3-9}$$

where x_S, y_S and z_S are the coordinates of the *Stationary marker*, x_T, y_T and z_T are the coordinates of the *Translating marker* in the 0.000 micrometer position, n_f is the number of frames (400 Hz x 10 sec = 4000) and n_{trials} is the number of trials

(equal to 3). The experimental measurement values are compared to the CMM measurements using the terms precision and bias, as described in the Measurement Accuracy Study. For each position of the translational apparatus, the bias between the two measurements is given by

$$Bias = abs\left(\left(Distance_1\right)_{CMM} - Distance_1\right) \quad \textbf{(3-10)}$$

while the precision is given by the standard deviation (S) of the measured population.

Statistical Analysis

Statistically significant differences between measurements taken in the two camera configurations were evaluated. For inter-marker distance measurements, three trials were performed for each of the 5 positions of the translational apparatus. Therefore, each camera configuration has a measurement population, each consisting of 15 measurements. To determine if statistical significance can be found between camera configurations, these 2 populations were compared by way of a student t-test using a 5 percent significance level (p-value = 0.05). The student t-test evaluated the null hypothesis (h_0) that data in *population x* and *population y* are independent random samples from normal distributions with equal means and equal but unknown variances, against the alternative (h_1) that the means are not equal.

3.1.2.4 Results

Marker Occlusion of Golfer with Reflective Markers

Marker occlusion results are given in Table 3-8 to Table 3-12, where the percentage of lost frames is given for the two camera configurations and for all markers placed on their respective segments. Each table provides results for markers placed on a single segment, where marker placement is given in Table 3-6.

Table 3-8: Percent occluded frames of the pelvis. IS denotes the percent frames where an indeterminate system is present (the position of three markers on the segment are occluded). Percent variation is the difference between the mean percent occluded frames of the two camera configurations, where a negative variation is a decrease and positive variation is an increase in occluded frames from the gait specific camera setup.

Camera Setup	Trial	Percent occluded frames Pelvis				
		P1 [%]	P2 [%]	P3 [%]	P4 [%]	IS [%]
1: Gait	1	54.76	0.00	2.38	3.17	3.97
	2	47.37	0.00	2.63	3.51	3.51
	3	50.00	0.00	3.92	5.88	6.86
	Mean	50.71	0.00	2.98	4.19	4.78
2: Golf	1	10.81	0.00	3.60	18.92	5.41
	2	9.09	0.00	8.26	16.53	6.61
	3	11.71	0.00	9.91	18.92	12.61
	Mean	10.54	0.00	7.26	18.12	8.21
Percent Variation		-40.17	0.00	4.28	13.93	3.43

Table 3-9: Percent occluded frames of the torso. IS denotes the percent frames where an indeterminate system is present (the position of three markers on the segment are occluded). Percent variation is the difference between the mean percent occluded frames of the two camera configurations, where a negative variation is a decrease and positive variation is an increase in occluded frames from the gait specific camera setup.

Camera Setup	Trial	Percent occluded frames Torso			
		T1 [%]	T2 [%]	T3 [%]	IS [%]
1: Gait	1	76.19	0.00	3.97	79.37
	2	81.58	0.00	0.00	81.58
	3	80.39	0.00	0.98	80.39
	Mean	79.39	0.00	1.65	80.45
2: Golf	1	34.23	16.22	0.00	40.54
	2	33.88	23.97	2.48	57.02
	3	46.85	24.32	1.80	66.67
	Mean	38.32	21.50	1.43	54.74
Percent Variation		-41.07	21.50	-0.22	-25.70

Table 3-10: Percent occluded frames of the shoulders. IS denotes the percent frames where an indeterminate system is present (the position of three markers on the segment are occluded). Percent variation is the difference between the mean percent occluded frames of the two camera configurations, where a negative variation is a decrease and positive variation is an increase in occluded frames from the gait specific camera setup.

Camera Setup	Trial	Percent occluded frames Shoulders				
		S1 [%]	S2 [%]	S3 [%]	S4 [%]	IS [%]
1: Gait	1	76.19	29.37	58.73	0.79	64.29
	2	81.58	25.44	60.53	0.00	67.54
	3	80.39	27.45	59.80	0.00	67.65
	Mean	79.39	27.42	59.69	0.26	66.49
2: Golf	1	34.23	0.00	0.00	0.00	0.00
	2	33.88	0.00	0.00	0.00	0.00
	3	46.85	0.00	0.00	0.00	0.00
	Mean	38.32	0.00	0.00	0.00	0.00
Percent Variation		-41.07	-27.42	-59.69	-0.26	-66.49

Table 3-11: Percent occluded frames of the left arm. IS denotes the percent frames where an indeterminate system is present (the position of three markers on the segment are occluded). Percent variation is the difference between the mean percent occluded frames of the two camera configurations, where a negative variation is a decrease and positive variation is an increase in occluded frames from the gait specific camera setup.

Camera Setup	Trial	Percent occluded frames Left Arm				
		A1 [%]	A2 [%]	A3 [%]	A4 [%]	IS [%]
1: Gait	1	0.79	18.25	57.94	1.59	20.63
	2	0.88	17.54	80.70	0.88	19.30
	3	2.94	16.67	67.65	0.98	19.61
	Mean	1.54	17.49	68.76	1.15	19.85
2: Golf	1	0.00	63.06	46.85	0.00	15.32
	2	0.00	77.69	70.25	4.96	60.33
	3	0.90	75.68	72.97	0.00	51.35
	Mean	0.30	72.14	63.36	1.65	42.33
Percent Variation		-1.24	54.65	-5.41	0.50	22.49

Table 3-12: Percent occluded frames of the club head. IS denotes the percent frames where an indeterminate system is present (the position of three markers on the segment are occluded). Percent variation is the difference between the mean percent occluded frames of the two camera configurations, where a negative variation is a decrease and positive variation is an increase in occluded frames from the gait specific camera setup.

Camera Setup	Trial	Percent occluded frames Club head				
		C1 [%]	C2 [%]	C3 [%]	C4 [%]	IS [%]
1: Gait	1	19.84	64.29	11.90	3.97	25.40
	2	13.16	59.65	14.91	1.75	21.93
	3	16.67	65.69	18.63	0.00	28.43
	Mean	16.56	63.21	15.15	1.91	25.25
2: Golf	1	4.50	12.61	1.80	0.90	5.41
	2	9.92	12.40	4.13	2.48	9.09
	3	11.71	27.93	6.31	0.90	11.71
	Mean	8.71	17.65	4.08	1.43	8.74
Percent Variation		-7.84	-45.56	-11.07	-0.48	-16.52

Measurement of Inter-Marker Distance Accuracy

Measurement bias and precision of inter-marker distance are given in Table 3-13 and Table 3-14, respectively. Statistical analysis of variance is carried by a student t-test, comparing the two measurement populations (one for each camera setup).

Table 3-13: Measurement bias (error relative to standard measurement) of inter-marker distance. Measurements taken at 5 positions and for 3 trials.

Camera Setup	Position	Measurement bias				Statistics
		Trial 1 [mm]	Trial 2 [mm]	Trial 3 [mm]	Mean [mm]	student t-test (p-value= 0.05)
Gait	1	0.092	0.097	0.083	0.090	
	2	0.219	0.231	0.247	0.232	
	3	0.660	0.689	0.668	0.672	
	4	0.094	0.102	0.098	0.098	
	5	1.022	0.987	0.993	1.001	0.934
Golf	1	0.397	0.397	0.408	0.401	
	2	0.084	0.090	0.085	0.086	
	3	0.236	1.701	0.291	0.743	
	4	0.048	0.040	0.042	0.043	
	5	0.712	0.827	0.802	0.781	

Table 3-14: Measurement precision (S: Standard deviation) of inter-marker distance. Measurements taken at 5 positions and for 3 trials.

Camera Setup	Position	Measurement precision (S) Trial 1 [mm]	Trial 2 [mm]	Trial 3 [mm]	Mean [mm]	Statistics student t-test (p-value= 0.05)
Gait	1	0.070	0.072	0.064	0.069	0.096
	2	0.092	0.100	0.068	0.087	
	3	0.044	0.045	0.054	0.048	
	4	0.057	0.062	0.056	0.058	
	5	0.108	0.081	0.081	0.090	
Golf	1	0.098	0.100	0.100	0.099	
	2	0.030	0.032	0.029	0.030	
	3	0.062	0.202	0.072	0.112	
	4	0.033	0.030	0.030	0.031	
	5	0.413	0.606	0.682	0.567	

3.1.2.5 Discussion

Marker Occlusion of Golfer with Reflective Markers

The occurrence of marker occlusion for both camera configurations, quantified in terms of percent occluded frames, for the pelvis, torso, shoulders, left arm and club head, are listed in Table 3-8 to Table 3-12. For the pelvis, marker occlusion decreased by 40 percent for P1, accompanied by an increase of 14 percent for P4. For both camera configurations, the occurrence of an indeterminate system was below 10 percent, relatively unchanged between them. A tradeoff was experienced in occlusion of the pelvic markers, as a decrease of 41 percent for T1 was followed by an increase of 21 percent for T2. Although an overall improvement was experienced, the incidence of an indeterminate system was high, 56 percent, as a combination of high marker occlusion and the limited number of markers (3). The largest reduction is marker occlusion was experienced for markers placed on the shoulders, as markers S1, S2 and S3 were are reduced by at least 27 percent. Furthermore, no data frames were consistent with an indeterminate system. Conversely, the largest increase in marker occlusion was experienced on the left arm, as an increase of 55 percent was experienced for

marker A2. Along with the high occlusion of marker A3, the occurrence of an indeterminate system increased to 42 percent. Therefore, it would be advantageous to add another marker to analyze the motion of the left arm. For example, a marker could be placed on the left forearm (which will be discussed in Section 3.4). Finally, marker occlusion was reduced for all markers of the club head, the largest reduction being 45 percent for marker C2, and the occurrence of an indeterminate system was decreased to below 10 percent.

Measurement of Inter-Marker Distance Accuracy

The bias and precision of inter-marker distance measurements for the two camera configurations are shown in Table 3-13 and Table 3-14, respectively. Measurement bias, when averaged over the 3 trials, varied from 0.090 mm to 1.001 mm for all 5 positions in the gait camera configuration. For measurements taken within the golf specific camera setup, measurement bias varied from 0.043 mm to 0.781 mm. In both cases, the highest bias values were obtained in position 5. For the golf specific setup, 3 out of the 4 bias values exceeding half a millimeter were obtained in position 5. This increase in bias can be explained by camera positioning, as position 5 is located far from the body and on the outer edge of the working envelop of the golf swing. The student t-test comparing the two measurement populations produced a p-value of 0.934, stating that the null hypothesis of equal but unknown means could not be rejected at a 5 percent significance level.

Measurement precision, evaluated from standard deviation, varied from 0.058 mm to 0.090 mm for all measurements taken at the 5 positions in the gait specific configuration. For measurement taken with the golf specific camera configuration, standard deviation varied from 0.030 mm to 0.567 mm when averaging the 3 trials. As with measurement bias, standard deviation was highest in position 5, where the two values exceeding 0.5 mm were both observed in position 5. The student t-test comparing the two measurement populations produced a p-value of 0.096, stating that the null hypothesis of equal but unknown means could not be rejected at a 5 percent significance level.

3.1.2.6 Conclusion

Changing the camera setup from the gait specific configuration, shown in Figure 3-1, to the golf specific configuration, shown in Figure 3-6, reduced the occurrence of marker occlusion for markers placed on the shoulders and club head, while markers placed on the pelvis and torso remained relatively unchanged. As one of the markers placed on the arm experienced an increase in marker occlusion, another marker should be placed on the arm to reduce the occurrence of an indeterminate system. This overall decrease in the instances of marker occlusion, from the change to the golf specific configuration, did not result in any statistically significant changes to measurement bias or precision.

3.1.3 Experimental Apparatus: conclusions of Measurement Accuracy and Marker Occlusion studies relative to experimental setup

When performing data collection with a stereophotogrammetric system, the choice of camera settings, camera positions and marker placement are the main variables. The Measurement Accuracy study concluded that measurement bias and precision was unaffected by sampling rate but was affected by the position of the markers within the measurement volume. The cameras of the stereophotogrammetric system of the Syncrude Centre for Motion and Balance, shown in Figure 3-1, can maintain a full field of view up to a threshold of 400 Hz, after which the field of view decreases. Therefore, in order to maintain full field of view, resulting in the largest measurement volume for the given camera configuration, an upper limit of 400 Hz was established for the given system.

These conclusions placed a focus on camera placement rather can camera settings. The Marker Occlusion study showed that a golf specific camera configuration reduces the occurrence of marker occlusion while maintaining the measurement accuracy characteristics of a gait specific configuration. Therefore, the golf specific camera configuration was used to measure marker displacement.

3.2 ISA Computation from Rigid Body Motion

At any one instant, the displacements of a rigid body can be expressed in terms of movement about an ISA, where the displacement of all features on the body can be expressed as a single rotation and a single translation in the direction of the ISA [Woltring et al. (1985)]. The computation of an ISA from the motion of a rigid body is shown in the following section.

3.2.1 Rigid Body Motion of Defined ISA

The position and orientation of the ISA of a rigid body can be computed from the displacement of three, non-collinear, features belonging to that body [Eberharter and Ravani (2006)]. To illustrate the computation of ISA from rigid body displacements, three non-collinear markers were placed on an analytical cylinder, shown in Figure 3-10.

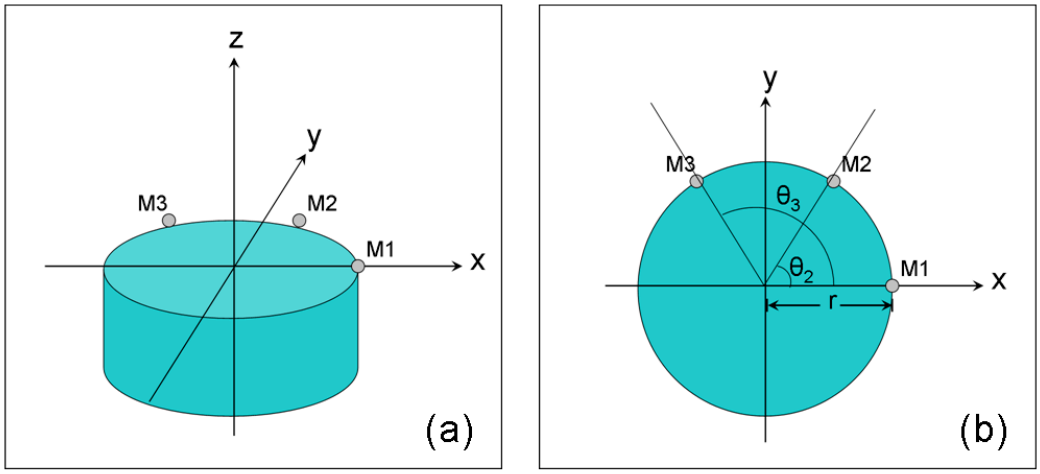

Figure 3-10: Analytical cylinder; (a) isometric view, (b) xy-plane projection

The three markers, M1, M2 and M3, were positioned at the outer edge of the cylinder, at a radius r from the centroidal axis of the cylinder. To ensure that all markers were non-collinear, three phase angles θ_1, θ_2, and θ_3 (θ_1= 0), were introduced between markers, expressed relative to the positive x-axis. For simplicity, a single screw motion was imposed on the cylinder, consisting of a

constant angular velocity $\vec{\omega}$ about the centroidal axis and a constant translation of velocity $\vec{v}_{//}$, parallel to the centroidal axis, as shown in Figure 3-11 (a).

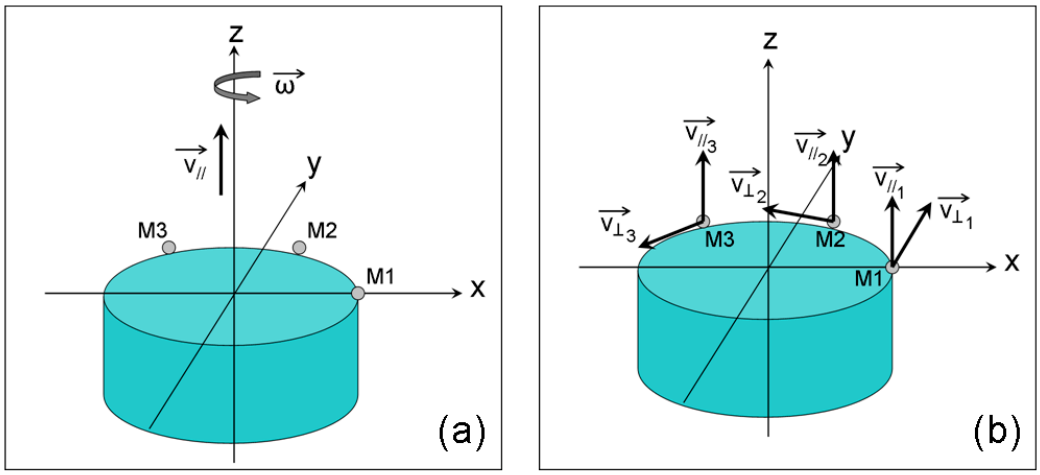

Figure 3-11: Analytical cylinder; (a) applied screw motion, (b) marker velocities

From the imposed motion of the cylinder, the position of each marker, relative to the global reference frame, is given by

$$\vec{p}_i = x_i(t)\vec{i} + y_i(t)\vec{j} + z_i(t)\vec{k} \qquad \textbf{(3-11)}$$

where

$x_i(t) = r\cos(\omega t + \theta_i)$

$y_i(t) = r\sin(\omega t + \theta_i)$

$z_i(t) = v_{//}t$

where i = [1, 2, 3], for each of the three markers, and t is the time variable. The velocity of each marker consists of two components: a component parallel to the ISA, $\vec{v}_{//}$, and a component perpendicular to the ISA, $\vec{v}_{\perp}$, as shown in Figure 3-11 (b). The parallel component is equal to the parallel velocity of the rigid body, $v_{//}$, while the perpendicular component is found by calculating the cross product of

the applied angular velocity, $\vec{\omega}$, and the radius of the markers relative to the origin. The total velocity of each marker is thus given by:

$$\begin{aligned}\vec{v}_i(t) &= \overrightarrow{v_{\perp_i}} + \overrightarrow{v_{//}} \\ &= [\vec{\omega} \times \vec{r}_i(t)] + \overrightarrow{v_{//}} \\ &= [\omega\vec{k} \times (x_i(t)\vec{i} + y_i(t)\vec{j} + z_i(t)\vec{k})] + v_{//}\vec{k}\end{aligned} \quad \textbf{(3-12)}$$

where $\vec{\omega}$ and $\overrightarrow{v_{//}}$ are both vectors in the z-axis direction, coinciding with the centroidal axis of the cylinder (see Figure 3-11 (a)).

From the displacements of marker M1, M2 and M3, the ISA of the rigid body can be computed in two steps: (1) determine the orientation of the ISA and (2) determine the location of the ISA relative to the global reference frame. Although the ISA can be computed in alternate manners, the following method computes the ISA from the position and instantaneous velocity of three markers [Eberharter and Ravani (2006)]. The first step involves determining the direction of the ISA or a unit vector parallel to the ISA, labeled $\overrightarrow{ISA_o}$. This unit vector is determined by computing the cross product of two vectors: the relative velocity of marker M2 to marker M1, $\overrightarrow{v_{2-1}}$, and the relative velocity of marker M3 to marker M1, $\overrightarrow{v_{3-1}}$ [Eberharter and Ravani (2006)]. These two vectors represent the relative velocities of markers M2 and M3 relative to marker M1; however the choice of marker M1 is arbitrary and could be chosen as any of the other two markers. The unit vector $\overrightarrow{ISA_o}$ is given by the cross product of these two vectors, as follows:

$$\begin{aligned}\overrightarrow{ISA_o} &= \frac{\overrightarrow{v_{2-1}} \times \overrightarrow{v_{3-1}}}{\left\| \overrightarrow{v_{2-1}} \times \overrightarrow{v_{3-1}} \right\|} \\ &= \frac{\left(\vec{v}_2 - \vec{v}_1\right) \times \left(\vec{v}_3 - \vec{v}_1\right)}{\left\| \left(\vec{v}_2 - \vec{v}_1\right) \times \left(\vec{v}_3 - \vec{v}_1\right) \right\|}\end{aligned} \quad \textbf{(3-13)}$$

where v_1, v_2 and v_3 represent the velocity of markers M1, M2 and M3, respectively, and computed from equation (3-12). In the present case, the parallel component of marker velocity, $\overrightarrow{v_{//_i}}$, is consistent for all three markers and the perpendicular component of marker velocity is contained within the xy plane. Therefore, the relative velocities $\overrightarrow{v_{2-1}}$ and $\overrightarrow{v_{3-1}}$ are both contained within the xy plane, and their cross product will produce a vector in the $\vec{k}$ direction. Therefore, $\overrightarrow{ISA_o}$ will be parallel to the applied angular velocity $\vec{\omega}$, consistent with a screw motion. Once the orientation of ISA has been established, the velocity of each marker can be decomposed into its parallel and perpendicular components, as shown in Figure 3-11 (b). Before this can be carried out, it must be determined if the $\overrightarrow{ISA_o}$ is in the same direction as the parallel vector component of each marker, $\overrightarrow{v_{//_i}}$, as the cross product cannot determine the direction of parallel velocity. To verify the direction of $\overrightarrow{ISA_o}$, the dot product between the velocity of marker M1 and $\overrightarrow{ISA_o}$ is computed. Again the choice of marker M1 is an arbitrary one. The dot product, $ISA_{Diagnostic\ 1}$, between these two vectors is given as follows:

$$\begin{aligned} ISA_{Diagnostic\ 1} &= \overrightarrow{ISA_o} \cdot \vec{v_1} \\ &= \overrightarrow{ISA_o} \cdot (\overrightarrow{v_{\perp_1}} + \overrightarrow{v_{//_1}}) \\ &= \overrightarrow{ISA_o} \cdot \overrightarrow{v_{//_1}} \end{aligned} \qquad \textbf{(3-14)}$$

where, in the present case, the perpendicular component $\overrightarrow{v_{\perp_i}}$ is dropped as its dot product with $\overrightarrow{ISA_o}$ is zero (as they are perpendicular to one another). Furthermore, the magnitude of $ISA_{Diagnostic\ 1}$, in the present case, is equal to the magnitude of $\overrightarrow{v_{//_i}}$, as the two vectors are parallel. If the value of $ISA_{Diagnostic\ 1}$ is positive, then $\overrightarrow{ISA_o}$ and the parallel velocity of marker M1, and all markers, are in the same direction. However, if the value of $ISA_{Diagnostic\ 1}$ is negative, then $\overrightarrow{ISA_o}$ and the parallel velocity component of all markers are of opposite direction. As the

direction of $\overrightarrow{ISA_o}$ is arbitrary, as it can be defined from the direction of parallel velocity or angular velocity of the rigid body (which could be in the same or opposite directions), the choice of $\overrightarrow{ISA_o}$ direction is purely for computational purposes. For simplicity, the unit vector $\overrightarrow{ISA_o}$ is forced in the same direction as the parallel component of marker velocity. Once the direction of $\overrightarrow{ISA_o}$ has been established, the parallel and perpendicular components of marker velocity, as shown in Figure 3-11 (b), can be computed as follows:

$$\left(\overrightarrow{v_{//}}\right)_i = \left(\overrightarrow{v_i} \cdot \overrightarrow{ISA_o}\right)\overrightarrow{ISA_o}$$
$$\left(\overrightarrow{v_{\perp}}\right)_i = \overrightarrow{v_i} - \left(\overrightarrow{v_i} \cdot \overrightarrow{ISA_o}\right)\overrightarrow{ISA_o} \qquad \textbf{(3-15)}$$

where i = [1, 2, 3], for each of the three markers M1, M2 and M3. The magnitude of the parallel component of marker velocity corresponds to the translation of the rigid body in the direction of the ISA. In the present case, this corresponds to velocity $\overrightarrow{v_{//}}$ from the screw motion.

The second step of ISA computation involves determining the location of ISA within the global reference frame. From the previous computational step, the perpendicular component of marker velocity was established for all markers. For each marker, a plane can be defined by its perpendicular velocity, acting as the normal vector to the plane, and its position, acting as a point on the plane [Nicholson (2003)]. These three planes defined by marker M1, M2 and M3 are shown in Figure 3-12. The position of the ISA is given by the line of intersection of these three planes.

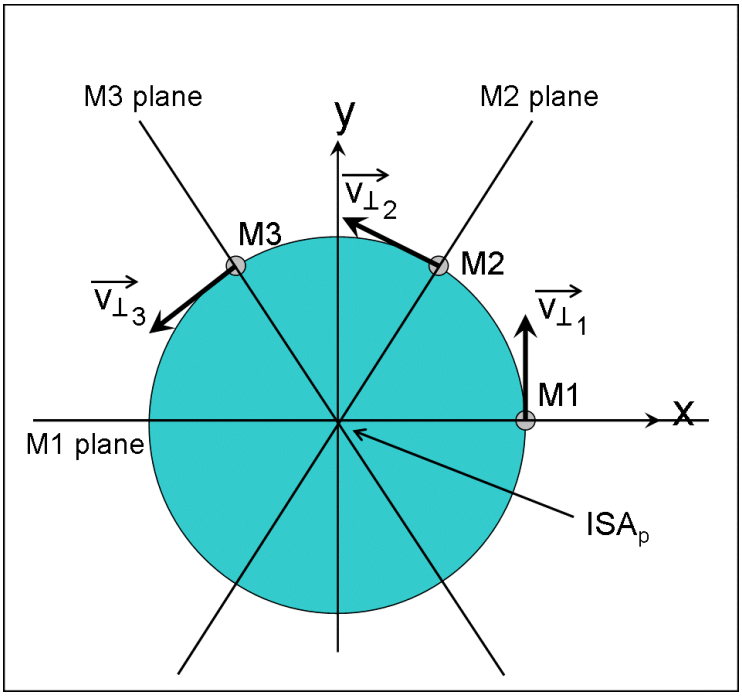

Figure 3-12: Top projection of planes formed by points M1, M2 and M3 with normal vectors $\overrightarrow{v_{\perp_1}}$, $\overrightarrow{v_{\perp_2}}$ and $\overrightarrow{v_{\perp_3}}$, respectively. Position of ISA, ISAp, coincides with intersection of three planes.

The position of ISA can be found by the intersection of only two of the three planes shown in Figure 3-12. Therefore, the position of the ISA can be computed in three ways: intersection of planes defined by markers M1 and M2, markers M1 and M3, and markers M2 and M3. For the case of analytical rigid body motion, the choice is arbitrary and, for this example, is chosen as the intersection of the planes defined by markers M1 and M2 and their respective perpendicular velocities. The equation of these two planes is given by the dot product of the normal vector to the plane and a point belonging to that plane, given as follows:

$$C_i = \overrightarrow{(v_\perp)_i} \cdot \overrightarrow{p_i}$$
$$C_i = \left((v_{\perp x})_i \vec{i} + (v_{\perp y})_i \vec{j} + (v_{\perp z})_i \vec{k}\right)(x_i \vec{i} + y_i \vec{j} + z_i \vec{k}) \quad \textbf{(3-16)}$$

where i= [1, 2] for markers M1 and M2, and C_i corresponds to the plane constant [Nicholson (2003)]. The intersection of these two planes is a line corresponding to ISA, which can be represented by a single point, along the intersection line, and a

unit vector parallel to ISA. As a unit vector in ISA direction has been computed in the previous step, a single point belonging to the intersection line is required to fully define ISA. When grouping the equations of the planes formed by markers M1 and M2, the followings linear system of equations is given:

$$\begin{bmatrix} (v_{\perp x})_1 & (v_{\perp y})_1 & (v_{\perp z})_1 \\ (v_{\perp x})_2 & (v_{\perp y})_2 & (v_{\perp z})_2 \end{bmatrix} \begin{bmatrix} x \\ y \\ z \end{bmatrix} = \begin{bmatrix} C_1 \\ C_2 \end{bmatrix} \quad \textbf{(3-17)}$$

where *(x, y, z)* are the coordinates of a point belonging to the intersection line. This linear system consists of two equations and three unknowns. To solve for *(x, y, z)*, the point coinciding with the intersection line and the xy-plane is determined, labeled (x_{xy}, y_{xy}, z_{xy}). This sets the *z*-coordinate, z_{xy}, to zero, and the following system is linear equations is given:

$$\begin{bmatrix} (v_{\perp x})_1 & (v_{\perp y})_1 & (v_{\perp z})_1 \\ (v_{\perp x})_2 & (v_{\perp y})_2 & (v_{\perp z})_2 \end{bmatrix} \begin{bmatrix} x_{xy} \\ y_{xy} \\ 0 \end{bmatrix} = \begin{bmatrix} C_1 \\ C_2 \end{bmatrix}$$

$$\begin{bmatrix} (v_{\perp x})_1 & (v_{\perp y})_1 \\ (v_{\perp x})_2 & (v_{\perp y})_2 \end{bmatrix} \begin{bmatrix} x_{xy} \\ y_{xy} \end{bmatrix} = \begin{bmatrix} C_1 \\ C_2 \end{bmatrix} \quad \textbf{(3-18)}$$

resulting in a linear system of two equations and two unknowns. The values of (x_{xy}, y_{xy}) can be solved as follows:

$$\begin{bmatrix} x_{xy} \\ y_{xy} \end{bmatrix} = \begin{bmatrix} (v_{\perp x})_1 & (v_{\perp y})_1 \\ (v_{\perp x})_2 & (v_{\perp y})_2 \end{bmatrix}^{-1} \begin{bmatrix} C_1 \\ C_2 \end{bmatrix} \quad \textbf{(3-19)}$$

where the exponent *-1* denotes the matrix inverse. In the present case, the coordinates (x_{xy}, y_{xy}, z_{xy}) correspond to the origin of the global reference frame, (0, 0, 0), as $\overrightarrow{v_{\perp_1}}$ of all markers is perpendicular to the radius from the applied angular

velocity, at the centroidal axis, to each marker coordinate (shown in Figure 3-12). Therefore, the single point defining the position of the ISA, ISA_p, becomes:

$$ISA_p = (x_{xy}, y_{xy}, 0) \tag{3-20}$$

Therefore, the coordinates of any point along the ISA is given by the multiplication of the unit vector $\overrightarrow{ISA_o}$ by a given constant, C, to the coordinates of the point ISA_p, as follows:

$$\overrightarrow{ISA} = C\,\overrightarrow{ISA_o} + \overrightarrow{ISA_p} \tag{3-21}$$

In the present case, ISA coincides with the centroidal axis of the given cylinder, as the direction of $\overrightarrow{ISA_o}$ is parallel to the z-axis and ISA_p coincides with the origin of the global reference frame, as shown in Figure 3-13.

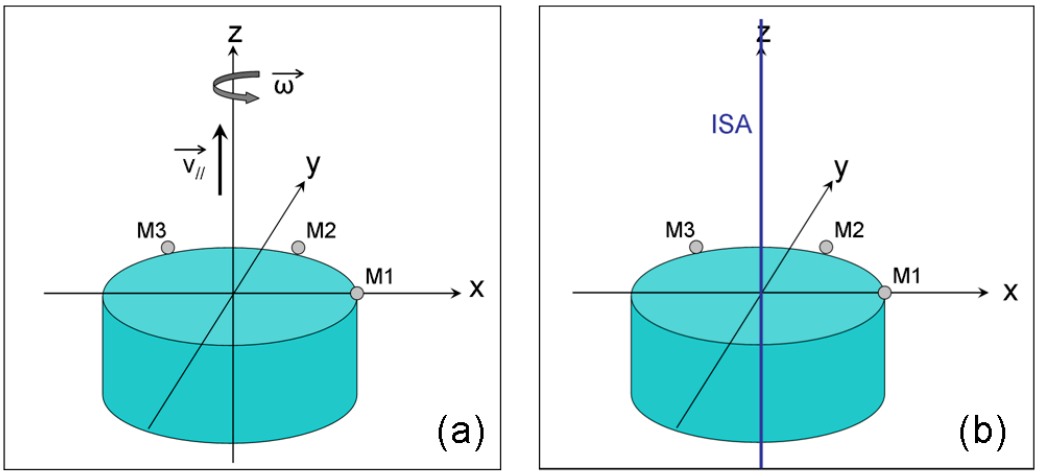

Figure 3-13: Analytical cylinder; a) applied screw motion; (b) ISA position and orientation

In the case where rigid-body motion is unknown and marker position and velocity are measured, as is the case with stereophotogrammetric data, ISA position and orientation are computed as described above. The magnitude of segment parallel velocity, $\left\|\overrightarrow{v_{//}}\right\|$, is determined from the projection of marker velocity $\vec{v}$ in the ISA

direction. The magnitude of segment angular velocity, $\left\|\vec{\omega}\right\|$, can be computed from the magnitude of a given marker's velocity and it's radius to the ISA, as described in Equation (3-12). The radius, $\vec{r}_i$, is defined as the vector spanning from the ISA to the position of the given marker while remaining perpendicular to the ISA. As the orientation of segment angular velocity is known, parallel to the ISA, the magnitude can be determined from the magnitude perpendicular marker velocity, $\left\|\overrightarrow{v_{\perp}}\right\|$, and the magnitude of vector $\vec{r}_i$. Therefore, segment motion about the ISA can be computed from marker displacement and ISA position and orientation.

3.2.2 Rigid Body Motion of Undefined ISA

The computation of ISA consists of two main steps: determining ISA direction, $\overrightarrow{ISA_o}$, and determining ISA position, ISA_p. The ISA of a rigid body cannot be defined for specific cases of rigid body motion. Theses instance will be discussed relative to the two computational steps. The first computational step consists of determining $\overrightarrow{ISA_o}$ from the cross product of two relative velocity vectors, computed from equation (3-13). This cross product cannot be computed for two cases: (1) for a pure translation of the rigid body and (2) parallel relative velocity vectors. In the first case, a pure translation of the rigid body does not produce relative motion between markers, resulting in a zero $\overrightarrow{ISA_o}$ vector. In this particular case, a unique ISA cannot be determined, as an infinite number of solutions are possible, where the ISA is parallel to the rigid body translation, with zero angular velocity in the ISA direction, and an infinite number of positions. In the second case, the two relative velocity vectors, $\overrightarrow{v_{2-1}}$ and $\overrightarrow{v_{3-1}}$, are parallel, resulting in a zero $\overrightarrow{ISA_o}$ vector. Computationally, the two cases above can be identified by a dot product between vectors $\overrightarrow{v_{2-1}}$ and $\overrightarrow{v_{3-1}}$, labeled $ISA_{Diagnostic\ 2}$, as follows:

$$ISA_{Diagnostic\ 2} = \left\| \overrightarrow{v_{2-1}} \cdot \overrightarrow{v_{3-1}} \right\| \quad \textbf{(3-22)}$$

where the absolute value is taken for simplicity, as the dot product will vary from 0 to 1 as opposed to -1 to 1. In the case of parallel vectors, the dot product is equal to 1. However, computational issues arise when vectors $\overrightarrow{v_{2-1}}$ and $\overrightarrow{v_{3-1}}$ approach a parallel state, causing discontinuities in $\overrightarrow{ISA_o}$. To compensate for these discontinuities, a threshold is set to limit ISA computation to instances where $ISA_{Diagnostic\ 2}$ is smaller than 0.999, near the case of parallel vectors. Therefore, rigid body motions that exceed this threshold are not computed, as follows:

$$ISA_{Diagnostic\ 2} = \left\| \overrightarrow{v_{2-1}} \cdot \overrightarrow{v_{3-1}} \right\| \quad > \quad 0.999 \quad \textbf{(3-23)}$$

where the threshold value of 0.999 was determined empirically, as it identified discontinuities in $\overrightarrow{ISA_o}$ without appreciably affecting instances surrounding these discontinuities.

The second computational step consists of determining the position of ISA by locating a single point, ISA_p, belonging to the ISA and the xy plane, computed from equation (3-19). This linear system of equations cannot be computed for two specific cases: (1) for a pure translation of the rigid body and (2) parallel perpendicular velocity components. As shown above, the case of a pure translation results in an infinite number of solutions for ISA. To locate the ISA, the linear system of equation cannot be solved, as the perpendicular velocities $\overrightarrow{v_{\perp_1}}$ and $\overrightarrow{v_{\perp_2}}$ are zero. In the second case, where $\overrightarrow{v_{\perp_1}}$ and $\overrightarrow{v_{\perp_2}}$ are parallel, the system of linear equations of equation (3-19) is indeterminate, as the system consists of one repeating equation and two unknowns. Computationally, the two cases above can be identified by a dot product between vectors $\overrightarrow{v_{\perp_1}}$ and $\overrightarrow{v_{\perp_2}}$, labeled $ISA_{Diagnostic\ 3}$, as follows:

$$ISA_{Diagnostic\ 3} = \left\| \overrightarrow{v_{\perp_1}} \cdot \overrightarrow{v_{\perp_2}} \right\| \quad \textbf{(3-24)}$$

In the case of parallel vectors, the dot product is equal to 1. However, computational issues arise when vectors $\overrightarrow{v_{\perp_1}}$ and $\overrightarrow{v_{\perp_2}}$ approach a parallel state, causing discontinuities in ISA_p (as with the computation of $\overrightarrow{ISA_o}$). To compensate for these discontinuities, a threshold is set to limit ISA computation to instances where $ISA_{Diagnostic\ 3}$ is smaller than 0.999, near the case of parallel vectors. Therefore, rigid body motions that exceed this threshold are not computed, as follows:

$$ISA_{Diagnostic\ 3} = \left\| \overrightarrow{v_{\perp_1}} \cdot \overrightarrow{v_{\perp_2}} \right\| \quad > \quad 0.999 \quad \textbf{(3-25)}$$

where the threshold value of 0.999 was determined empirically, as with the previous diagnostic.

By introducing theses two diagnostics, $ISA_{Diagnostic\ 2}$ and $ISA_{Diagnostic\ 3}$, gaps are formed in the data of $\overrightarrow{ISA_o}$ and ISA_p, similar to the gaps introduced by marker occlusion (discussed in Section 3.1.2). As these gaps are of short duration, generally only a few data points, they are filled by spline interpolation of the $\overrightarrow{ISA_o}$ vectors components and coordinates of ISA_p. The method of spline interpolation is discussed in length in Section 3.3.3.1.

3.2.3 Relative ISA computation of rigidly linked bodies

When two segments are rigidly linked to one another, it is possible to compute a relative ISA between them. This is of particular interest in biomechanical analysis, as the relative motion between physiologically linked segments can be expressed through an ISA, examples of which have been discussed in Section

2.2.2. To illustrate the computation of a relative ISA, the analytical cylinder of the above section has been modified, as shown in Figure 3-14.

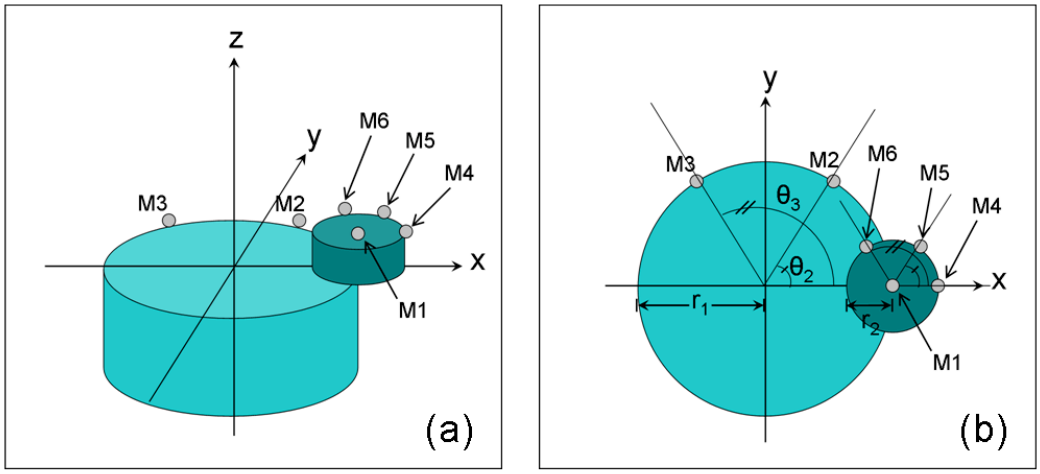

Figure 3-14: Analytical cylinders (RB_1 and RB_2); (a) isometric view, (b) xy-plane projection

This analytical system is comprised of two rigid bodies: the analytical cylinder with affixed markers M1, M2 and M3, which will be labeled RB_1, and a second cylinder rigidly attached to RB_1 (pined to RB_1 below marker M1) with affixed markers M4, M5 and M6, which will be labeled RB_2. These two rigid bodies act as two physiologically linked segments, such as the upper and lower arm, or as the links of a robot manipulator, where the motion of the proximal segment is fully transmitted to distal segment. Furthermore, the distal segment is free to move relative to the proximal segment, producing a relative motion between them. In the present case, RB_1 acts as the proximal segment and RB_2 acts as the distal segment, as the full motion of RB_1 is transmitted to RB_2, while RB_2 is free to rotate about its pinned connection, generating a relative motion between them. This is similar to the kinematics of the arm, as the motion of the upper arm, caused by rotation about the shoulder joint, is fully transmitted to the lower arm, which in turn is free to rotate about the elbow joint generating a relative motion between them. To simulate the motion of rigidly linked segments, a single screw motion was imposed on RB_1 and RB_2, consisting of a constant angular velocity $\vec{\omega}_1$ about the centroidal axis of RB_1 and a constant translation of velocity $\vec{v}_{//}$, parallel

to the centroidal axis of RB_1, as shown in Figure 3-15. Furthermore, RB_2 was given a constant angular velocity $\vec{\omega}_2$ about its centroidal axis, generating a relative motion between the two rigid bodies, as shown in Figure 3-15.

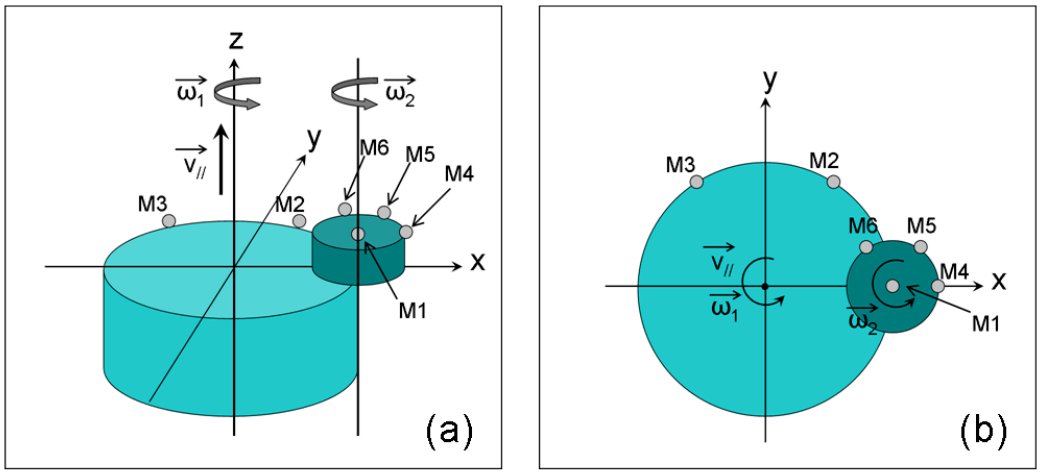

Figure 3-15: Analytical cylinders (RB_1 and RB_2); (a) applied angular velocities $\vec{\omega}_1$ and $\vec{\omega}_2$, and parallel velocity $\vec{v}_{//}$, (b) Motions $\vec{\omega}_1$ and $\vec{v}_{//}$ (direction out of the page) applied at the origin, and motion $\vec{\omega}_2$ applied at marker M1

From the imposed motion of the system, the position and velocity of each marker on RB_1, relative to the global reference frame, is given by equation (3-11) and equation (3-12), respectively, where the magnitude of angular velocity is ω_1 and the cylinder radius r_1. The position of each marker affixed to RB_2, relative to the global reference frame, is given by

$$\begin{aligned}\vec{P}_i &= \vec{P}_1 + \overrightarrow{P_{i/1}} \\ &= \vec{P}_1 + \left[r_2\cos\left((\omega_1+\omega_2)t+\theta_i\right)\vec{i} + r_2\sin\left((\omega_1+\omega_2)t+\theta_i\right)\vec{j}\right]\end{aligned} \quad \textbf{(3-26)}$$

where i = [4, 5, 6], for each of the three markers, and $\overrightarrow{P_{i/1}}$ denotes the relative position of marker Mi relative to marker M1. The velocity of each marker affixed to RB_2, relative to the global reference frame, is computed as follows

$$\begin{aligned}\vec{V}_i &= \vec{V}_1 + \left(\overrightarrow{P_{i/1}}\right)' \\ &= \vec{V}_1 + \left[-r_2(\omega_1+\omega_2)\sin\left((\omega_1+\omega_2)t+\theta_i\right)\vec{i} + r_2(\omega_1+\omega_2)\cos\left((\omega_1+\omega_2)t+\theta_i\right)\vec{j}\right]\end{aligned} \quad \textbf{(3-27)}$$

where $\left(\overrightarrow{P_{i/1}}\right)'$ denotes the derivative with respect to time of the relative position of marker Mi relative to marker M1. This computation is similar to the computation of the end effecter velocity of a 2 dimensional 2-link manipulator [Craig (2005)].

As the position and velocity of all markers in the system are known, three markers per rigid body, the ISA of RB_1, labeled ISA_1, and the relative ISA of RB_2 relative to RB_1, labeled ISA_2, can be computed. This analysis is conducted in three steps. First, ISA_1 is computed from the displacements of marker M1, M2 and M3. As shown in Section 3.2.1, the ISA computed from the displacement of markers M1, M2 and M3 yields an ISA_1 that coincides with the centroidal axis of RB_1, with an angular velocity of $\vec{\omega}_1$ and parallel velocity $\vec{v}_{//}$, both in the direction of ISA_1. Second, the motion about ISA_1 is fully transmitted to markers M4, M5 and M6, as RB_2 is rigidly connected to RB_1. This involves computing the velocity of markers M4, M5 and M6 about ISA_1, $\overrightarrow{v_{ISA_1}}$, and computing the relative velocity of each marker relative to RB_1, $\overrightarrow{v_{i/ISA_1}}$. The velocity of each marker relative to ISA_1 is given by:

$$\begin{aligned}\overrightarrow{v_{ISA_1}} &= \vec{\omega}_1 \times \vec{P}_i + \vec{v}_{//} \\ &= \vec{\omega}_1 \times \left(\vec{P}_1 + \overrightarrow{P_{i/1}}\right) + \vec{v}_{//} \\ &= \left[\left(\vec{\omega}_1 \times \vec{P}_1\right) + \vec{v}_{//}\right] + \left(\vec{\omega}_1 \times \overrightarrow{P_{i/1}}\right) \\ &= \vec{v}_1 + \left(\vec{\omega}_1 \times \overrightarrow{P_{i/1}}\right) \\ &= \vec{v}_1 + \left(\omega_1\vec{k} \times \left[r_2\cos\left((\omega_1+\omega_2)t+\theta_i\right)\vec{i} + r_2\sin\left((\omega_1+\omega_2)t+\theta_i\right)\vec{j}\right]\right) \\ &= \vec{v}_1 + \left(\omega_1 r_2\cos\left((\omega_1+\omega_2)t+\theta_i\right)\vec{j} - \omega_1 r_2\sin\left((\omega_1+\omega_2)t+\theta_i\right)\vec{i}\right)\end{aligned} \quad \textbf{(3-28)}$$

where i = [4, 5, 6] and $\vec{P}_i$ becomes the radius between markers M4, M5 and M6 to ISA_1. Therefore, the relative velocity of markers M4, M5 and M6 relative to RB_1 becomes the difference between marker velocity relative to the global reference frame, from equation (3-12), and marker velocity about ISA_1, from equation (3-28). Relative marker velocity, $\overrightarrow{v_{i/ISA_1}}$, is computed as follows:

$$\begin{aligned}\overrightarrow{v_{i/ISA_1}} &= \vec{v}_i - \overrightarrow{v_{ISA_1}} \\ &= -\omega_2 r_2 \sin\left((\omega_1+\omega_2)t+\theta_i\right)\vec{i} + \omega_2 r_2 \cos\left((\omega_1+\omega_2)t+\theta_i\right)\vec{j}\end{aligned} \quad \textbf{(3-29)}$$

As motion was imposed on this system of rigid bodies, it is known that the relative motion was a result of angular velocity $\overrightarrow{\omega_2}$ imposed at the pinned joint between the two segments. Therefore, the relative ISA would coincide with the position of the pinned joint. To demonstrate the position of ISA_2, the resulting marker velocity from a rotation about $\overrightarrow{\omega_2}$, would be computed as

$$\begin{aligned}\overrightarrow{v_{ISA_2}} &= \overrightarrow{\omega_2} \times \overrightarrow{P_{i/1}} \\ &= \omega_2\vec{k} \times \left[r_2 \cos\left((\omega_1+\omega_2)t+\theta_i\right)\vec{i} + r_2 \sin\left((\omega_1+\omega_2)t+\theta_i\right)\vec{j}\right] \\ &= \omega_2 r_2 \cos\left((\omega_1+\omega_2)t+\theta_i\right)\vec{j} - \omega_2 r_2 \sin\left((\omega_1+\omega_2)t+\theta_i\right)\vec{i} \\ &= \overrightarrow{v_{i/ISA_1}}\end{aligned} \quad \textbf{(3-30)}$$

where i = [4, 5, 6]. As the velocity of markers affixed to RB_2 relative to RB_1, $\overrightarrow{v_{i/ISA_1}}$, can be expressed as a single rotation about the pinned joint, $\overrightarrow{v_{ISA_2}}$, the ISA_2 coincides with the pinned joint, as expected.

The procedure outlined above computes the relative ISA from the relative motion between two rigid bodies rigidly linked to one another. When it is assumed that multiple segments are rigidly linked to one another, it is assumed that the full movement of the most proximal segment is fully transmitted to all segments. Furthermore, the movement of each segment, from most distal to most proximal,

is fully transmitted to all more distal segments. Therefore, the full displacement of each segment can be represented as the sum of the movements about each relative ISA preceding it. From the preceding example, the displacement of markers M4, M5 and M6 affixed to RB_2 can be expressed as the sum of the movements about ISA_1 and ISA_2.

When studying physiologically linked segments, this type of analysis assumes that they are rigidly connected to one another. However, physiological joints are not perfectly rigid, as noticeable relative motion is present within some joints [Ehrig et al. (2007)]. To minimize the errors introduced by relative motion within joints, each relative ISA is computed from the movement of 2 segments, that is the full displacement of the more proximal segment and the relative motion of the more distal segment (as shown above). Theoretically, this computation is equivalent to summing each relative movement of the more proximal segment, about each relative ISA preceding it. In practice, this reduces the error induced by non-rigid joints, as the computation of each relative ISA is subjected only to the non-rigidity of its corresponding joint, as opposed to the sum of all non-rigidity preceding it.

3.3 ISA Computation from Stereophotogrammetric Data

In order to apply rigid body theory when studying the kinematics of body segments from stereophotogrammetric data, the position and velocity of at least three non-collinear markers must be known [Eberharter and Ravani (2006)]. In the present section, the procedure followed to generate rigid body motion from noisy marker data is described. Clean position marker data are generated by compensating for instrument error and soft tissue artifact formation. Clean velocity marker data are generated by differentiation of the position data. Once the position and velocity of three markers on a rigid body are known, the computation of the ISA can be done, as described previously in Section 3.2. Furthermore, it was desired to evaluate the effects of instrument error and soft

tissue artifact compensation on the computation of the ISA. For this purpose, an analytical model of a simple rigid body motion was developed.

3.3.1 Analytical Model

The objective of the analytical model was to generate a simple three-dimensional rigid body motion when the position and orientation of the ISA are known. This provides a known reference for the computation of the ISA and to study the effects, relative to the ISA, of each step in the generation of rigid body motion from noisy data. In an effort to model the movement of the pelvis, the analytical model chosen was a rigid body defined by the position and velocity of three non-collinear markers on a rotating cylinder. The analytical model is therefore the same rigid body as described in Section 3.2.1, where the undefined variables of the cylinder, radius r and phase angles θ_1, θ_2, and θ_3 (shown in Figure 3-10), and of the motion imposed on the cylinder, $\vec{\omega}$ and $\overrightarrow{v_{//}}$ (shown in Figure 3-11), are given analytical values to model the movement of the pelvis.

The radius of the cylinder, *r*, was chosen as the average distance from the three pelvis anatomical landmarks (markers P1, P2 and the midpoint between markers P3 and P4, shown in Table 3-6 and Figure 3-7) to the pelvis centroid. From the preliminary data of Subject 1, the radius of the cylinder was set to 0.120 m. This cylinder was given a constant angular velocity $\vec{\omega}$ about the centroidal axis and a constant translation of velocity $\overrightarrow{v_{//}}$, parallel to the centroidal axis (see Figure 3-11). Together, these imposed movements define a single screw motion where the position and orientation of the ISA are fixed and coincide with the centroidal axis of the cylinder, the angular velocity of the cylinder about the ISA has a constant magnitude ω and the translation along the ISA has a constant magnitude $v_{//}$ (as shown in Section 3.2.1). The magnitude of the angular velocity ω was established using preliminary data from Subject 1 and was set to approximately the maximum angular velocity of the pelvis during the downswing, 7.5 rad/s. The

magnitude of the parallel velocity $\overrightarrow{v_{//}}$ was chosen to mirror the tangential velocity of the markers from the angular rotation $\vec{\omega}$, which is 0.9 m/s.

The three markers, M1, M2 and M3, were positioned in the xy-plane at a distance of 0.120 m from the origin, at the outer radius of the cylinder. To ensure that all markers were non-collinear, three phase angles were introduced between markers, expressed relative to the positive x-axis. Markers M1, M2 and M3 were given phase angles θ_1, θ_2, and θ_3 of 0, π/3 and 2π/3 radians, respectively (see Figure 3-10). The position of each marker is computed from equation (3-11), where i = [1, 2, 3] and t = [0:1/100:1] sec, generating 100 data points and a rotation of 7.5 radians. The velocity of each marker is computed from equation (3-12), where $\vec{\omega}$ and $\overrightarrow{v_{//}}$ are both vectors in the z-axis direction, coinciding with the centroidal axis of the cylinder (see Figure 3-11) and given magnitudes of 7.5 rad/s and 0.9 m/s, respectively. Therefore, from the above marker positions and velocities, the ISA would coincide with the origin, (0,0,0), and its orientation would be in the positive z direction, $\vec{k}$ (see Figure 3-13).

3.3.1.1 Error Parameters of Analytical Model

The references values for the ISA, of the analytical model described above, will be used throughout the following section to assess the effects of noisy marker data on ISA parameters. The error in ISA orientation, ε_o, was calculated as the intersection angle between the ISA from clean marker data, ISA_{clean}, and the ISA from noisy marker data, ISA_{noisy}, along the plane formed by these two axes (see Figure 3-16 (a)). The intersection angle is computed from the cross product of the two vectors $\overrightarrow{ISA_{clean}}$ and $\overrightarrow{ISA_{noisy}}$ [Kreyszig (1999c)], as follows:

$$\varepsilon_o = \sin^{-1}\left(\frac{\left\|\overrightarrow{ISA_{clean}} \times \overrightarrow{ISA_{noisy}}\right\|}{\left\|\overrightarrow{ISA_{clean}}\right\|\left\|\overrightarrow{ISA_{noisy}}\right\|}\right) \quad \textbf{(3-31)}$$

The position of the ISA was defined as the intersection between the ISA and the plane formed by the three rigid body markers. The error in ISA position, ε_p, was given by the distance between the intersections of ISA_{clean} and ISA_{noisy} with the rigid body plane (see Figure 3-16 (b)), calculated as follows:

$$\varepsilon_p = \left\|\overrightarrow{Int_{clean}} - \overrightarrow{Int_{noisy}}\right\| \quad \textbf{(3-32)}$$

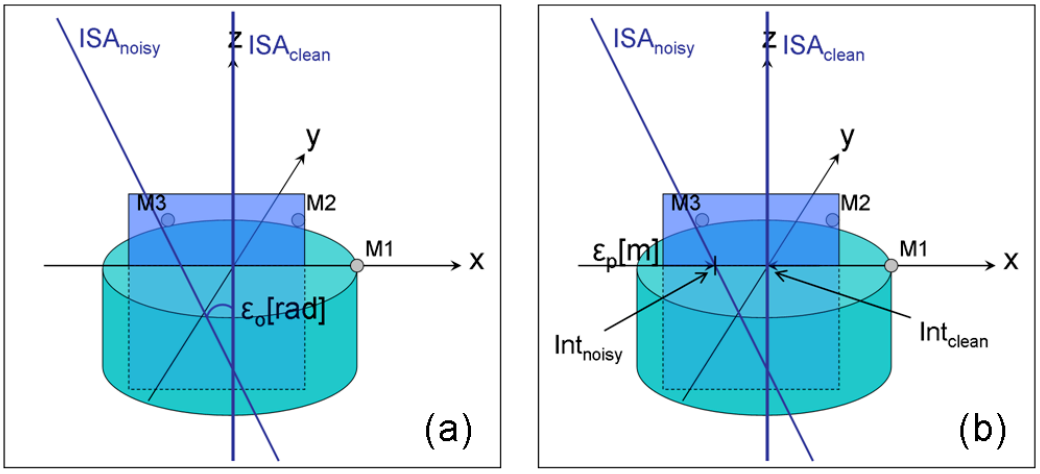

Figure 3-16: Error parameters (a) Error in ISA orientation, ε_o; (b) Error in ISA position, ε_p

Furthermore, the magnitude of the error of the parallel velocity along the ISA, ε_v, and that of the angular velocity about the ISA, ε_w, were also computed between ISA_{clean} and ISA_{noisy}. The error parameters of the analytical model were calculated as shown:

$$\varepsilon_v = \left\|\overrightarrow{v_{//\,clean}}\right\| - \left\|\overrightarrow{v_{//\,noisy}}\right\| \quad \textbf{(3-33)}$$

$$\varepsilon_{\omega} = \left\| \overrightarrow{\omega_{clean}} \right\| - \left\| \overrightarrow{\omega_{noisy}} \right\| \quad \textbf{(3-34)}$$

The purpose of the analytical model was to quantify the effects of instrument error and soft tissue artifact compensation on the error in computing a segment's ISA. It is of interest to compare these instrument errors to other sources of error involved in the measurement process, such as the effect of examiner variability, to better discuss the amplitude of ISA computational errors. To this effect, the magnitude of ISA error resulting from the known sources of stereophotogrammetric measurement error, specifically error in ISA orientation ε_o and error in ISA position ε_p, were compared to the magnitude of error in the computation of a segment's technical reference frame resulting from variability in marker placement. Della Croce et al. [Della Croce et al. (1999)] measured the error in determining the position and orientation of a technical reference frame resulting from the variability in the placement of reflective markers on anatomical landmarks. A total of 6 physical therapists, with gait laboratory experience, placed reflective markers on the lower extremities of two subjects, including the pelvis, and the position and orientation of technical reference frames were computed from the position of these markers.

Inter-examiner variability caused a RMSE of 21.18 mm in the position of each pelvic marker, when averaging the results over markers P1 to P4 (see Table 3-6). Furthermore, inter-examiner variability caused a RMSE 5.2, 3.7 and 4.1 degrees on the orientation of the *x*, *y* and *z* axes, respectively. The magnitude of these three orientation components, when added to form a resultant orientation vector (similar to an ISA), would be 7.6 degrees. The mean position error of 21.18 mm and orientation error of 7.6 degrees provide references values for the effect of marker placement on the position of a technical reference, and can serve as a source of comparison for the error in ISA computation from the stereophotogrammetric measurement errors that are investigated in the present section.

3.3.2 Positional Marker Data

As discussed in Section 2.3.2, positional measurements collected by video-based stereophotogrammetry are not free of measurement error. These measurements contain systematic instrument error, random instrument error and soft tissue artifacts [Chiari et al. (2005), Leardini et al. (2005)]. These measurement errors translate into spurious and real relative movements between the affixed retroflective markers and the underlying bone structure, which in turn affect the application of rigid body theory. The following section describes a data processing procedure, which aims to reduce measurement error and generate rigid body motion from noisy marker data.

3.3.3 Marker Occlusion and Instrument Error Compensation

3.3.3.1 Marker Occlusion

In order to compute the three-dimensional position of a retroflective marker in the capture volume of a video-based stereophotogrammetric system, the marker must be in the field of view of at least 2 cameras (see Section 2.3.2.1). Then, from two or more two-dimensional images, the three- dimensional position can be calculated. However, when a marker is occluded from the field of view of the cameras by a body segment or foreign object in the measurement volume [Chiari et al. (2005)], they loose sight of the marker. Consequently, the marker's three-dimensional position cannot be determined. Marker occlusion causes loss of positional data, resulting in an incomplete positional signal. To simulate marker occlusion, marker M1 of the analytical model was given an incomplete positional signal, by removing a series of data points from the data set. Figure 3-17 shows the trajectory of marker M1 where a single data point, *n*, approximately at the midpoint of the motion has been removed.

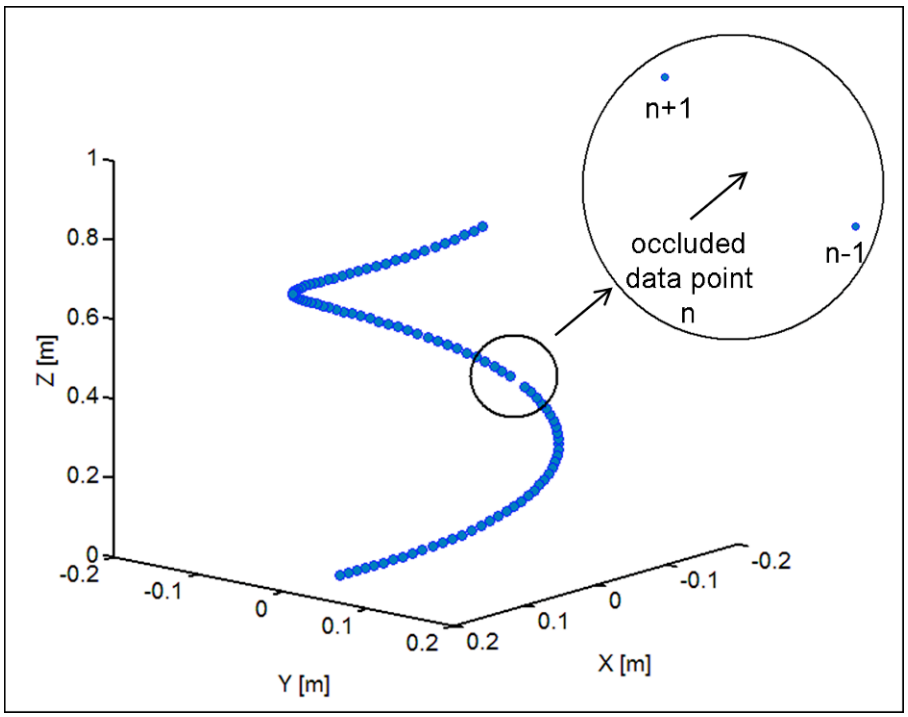

Figure 3-17: Trajectory of marker M1; occluded data point highlighted

A method of replacing the occluded marker data is to interpolate between the nearest data points before and after the missing data, that is between point *n-1* and *n+1* in Figure 3-17. This approximate method yields an analytical expression of the position, as a function of time, for the missing interval, that is from point *n-1* to *n+1*. To complete the data set, the analytical expression is evaluated at the missing data points, in this case point *n*. It is important to apply an interpolation method that produces a continuous signal to avoid introducing any discontinuities. Furthermore, as marker occlusion can occur multiple times in a single data set, it is of interest to apply an interpolation method that replaces all missing data points present in the signal in one step. To satisfy this criterion, the method of cubic splines was applied to the positional data to replace occluded data points. This method produces high quality interpolation while avoiding the oscillations that result from high order interpolants [Kreyszig (1999d)]. Spline interpolation divides an interval of points into subintervals and applies a low-degree polynomial at each subinterval. An interpolating function, or spline, is found by fitting all polynomials into a single curve, which yields a piecewise polynomial

interpolation [Kreyszig (1999d)]. A cubic spline is made up of third order polynomials, one at each subinterval, and forces the first and second derivates of adjacent polynomials to be equal. This yields a continuous function that has continuous first and second derivatives along the entire interval of points. To illustrate cubic spline interpolation, Figure 3-18 shows the *x* component of the incomplete trajectory of marker M1, where data point *n* has been removed. Figure 3-18 (a) shows the complete displacement of marker M1, highlighting the occluded data point, while Figure 3-18 (b) show the displacement from data points *n-2* to *n+2*.

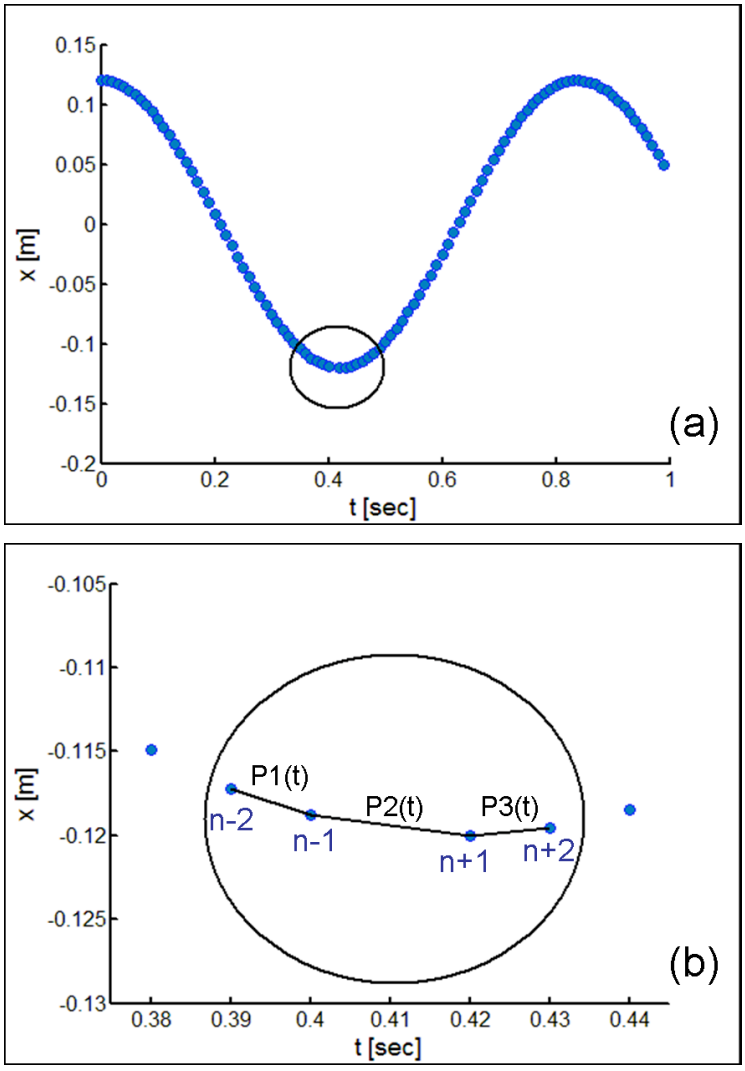

Figure 3-18: Position of marker M1 (a) *x* component; (b) Interpolating polynomial adjacent to point n

Each interpolant, $P_1(t)$, $P_2(t)$ and $P_3(t)$, represents a third order polynomial where the position of their respective end points is known. These polynomials, and their first and second derivatives, are defined as:

$$\begin{aligned} P_i(t) &= a_{1i} + a_{2i}t + a_{3i}t^2 + a_{4i}t^3 \\ p_i'(t) &= a_{2i} + 2a_{3i}t + 3a_{4i}t^2 \\ p_i''(t) &= 2a_{3i} + 6a_{4i}(t) \end{aligned} \quad \textbf{(3-35)}$$

where a_{1i}, a_{2i}, a_{3i} and a_{4i} are four coefficients that define each polynomial. To produce a continuous signal that is twice differentiable, the first and second derivatives of adjacent polynomial are made equal at common data points. For the current spline, these conditions can be expressed as follows:

$$\begin{aligned} P_1'(n-1) &= P_2'(n-1) & \qquad P_2'(n+1) &= P_3'(n+1) \\ P_1''(n-1) &= P_2''(n-1) & \qquad P_2''(n+1) &= P_3''(n+1) \end{aligned} \quad \textbf{(3-36)}$$

To solve for each cubic polynomial coefficients, a total of twelve equations are required, as each polynomial is defined by four coefficients. The value of each polynomial is known at their respective end points, for a total of six equations; forcing the first and second derivatives to be equal for adjacent polynomials provides four equations, for a total of 10 equations. Therefore, two additional equations are required to solve the system and will come in the form of end conditions. The end condition chosen forces the third derivative of the first and last polynomial to be equal to their adjacent polynomials at the shared data point. This imposes continuity of the third derivative at the second and second to last data points, and is referred to as the *not-a-knot* end condition. For the current spline, this end condition is expressed as follows:

$$P_1'''(n-1) = P_2'''(n-1)$$
$$P_2'''(n+1) = P_3'''(n+1) \quad \textbf{(3-37)}$$

These last two equations complete the linear system of equations that can now be solved and the polynomial coefficients found. Once the cubic spline is fully defined, that is when all coefficients are known, the data can be resampled for all data points, replacing any missing data points due to marker occlusion. In the case of marker M1, three separate interpolating cubic splines would be defined, one for each Cartesian components of the marker trajectory. These three polynomials would be evaluated at data point *n*, completing the positional signal. For example, the x component of data point n would be given by polynomial P2 and calculated as follows

$$P_2(n) = a_{12} + a_{22}t(n) + a_{32}t(n)^2 + a_{42}t(n)^3 \quad \textbf{(3-38)}$$

In order to determine the effects on ISA parameters of introducing an interpolating cubic spline to an incomplete positional signal, data points were removed from the positional signal of marker M1 (see Figure 3-18). A series of N_1 adjacent data points, ranging from N_1=1 to N_1=20 and either centered about point *n* or positioned at the beginning of the motion, were removed from the positional signal. Then, after applying an interpolating cubic spline to the *x*, *y* and *z* components of the position of marker M1, the ISA parameters were computed. The error of the ISA parameters was calculated and averaged over the corresponding N_1 data points of each series, and is shown in Table 3-15, for data centered about point *n*, and Table 3-16, for data removed at the beginning of the motion. To maximize the effects of the interpolating cubic spline, the position of the ISA, as well as the parallel velocity and angular velocity about the ISA were computed from the position and velocity of marker M1.

Table 3-15: ISA error resulting from interpolating cubic spline; occluded data at the midpoint of the motion. * Reference value 0.9m/s; ** reference value 7.5 rad/s.

Number of data points (N_I)	ISA Error ε_o [rad]	ε_p [m]	ε_v [m/s] (% relative error*)	ε_w [rad/s] (% relative error**)
1	8.55E-16	2.97E-10	1.22E-15 (1.35E-13)	3.41E-03 (4.55E-02)
5	8.64E-16	2.08E-05	1.23E-15 (1.37E-13)	2.93E-03 (3.90E-02)
10	8.02E-16	3.09E-04	1.13E-15 (1.26E-13)	1.10E-02 (1.47E-01)
20	7.50E-16	3.02E-03	1.06E-15 (1.18E-13)	1.16E-01 (1.54E+00)

Table 3-16: ISA error from interpolating cubic spline; occluded data at the beginning of the motion. *Reference value 0.9m/s; **reference value 7.5 rad/s.

Number of data points (N_I)	ISA Error ε_o [rad]	ε_p [m]	ε_v [m/s] (% relative error*)	ε_w [rad/s] (% relative error**)
1	9.74E-15	1.05E-03	1.39E-14 (1.55E-12)	3.43E-03 (4.57E-02)
5	8.27E-15	1.79E-03	1.18E-14 (1.31E-12)	9.98E-02 (1.33E+00)
10	1.13E-15	4.77E-03	1.57E-15 (1.75E-13)	4.10E-01 (5.46E+00)
20	1.37E-13	6.76E-03	1.95E-13 (2.17E-11)	2.23E+00 (2.97E+01)

The analytical model shows that ISA orientation is nearly unaffected by the application of an interpolating spline, as the maximum value of ε_o is 1.37×10^{-13} radians (7.82×10^{-12} degrees), as seen in Table 3-15 and Table 3-16. When the occluded data is at the midpoint of the motion, the error in ISA position is less than a millimeter for all but large series, as ε_p reached 3.02 mm when N_I=20 data points. However, when occluded data is at the beginning or end of the motion, the error in ISA position increases, as ε_p is approximately 1.8 mm for N_I=5 and

reaches 6.76 mm for N_I=20. When compared to the error from marker placement, the largest error in ISA position, 6.67 mm, is less than a third (0.319) of the error in locating the anatomical landmarks of the pelvis (see Section 3.3.1.1). The results show, for both locations of occluded data, that ε_p is proportional to the length of occlusion, N_I, and that ε_p is larger when occlusion occurs at an extremity of the motion, where the hole in the data is not surrounded by known data points. These results were expected, as it has generally been found that the accuracy of interpolation decreases as the duration of occlusion increases and the gap in data occurs at a free end, as the end conditions can have a pronounced effect on the behavior of the spline near the end points [Shikin and Plis (1995)]. In order to account for the increase in ε_p when occlusion occurs at a free end, a center portion of the data collected will be analyzed and discussed in Section 3.4. As for the movement about the ISA, the error in the parallel velocity is negligible for all trajectories of marker M1, while ε_w is $1.16\text{x}10^{-01}$ rad/s for the largest data series at the midpoint of motion, representing an error of 1.5 percent with respect to the know angular velocity. When occlusion is at the beginning of the motion, ε_w reaches a relative error of 1.3 percent when N_I=5 and 29.7 percent when N_I=20, which further demonstrates the importance of eliminating end effects when analyzing motion.

3.3.3.2 Random Instrument Error

As covered in Section 2.3.2.2, sources of random instrument error include marker flickering, the digitization process and marker image shape distortion [Chiari et al. (2005)]. Random instrument error, although brief in nature, can lead to unreliable calculations of positional derivatives [Woltring (1995)]. To illustrate the effects of random instrument error on marker position, the z-component of the RASIS pelvic marker during the downswing is shown in Figure 3-19 (a). This displacement was taken from Subject 1 preliminary data.

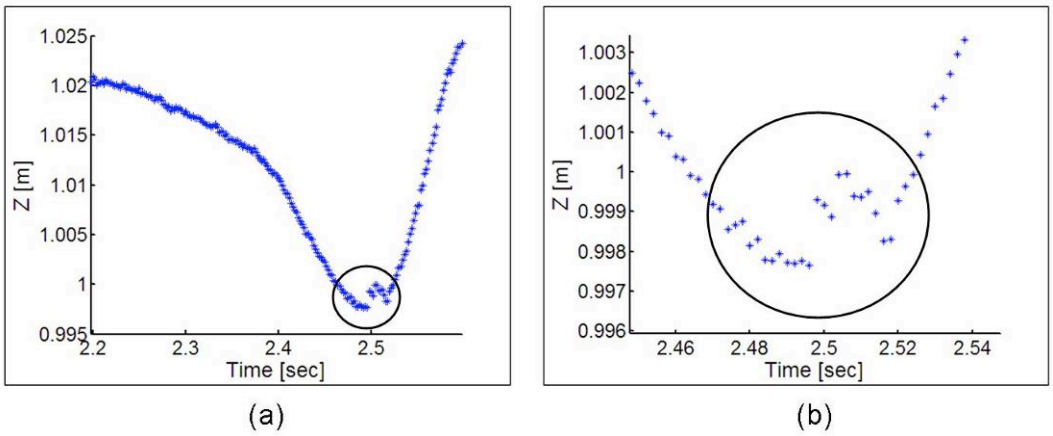

Figure 3-19: Displacement of the RASIS pelvis marker (a) z-component; (b) Close up of discontinuity in marker displacement

The motion of the pelvis during the downswing is continuous, free of rapid changes in direction or impacts, as shown by hip rotation plots produce by Burden et al. [Burden et al. (1998)]. This being said, the short-lived deviations in trajectory occurring from 2.50 sec to 2.52 sec as observed in Figure 3-19 (b) are assumed to be spurious data points, not belonging to the motion of the pelvis. This is an example of random instrument error, which appears as a sum of random impulses in a marker's trajectory. As random errors produce significant inaccuracies in the calculation of positional derivatives, it is of interest to identify such impulses and reduce their effects. In an effort to simulate these effects, random errors have been applied to the trajectory of marker M1, of the analytical model, in the form of controlled impulses. A series of N_2 adjacent impulses, ranging in duration from N_2=1 to N_2=10 and centered about data point n, as with the simulation of marker occlusion (see Section 3.3.3.1), were applied to the x, y and z coordinates of marker M1. To simulate random impulses, the magnitude of each x, y and z components was given any of the three following values: 2, 5 and 10 mm. Furthermore, each of the individual impulses, one for each data point, was randomly given 1 of the 27 possible combinations of these three magnitudes. Figure 3-20 shows the x component of the displacement of marker M1 to which a series of 10 impulses has been imposed.

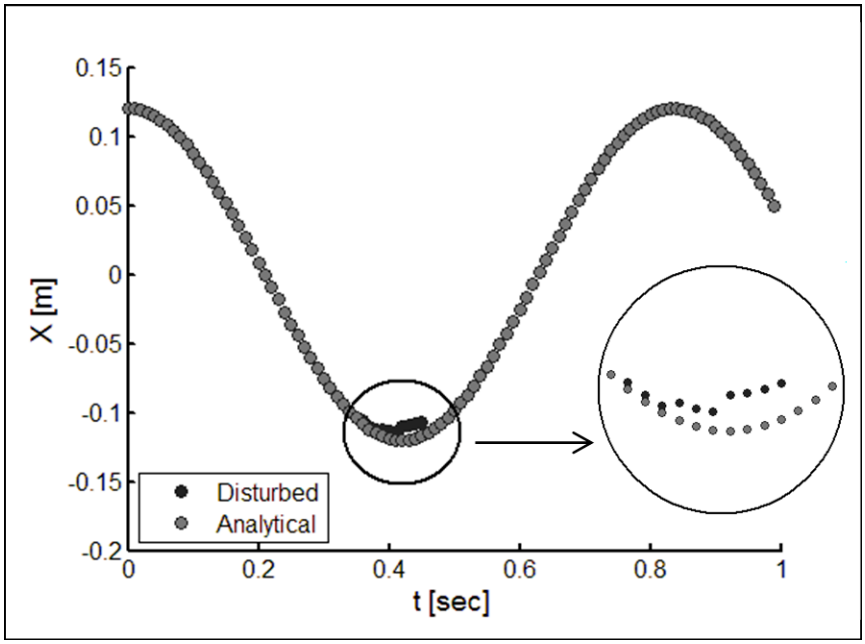

Figure 3-20: Displacement of marker M1, x coordinate with N_2=10 impulses; analytical displacement labeled *Analytical* and disturbed displacement, with added impulses, labeled *Disturbed*

To reduce random instrument error effects, the objective is to retrieve the base signal, which represents true body motion, identify random noise, which represent instrument error, and apply an error compensation method. Various methods have been used to compensate for random instrument errors, as described in Section 2.3.2.2. Of these methods, low-pass digital filters have been successively used to reduce high-frequency instrumental noise, by attenuating noise above a specified cutoff frequency [Winter (2004)]. Applying a digital low-pass filter to raw marker trajectories can reduce the effects of high-frequency random noise and provide a reference for the base signal. In the analytical model, the base signal is represented by the analytical displacement while the raw signal, with random instrument noise, is represented by the disturbed displacement. Of the different low-pass filters available, low-pass Butterworth filters have proven effective for this purpose, specifically the fourth order zero-phase-shift Butterworth filter [Winter (2004), Cappello et al. (1996), Giakas and Baltzopoulos (1997), Alonso et al. (2005)]. It should be noted that, while they attenuate undesirable high-frequency components from the raw signal, they also introduce a phase lag, causing phase distortion [Winter (2004)]. To compensate for this phase shift, the

signal is filtered in both directions, which eliminates any phase distortion and doubles the filter order. Therefore, to achieve the desired 4^{th} order filter, with no phase shift, a second order Butterworth filter is applied in both directions [Winter (2004)].

The performance of a low-pass filter is dependant on the choice of cutoff frequency, which is in turn a function of the frequency content of the raw signal. The magnitude of the cutoff frequency must be sufficiently low to attenuate the desired high frequencies, while sufficiently high as to avoid distortion of the base signal [Winter (2004)]. Two methods were followed to determine the optimal cutoff frequency: by visual inspection of the power spectral density (PSD) of the raw displacement signal, from preliminary data of Subject 1, and by a residuals analysis using the disturbed marker displacements of the analytical model. The PSD of a signal is obtained by Fourier Transform [Kreyszig (1999b)]. A Fourier transform can be computed for a discrete signal, such as the displacement signal of a marker, by Fast Fourier Transform and returns the intensity of the signal for a series of frequencies, yielding the frequency content of that signal. That being said, it is known that stereophotogrammetric signals have a high signal-to-noise ratio, where the base signal occurs at low frequencies [Chiari et al. (2005)] and the present noise is concentrated at high frequencies [Alonso et al. (2005)]. Furthermore, if it is assumed that the noise is white and of Gaussian nature, the PSD should be a straight line [Alonso et al. (2005)]. Consequently, the cutoff frequency can be determined by visual inspection of the PSD, were the amplitude after the cutoff frequency is very low, considerably smaller than before the cutoff frequency, and forms a straight line [Alonso et al. (2005)]. The PSD of the x component of the displacement of the RASIS pelvic marker, obtained by Fast Fourier Transform of the raw signal, is shown in Figure 3-21.

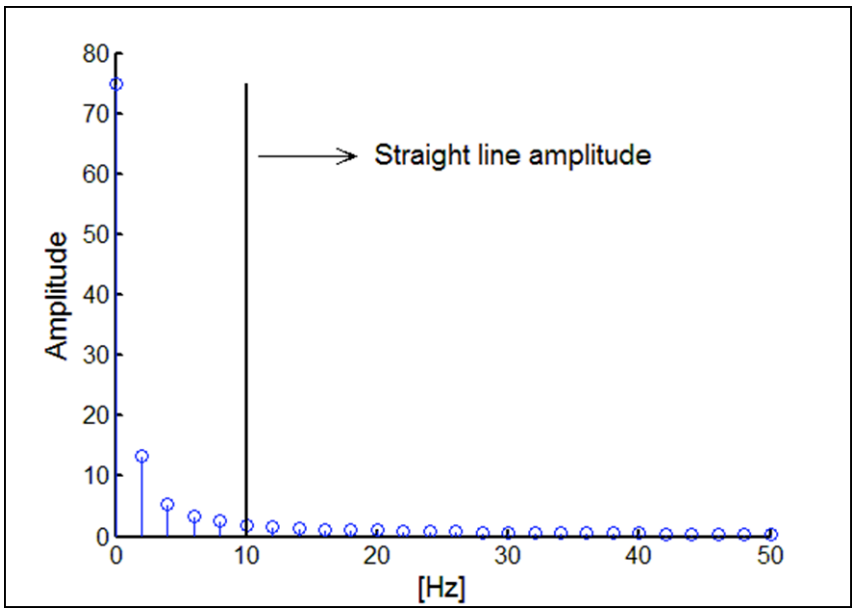

Figure 3-21: PSD of marker displacement, x component; marker placed on the RASIS of the pelvis

The PSD of the marker displacement shows that the signal intensity is concentrated at low frequencies, below approximately 10 Hz, and rapidly decreases and transitions into a straight line, as expected. Assuming white Gaussian noise, the PSD of the displacement indicates that the cutoff frequency is situated at approximately 10Hz. Although this method relies on visual inspection only, it certainly provides an appropriate approximation of the cutoff frequency. The second method followed to select the cutoff frequency is the optimization analysis described by Cappello et al. [Cappello et al. (1996)]. This residuals analysis consists of applying the same digital filter at various cutoff frequencies. The root mean square error (RMSE) is calculated between the base signal and the filtered signal. The filtered signal is determined by applying a low-pass digital filter to the base signal to which artificial noise has been added. In the present case, the base signal would be associated with the analytical displacement of marker M1, while the noisy signal would be associated with the disturbed displacement of marker M1. Therefore, the resulting RMSE for a single cutoff frequency would be calculated as:

$$RMSE = \sqrt{\frac{1}{n_f}\sum_{i=1}^{n_f}\left(x_i - x_{F_i}\right)^2 + \left(y_i - y_{F_i}\right)^2 + \left(z_i - z_{F_i}\right)^2} \qquad \textbf{(3-39)}$$

where n_f represents the number of frames, or data points, x, y and z represent the coordinates of marker M1, and x_F, y_F and z_F represent the filtered coordinates of the disturbed displacement of marker M1. The rational of this analysis is that the RMSE error will decrease proportionally with the cutoff frequency up to its optimal value, beyond which the RMSE error will increase significantly. When the RMSE error increases, the cutoff frequency is set too low and signal distortion occurs [Winter (2004)]. This analysis was carried out for cutoff frequencies of 5 to 15 Hz (by 1 Hz increments), 20 Hz and 25 Hz, and for four different series of adjacent impulses, were N was equal to 1, 3, 5 and 10. The frequency interval was chosen to include the cutoff frequency of 10 Hz determined by visual inspection of the PSD. In Figure 3-22, the RMSE of the displacement of marker M1 is shown as a function of the cutoff frequency, where the applied filter was a second order Butterworth filter applied in the forward and backward directions.

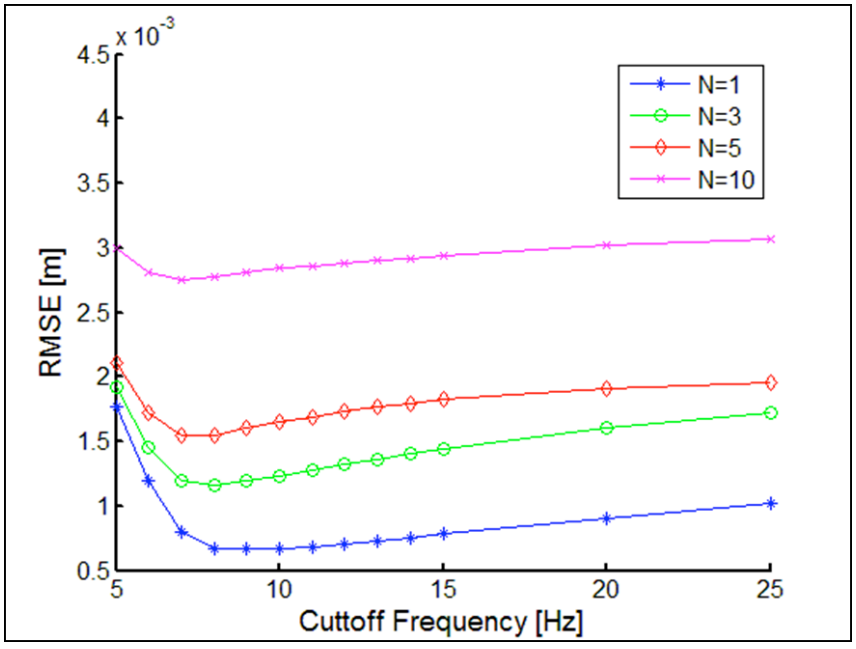

Figure 3-22: RMSE as a function of cutoff frequency

It can be seen that the RMSE decreases up to a frequency slightly inferior to 10 Hz, after which the error increases rapidly. The average frequency associated with a minimum RMSE, for the four different impulse durations, was 8 Hz. Therefore, according to this error analysis, the optimal cutoff frequency for the displacement signal of marker M1 would be 8 Hz. This result is very near the frequency of 10 Hz determined by visual inspection of the PSD of the raw marker displacement. Although the cutoff frequency of 8 Hz further reduces the error caused by the applied impulses, it also introduces a very slight distortion of the base signal. In an effort to conserve the characteristics of the base signal, a cutoff frequency of 10 Hz was chosen. The x-coordinate of marker M1 following the application of the chosen Butterworth filter, with a cutoff frequency of 10Hz, is shown in Figure 3-23. The RMSE, relative to the analytical displacement, has been noticeably reduced as shown in Table 3-17.

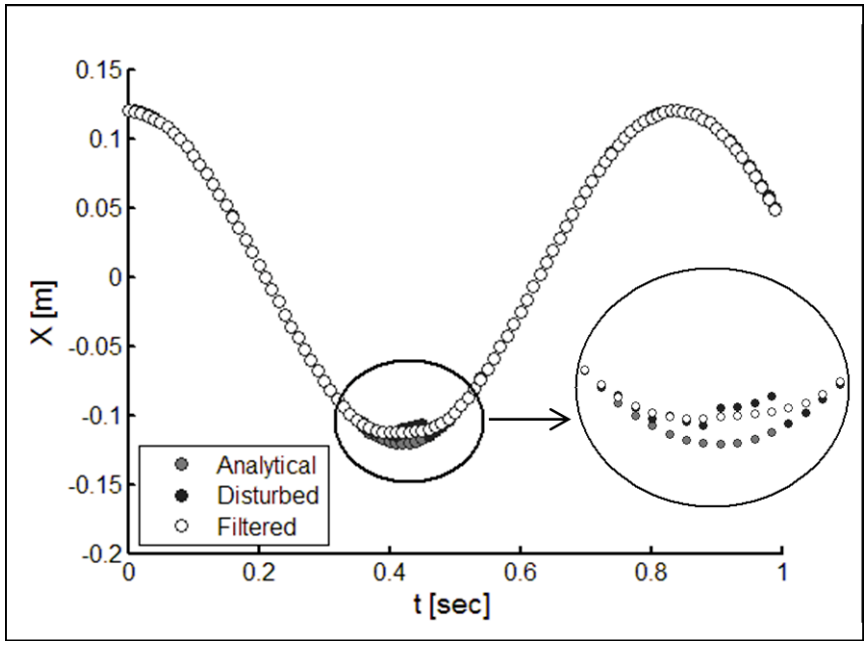

Figure 3-23: Application of second order Butterworth filter with a cutoff frequency of 10 Hz, applied in the forward and backward directions; analytical displacement labeled *Analytical*, disturbed displacement, with added impulses, labeled *Disturbed* and filtered displacement labeled *Filtered*

Table 3-17: RMSE of the displacement of marker M1 as function of number of impulses N_2. Percent difference was calculated as the ratio of the difference between the disturbed and filtered RMSEs divided by the disturbed RMSE, expressed in percent. A positive percent difference indicates an increase in RMSE, of the filtered error relative to the disturbed error, while a negative percent difference indicates a reduction in RMSE.

Data	RMSE			
	N_2=1 [m]	N_2=3 [m]	N_2=5 [m]	N_2=10 [m]
Disturbed	0.00150	0.00197	0.00220	0.00333
Filtered	0.00067	0.00120	0.00160	0.00279
Percent Difference	-55.2	-38.9	-27.6	-16.4

The first objective to reduce random instrument noise was to retrieve the base signal, which was accomplished by applying a second order Butterworth filter with a cutoff frequency of 10 Hz and in the forward and backward directions. The second objective was to identify random noise within the raw displacement signal. This can be achieved by comparing the filtered displacement signal to the raw displacement signal, more specifically by calculating the error between the two at every data point. When examining Figure 3-23, it can be seen that the error between the disturbed and filtered displacements is noticeably higher when random instrument noise is present. Therefore, if the error between the two displacements is considerably higher at specific data points, compared to the mean error, then it can be assumed that random instrument error is the source of this disparity. As a consequence, if any outliers are present in the error between the two displacements, these data points will be associated with random instrument error. Outliers in the error between the two displacements, calculated as the distance between data points, are identified with Chauvenet's criterion [Taylor (1982c), Schenck (1979), Holman (1984)]. This criterion states that if the probability of having a measurement as far from the mean as the suspected measurement is less than 0.5 of a measurement, assuming the measurements belong to a Gaussian distribution, then this measurement can be labeled an outlier [Taylor (1982c)]. To apply Chauvenet's criterion to the present situation, the error between the two displacements, ε_F, is calculated for all frames, along with the mean, $\overline{\varepsilon_F}$, and standard deviation, S_{ε_F}, of this series. For each data point within

this series, the number of standard deviations away from the mean is calculated, as follows:

$$t_S = \frac{\varepsilon_F - \overline{\varepsilon_F}}{S_{\varepsilon_F}} \quad \textbf{(3-40)}$$

where t_S is the multiple of standard deviations. As the series is assumed to follow a Gaussian distribution, the probability of having an error ε_F of t_S standard deviations away from the mean is given by

$$P(outside\ t_S \times S_{\varepsilon_F}) = 1 - P(inside\ t_S \times S_{\varepsilon_F}) \quad \textbf{(3-41)}$$

where P is given by the probability density function of a Gaussian distribution [Kreyszig (1999a)]. In order to determine the number of possible measurements of this series, outside of this region, the probability P is multiplied by the number of frames as follows

$$N_{outliers} = n_f \times P(outside\ t_S \times S_{\varepsilon_F}) \quad \textbf{(3-42)}$$

where $N_{outliers}$ is the number of data points farther away from the mean. If $N_{outliers}$ is inferior to 0.5, Chauvenet's criterion states that this data point can be considered an outlier, as less than half of a single measurement, of the n_f measurements, would be farther from the mean [Taylor (1982c)]. In Figure 3-24 the outliers identified in the disturbed displacement of marker M1, when a series of N_2=10 impulses has been applied, are shown. It can be seen that 5 data points have been identified as possible outliers, all contained within the series of added impulses.

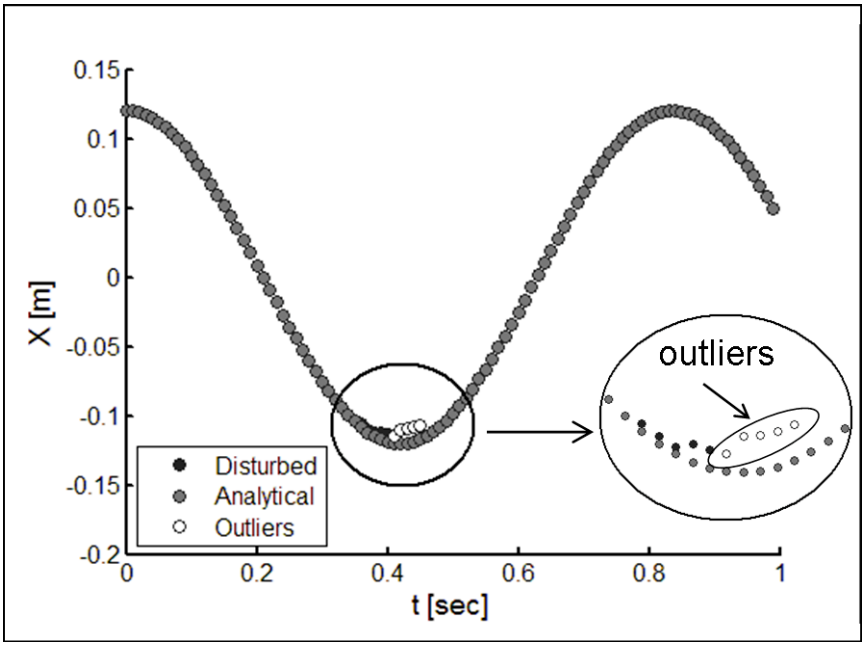

Figure 3-24: Random instrument error, trajectory outliers, identified by Chauvenet's criterion; analytical displacement labeled *Analytical*, disturbed displacement, with added impulses, labeled *Disturbed* and identified trajectory outliers labeled *Outliers*

The application of Chauvenet's criterion has fulfilled the second object of identifying instances of random instrument error within the trajectory of a marker. The third objective is to compensate for theses errors, in order to reduce their effects on ISA computation. It can be seen in Figure 3-23 that applying a low-pass digital filter approaches the disturbed displacement to the analytical displacement of marker M1, reducing the RMSE between the two. Therefore, in the case of data points that have been identified as outliers, the corresponding filtered data points are closer to the base signal and represent possible replacements for these cases of random error. Therefore, data points that fail to satisfy Chauvenet's criterion will be replaced by their corresponding filtered data points. This provides a modified "raw" displacement signal, where random instruments errors have been attenuated. In the analytical model, this reduction random instrument error can be assessed by calculating the mean and standard deviation of the error relative to the analytical signal. The tabulated values of the error are shown in Table 3-18, mean and standard deviation, for the disturbed signal and the modified signal, free of outliers. It can be seen that the mean and standard deviation are both reduced following the removal of outliers.

Table 3-18: Error in marker M1displacement relative to analytical displacement; mean and standard deviation

Number of impulses (N_2)	Positional Error			
	Mean		Standard deviation	
	Disturbed [m]	Outlier-free [m]	Disturbed [m]	Outlier-free [m]
1	1.50E-04	1.78E-06	1.50E-03	1.78E-05
3	2.94E-04	3.70E-05	1.95E-03	1.43E-04
5	4.59E-04	3.38E-05	2.17E-03	1.19E-04
10	9.74E-04	5.97E-04	3.20E-03	1.90E-03

Although random instrument errors have been reduced, it is possible that data points still do not satisfy Chauvenet's criterion in the modified signal. Most authorities agree that Chauvenet's criterion should not be reapplied a second time, with the modified values of mean and standard deviation [Taylor (1982c)]. However, in the present situation, the data points do not represent the same quantity being resampled, but rather the time varying trajectory of a marker. Therefore, the application of the criterion is not to determine a fixed value, in which case the criterion should not be reapplied, but rather to filter out errant data points within the trajectory. Therefore, the procedure outlined above, of replacing outliers with their filtered counter parts, will be reapplied until the displacement is free of outliers. This will produce a modified "raw" displacement signal where random instrument errors have been significantly reduced and care has been taken to leave the base signal unaffected. Figure 3-25 displays the analytical displacement, the disturbed displacement (with added impulses), and the final modified displacement (free of outliers). This clearly shows that the effects of random instrument error have been attenuated, as the displacement of marker M1 gets closer to the analytical displacement.

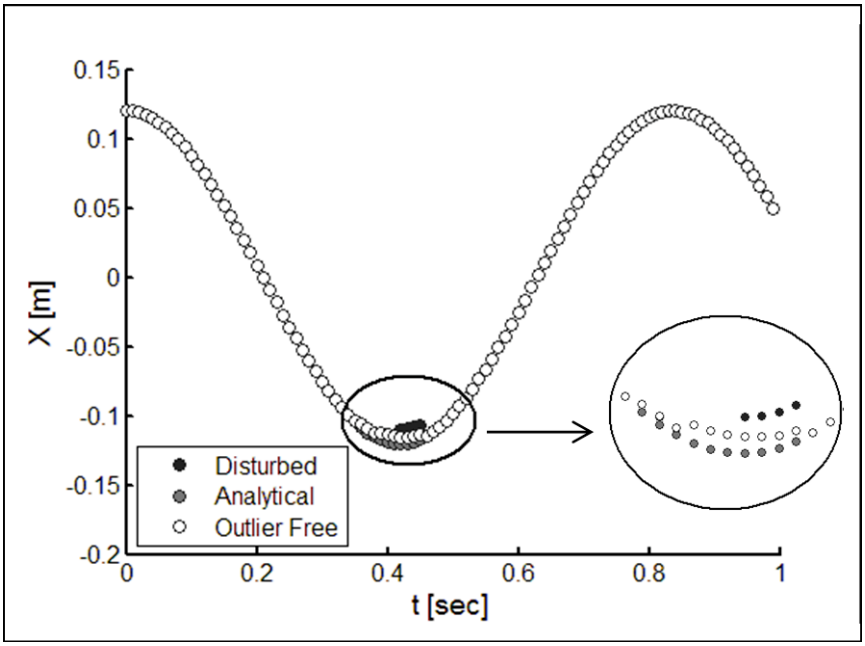

Figure 3-25: Modified displacement of marker M1, free of outliers; analytical displacement labeled *Analytical*, disturbed displacement, with added impulses, labeled *Disturbed* and displacement free of outliers labeled *Outlier Free*

The procedure outlined above fulfills the objective of retrieving the base displacement signal, from raw marker data, identifying instances of random instrument error, by applying Chauvenet's criterion, and finally by replacing these outliers by their corresponding filtered data points. As previously discussed, it is of interest to determine the effects of random instrument error on ISA computation, and to determine the change in error from the procedure described above. Table 3-19 displays the errors in ISA computation from the disturbed displacement of marker M1, with added impulses, and following the removal of trajectory outliers.

Table 3-19: ISA error resulting from random instrument error, calculated from the disturbed displacement and outlier free displacement. Percent difference was calculated as the ratio of the difference between disturbed error and outlier-free error divided by the disturbed error, expressed in percent. A positive percent difference denotes an increase in error, while a negative percent difference denotes a decrease. * Reference value 0.9m/s; ** reference value 7.5 rad/s.

Marker Position	Number impulses (N_2)	ISA Error ε_o [rad]	ε_p [m]	ε_v [m/s] (% relative error*)	ε_w [rad/s] (% relative error**)
Disturbed	1	9.97E-16	6.53E-03	1.42E-15 (1.57E-13)	4.20E-01 (5.60E+00)
	3	7.76E-02	8.87E-03	1.09E-01 (1.21E+01)	9.77E-01 (1.30E+01)
	5	3.83E-02	1.76E-02	5.44E-02 (6.04E+00)	1.43E+00 (1.91E+01)
	10	3.66E-02	1.76E-02	5.18E-02 (5.76E+00)	1.40E+00 (1.86E+01)
Outlier-Free	1	1.29E-09	6.19E-05	1.84E-09 (2.05E-07)	5.36E-03 (7.14E-02)
	3	2.17E-03	2.73E-04	3.09E-03 (3.44E-01)	3.11E-02 (4.14E-01)
	5	1.43E-03	6.63E-04	2.03E-03 (2.26E-01)	5.40E-02 (7.21E-01)
	10	3.46E-02	9.93E-03	4.92E-02 (5.46E+00)	1.06E+00 (1.41E+01)
Percent Difference	1	1.30E+08	-99.1	1.30E+08	-98.7
	3	-97.2	-96.9	-97.1	-96.8
	5	-96.3	-96.2	-96.3	-96.2
	10	-5.5	-43.5	-5.1	-24.2

The analytical model shows that ISA orientation can be appreciably affected by random instrument error, as the error varies from a negligible magnitude, 10^{-16} radians, up to 7.76×10^{-2} radians (4.45 degrees). When outliers are removed from the displacement, the error in ISA orientation is reduced, from negligible magnitude, 10^{-9} radians, up to 3.46×10^{-2} radians (1.98 degrees). This orientation error of less than 2 degrees is approximately a quarter of the error from marker placement of 7.6 degrees (see Section 3.3.1.1). When compared to the error in marker placement, other than the case of a single impulse, where the error was negligible in both cases, the reduction in error was significant for N_2=3 and N_2=5, but only a slight improvement was achieved from N_2=10. The error in position of the ISA reaches magnitudes up to 17.6 mm, when calculated with the disturbed

displacements, but is reduced to a maximum value of 9.93 mm when using outlier free marker displacements. Although an error of approximately 10 mm appears high, it is still less than half the error caused by marker placement variability (see Section 3.3.1.1). On average, the error in ISA position was reduced by 83.9 percent when using outlier free marker displacements. As for the movement about the ISA, the error in parallel velocity reaches a maximum of 0.109 m/s, as is reduced to a maximum value of 0.0492 m/s, which represents a relative error of 5.46 percent, relative to the known magnitude of 0.9 m/s. The error in angular velocity reaches a maximum magnitude of 1.43 rad/s, but is reduced to 1.06 rad/s for outliers free marker displacements. On average, the error in angular velocity about the ISA was reduced by 79.0 percent when using outlier free marker displacements.

It is shown in Table 3-19 that the error in ISA orientation and position, as well as the error in the movement about the ISA, has been reduced when outlier free displacements are used during computation, as opposed to using the raw displacements. It should be noted that further reduction in random instrument error can be achieved by applying the chosen low-pass digital filter to the outlier free displacements. This will be preformed in the following section.

3.3.3.3 Systematic Instrument Error

As detailed in Section 2.3.2.2, sources of systematic instrument error include photogrammetric calibration inaccuracies and non-linearities that the model could not remove, the magnitudes of which are affected by the size of the measurement field and the position that the marker assumes within it [Chiari et al. (2005)]. To simulate the effects on ISA computation, systematic instrument error was added to the displacement of marker M1, of the analytical model, by way of a continuous noise model adapted from Chèze et al. [Chèze et al. (1998)]. The continuous noise model generates systematic instrument error, in the x, y and z directions, as follows

$$\vec{N} = A_x \sin(\omega_N t + \phi_x)\vec{i} + A_y \sin(\omega_N t + \phi_y)\vec{j} + A_z \sin(\omega_N t + \phi_z)\vec{k} \quad \textbf{(3-43)}$$

where $\vec{N}$ is the applied noise, A_x, A_y and A_z are the signals amplitudes, in their respective directions, ω_N is the noise angular velocity (a function of noise frequency) and φ_x, φ_y and φ_z are the phases angles of each x, y and z noise component. The amplitude of the applied noise was selected from the study of system accuracy, where the precision (standard deviation) of system measurements was determined at 6 different settings within the measurement field, as described in Section 3.1.1. When averaging the maximum values of measurement precision recorded at these 6 settings, a mean value of 0.488 mm is obtained. Therefore, the total amplitude of the applied noise $\left\|\vec{A}\right\|$, the magnitude of the combined A_x, A_y and A_z components, was set to 0.5 mm. The frequency of the applied noise was selected as half of the sampling frequency of the photogrammetric system, 50 Hz. This choice of frequency is supported by the fact that instrument noise is concentrated at high frequencies [Alonso et al. (2005)], and that it is reasonable to assume that the applied noise be halfway between the sampling frequency and the frequency of the base signal. Three phases angles, φ_x, φ_y and φ_z, were introduced to allow for a phase relationship between noise components. In order to maintain a constant magnitude of applied noise $\vec{N}$, phase angles of *0*, *2π/3* and *-2π/3* were selected, corresponding to φ_x, φ_y and φ_z, respectively. Furthermore, the amplitude of each noise component was set to the same value and calculated as

$$A_x = A_y = A_z = \sqrt{\frac{2\left\|\vec{A}\right\|^2}{3}} \quad \textbf{(3-44)}$$

ensuring that, along with the chosen phase angles, the total noise amplitude remains at a constant value $\left\|\vec{A}\right\|$. The x coordinate of marker M1 following the

addition of the continuous noise model is shown in Figure 3-26 as a representative example.

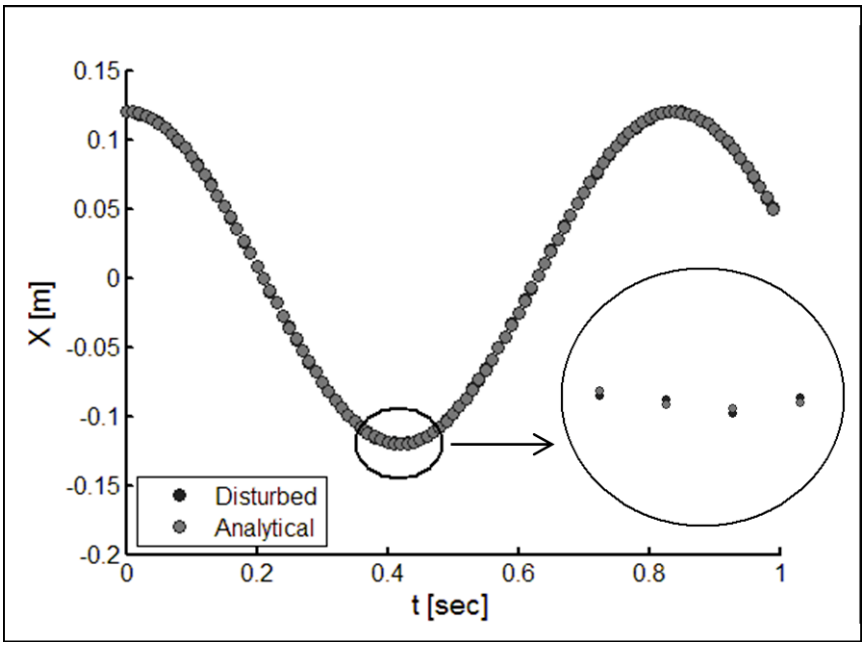

Figure 3-26: Displacement of marker M1, x-coordinate, with added continuous noise model

As was the case with random instrument error, it is of interest to attenuate systematic instrument error and retrieve the base signal, thus reducing the errors on ISA computation. This can be accomplished by using the techniques employed to identify instances of random instrument error (see Random Instrument Error) and with the properties of systematic instrument error. As previously discussed, it is known that stereophotogrammetric signals have a high signal-to-noise ratio, where the base signal occurs at low frequencies [Chiari et al. (2005)] and that the noise is concentrated at high frequencies [Alonso et al. (2005)]. Consequently, applying a low-pass digital filter, as the Butterworth filter used to identify random instrument error, can attenuate high frequency systematic instrument noise and retrieve the base signal. As systematic instrument error affects all data points, as opposed to a given number of outliers, the low-pass digital filter is applied to the disturbed displacement and the resulting data series, all data points, will be chosen. The error in ISA computation from the disturbed displacement of marker M1, with added continuous noise model, and following the application of the

chosen Butterworth filter, with a cutoff frequency of 10Hz, is shown in Table 3-20.

Table 3-20: ISA error resulting from systematic instrument error calculated from Disturbed marker displacement (base signal with added continuous noise model) and Filtered displacement (raw displacement with applied low-pass digital filter). Percent difference was calculated as the ratio of the difference between Disturbed error and Filtered error divided by the Disturbed error, expressed in percent. A positive percent difference denotes an increase in error, while a negative percent difference denotes a decrease. * Reference value 0.9m/s; ** reference value 7.5 rad/s.

Displacement	ISA Error			
	ε_o [rad]	ε_p [m]	ε_v [m/s] (% relative error)*	ε_w [rad/s] (% relative error)**
Disturbed	2.653E-02	1.856E-03	3.854E-02 (4.28E+00)	2.342E-01 (3.12E+00)
Filtered	6.478E-03	2.434E-03	9.174E-03 (1.02E+00)	1.078E-01 (1.44E+00)
Percent Difference	-75.6	31.2	-76.2	-54.0

The analytical model shows that ISA orientation deviates by approximately 2.65 $x10^{-2}$ radians (1.52 degrees) as a result of systematic instrument noise, but is reduced by approximately 76 percent to $6.478x10^{-3}$ radians (0.37 degrees), both of which are below the orientation error of 7.6 degrees consistent with marker placement error (see Section 3.3.1.1). Conversely, the error in ISA position is increased with the application of the low-pass filter, from 1.86 mm to 2.43mm. However, in both computations, with raw and filtered data, the error in ISA position is an order of magnitude less than the error caused by marker placement variability (see Section 3.3.1.1). The error in the movement about the ISA is reduced by at least 50 percent following the application of the low-pass filter, for both the parallel and angular velocities. In both cases, the relative error is less than 5 percent when compared to the known magnitudes of the analytical model. These results show that applying a low-pass digital filter can effectively reduce the effects of systematic instrument error.

In the previous section (Random Instrument Error), it was mentioned that further reduction in random instrument error could be achieved by applying the chosen low-pass digital filter to the outlier free displacements. Therefore, in the case of displacements measured by stereophotogrammetry, which contain both random and systematic instrument error, the chosen low-pass digital filter would be applied to the outlier free raw signal. This would solve two problems in parallel, reducing the effects of random instrument error while attenuating the high frequency systematic instrument error.

3.3.4 Soft Tissue Artifact

As discussed in Section 2.3.2.3, soft tissue artifact is the result of skin mounted markers moving relative to the underlying bone structure due to skin deformation and movement, and represents the largest source of error present in human motion analysis [Leardini et al. (2005)]. Unlike random and systematic instrument errors, its frequency content is similar to that of bone movement [Leardini et al. (2005)], and is therefore concentrated at low frequencies [Chiari et al. (2005)]. This eliminates digital filtering as a compensation technique. In an effort to simulate its effects on ISA computation, soft tissue artifact was added to the displacement of marker M1, of the analytical model, by way of the continuous noise model as described in the above section (see Systematic Instrument Error). The values of noise amplitude $\left\|\vec{A}\right\|$ and noise angular velocity, ω_N, were modified to represent the properties of soft tissue artifact. As discussed in Section 2.3.2.3, many studies have quantified the extent of soft tissue artifact on the lower extremity. Discrepancies in the amplitude of soft tissue artifact result from differences in methodology, variability between subjects and the different locations of skin-mounted markers [Leardini et al. (2005)]. From the amplitude values given in Section 2.3.2.3, it would appear that a displacement of 20 mm represents an appropriate mean value for soft tissue artifact. To recreate expected errors due to soft tissue artifact, an amplitude $\left\|\vec{A}\right\|$ of 10 mm was selected for the continuous

noise model, where the total signal would span 20 mm. The selection of noise frequency is debatable, as it is similar to the frequency of body motion and thus difficult to determine. In order to approach the frequency of the base signal, which is approximately 1.2 Hz (7.5 [rad/s] / 2π [rad/cycle]), a series of sampling frequencies from 1 to 2 Hz were investigated. As the error in ISA computation was proportional to the sampling frequency, as shown in Appendix 3, a frequency of 2 Hz was selected, resulting in an angular velocity ω_N of 4π rad/s. Finally, the values of the phases angles, φ_x, φ_y and φ_z , from the systematic instrument error model were applied to the current noise model, and equation (3-44) was used to determine the amplitude of each x, y and z noise components. This ensured that the amplitude of the signal remains constant, of magnitude $\left\|\vec{A}\right\|$, during the entire signal. The triangle formed by markers M1, M2 and M3 is shown in Figure 3-27 following the application of the continuous noise model. The change in shape of the resulting triangle clearly shows the movement of markers relative to each other resulting from the addition of soft tissue artifact. This relative movement between markers will be referred to as inter-marker variability.

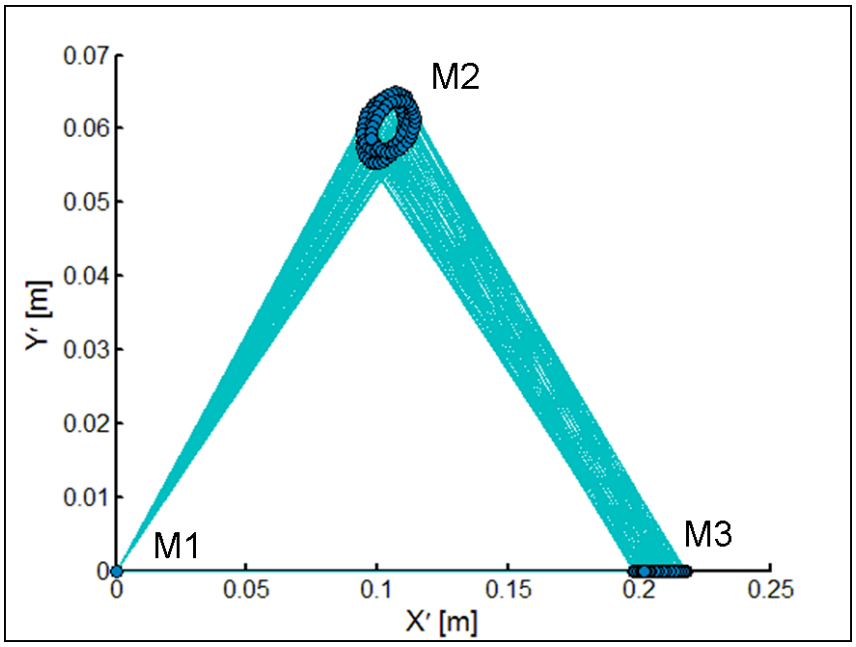

Figure 3-27: Change in shape of the M1, M2 and M3 triangle due to soft tissue artifact. Where M1 was placed at the origin, M3 was confined to the X′ axis and M2 was calculated in the X′ Y′ plane.

Various methods have been used to compensate for soft tissue artifacts, as detailed in Section 2.3.2.3. Of these methods, a solidification procedure can be applied to three non-linear markers, belonging to the same body segment, to produce maker trajectories consistent with the rigid body assumption [Chèze et al. (1995)]. As soft tissue artifacts cause makers to move relative to each other, the solidification procedure imposes a rigid geometry at all time steps, eliminating inter-marker variability and producing a rigid body motion. Although this procedure does not eliminate soft tissue artifacts, a problem which has yet to be solved, is does allow for the explicit use of rigid body kinematics on marker data [Chèze et al. (1995)].

The solidification procedure begins by identifying the best-fit rigid body for the given motion of a body segment and is divided into 4 steps. As a minimum of three markers are required to compute rigid body kinematics of a three dimensional motion [Eberharter and Ravani (2006)], step one consists of defining the triangle formed by the position of three markers placed on the same segment. In the present case, the triangle would be formed by markers M1, M2 and M3 of the analytical model, each one representing a different vertex of the triangle. In the second step, the geometrical characteristic of this triangle, the magnitude of each angle and side, are computed for all sampled data points. Furthermore, the standard deviation of each angle is computed and the angle with the smallest standard deviation is identified. This represents the least-varying angle of the triangle, and will be used to determine the instances where the resulting triangle is the most variable, that is farthest from the mean geometry. The third step in the process is to identify and eliminate the 25 percent most variable triangles in the time series. This is accomplished by calculating, at each time step, the distance from the mean of the least-varying angle and to eliminate the 25 percent with the highest distances. The fourth step consists of building a triangle with the least and second least varying angles, θ_1 and θ_2 respectively, and the side between them, L_1. This triangle will define the best-fit rigid body of the given segment data.

The solidification procedure continues by imposing the best-fit geometry at every time step, in the process creating rigid body motion. This positioning of the rigid geometry poses a problem, as the rigid triangle differs from the triangle formed at every time step. This positioning problem is solved using the least-squares technique developed by Söderkvist and Wedin [Söderkvist and Wedin (1993)], and will be described for three markers placed on a single body segment, therefore applicable to the analytical model, and for a single time step (notation from Chèze et al. [Chèze et al. (1995)]). This method, shown in Figure 3-28, involves moving the rigid geometry from pre-determined positions of the three markers, a_{1s}, a_{2s} and a_{3s}, within the global reference frame, to a location approaching the measured positions of the three markers, b_1, b_2 and b_3, which minimizes the squared error between them. This final location of the rigid geometry corresponds to the solidified coordinates of the three markers and is noted as b_{1s}, b_{2s} and $b_{3s.}$ In this notation, positions a_{1s}, b_1 and b_{1s} correspond to the location of the least-varying angle, θ_1, in their respective triangles, while positions a_{2s}, b_2 and b_{2s} correspond to the second least-varying angle, θ_2. Furthermore, it is shown in Figure 3-28 that the pre-determined position of the rigid geometry was contained within the xy plane of the global reference frame. Vertex a_{2s} was located at the origin, a_{1s} was placed at a distance L_1 along the x axis and a_{3s} was constructed in the xy plane to complete the triangle.

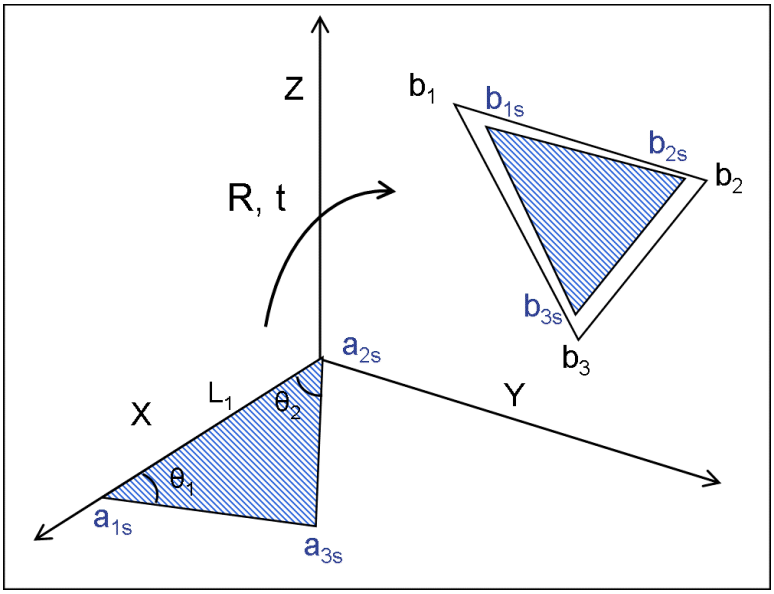

Figure 3-28: Displacement of solid triangle from pre-determined coordinates (a_{1s}, a_{2s}, a_{3s}), to the solidified coordinates (b_{1s}, b_{2s}, b_{3s}) that minimize the least-squares problem. Coordinates (b_1, b_2, b_3) denote the measured positions of markers M1, M2 and M3, respectively. (adapted from Chèze et al. [Chèze et al. (1995)])

This displacement of the rigid geometry is described by a 3x3 rotation matrix *R* and a 3x1 translation vector *t*. The rotation matrix R rotates triangle (a_{1s}, a_{2s}, a_{3s}) into a plane parallel to the plane of triangle (b_1, b_2, b_3), while the translation vector t translates the centroid of triangle (a_{1s}, a_{2s}, a_{3s}) to the centroid of triangle (b_1, b_2, b_3). When the rotation matrix *R* and the translation vector *t* are applied to the chosen position of the rigid triangle, the solidified position is found as follows:

$$b_{is} = [R]a_{is} + t \qquad \textbf{(3-45)}$$

where i =[1, 2, 3], for marker *M1*, *M2* and *M3* respectively, and b_{is} represents the solidified position. The values of the rotation vector *R* and translation vector *t* are chosen to minimize the squared error between the measured marker positions and the solidified marker positions, described as

$$\min \sum_{i=1}^{3} \left\| \left([R] a_{is} + t \right) - b_i \right\|^2 \qquad \textbf{(3-46)}$$

where i =[1, 2, 3], for marker *M1*, *M2* and *M3* respectively. Given this least-squares minimization, solving for the rotation matrix R and translation vector t becomes a non-linear problem. It is proposed by Söderkvist and Wedin [Söderkvist and Wedin (1993)] to solve for rotation matrix R and translation vector t by singular value decomposition of a defined matrix C, which is a function of the solid triangle position and the measured marker positions. The following three steps are required to find matrix C. First, the position of the centroid is computed for both triangles, solidified and measured, as follows

$$\overline{a_s} = \frac{1}{3} \sum_{i=1}^{3} a_{is} \qquad \bar{b} = \frac{1}{3} \sum_{i=1}^{3} b_i \qquad \textbf{(3-47)}$$

where $\overline{a_s}$ and $\bar{b}$ are the centroids of the solid and measured triangles, respectively. Second, the vector from each triangle vertex, marker, to its corresponding centroid is calculated as

$$A = \begin{bmatrix} a_{1s} - \overline{a_s} & a_{2s} - \overline{a_s} & a_{3s} - \overline{a_s} \end{bmatrix} \qquad B = \begin{bmatrix} b_1 - \bar{b} & b_2 - \bar{b} & b_3 - \bar{b} \end{bmatrix} \qquad \textbf{(3-48)}$$

where the columns of the 3x3 matrices A and B correspond to the vectors from each marker to its triangle centroid. Third, the matrix C is computed by multiplying matrix B by the transpose of matrix A, as shown below

$$C = BA^T \qquad \textbf{(3-49)}$$

where the superscript T designates the transpose of A. Once matrix C has been found, the singular value decomposition can be computed as follows

$$P \Gamma Q^T = C \tag{3-50}$$

where P and Q are 3x3 orthogonal matrices, and Γ is a 3x3 diagonal matrix containing the singular values of C [Söderkvist and Wedin (1993)]. More specifically, the columns of matrix P represent the eigenvectors of matrix CC^T, the columns of matrix Q^T represent the eigenvectors of matrix C^TC, and the diagonal of matrix Γ contains the square root of the eigenvalues, also referred to as singular values, of matrices CC^T or C^TC [Söderkvist and Wedin (1993)]. This decomposition of matrix C provides a solution for the rotation matrix R and translation vector t, shown below:

$$R = P \begin{bmatrix} 1 & 0 & 0 \\ 0 & 1 & 0 \\ 0 & 0 & \det\left(PQ^T\right) \end{bmatrix} Q^T \tag{3-51}$$

$$t = \bar{b} - [R]\bar{a}_s \tag{3-52}$$

Once the values of R and t have been computed, the displacement of the solid triangle is carried out, with equation (3-45), to find the solidified positions, b_{1s}, b_{2s} and b_{3s} of the three markers that minimizes equation (3-46).

Chèze et al. [Chèze et al. (1995)] studied the performance of this algorithm and determined that in cases where one of the vertices, of the measured triangles, is more variable than the other two, it is advantageous to determine the rotation matrix R and translation vector t from modified versions of the rigid and measured triangles. The first modified triangle is formed by vertices p_{1s}, p_{2s} and p_{3s}, modified from the rigid triangle (a_{1s}, a_{2s}, a_{3s}), and the second triangle is formed by vertices q_1, q_2 and q_3, modified from the measured triangle (b_1, b_2, b_3), both shown in Figure 3-29. These two triangles are constructed in the same manner, and therefore only the modified rigid triangle (p_{1s}, p_{2s}, p_{3s}) will be discussed. The vertex p_{1s} is made to coincide with a_{1s}, which corresponds to angle θ_1, and vertex

p_{2s} is placed at a unit length away from vertex p_{1s}, along the line joining a_{1s} and a_{2s}. Furthermore, the vertex p_{3s} is also placed at a unit length away from vertex p_{1s}, this time along the line joining a_{1s} and a_{3s}. This forms an isosceles triangle, where the congruent sides have unit lengths and the angles joining them is the least-varying angle θ_1. This same procedure produces a second isosceles triangle around the vertex q_1, corresponding to the least-varying angle of the measured triangle. Chèze et al. [Chèze et al. (1995)] have shown that calculating the rotation matrix R and translation vector t from theses two isosceles triangles, which weights the least-varying vertex the heaviest while still solving the un-weighted least-squares problem of Söderkvist and Wedin [Söderkvist and Wedin (1993)], increases the performance of the algorithm (reduces the least-square error). Furthermore, when all the triangles vertices vary similarly, this methodology produces comparable results to the un-modified triangles [Chèze et al. (1995)]. To minimize the error introduced on the original marker positions (b_1, b_2, b_3), two methods were used to compute the rotation matrix R and the translation vector t: (1) from the rigid triangle (a_{1s}, a_{2s}, a_{3s}) and measured triangle (b_1, b_2, b_3), shown in Figure 3-28, and (2) from the modified isosceles triangles (p_{1s}, p_{2s}, p_{3s}) and (q_1, q_2, q_3), shown in Figure 3-29. Once the transformation matrices were determined, they were both applied to the rigid triangle (a_{1s}, a_{2s}, a_{3s}) to produce two solidified triangles (b_{1s}, b_{2s}, b_{3s}), computed from equation (3-45). The method, between (1) and (2), that reduced the RMSE between the measured triangle (b_1, b_2, b_3) and the solidified triangle (b_{1s}, b_{2s}, b_{3s}) was used to established rigid body motion of that segment. This ensured that rigid body motion was generated while reducing the error imposed on measured marker displacements.

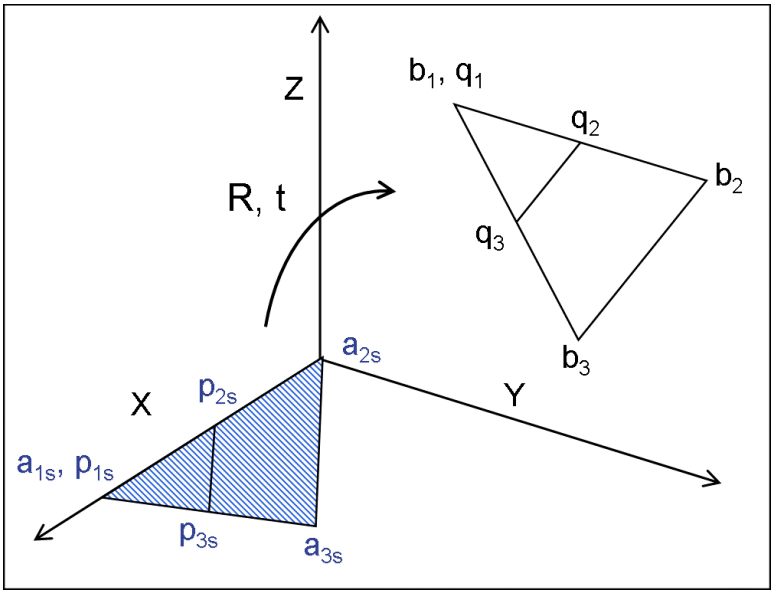

Figure 3-29: Solidification procedure from reduced triangle [Chèze et al. (1995)]; reduced rigid triangle (a_{1s}, a_{2s}, a_{3s}) and reduced measured triangle (b_{1s}, b_{2s}, b_{3s})

When carried out for all time steps of a given motion, the solidification procedure eliminates inter-marker variability and produces a rigid body motion. This allows for the explicit use of rigid body kinematics on marker data [Chiari et al. (2005)] as opposed to relying on a rigid body assumption. When applied to the analytical model, after soft tissue artifact was added to the displacement of marker M1, a new rigid body motion was generated. However, this rigid triangle differs from the original geometry of the analytical model, as shown in Figure 3-30. This change in geometry translates to a relative difference in area of less than 0.05 percent, where the changes in position of the triangle vertices are of 0.4 and 0.5 mm. This verifies that the original geometry has been retrieved within the error associated with marker placement (see Section 3.3.1.1).

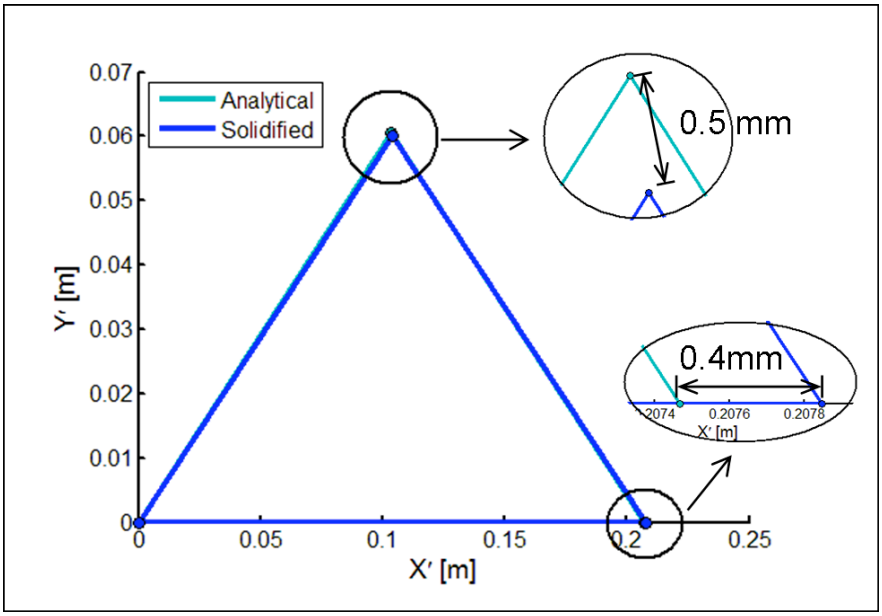

Figure 3-30: Solidified triangle compared to the Analytical triangle. Where M1 was placed at the origin, M3 was confined to the X′ axis and M2 was calculated in the X′ Y′ plane.

Although the solidified triangle closely resembles the analytical triangle, as shown in Figure 3-30, its displacement contains a component that is not part of the original motion imposed on the analytical model. As a consequence, the solidification procedure cannot eliminate the errors on the displacement of marker M1, and will introduce errors on the displacements of markers M2 and M3. The RMSE of marker positions is shown in Table 3-21, before and after the solidification procedure. For the position of marker M1, the RMSE is reduced by approximately 24 percent following the solidification procedure. Furthermore, the RMSE introduced on the displacements of markers M2 and M3 represent approximately 1/3 of the error of marker M1, both below 5 mm (compared to the 21 mm associated with variability in the placement of pelvic markers, as discussed in Section 3.3.1.1). It is important to note that the performance of the solidification procedure is dependant on both the amplitude of soft tissue artifact and the number of markers that are affected by soft tissue artifact. For example, the RMSE on marker positions is shown in Table 3-22 when the continuous noise model was applied to markers M1, M2 and M3 of the analytical model (where the order to phase angles φ_x, φ_y and φ_z was changed to introduce a phase relationship between markers). This represents the worst case scenario that can be expected

from soft tissue artifact on a body segment. Results indicate that the RMSE is reduced for the position of all markers, ranging from a reduction of 8 percent for marker M1 and 30 percent for marker M2. Furthermore, it was determined that the change in geometry from the analytical triangle to the solidified triangle translates to a relative difference in area of approximately 2 percent. This shows that, in a worst case scenario, the solidification procedure is effective in retrieving the original geometry of a given segment, while the RMSE introduced on marker displacement is well within the error introduced by soft tissue artifact and marker placement variability.

Table 3-21: RMSE on marker positions before the solidification procedure, Disturbed, and following the solidification procedure, Solidified; continuous noise model applied to displacement of marker M1

Displacement	RMSE		
	M1 [m]	M2 [m]	M3 [m]
Disturbed	1.00E-02	0	0
Solidified	7.61E-03	2.78E-03	2.23E-03
Percent Difference	-23.9	NA	NA

Table 3-22: RMSE on marker positions before the solidification procedure, Disturbed, and following the solidification procedure, Solidified; continuous noise model applied to displacement of markers M1, M2 and M3

Displacement	RMSE		
	M1 [m]	M2 [m]	M3 [m]
Disturbed	1.00E-02	1.00E-02	1.00E-02
Solidified	9.16E-03	7.00E-03	8.13E-03
Percent Difference	-8.4	-30.0	-18.7

The above results have shown that the solidification procedure can be used for cases of limited soft tissue artifact, where one marker is affected, and of significant soft tissue artifact, where all three markers are affected. As this procedure will be applied to all body segments, it is of interest to determine the effects of soft tissue artifact on ISA computation, and to determine the change in

error from the application of the solidification procedure. Table 3-23 displays the errors in ISA computation from the disturbed displacement of marker M1, following the application of the continuous noise model, and following the solidification procedure.

Table 3-23: ISA error resulting from soft tissue artifact calculated from the disturbed displacement and solidified displacement. Percent difference was calculated as the ratio of the difference between disturbed error and solidified error divided by the disturbed error, expressed in percent. A positive percent difference denotes an increase in error, while a negative percent difference denotes a decrease. * Reference value 0.9m/s; ** reference value 7.5 rad/s.

Displacement	ISA Error			
	ε_o [rad]	ε_p [m]	ε_v [m/s] (% relative error)*	ε_w [rad/s] (% relative error)**
Perturbed	9.385E-02	1.917E-02	1.333E-01 (1.48E+01)	1.326E+00 (1.77E+01)
Solidified	9.279E-02	1.359E-02	1.319E-01 (1.47E+01)	8.542E-01 (1.14E+01)
Percent Difference	-1.1	-29.1	-1.0	-35.6

The analytical model shows that soft tissue artifact has a larger effect on ISA parameters when compared to the others sources of error previously discussed. The error on ISA orientation reaches up to 9.39 $x10^{-2}$ radians and is essentially unaffected by the solidification procedure, taking a similar value of $9.28x10^{-2}$ radians (5.32 degrees). The error in position of the ISA reaches magnitudes up to 19.2 mm, when calculated with the disturbed displacements, but is reduced to a value of 13.59 mm when using solidified marker displacements. This represents a reduction of 29 percent when applying the solidification procedure. For both the errors in ISA orientation and position, the magnitudes are inferior to the errors of 7.6 degrees and 21.18mm associated with marker placement variability (see Section 3.3.1.1). As for the movement about the ISA, the error in parallel velocity reaches a maximum of 0.133 m/s, and is virtually unchanged when using solidified data. This represents an error of 14.8 percent, relative to the known magnitude of 0.9 m/s. This is the highest relative error encountered in the analysis

of ISA parameters. The error in angular velocity reaches a maximum magnitude of 1.33 rad/s, but is reduced to 0.85 rad/s for solidified marker displacements. Therefore, these results indicate that the error in ISA orientation and the error in parallel velocity along the ISA are unaffected by the solidification procedure. However, the error in ISA position and the error in angular velocity about the ISA were reduced by approximately 28 and 36 percent, respectively.

3.3.5 Velocity Marker Data

In order to compute the ISA of a body segment with the method described in Section 3.2.1, the position and velocity of at least three non-collinear markers must be known [Eberharter and Ravani (2006)]. Marker displacements, as a function of time, can be obtained by stereophotogrammetric measurements. Marker velocities can be computed from these discrete marker position measurements. This can be accomplished by numerical differentiation, where the velocity is computed from the derivative of some form of interpolating polynomial [Kreyszig (1999d)]. In Section 3.3.3.1, cubic spline interpolation was used to solve the instrumental limitation of marker occlusion, where occluded data points were replaced by interpolated values. As previously discussed, one of the main advantages of cubic spline interpolation is it capacity to be twice differentiable [Kreyszig (1999d)]. Therefore, the velocity will be obtained from differentiation of each individual cubic spline, computed from equation (3-35). These derivatives are then sampled at each time frame to generate discrete marker velocities. To determine the effects on ISA parameters of computing marker velocity from differentiation of interpolating cubic splines, the velocity of marker M1 was calculated by cubic spline interpolation. The x component of the velocity of marker M1 is shown in Figure 3-31, where the analytical velocity is compared to that calculated by cubic spline interpolation. It is shown that both velocities are essentially superimposed, where the RMSE between them is approximately $1x10^{-5}$ m/s. Furthermore, the error of the ISA parameters resulting from the use of

numerical differentiation to determine the velocity of marker M1 is shown in Table 3-24.

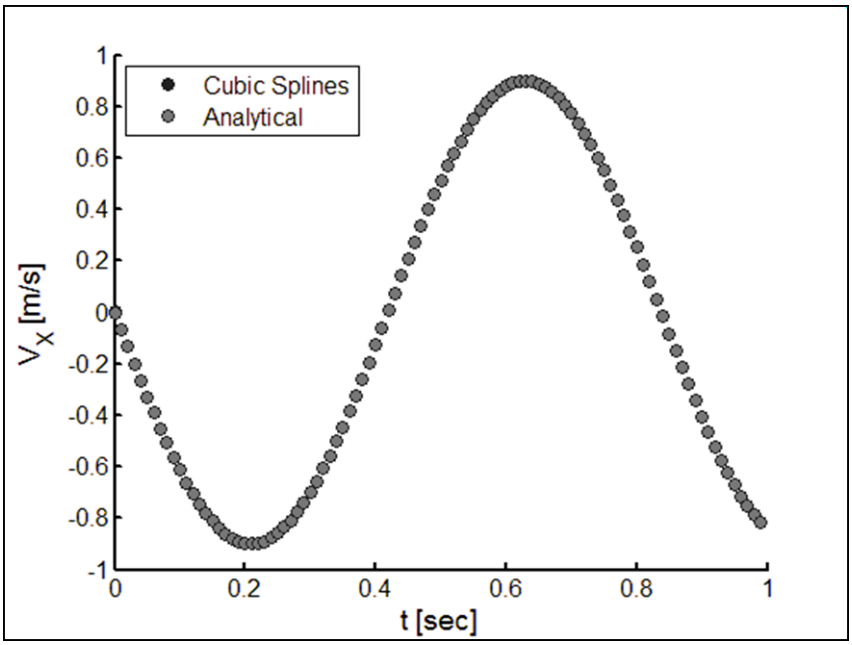

Figure 3-31: Velocity of marker M1, x-component; analytical velocity (Analytical) compared to the velocity obtained from differentiation of interpolating cubic splines (Cubic Splines)

Table 3-24: ISA error resulting from differentiation of interpolating cubic splines. ISA parameters: orientation error ε_o, position error ε_p, error in parallel velocity along ISA ε_v, and error in angular velocity in the direction of ISA ε_ω.* Reference value 0.9m/s; ** reference value 7.5 rad/s.

Marker Velocity	ISA Error			
	ε_o [rad]	ε_p [m]	ε_v [m/s] (% relative error)*	ε_w [rad/s] (% relative error)**
Cubic Splines Velocity	3.550E-16	1.537E-06	5.124E-16 (5.69E-14)	4.840E-05 (6.45E-04)

The analytical model indicates that error in ISA orientation and position, as well as error in the movement about the ISA, is several orders of magnitude smaller than the reference error values (see Section 3.3.1.1). This indicates that for marker displacements free of measurement error, the differentiation of interpolating cubic

splines can be used to determine maker velocity with negligible error to ISA parameters.

Although the methodologies of Sections 3.3.3 through 3.3.5 produce marker displacements consistent with rigid body motion, the effects of measurement error cannot be completely attenuated. Therefore, it is of interest to determine how measurement errors, associated with marker displacements, affect velocity calculations. In an attempt to study theses affects, the disturbed displacements of marker M1 to which random instrument error has been added (see Section 3.3.3.2) were used to compute marker velocity. It is assumed that the addition of these series of impulses to the displacement of marker M1 will create even larger errors on the calculation of marker velocity, as errors on marker displacements have deleterious affects on derivative estimates [Woltring (1995)]. The displacement of marker M1 following the addition of random impulses is shown in Figure 3-20, while the corresponding velocity is shown in Figure 3-32.

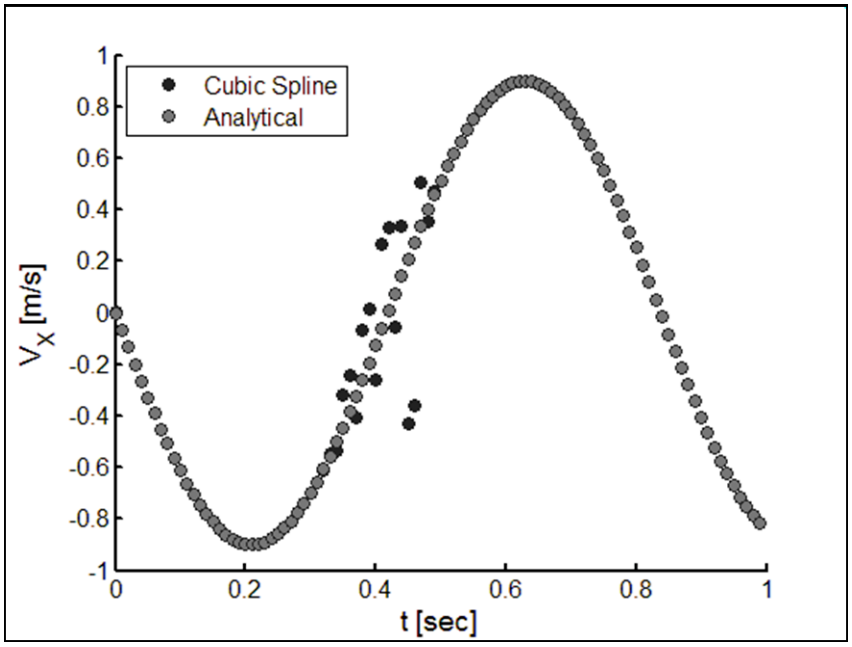

Figure 3-32: Velocity of marker M1, x-coordinate; analytical velocity labeled *Analytical* and velocity from numerical differentiation (of marker displacement with N_2=10 impulses) labeled *Cubic Spline*

These results indicate that the added impulses produce errors in the computation of maker velocity, affecting not only the specific data points where impulses were added but rather a series of points surrounding these impulses. This is an expected result, as numerical differentiation roughens data, as opposed to numerical integration which smoothes data [Kreyszig (1999d)]. That being said, it is desirable to attenuate the propagation of measurement errors from marker displacement to marker velocity. As previously discussed, stereophotogrammetric signals have a high signal-to-noise ratio, where the base signal occurs at low frequencies [Chiari et al. (2005)] and the present noise is concentrated at high frequencies [Alonso et al. (2005)]. The power spectral density of a marker's velocity is shown in Figure 3-33, which was obtained by numerical differentiation of the unfiltered measured displacement of a pelvic marker. This illustrates that the base signal is also concentrated at low frequencies.

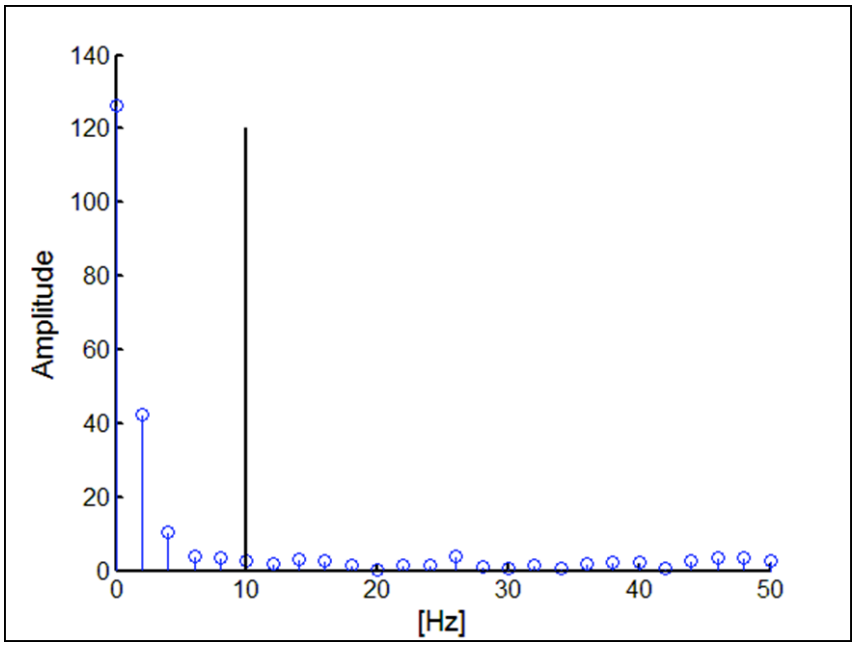

Figure 3-33: Power spectral density of marker velocity, x-component, calculated from unfiltered displacement; marker placed on the RASIS of the pelvis

Consequently, a low-pass digital filter could be used to attenuate the effects of high frequency instrument errors that propagate in the calculation of marker velocity. As with the power spectral density of unfiltered marker displacements

(see Figure 3-21), the power spectral density of marker velocity assumes a straight line behavior beyond a frequency of approximately 10 Hz. Therefore, the same fourth order Butterworth low-pass digital filter, with a cutoff frequency of 10Hz (used in Sections 3.3.3.2 and 3.3.3.3 to attenuate systematic and random instrument error), will be applied to marker velocities following numerical differentiation. The velocity of marker M1 obtained from numerical differentiation with post-filtering is shown in Figure 3-34. In order to quantify the reduction in velocity computational error due to the application of a low-pass digital filter, the RMSE between the analytical velocity of marker M1 and the velocity obtained by differentiation of cubic splines of the disturbed marker displacement (with added impulses) is shown in Table 3-25. Theses results indicate that the RMSE, relative to the analytical velocity, is reduced by at least 73.5 percent following the application of the chosen low-pass filter. This indicates that post-filtering can reduce the effects of measurement error that have not been fully attenuated, as illustrated in Figure 3-34.

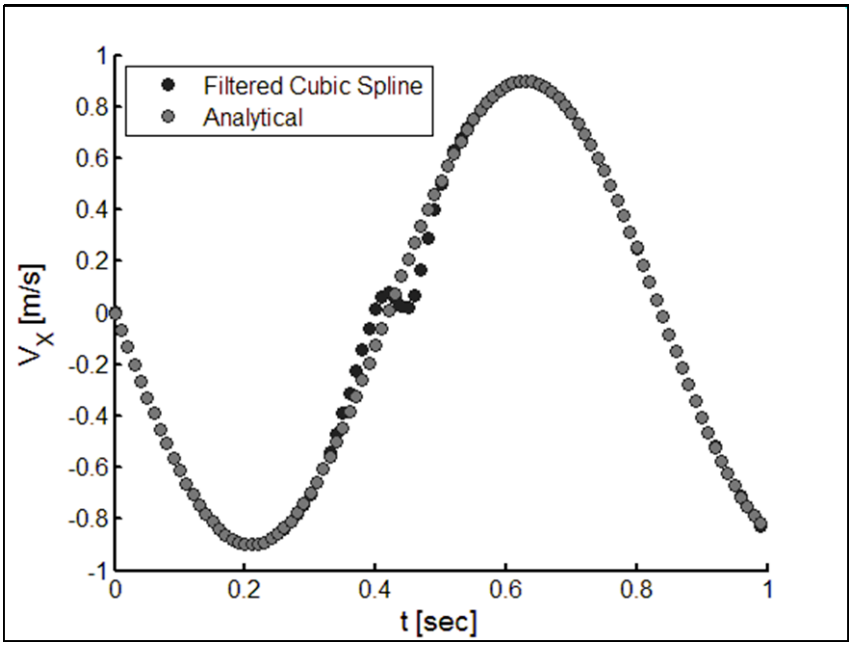

Figure 3-34: Velocity of marker M1, x-coordinate; analytical velocity labeled *Analytical* and velocity from numerical differentiation (of marker displacement with N_2=10 impulses) with post-filtered labeled *Filtered Cubic Spline*

Table 3-25: RMSE between the analytical velocity and marker velocity determined by numerical differentiation of cubic splines (Cubic Splines) and filtered differentiation of cubic splines (Filtered Cubic Splines), where N_2 denotes the number of impulses added to the displacement. Percent difference was calculated as the ratio of the difference between Cubic Splines error and Filtered Cubic Splines error divided by the Cubic Splines error, expressed in percent. A positive percent difference denotes an increase in error, while a negative percent difference denotes a decrease.

Marker Velocity	RMSE			
	N_2=1 [m/s]	N_2=3 [m/s]	N_2=5 [m/s]	N_2=10 [m/s]
Cubic Splines	1.77E-01	1.84E-01	1.91E-01	2.36E-01
Filtered Cubic Splines	2.17E-02	3.95E-02	4.78E-02	6.26E-02
% Difference	-87.7	-78.6	-75.0	-73.5

The procedure outlined above was used to determine marker velocities from measured marker displacements. This procedure includes the numerical differentiation of interpolating cubic splines followed by post-filtering using a fourth order Butterworth filter with a cutoff frequency of 10 Hz. It should be noted that this procedure was followed to compute marker velocities in the previous sections, where error on ISA parameters was calculated (see Sections 3.3.3 to 3.3.4).

3.3.6 Computational Procedure

Theoretically, the ISA of a rigid body can be computed from any three non-collinear markers belonging to that body and will yield the same result, since they define the same rigid body motion [Eberharter and Ravani (2006)], as explained in Section 3.2.1. However, when rigid body data is obtained by applying a solidification procedure to measured displacements obtained by stereophotogrammetry (see Section 3.3.4), the above statement does not hold, as two different sets of three markers placed on the same segment will not necessarily produce the exact same rigid body motion. Furthermore, ISA computation from a single set of three markers offers multiple alternatives, such as the choice of ISA position and the magnitude of the movements about the ISA (see Section 3.2.1). Therefore, it is necessary to establish a systematic approach

to compute the ISA of a segment from the positions and velocities obtained from sections 3.3.3 to 3.3.5.

3.3.6.1 Minimization Problem

Marker velocity can be obtained by numerical differentiation of a marker's displacement, as shown in Section 3.3.5. This marker velocity will be referred to as *Measured* velocity, as it was obtained from measured displacement. As discussed in Section 3.2.1, instantaneous marker velocity can be expressed as the sum of two components: a parallel component resulting from the body's translational velocity along the ISA and a perpendicular component resulting from the body's angular velocity in the direction of the ISA [Eberharter and Ravani (2006)]. Therefore, from marker displacement and the known ISA position and orientation, as well as the known movement about ISA, the velocity of a marker can be computed from equation (3-12). This marker velocity will be referred to as *Computed* velocity, as it was obtained from measured displacement and computation of ISA. Theoretically, *Measured* and *Computed* velocities are equal, as the *Computed* velocity (from movement about the ISA) is a function of *Measured* velocity (which generates ISA). However, rounding errors, computational limitations (when velocities approach a collinear state) and error from the rigid body assumption, when calculating ISA of the relative movement between physiologically linked segments (see Section 3.2.3), introduce error between the *Measured* and *Computed* velocities. Each of theses sources can be affected by variables related to ISA computation, such as: the choice of markers, the position of ISA and the magnitude of the movements about ISA (see Section 3.2.1). Therefore, it is possible to reduce the error between the *Measured* and *Computed* velocities by changing the variables related to ISA computation. This provides an approach to compute ISA of a given segment by way of a minimization problem. For all possible computations of ISA of a given segment, RMSE between the *Measure*d and *Computed* velocities, of all three markers involved in the computation, is measured. The computation that minimizes RMSE

will determine the ISA of the segment, as it best represents the given rigid-body motion. The variables that are involved in this minimization problem are: the three markers chosen on the body segment, var_1, the position of ISA (pair of markers used to determine ISA position, see Section 3.2.1), var_2 and the magnitude of the movement about ISA (marker used to the magnitude of parallel and angular velocities, see Section 3.2.1), var_3.

Segment markers

Three markers are required to compute the kinematics of a three-dimensional motion [Eberharter and Ravani (2006)]. However, it is advantageous to affix three or more markers, when possible, on the relevant anatomical landmarks of a given segment, as this introduces redundancy and provides multiple options to determine segment kinematics [Eberharter and Ravani (2006)]. For example, if a number of markers, n_m, are placed on the same segment, it is possible to compute the kinematics in var_1 different ways, as follows:

$$\mathrm{var}_1 = \begin{pmatrix} n_m \\ 3 \end{pmatrix} = \frac{n_\mathrm{m}!}{(n_\mathrm{m} - 3)!3!} \tag{3-53}$$

where *!* denotes the factorial of the given number, and $\begin{pmatrix} n_\mathrm{m} \\ 3 \end{pmatrix}$ represents the number of possible combination of three different markers that can be formed out of the n_m placed on the segment [Ross (1987)]. For example, if three markers are placed on the segment, var_1=1 as there is only one possible combination of three different markers. However, if four markers are placed on the segment, var_1= 4 as there are four possible combinations of three different markers.

Position of ISA

From a single combination of three markers on a given segment, the position of ISA within the global reference frame can be computed from the position and velocity of only two markers, as discussed in Section 3.2.1. Therefore, for each

combination of three markers affixed to the same segment, the number of possible ways to compute the position of the ISA, var_2, is equal to

$$\mathrm{var}_2 = \binom{3}{2} = \frac{3!}{(3-2)!\,2!} = 3 \tag{3-54}$$

where var_2 is the number of possible combinations of 2 markers out of the three affixed to the given segments [Ross (1987)]. Furthermore, it has been suggested by Eberharter and Ravani [Eberharter and Ravani (2006)] to determine the position of ISA from the average of the three possible computations, one for each pair of markers. This recommendation is considered, as a total of 4 possible positions of the ISA are computed for each combination of three markers: one for each pair of markers (3) and the average position of all three (4). Therefore, the value of var_2 is set to four.

Magnitude of the movement about the ISA

As described in Section 3.2.1, the magnitude of the parallel velocity along the ISA and the magnitude of the angular velocity in the direction of the ISA, can be computed from the position and velocity of a single marker. Therefore, for a single combination of three markers on a given segment, these two magnitudes can be computed from each of the three markers. Furthermore, similar to the recommendation of Eberharter and Ravani [Eberharter and Ravani (2006)] when computing ISA position, the mean of the three separate computations, one for each marker, is also calculated. Therefore, the number of possible computations of the magnitudes of parallel velocity along the ISA and angular velocity in the direction of the ISA, var_3, is set to four.

RMSE between *Measured* and *Computed* velocities

The total number of possible computations of the ISA, and of the movement about the ISA, can be found by multiplying the number of computations of each

variable discussed above. Therefore, the total number of computations, n_c, for a given segment becomes:

$$\begin{aligned} n_c &= \text{var}_1\ \text{var}_2\ \text{var}_3 \\ &= \binom{n_m}{3}(4)(4) \\ &= 16\,\frac{n_m!}{(n_m-3)!\ 3!} \end{aligned} \tag{3-55}$$

This determines the number of computations that can be conducted for a single segment, given a number of markers, n_m, placed on that segment. The minimization problem is solved by identifying the computation, out of the n_c conducted, that minimizes the RMSE between the *Measured* and *Computed* velocities. This error, $RMSE_{velocity}$, is calculated as:

$$RMSE_{velocity} = \sqrt{\frac{1}{n_f}\sum_{i=1}^{3}\sum_{j=1}^{n_f}\begin{pmatrix}(vix_M(j)-vix_C(j))^2+(viy_M(j)-viy_C(j))^2\\+(viz_M(j)-viz_C(j))^2\end{pmatrix}} \tag{3-56}$$

where i denotes the marker, from marker 1 to marker 3, j denotes the analyzed frames, from 1 to the total number of frames (n_f), $vix_M(j)$ is the *Measured* velocity of marker i in the x-direction at frame j, and $vix_C(j)$ is the *Computed* velocity of marker i in the x-direction at frame j.

Application of Minimization Problem to the Analytical Model

To study the effects of the above method on ISA parameters, the minimization problem was solved for the movement of the analytical model. To evaluate the minimization problem from marker displacements that best represent stereophotogrammetric measurements, all sources of errors (marker occlusion, random and systematic instrument error, and soft tissue artifact) were applied to all three markers (M1, M2 and M3) of the analytical model. The addition of the measurement error was carried out in three steps. First, systematic instrument

error was applied to all three markers using the continuous noise model described in Section 3.3.3.3, with the corresponding noise amplitude frequency values. Second, soft tissue artifacts were applied to all three markers using the continuous noise model described in Section 3.3.4, again with the corresponding noise amplitude and frequency values. In order to ensure a phase relationship between markers, the three phase angles θ_x, θ_y and θ_z, described in Section 3.3.3.3, where applied to the three displacement components in three separated orders. Third, two instances of marker occlusion, where N_1=5 data points were removed from marker displacement (see Section 3.3.3.1), and one instance of random instrument error, where N_2=5 impulses were added to marker displacement (see Section 3.3.3.2), were introduced to each marker of the analytical model. In total, nine separate instances of either marker occlusion or random instrument error were imposed on the displacements of markers M1, M2 and M3. In an attempt to randomly distribute theses series of errors, each of the nine errors was centered about a given data point, as described in Table 3-26. These data points were randomly selected from the entire data series of the motion, from data point 0 to data point 100. The resulting x-component of the displacement of marker M1 is shown in Figure 3-35.

Table 3-26: Measurement error added to marker displacements, where Marker Occlusion denotes a series of N_1=5 removed data points, Random Impulses denotes a series of N_2=5 added random impulses, both centered about their Data Point

Marker	Data Point of Applied Error		
	Random Impulses	Marker Occlusion	
M1	15	26	52
M2	59	9	78
M3	90	18	36

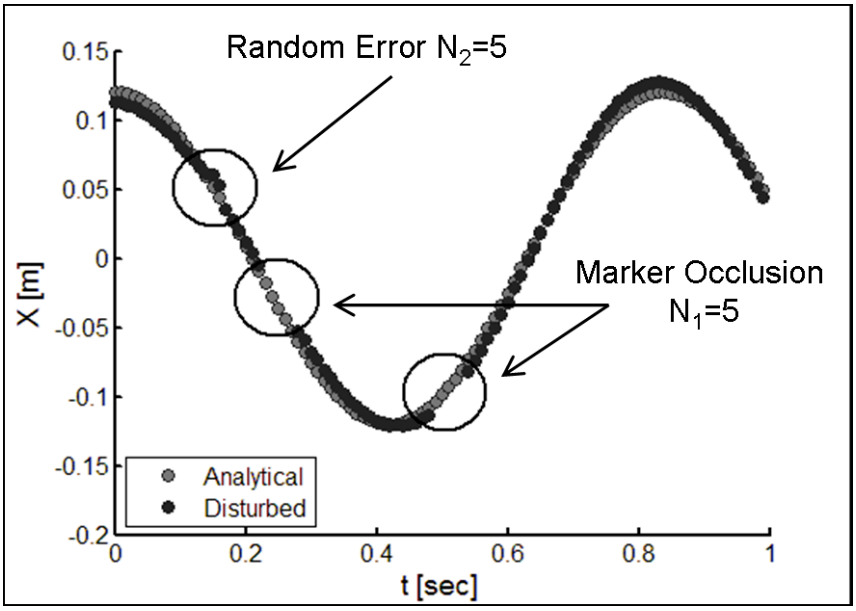

Figure 3-35: Displacement of marker M1, x-component, following addition of measurement error

From the disturbed marker displacements of the analytical model, the compensation methods described in Section 3.3.3 and 3.3.4 were applied to generate marker displacements consistent with rigid body motion. The x-component of the displacement of marker M1 is shown in Figure 3-36 following error compensation and the RMSE on marker displacement, relative to the analytical displacement, is listed in Table 3-27. Also, the three dimensional displacement of marker M1 following error compensation is shown in Figure 3-37.The velocity of markers M1, M2 and M3 were then obtained from numerical differentiation of the rigid body marker displacements, as described in section 3.3.5. Lastly, the minimization problem was solved to determine ISA and the movements about the ISA that reduced the RMSE between the *Measured* and *Computed* marker velocities. The resulting error in ISA parameters is shown in Table 3-28.

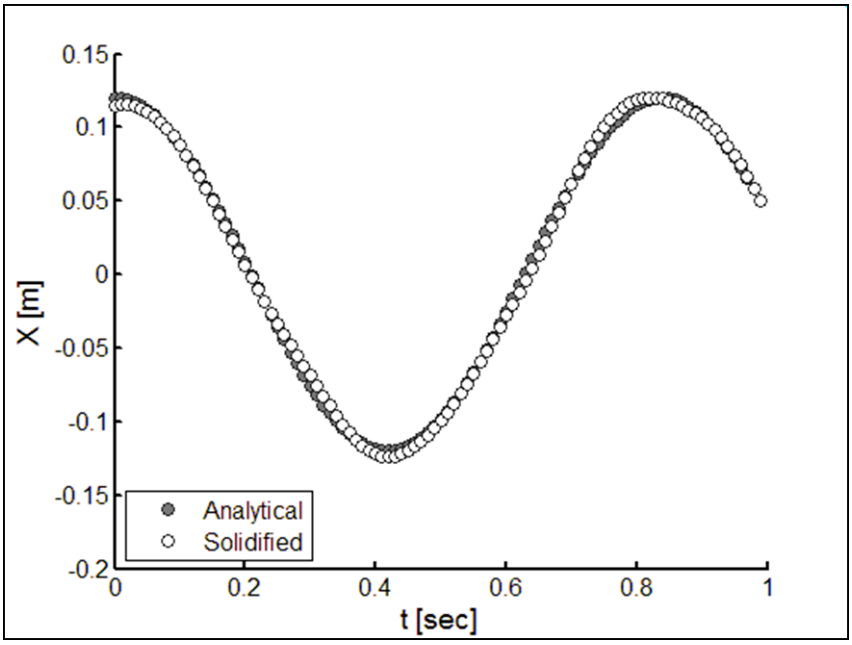

Figure 3-36: Displacement of marker M1, x component, following the use of measurement error compensation methods of Sections 3.3.3 and 3.3.4

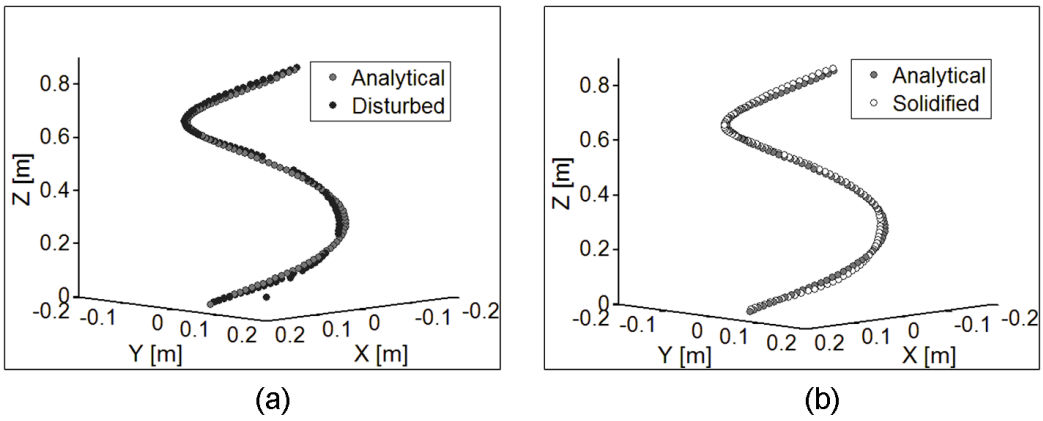

Figure 3-37: Three-dimensional displacement of marker M1 (a) following addition of measurement error and (b) following the use of measurement error compensation methods of Sections 3.3.3 and 3.3.4

Table 3-27: RMSE between the analytical displacement and disturbed marker displacement (Disturbed) and marker displacement following error compensation (Solidified). Percent difference was calculated as the ratio of the difference between Disturbed error and Solidified error divided by the Disturbed error, expressed in percent. A positive percent difference denotes an increase in error, while a negative percent difference denotes a decrease.

Displacement	RMSE: Marker Displacement			
	M1 [m]	M2 [m]	M3 [m]	All [m]
Disturbed	1.012E-02	1.024E-02	1.018E-02	1.018E-02
Solidified	9.150E-03	6.943E-03	8.267E-03	8.170E-03
% Difference	-9.6	-32.2	-18.8	-19.8

Table 3-28: ISA error resulting from perturbed marker displacements and marker displacements obtained by measurement error compensation. ISA parameters: orientation error ε_o, position error ε_p, error in parallel velocity along ISA ε_v, and error in angular velocity in the direction of ISA ε_ω.* Reference value 0.9m/s; ** reference value 7.5 rad/s.

Data Type	ISA Error			
	ε_o [rad]	ε_p [m]	ε_v [m/s] (% relative error)*	ε_w [rad/s] (% relative error)**
Perturbed	1.691E-01	2.748E-02	1.888E-01 (2.10E+01)	1.749E+00 (2.33E+01)
Solidified	1.589E-01	2.451E-02	1.775E-01 (1.97E+01)	1.546E+00 (2.06E+01)
Percent Difference	-6.0	-10.8	-6.0	-11.6

The results shown in Table 3-27 indicate that the RMSE, relative to the analytical marker displacements, is reduced for all markers following measurement error compensation. Considering all markers, the RMSE was reduced by 19.8 percent, from 10.18 mm to 8.17mm. This shows that the applied compensation techniques produced marker displacements closer to those of the analytical model. The results of Table 3-28 indicate that all sources of measurement error combined have the greatest effect on ISA parameters when compared to each individual source, as expected. The error on ISA orientation was reduced by 6.0 percent when using the solidified marker displacements, reaching a minimum value of

$1.59x10^{-1}$ radians (9.1 degrees). This value is within 1.5 degrees of the orientation error caused by marker placement error (see Section 3.3.1.1). The error in position of the ISA reaches a magnitude of 27.5 mm when calculated with the disturbed displacements and is reduced by 10.8 percent to a value of 24.5 mm when using solidified marker displacements. This magnitude is within 5 mm of the error in placing markers on anatomical landmarks (see Section 3.3.1.1). As for the movement about the ISA, the error in parallel and angular velocity were reduced by 6.0 and 10.9 percent following the application of measurement error compensation, respectively. The error in parallel velocity reaches a value of 0.177 m/s and the error in angular velocity reaches a value of 1.546 rad/s, representing relative errors of 19.7 and 20.6 percent, respectively.

Although these ISA errors are high, considering that relative errors of 10 percent are usually characterized as rough experimental measurements [Taylor (1982d)], they are proportional to the amplitude of soft tissue artifact added to the displacements of the analytical model. In the present case, the continuous noise model used to generate soft tissue artifact is applied to all markers with an amplitude of 10mm. This represents a case where all three markers are affected by large amounts of soft tissue artifact (see Section 2.3.2.3). However, if the amplitude of soft tissue artifact is set to 5mm, the error in ISA orientation and position is reduced to 4.84 degrees and 13.2mm, and the relative error of the parallel velocity and angular velocity are both reduced to 10.9 percent.

3.4 Golf Swing Model

The purpose of this thesis is to determine the kinematic sequence of the golf swing. As the golf swing consists primarily of gross rotations of the lower body, upper body and arms, it is of interest to study the rotational motion of the major body segments involved in the golf swing. This includes the angular velocity of body segments, as well as the position and orientation of the dominant axes of rotation. This was accomplished by studying the motion of the body during the

downswing as a kinematic chain of ISAs, which will be referred to as the golf swing model. This involved decomposing the body into a collection of body segments, were the motion of each segment would be described with an ISA. To examine the movement of the body, a total of 4 segments were analyzed: the left leg, pelvis, shoulders and left arm. Also, three markers were placed on the golf club by way of a rigid triad fixed to the golf shaft and an additional marker, not used in ISA computation, was screwed into the golf club head. The position of all reflective makers on each segment is described in Table 3-29 and illustrated in Figure 3-38, for markers mounted on the body, and Figure 3-39, for markers on the golf club. Although a minimum of three markers is required to compute ISA of each segment [Eberharter and Ravani (2006)], four or five markers were placed on relevant anatomical landmarks when possible. This redundancy in markers increases the number of possible computations of ISA, n_c, from 16 (n_m= 3) to 160 (n_m= 5) which can potentially decreases the $RMSE_{velocity}$ of the minimization problem (see Section 3.3.6.1). Furthermore, two additional markers, L4 and L5, were placed on the left ankle to compute the orientation of the left leg, but were not used in ISA computation.

Anatomical landmarks were chosen as the most prominent landmarks of each segment, to limit soft tissue artifact and be easily identifiable through manual palpations. In the case of markers being placed on upper or lower limbs, but not at their joints, wrappings were used to reduce soft tissue artifact. This involved wrapping the limb with hypoallergenic 3M Microfoam surgical tape (3M Canada, Ontario, Canada) and the markers were placed on the wrapped area of the segment. This technique was used for markers placed on the left thigh (L3) and on the forearm (A5).

Table 3-29: Marker Placement Guide (anatomical landmarks from Moore and Dalley [Moore and Dalley (2006)])

Segment	Number of marker (n_m)	Marker Placement	Marker Label
Left Leg	3	Lateral epicondyle of the left femur	L1
		Medial epicondyle of the left femur	L2
		Left thigh	L3
		Lateral malleolus (not included in n_m)	L4
		Medial malleolus (not included in n_m)	L5
Pelvis	4	Right anterior superior iliac crest	P1
		Left anterior superior iliac crest	P2
		Right posterior superior iliac crest	P3
		Left posterior superior iliac crest	P4
Shoulders	4	Jugular notch	S1
		C7 cervical vertebra	S2
		Right acromion	S3
		Left acromion	S4
Left Arm	5	Left elbow, humerus lateral epicondyle	A1
		Left elbow, humerus medial epicondyle	A2
		Left wrist, radius styloid process	A3
		Left wrist, ulna styloid process	A4
		Left forearm	A5
Golf Club	3	Marker 1 of the shaft solid triad	C1
		Marker 2 of the shaft solid triad	C2
		Marker 3 of the shaft solid triad	C3
		Golf club head (not included in n_m)	C4

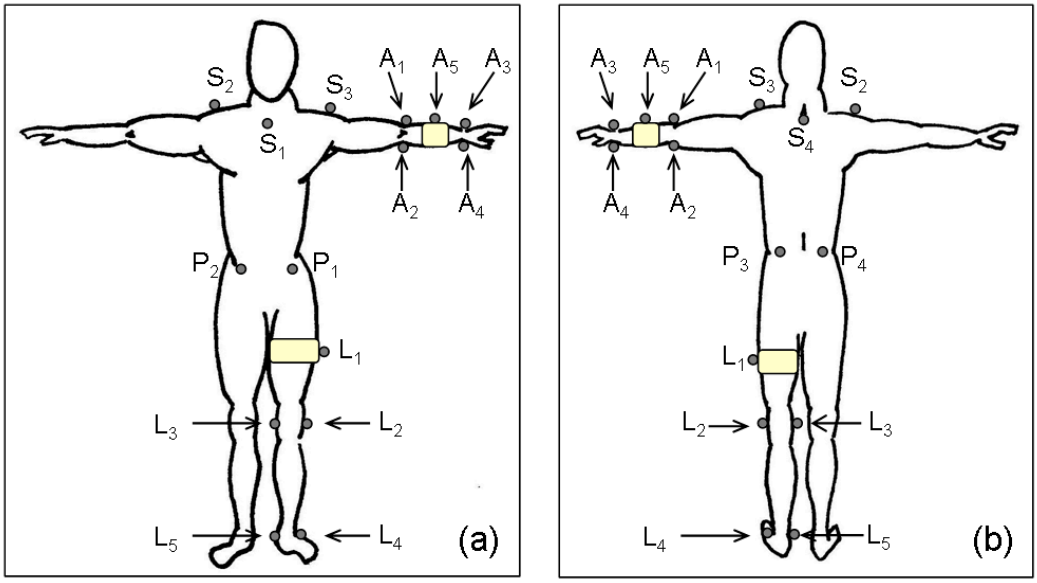

Figure 3-38: Marker Placement Guide; (a) Front view, (b) Rear view. Individual marker labels listed in Table 3-29

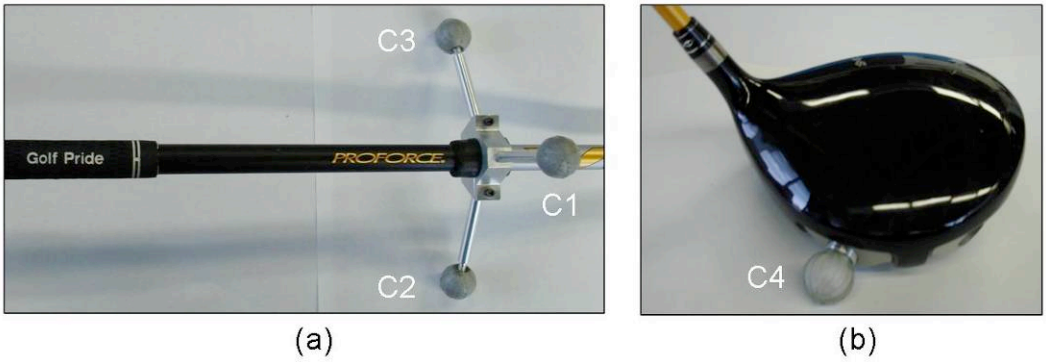

Figure 3-39: Reflective markers affixed to the golf club; (a) Markers C1, C2 and C3 of the shaft rigid triad, (b) Marker C4 affixed to the club head

The kinematic chain of ISAs begins with the calculation of ISA of each segment relative to the global reference frame, as described in Section 3.2.1. These ISAs describe the full motion of each individual segment relative to the global reference frame. A total of five ISAs are computed, one for each segment, and are labeled in Table 3-30. The golf swing model consists of a sequence of ISAs of the relative motion between physiologically linked segments. This describes the motion of the body as a series of ISAs, where each ISA defines the motion of a more distal segment relative to a more proximal segment, as described in Section

3.2.3. The golf swing model therefore describes the body as a system of rigid bodies, one for each segment, moving about non-rigid spherical joints, where the motion about each joint is given as a single rotation and translation about the resulting axis of rotation (ISA). These spherical joints can represent a physiological joint or a functional joint, were the motion between rigid bodies is not necessarily the result of motion about a single physiological joint.

Table 3-30: ISA labels for each segment; reference and relative segments given for each ISA of relative motion

Segment	ISA			
	Global reference frame Notation	Relative motion		
		Notation	Segments	
			Proximal	Distal
Left Leg	ISA_L	NA	NA	NA
Pelvis	ISA_P	$ISAr_P$	Left Leg	Pelvis
Shoulders	ISA_S	$ISAr_S$	Pelvis	Shoulders
Left Arm	ISA_A	$ISAr_A$	Shoulders	Left Arm
Golf Club	ISA_C	$ISAr_C$	Left Arm	Golf Club

From the five ISAs, relative to the global reference frame, a total of four relative ISAs are computed, and are labeled in Table 3-30.

$ISAr_P$: The first relative ISA is computed for the movement of the pelvis relative to the left leg. As the pelvis moves about two anatomical joints, the right and left hip joints, $ISAr_p$ describes the motion of the pelvis about a single functional joint resulting from the motion about these two anatomical joints. The ISA is computed relative to the left leg in an effort to isolate the rotational component of pelvis motion, reducing the effects of weight transfer during the downswing [Burden et al. (1998)], which appears as lateral shift of the pelvis.

$ISAr_S$: The second relative ISA is computed from the relative movement of the shoulders relative to the pelvis, $ISAr_S$. As the main motion of the shoulders during the golf swing is a rotation about the spine, $ISAr_S$ is expected to represent the anatomical joint that coincides with the longitudinal axis of the spine.

$ISAr_A$: The third relative ISA represents the motion of the left arm relative to the shoulders. Assuming the entire left arm, from the left shoulder to the left wrist, acts as a rigid body during the downswing, the motion of the left arm would occur about the left glenohumeral joint (shoulder joint). Therefore, $ISAr_A$ represents the motion of the left arm about the left glenohumeral joint.

$ISAr_C$: The fourth, and last, relative ISA describes the motion of the golf club relative to the left arm, labeled $ISAr_C$. Assuming the left arm acts as a rigid body and that the golf club is rigid, neglecting the flexibility of the shaft between the rigid triad and the hands, the relative displacements between the two would be a result of wrist motion. Therefore, $ISAr_C$ represents the motion of the anatomical wrist joint.

3.4.1 Golf Swing Model: Verification of Objectives

When studying relative motion between rigid bodies of the golf swing model, it is suggested that the magnitude of the perpendicular component of marker velocity will far exceed the parallel component of marker velocity, as the allowable motion between segments is largely rotational. That being said, the majority of marker displacement is through a rotation about ISA, therefore the magnitude of the angular velocity in the direction of ISA is an important result, as it will provide insight into the kinematic sequence of the downswing. Therefore, the magnitude of the angular velocity in the direction of ISA will be studied for all segments. Specifically, the instances, during the downswing, where these angular velocities reach their respective maxima will be investigated. This includes the time in the downswing when the maximum occurs, as well as ISA position and orientation at maximum angular velocity. ISA position will be given as the intersection between ISA and the plane formed by the three markers used for computation. For example, the position of $ISAr_P$ will be determined by its intersection with the plane formed by the three markers, out of markers P_1, P_2, P_3 and P_4, used for computation. ISA orientation was measured as the relative angle to the spine,

which was measured as the vector connecting the pelvis and shoulders centroids. Furthermore, to confirm that the rotational component of marker displacement far outweighs the translation component, as far as the contribution to marker velocity, the ratio of perpendicular velocity to parallel velocity is computed.

It was desired to study the downswing portion of the golf swing, from the transition between the backswing to the downswing, to the instance of impact. As trials are not of constant duration, it is necessary to normalize the results. Trials were normalized by downswing duration and expressed in terms of percent downswing. This required two distinct time frames to be identified: the frame that marks the beginning of the downswing, t_o, and the frame coinciding with or closest to impact, t_I. These instances were identified with the displacement of a marker placed on the golf club head, which forms two distinct arcs during the golf swing, as shown in Figure 3-40. The first arc is formed during the backswing, where the club begins at address and undergoes a circular patch until pausing at the top of the swing. The second arc is formed during the downswing and follow-through, where the golf club rotates to impact and continues until rest in the follow-through. At the transition between the two arcs, the z-component of club head velocity shifts from negative to positive, as it undergoes a decrease in elevation, z-component of the displacement, followed by an increase of elevation at the beginning of the downswing. The time frame that coincides with the first positive z-component of marker velocity is identified as t_o. To identify club head impact, it was found that the lowest point on the downswing arc, where the elevation of the club head marker is at a minimum, coincides with impact. Therefore, the time frame that produces the lowest z-component of marker displacement is identified as t_I. Another method was investigated to determine the instant corresponding to impact, which consisted of identifying the time frame where the distance between the club head during the downswing and its position at address was minimized. Results indicated that both methods produced similar results and therefore clubhead elevation was used for simplicity.

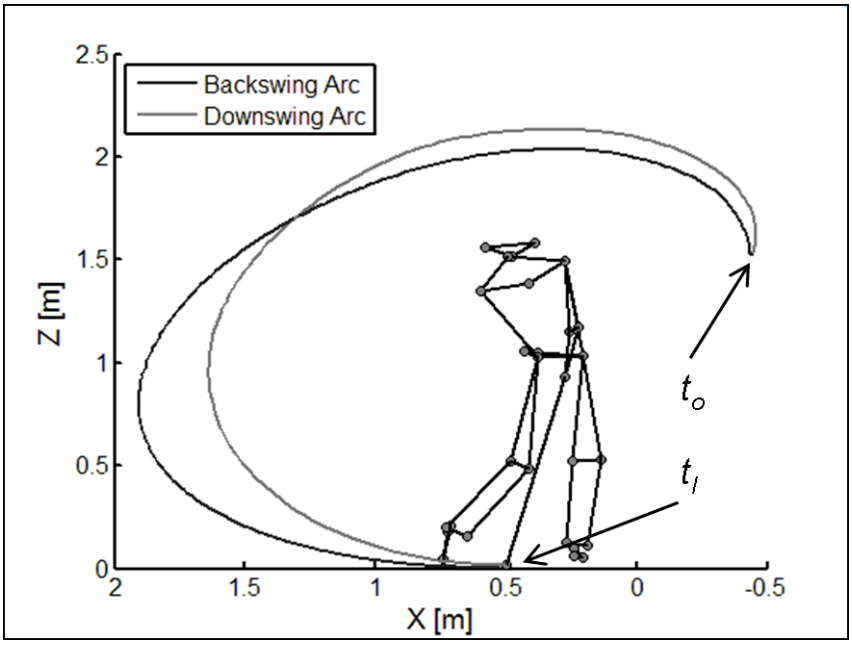

Figure 3-40: Displacement of the golf club head during the backswing, *Backswing Arc*, and downswing, *Downswing Arc*. The beginning of the downswing, t_o, and the end of the downswing, t_I, are shown. Markers placed on body segments are shown at impact, t_I.

The duration of the downswing is given by the difference between t_I and t_o. For a given time frame, t_i, normalized time is given by the difference between t_i and t_o, divided by the duration of the downswing and multiplied by 100 percent, as followed:

$$t_{iN} = \frac{(t_i - t_o)}{(t_I - t_o)} \times 100 \quad [percent\ downswing] \tag{3-57}$$

where t_{iN} is the normalized equivalent of frame t_i. Following normalization, all trials have the same time series, from 0 to 100 percent downswing. However, the individual time frames are not consistent between trials, as the number of frames within a single trial is dependant on trial duration, which restricts the computation of means and standard deviations of multiple trials. Therefore, the data of each trial are resampled to a constant number of time frames. This was accomplished by applying interpolating cubic splines to the calculated data and reevaluating these splines at given time frames, consistent with the methodology of Section 3.3.3.1. From preliminary data of Subject 1, it was determined that the average

duration of the downswing, from time frames t_o and t_I, was 0.5 sec, corresponding to 200 data points at the given sampling rate of 400 Hz. Therefore, an equally distributed time series varying from 0 to 100 percent downswing, with increments of 0.5 percent, was used to resample the calculated data. The normalized time of all trials is therefore given as follows:

$$t_{iN} = [0 : 0.5 : 100] \quad \textbf{(3-58)}$$

where i= [1:1:201], as 201 data points are required to complete the time series. This methodology was carried out for the following calculated data: magnitude of angular velocity, the intersection of ISA with its respective rigid body and ISA orientation relative to the spine angle.

3.4.2 Data collection

Data collection was carried out at the Syncrude Centre for Motion and Balance, Glenrose Rehabilitation Hospital, Edmonton, Alberta, Canada. The eight cameras of the stereophotogrammetric system, discussed in Section 3.1.1, were placed in the configuration shown in Figure 3-6 following the recommendations of the Marker Occlusion Study to reduce the occurrence of marker occlusion during the downswing. Furthermore, data was collected at a sampling rate of 400 Hz following the recommendations of the Measurement Accuracy Study, as this represents the highest sampling rate at which the cameras can operate at full field of view. Three-dimensional marker displacement was generated from the system's EVaRT v.4.2 software and then imported into MATLAB software (MathWorks, Natick, Massachusetts, USA) for post-processing and data analysis. The sampling population consisted of 5 male, low-handicap, right-handed golfers. The age, physical attributes and golf experience of each subject is summarized in Table 3-31.

Table 3-31: Sampling population- Age, physical attributes and golfing experience of Subjects 1 to 5

Subject	Age [years]	Height [feet-inch]	Weight [lbs]	Experience [years]	Rounds/Year [rounds/year]	Handicap
1	26	5'-6"	185	14	15	6
2	22	6'-1"	190	10	20	9
3	24	6'	180	11	35	7
4	40	6'-1"	175	20	25	10
5	66	5'-10"	160	40	25	11

During data collection, subjects were instructed to wear shorts, ankle socks and running shoes. Reflective markers were placed on the subject's body according to the marker placement guide shown in Figure 3-38. Once subjects were placed in the capture volume, feet placed in the center of the volume (as shown in Figure 3-6), they were instructed to make smooth, controlled golf swings, consistent with their regular motion. Each golf swing was recorded for 10 seconds duration and a total of 5 golf swings were analyzed for each subject. Ethics approval for this study was received on October 1st 2007 and was granted by the Health Research Ethics Board-Panel B (HREB File # B-131004).

Chapter 4 Results

The following chapter outlines the results of the golf swing model and is divided into three sections. The first section, Applied Error in Marker Displacement, discusses the amount of error introduced on marker position, from the applied error compensation techniques, and on marker velocity, from relative ISA computation. The second section, Marker Velocity about ISA and ISAr, verifies the assumption that the majority of marker displacement is a result of rotation about the segment's ISA. The third section, ISA Angular Velocity, discusses the magnitude of angular velocity about each segment's ISA, computed relative to the global reference frame, and ISAr, computed from the relative motion between two physiologically linked segments.

4.1 Applied Error on Marker Displacement

The error compensation techniques introduced in Section 3.3.3 to 3.3.4 produce marker displacement consistent with rigid body motion from stereophotogrammetric measurements. These techniques replace occluded data points, reduce the effects of random and systematic instrument error and eliminate inter-marker variability. These methodologies introduce error on the measured marker displacements. Furthermore, from marker position and velocity, the relative displacement between linked segments was modeled as the movement about a relative ISA. This computation assumes that two segments are rigidly connected and, when the assumption does not hold, produces an approximation of the motion between them. This manifests itself as error between measured velocity, from numerical differentiation of measured displacement, and marker velocity from movement about the relative ISA. Further errors between measured and computed marker velocity are caused by instances approaching an undefined ISA and have not been fully attenuated by the applied diagnostics, as discussed in Section 3.2.2.

The amount of error introduced on marker position, from error compensation techniques, and marker velocity, from relative ISA computation, was measured. This quantifies the extent of error introduced during analysis, which can then be compared to known sources of marker displacement error.

4.1.1 RMSE on Marker Position

To quantify the error introduced on marker displacement from the compensation technique of Sections 3.3.3 and 3.3.4, the RMSE between measured marker displacements and the computed rigid body marker displacements was calculated. Specifically, RMSE was computed between measured and computed marker displacements of the three markers used in ISA computation for each segment and trial. These results were then averaged for the 5 trials of each subject. Complete results of Subject 1 are shown in Table 4-1, while averaged results for Subjects 1 to 5 are shown in Table 4-2. Furthermore, complete results of Subjects 2 to 5 are shown in Table A4-1 to Table A4-4 of Appendix 4.

Table 4-1: Subject 1-RMSE on marker position. Error computed between measured marker position and solidified marker position, for the three markers of each segment used in the computation of ISA.

Trial	Position RMSE				
	Left Leg [m]	Pelvis [m]	Shoulders [m]	Left Arm [m]	Golf Club [m]
1	0.00070	0.00161	0.01278	0.00166	0.00109
2	0.00081	0.00171	0.00466	0.00363	0.00144
3	0.00059	0.00142	0.01412	0.00207	0.00091
4	0.00077	0.00174	0.00425	0.00200	0.00167
5	0.00078	0.00166	0.01435	0.00166	0.00126
Mean	0.00073	0.00163	0.01003	0.00220	0.00127

Table 4-2: Subjects 1 to 5-RMSE on marker position. Error computed between measured marker position and solidified marker position, for the three markers of each segment used in the computation of ISA. Results averaged over the 5 trials of each subject.

Subject	Position RMSE				
	Left Leg [m]	Pelvis [m]	Shoulders [m]	Left Arm [m]	Club [m]
1	0.00073	0.00163	0.01003	0.00220	0.00127
2	0.00064	0.00306	0.00547	0.00432	0.00474
3	0.00139	0.00231	0.01449	0.00478	0.00639
4	0.00133	0.00355	0.00967	0.00396	0.00560
5	0.00135	0.00210	0.00657	0.00427	0.00228
Mean	0.00109	0.00253	0.00924	0.00391	0.00406

4.1.2 RMSE on Marker Velocity

To quantify the error introduced from the assumption of rigidly connected segments in relative ISA computation and from instances approaching an undefined ISA, RMSE between measured marker velocity and marker velocity computed from the motion about a relative ISA was calculated. Specifically, RMSE was computed between measured and computed marker velocity of the three markers used in relative ISA computation for each segment and trial.

4.1.2.1 RMSE on Marker Velocity about ISA

RMSE was computed between measured and computed marker velocity of the three markers used in ISA computation for each segment and trial. These results were then averaged for the 5 trials of each subject. Results are shown for the five ISAs of the golf swing model, computed relative to the global reference frame. This includes ISA_L, from displacement of the left leg, ISA_P, from displacement of the pelvis, ISA_S, from displacement of the shoulders, ISA_A, for displacement of the left arm and ISA_C, for displacement of the golf club. Complete results of Subject 1 are shown in Table 4-3, while averaged results for Subjects 1 to 5 are shown in Table 4-4. Furthermore, complete results of Subjects 2 to 5 are shown in Table A4-5 to Table A4-8 of Appendix 4.

Table 4-3: Subject 1-RMSE on marker velocity. Error computed between measured marker velocity from numerical differentiation, of solidified marker position, and from movement about the ISA. Results shown for the RMSE on the three markers of each segment used in the computation of ISA.

Trial	Velocity RMSE				
	ISA_L [m/s]	ISA_P [m/s]	ISA_S [m/s]	ISA_A [m/s]	ISA_C [m/s]
1	0.00084	0.00077	0.00249	0.00524	0.03852
2	0.00059	0.00110	0.00259	0.00645	0.07210
3	0.00065	0.00042	0.00111	0.00712	0.03482
4	0.00071	0.00058	0.00260	0.00885	0.03577
5	0.00067	0.00055	0.00417	0.00839	0.04601
Mean	0.00069	0.00068	0.00259	0.00721	0.04544

Table 4-4: Subjects 1 to 5-RMSE on marker velocity. Error computed between measured marker velocity from numerical differentiation, of solidified marker position, and from movement about the ISA. Results shown for the RMSE on the three markers of each segment used in the computation of ISA. Results averaged over the 5 trials of each subject.

Subject	Velocity RMSE				
	ISA_L [m/s]	ISA_P [m/s]	ISA_S [m/s]	ISA_A [m/s]	ISA_C [m/s]
1	0.00069	0.00068	0.00259	0.00721	0.04544
2	0.00167	0.00402	0.01099	0.03156	3.76030
3	0.00267	0.00708	0.00609	0.03414	6.92356
4	0.00237	0.00510	0.01922	0.01497	0.98593
5	0.00404	0.00496	0.00401	0.01220	0.29078
Mean	0.00229	0.00437	0.00858	0.02002	2.40120

4.1.2.2 RMSE on Marker Velocity about ISAr

RMSE was computed between measured and computed marker velocity of the three markers used in ISAr computation for each segment and trial. These results were then averaged for the 5 trials of each subject. Results are shown for the four ISAr of the golf swing model, computed from the relative movement to the preceding segment. This includes $ISAr_P$, from the displacement of the pelvis relative to the left leg, $ISAr_S$, from the displacement of the shoulders relative to the pelvis, $ISAr_A$, from the displacement of the left arm relative to the pelvis, and

$ISAr_C$, from the displacement of the golf club relative to the left arm. Complete results of Subject 1 are shown in Table 4-5, while averaged results for Subjects 1 to 5 are shown in Table 4-6. Furthermore, complete results of Subjects 2 to 5 are shown in Table A4-9 to Table A4-12 of Appendix 4.

Table 4-5: Subject 1-RMSE on marker velocity. Error computed between measured marker velocity from numerical differentiation, of solidified marker position, and from movement about the ISAr. Results shown for the RMSE on the three markers of each segment used in the computation of ISAr.

Trial	Velocity RMSE			
	$ISAr_P$ [m/s]	$ISAr_S$ [m/s]	$ISAr_A$ [m/s]	$ISAr_C$ [m/s]
1	0.00101	0.00464	0.00548	0.04028
2	0.00099	0.00688	0.00834	0.09875
3	0.00070	0.00194	0.00542	0.03851
4	0.00100	0.00529	0.00602	0.03728
5	0.00146	0.00502	0.00690	0.27516
Mean	0.00103	0.00475	0.00643	0.09800

Table 4-6: Subjects 1 to 5-RMSE on marker velocity. Error computed between measured marker velocity from numerical differentiation, of solidified marker position, and from movement about the ISAr. Results shown for the RMSE on the three markers of each segment used in the computation of ISAr. Results averaged over the 5 trials of each subject.

Subject	Velocity RMSE			
	$ISAr_P$ [m/s]	$ISAr_S$ [m/s]	$ISAr_A$ [m/s]	$ISAr_C$ [m/s]
1	0.00103	0.00475	0.00643	0.09800
2	0.01326	0.01770	0.04615	1.39597
3	0.01415	0.02246	0.03577	2.13647
4	0.01871	0.03078	0.03107	0.56421
5	0.00426	0.00546	0.02493	0.36262
Mean	0.01028	0.01623	0.02887	0.91145

4.2 Marker Velocity about ISA and ISAr

When the displacement of a rigid body is expressed in terms of an ISA, marker displacement is divided into two components: parallel velocity, from translation

along the ISA, and perpendicular velocity, from a rotation on ISA direction [Eberharter and Ravani (2006)]. The golf swing model assumes that the magnitude of the perpendicular component of marker velocity will far exceed the parallel component of marker velocity and therefore the majority of marker displacement is through a rotation about ISA (see Section 3.4). To verify this assumption, the magnitude of parallel marker velocity was compared to the magnitude of total marker velocity by way of a velocity ratio. This was computed as the ratio of parallel marker velocity magnitude to total marker velocity magnitude, expressed in percentage. This quantifies the extent of motion that is not fully expressed by a rotation about the ISA.

4.2.1 Marker Velocity Ratio about ISA

Velocity ratio was computed between parallel and total marker velocity of the three markers used in ISA computation, averaged for these three markers, and shown for each segment and trial. These results were then averaged for the 5 trials of each subject. Results are shown for the five ISA of the golf swing model, computed relative to the global reference frame. Complete results of Subject 1 are shown in Table 4-7, while averaged results for Subjects 1 to 5 are shown in Table 4-8. The standard deviation for all subjects, presented here for Subject 1 only, varied from 1.6 percent to 8.5 percent for computation of body segment ISA, and varied from 0.8 percent to 10.4 percent for computation of golf club ISA. Complete results, including standard deviations, of Subjects 2 to 5 are shown in Table A4-13 to Table A4-16 of Appendix 4.

Table 4-7: Subject 1-Velocity ratio computed as the ratio between the parallel component of marker velocity, parallel to ISA, and total marker velocity, expressed in percentage. Results shown are the mean velocity ratios of the three markers of each segment used in ISA computation.

Trial	Parallel Velocity / Total Velocity				
	ISA_L [%]	ISA_P [%]	ISA_S [%]	ISA_A [%]	ISA_C [%]
1	32.4	18.2	15.4	11.7	1.5
2	32.3	19.2	12.0	9.6	3.4
3	35.1	17.8	13.3	10.8	1.3
4	33.4	16.3	14.0	9.1	2.0
5	33.5	20.5	15.8	9.9	1.6
Mean	33.3	18.4	14.1	10.2	2.0
S	1.1	1.6	1.5	1.0	0.8

Table 4-8: Subjects 1to 5-Velocity ratio computed as the ratio between the parallel component of marker velocity, parallel to ISA, and total marker velocity, expressed in percentage. Results shown are the mean velocity ratios of the three markers of each segment used in ISA computation. Results averaged over the 5 trials of each subject.

Subject	Parallel Velocity / Total Velocity				
	ISA_L [%]	ISA_P [%]	ISA_S [%]	ISA_A [%]	ISA_C [%]
1	33.3	18.4	14.1	10.2	2.0
2	27.3	15.7	13.7	12.6	20.3
3	40.3	22.5	11.3	12.2	22.6
4	36.6	26.2	17.0	14.8	15.0
5	37.7	11.6	9.2	17.5	10.0
Mean	35.0	18.9	13.1	13.5	14.0

4.2.2 Marker Velocity Ratio about ISAr

Velocity ratio was computed between parallel and total marker velocity of the three markers used in ISAr computation, for each segment and trial, and averaged for these three markers. These results were then averaged for the 5 trials of each subject. Results are shown for the four ISAr of the golf swing model, computed from the relative movement to the preceding segment. Complete results of Subject 1 are shown in Table 4-9, while averaged results for Subjects 1 to 5 are shown in Table 4-10. The standard deviation for all subjects, presented here for Subject 1

only, varied from 4.0 percent to 6.2 percent for computation of body segment ISA, and varied from 5.1 percent to 21.1 percent for computation of golf club ISA. Complete results, including standard deviations, of Subjects 2 to 5 are shown in Table A4-17 to Table A4-20 of Appendix 4.

Table 4-9: Subject 1-Velocity ratio computed as the ratio between the parallel component of marker velocity, parallel to ISAr, and total marker velocity, expressed in percentage. Results shown are the mean velocity ratios of the three markers of each segment used in ISAr computation.

Trial	Parallel Velocity / Total Velocity			
	$ISAr_P$ [%]	$ISAr_S$ [%]	$ISAr_A$ [%]	$ISAr_C$ [%]
1	26.5	15.8	15.3	21.2
2	15.5	15.6	7.3	28.7
3	27.8	12.6	19.6	13.7
4	27.2	11.6	9.2	17.4
5	28.3	16.3	12.8	28.7
Mean	25.0	14.4	12.8	22.0
S	5.4	2.1	4.9	6.7

Table 4-10: Subjects 1to 5-Velocity ratio computed as the ratio between the parallel component of marker velocity, parallel to ISAr, and total marker velocity, expressed in percentage. Results shown are the mean velocity ratios of the three markers of each segment used in ISAr computation. Results averaged over the 5 trials of each subject.

Subject	Parallel Velocity / Total Velocity			
	$ISAr_P$ [%]	$ISAr_S$ [%]	$ISAr_A$ [%]	$ISAr_C$ [%]
1	25.0	14.4	12.8	22.0
2	10.1	17.9	17.3	46.7
3	15.5	16.1	13.7	35.6
4	16.9	23.5	12.0	58.5
5	7.6	14.4	14.9	51.2
Mean	15.0	17.3	14.1	42.8

4.3 ISA Angular Velocity

The purpose of this thesis was to determine the kinematic sequence of the golf swing, a motion which consists primarily of gross rotations of the lower body, upper body and arms. It is of particular interest to determine the sequence of these rotations, which can be accomplished by studying the angular velocity of each segment relative to their ISA.

4.3.1 Time Varying Angular Velocity about ISA

The magnitude of the angular velocity of each analyzed segment, about their respective ISA, was determined as a function of percent downswing. Plotting the magnitude of angular velocity as a function of percent downswing provides insight into the velocity and acceleration of each segment.

4.3.1.1 Angular Velocity about ISA

The magnitude of the angular velocity about each ISA, computed relative to the global reference frame, was plotted as a function of percent downswing. Each angular velocity, one for each ISA, was plotted as the mean magnitude plus or minus one standard deviation, computed from the 5 measured trials. Results are shown in Figure 4-1 for Subject 1, while results for Subjects 2 to 5 are shown in Figure A4-1 to Figure A4-4 of Appendix 4.

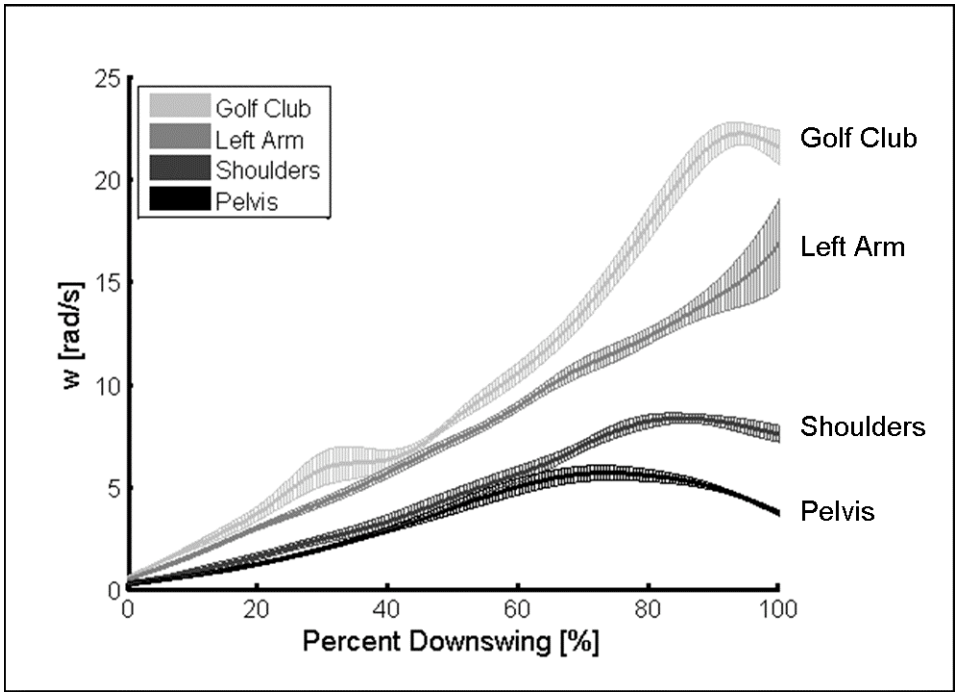

Figure 4-1: Subject 1- Magnitude of segment angular velocity about their ISA, relative to the global reference frame.

4.3.1.2 Angular Velocity about ISAr

The magnitude of the angular velocity about each ISAr, computed relative to the preceding body segment, was plotted as a function of percent downswing. Each angular velocity, one for each ISAr, was plotted as the mean magnitude plus or minus one standard deviation, computed from the 5 measured trials. Results are shown in Figure 4-2 for Subject 1, while results for Subjects 2 to 5 are shown in Figure A4-5 to Figure A4-8 of Appendix 4. It should be noted that the angular velocity about $ISAr_C$, the relative ISA between the left arm and the golf club, was not included in the angular velocity plots. The reason for this omission was that the angular velocity curves about $ISAr_C$ displayed a number of sharp discontinuities, making it difficult to plot all curves clearly in the same figure. Complete analysis was conducted in the following section, which displays the effects of these discontinuities.

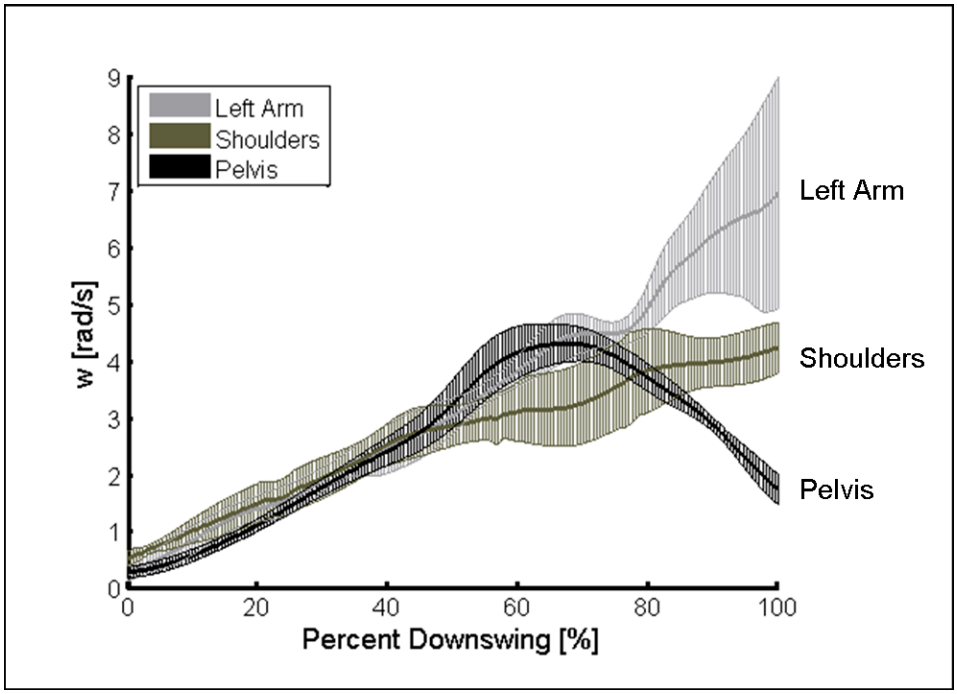

Figure 4-2: Subject 1- Magnitude of segment angular velocity about their ISAr, relative to the preceding body segment.

4.3.2 Instances of Maximum Angular Velocity

The kinematic sequence of the golf swing can be determined by studying the angular velocity of each segment relative to their ISA. Furthermore, the instance where each angular velocity is at its maximum is of particular interest, as the order in which segments sequentially achieves their respective maximum yields the kinematic sequence. The following results were computed at the instant where each ISA and ISAr achieved its respective maximum: magnitude of angular velocity, ω_{max}, the percent downswing corresponding to that instant, ISA position and ISA orientation. The final two variables, ISA position and orientation, are computed differently for each ISA and chosen to compare the ISA to the expected gross axis of rotation of that segment.

ISA Position at Maximum Angular Velocity

ISA_P and $ISAr_P$

The position of the pelvis ISA was computed from the local coordinate frame of the pelvis, computed from Cappozzo et al. [Cappozzo et al. (1995)] and shown in Figure 4-3. The position was given as the intersection between the pelvis ISA and the xy-plane of the pelvis local coordinate frame. Results are then shown as a plot of the pelvis markers, P1 to P4, and the intersection point, all within the local coordinate frame of the pelvis. Furthermore, the position of the right and left hip joint centers, labeled RHJC and LHJC and computed from Leardini et al. [Leardini et al. (1999)] (for the x- and y-components) and Bell et al. [Bell et al. (1990)] (for the z-component) and shown in the local coordinate frame of the pelvis (see Figure 4-3). This provides a reference for the position of the joint centers of the segment. Two references were used to locate the hip joints centers to accommodate the chosen marker set. The orientation of the pelvis ISA was computed as the angle between the ISA and two reference axes: the spine axis and axis of the left leg, as the expected orientation would be a combination of the two. The spine axis was computed as the line connecting the pelvis and shoulders centroids, where each centroid was computed from the position of the four affixed markers. The axis of the left leg was given as the line connecting the left hip joint centre, computed as described above, and the centroid of the left ankle, computed as the center point between markers L4 and L5 affixed to the left ankle (see Section 3.4).

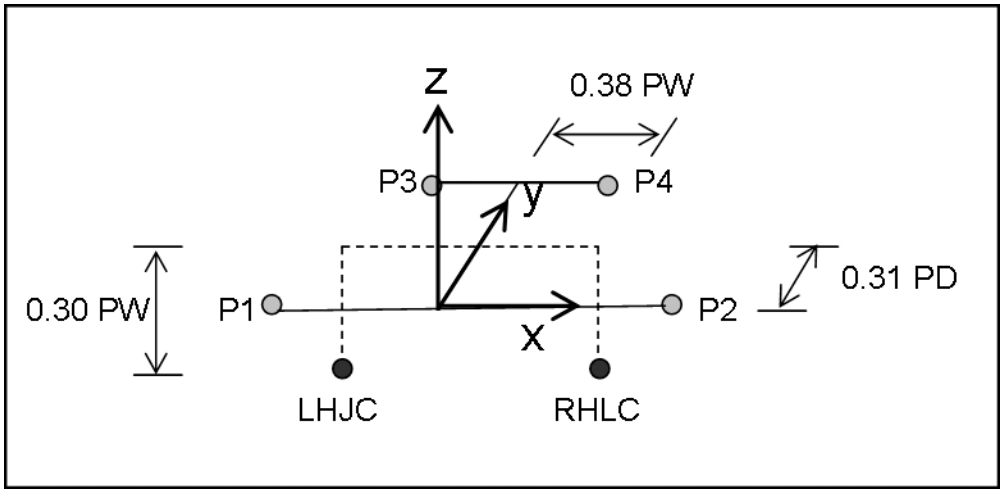

Figure 4-3: Local coordinate frame of the pelvis, computed from Cappozzo et al. [Cappozzo et al. (1995)]. Left and right hip joint centers, LHJC and RHJC, computed from Leardini et al. [Leardini et al. (1999)] and Bell et al. [Bell et al. (1990)]. PW: distance between markers P1 and P2; PD: distance between the origin (midpoint of P1 and P2) and the midpoint between P3 and P4.

ISA_S and $ISAr_S$

The position of the shoulders ISA was computed from the local coordinate frame of the shoulders. This coordinate system is shown in Figure 4-4 and was computed from the recommendations of Wu et al. [Wu et al. (2005)]; however some changes were made to accommodate the current marker set. The position was given as the intersection between the shoulders ISA and the xy-plane of the shoulders local coordinate frame. Results are then shown as a plot of the shoulder markers, S1 to S4, and the intersection point, all within the local coordinate frame of the shoulders. The orientation of the shoulders ISA was computed as the angle between the ISA and the spine axis, computed as described above. Assuming the main degree of freedom between the shoulders and the pelvis can be modeled as a torsional spring parallel to the spine, the spine axis represents the expected orientation of shoulder rotation.

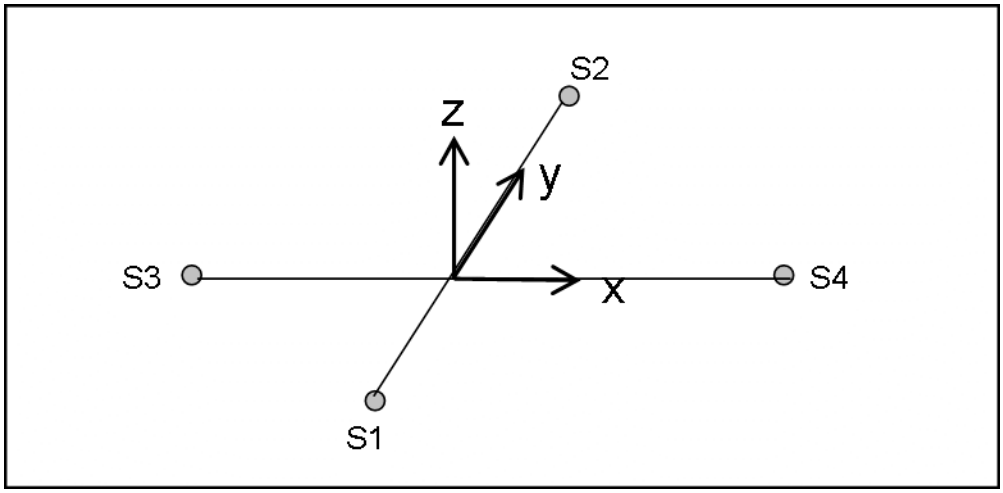

Figure 4-4: Local coordinate frame of the shoulders, computed from the recommendations of Wu et al. [Wu et al. (2005)]. Origin determined from the centroid of markers S1 to S4. X-axis along the vector connecting S3 and S4, z-axis determined from the cross product of the x-axis and the vector along S1 and S2. Finally, y-axis determined from the cross product of the x-axis and z-axis.

ISA_A and $ISAr_A$

The position of the left arm ISA was computed from the local coordinate frame of the shoulders, as shown in Figure 4-4. The position was given as the intersection between the left arm ISA and the xy-plane of the shoulders local coordinate frame. Results are then shown as a plot of the shoulder markers, S1 to S4, and the intersection point, all within the local coordinate frame of the shoulders. The orientation of the left arm ISA was computed as the angle between the ISA and two reference axes: the spine axis and the supination axis of the wrist. These two reference axes were used to locate the ISA as the expected motion of the left arm would be a combination of movement about the left shoulder joint and supination about the left wrist. The supination axis of the left arm was computed as the line connecting the centroid of the wrist and centroid of the elbow. The centroid of the wrist was computed as the center point between markers A3 and A4 affixed to the wrist, while the centroid of the elbow was computed as the center point between markers A1 and A2 affixed to the elbow. It is assumed that the supination of the left forearm is conducted about this axis.

ISA_C and $ISAr_C$

The position of the golf club ISA was computed as the shortest distance between the ISA and the centroid of the wrist joint. This centroid, computed as described above, provides an approximation for the wrist joint center. The orientation of the golf club ISA was computed as the angle between the ISA and the supination axis of the left forearm, computed as described above. The supination axis represents the orientation of one the components of golf club rotation relative to the left arm.

4.3.2.1 Maximum Angular Velocity about ISA

The four variables computed at maximum angular velocity (ω_{max}, percent downswing corresponding to ω_{max}, ISA position and ISA orientation) are given for each ISA and subject. For each ISA, complete results are given for Subject 1 and mean results are provided for all 5 subjects.

ISA_P: ISA of the pelvis relative to the global reference frame

Complete results of Subject 1 are shown in Table 4-11 and Figure 4-5, while mean results of Subjects 1 to 5 are shown in Table 4-12, Table 4-13 and Figure 4-6. Complete results of Subjects 2 to 5 are shown in Table A4-21 to Table A4-24 in Appendix 4. For each table of results, the corresponding ISA position plot is provided directly below it.

Table 4-11: Subject 1- ISA_P angular velocity, position, orientation and normalized time at maximum angular velocity. Position computed in the local reference frame of the pelvis, and orientation computed relative to the spine axis and axis of the left leg.

Trial	ω_{max}	Percent	Position			Orientation	
						Spine	Left Leg
		Downswing	x	y	z	Axis	Axis
	[rad/s]	[%]	[m]	[m]	[m]	[deg]	[deg]
1	5.764	72.5	-0.009	0.125	0.000	15.55	12.37
2	5.820	73.5	-0.017	0.122	0.000	15.53	13.74
3	5.113	76.0	-0.022	0.131	0.000	13.66	14.75
4	5.960	73.0	-0.019	0.138	0.000	15.67	13.00
5	5.940	72.0	-0.016	0.133	0.000	15.80	11.92
Mean	5.719	73.4	-0.016	0.130	0.000	15.24	13.16
S	0.349	1.6	0.005	0.006	0.000	0.89	1.12

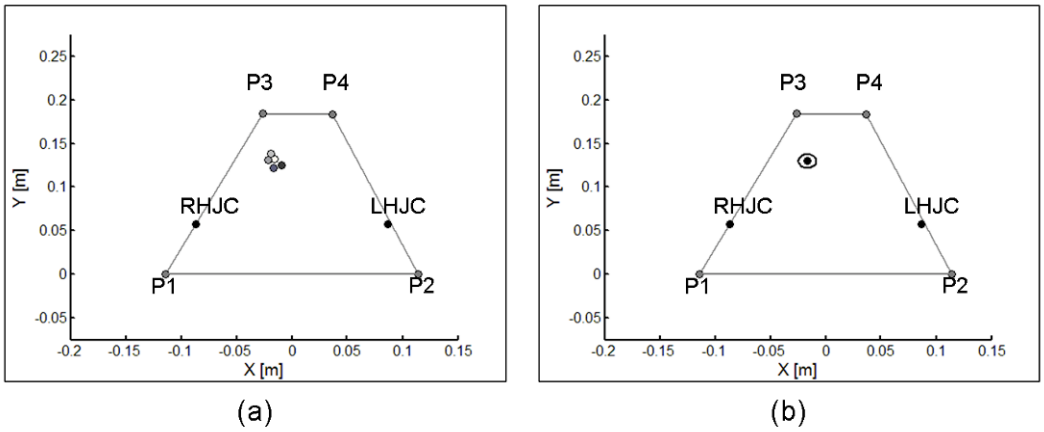

Figure 4-5: Subject 1- Intersection of ISA_P with the xy-plane of the local coordinate frame of the pelvis; (a) intersection point of trials 1 to 5, (b) mean intersection point and radius of standard deviation (r_S= 0.0078 m)

Table 4-12: Subjects 1 to 5- Mean ISA_P angular velocity, position, orientation and normalized time at maximum angular velocity. Position computed in the local reference frame of the pelvis, and orientation computed relative to the spine axis and axis of the left leg.

Subject	ω_{max}	Percent	Position			Orientation	
		Downswing	x	y	z	Spine Axis	Left Leg Axis
	[rad/s]	[%]	[m]	[m]	[m]	[deg]	[deg]
1	5.719	73.4	-0.016	0.130	0.000	15.24	13.16
2	7.602	73.9	-0.005	0.090	0.000	9.71	43.59
3	7.762	68.2	-0.003	0.161	0.000	16.71	25.55
4	9.563	74.5	0.006	0.083	0.000	11.06	35.26
5	7.280	83.7	0.012	0.149	0.000	8.05	31.47

Table 4-13: Subjects 1 to 5- Standard deviation of ISA_P angular velocity, position, orientation and normalized time at maximum angular velocity. Position computed in the local reference frame of the pelvis, and orientation computed relative to the spine axis and axis of the left leg.

Subject	ω_{max}	Percent	Position			Orientation	
		Downswing	x	y	z	Spine Axis	Left Leg Axis
	[rad/s]	[%]	[m]	[m]	[m]	[deg]	[deg]
1	0.349	1.6	0.005	0.006	0.000	0.89	1.12
2	0.465	2.0	0.003	0.004	0.000	1.42	1.89
3	0.334	3.2	0.008	0.002	0.000	1.84	1.50
4	0.336	3.1	0.002	0.005	0.000	2.23	1.38
5	0.249	2.3	0.012	0.011	0.000	0.90	2.35

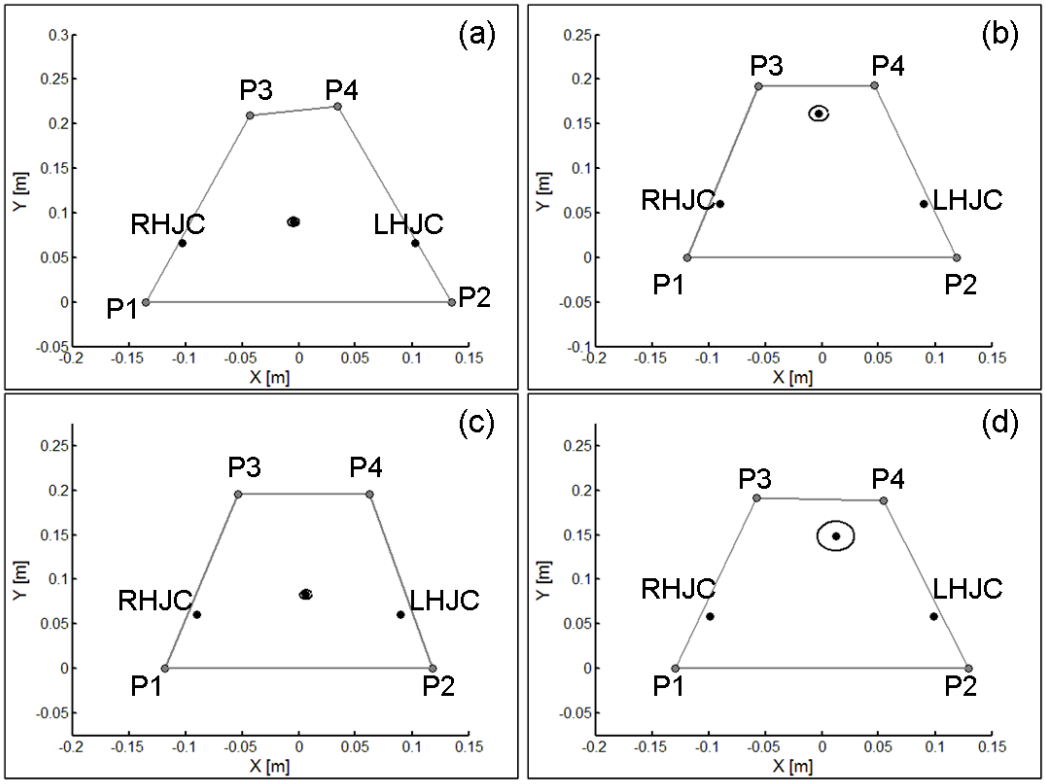

Figure 4-6: Subjects 2 to 5- Intersection of ISA_P with the xy-plane of the local coordinate frame of the pelvis. Results given as mean intersection and radius of standard deviation, r_S (computed from trials 1 to 5); (a) Subject 2 (r_S= 0.0050 m), (b) Subject 3 (r_S= 0.0082 m), (c) Subject 4(r_S= 0.0054 m), (d) Subject 5 (r_S= 0.0163 m)

ISA_S: ISA of the shoulders relative to the global reference frame

Complete results of Subject 1 are shown in Table 4-14 and Figure 4-7, while mean results of Subjects 1 to 5 are shown in Table 4-15, Table 4-16 and Figure 4-8. Furthermore, complete results of Subjects 2 to 5 are shown in Table A4-25 to Table A4-28 in Appendix 4. For each table of results, the corresponding ISA position plot is provided directly below it.

Table 4-14: Subject 1- ISA_S angular velocity, position, orientation and normalized time at maximum angular velocity. Position computed in the local reference frame of the shoulders, and orientation computed relative to the spine axis.

Trial	ω_{max}	Percent Downswing	Position			Orientation
			x	y	z	
	[rad/s]	[%]	[m]	[m]	[m]	[deg]
1	8.214	88.0	-0.022	-0.001	0.000	6.22
2	8.674	86.5	-0.028	-0.004	0.000	3.87
3	8.217	87.0	-0.030	0.008	0.000	7.24
4	8.310	82.0	-0.032	0.009	0.000	4.00
5	8.623	82.5	-0.028	0.003	0.000	6.31
Mean	8.408	85.2	-0.028	0.003	0.000	5.53
S	0.224	2.8	0.004	0.006	0.000	1.51

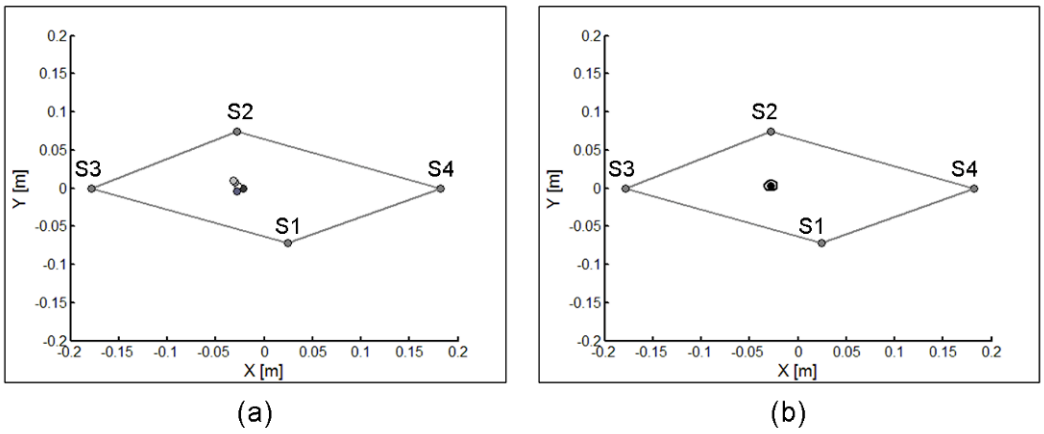

Figure 4-7: Subject 1- Intersection of ISA_S with the xy-plane of the local coordinate frame of the shoulders; (a) intersection point of trials 1 to 5, (b) mean intersection point and radius of standard deviation (r_S= 0.0072 m)

Table 4-15: Subjects 1 to 5- Mean ISA_S angular velocity, position, orientation and normalized time at maximum angular velocity. Position computed in the local reference frame of the shoulders, and orientation computed relative to the spine axis.

Subject	ω_{max}	Percent Downswing	Position			Orientation
			x	y	z	
	[rad/s]	[%]	[m]	[m]	[m]	[deg]
1	8.408	85.2	-0.028	0.003	0.000	5.53
2	10.918	66.9	-0.018	-0.022	0.000	4.30
3	10.381	72.8	-0.045	-0.016	0.000	10.11
4	13.514	76.4	-0.055	-0.046	0.000	4.29
5	10.062	82.4	-0.063	-0.012	0.000	12.22

Table 4-16: Subjects 1 to 5- Standard deviation of ISA_S angular velocity, position, orientation and normalized time at maximum angular velocity. Position computed in the local reference frame of the shoulders, and orientation computed relative to the spine axis.

Subject	ω_{max}	Percent Downswing	Position			Orientation
			x	y	z	
	[rad/s]	[%]	[m]	[m]	[m]	[deg]
1	0.224	2.8	0.004	0.006	0.000	1.51
2	0.360	2.5	0.003	0.002	0.000	1.65
3	0.470	1.7	0.006	0.003	0.000	1.64
4	0.443	2.2	0.008	0.006	0.000	0.91
5	0.162	16.1	0.034	0.020	0.000	5.68

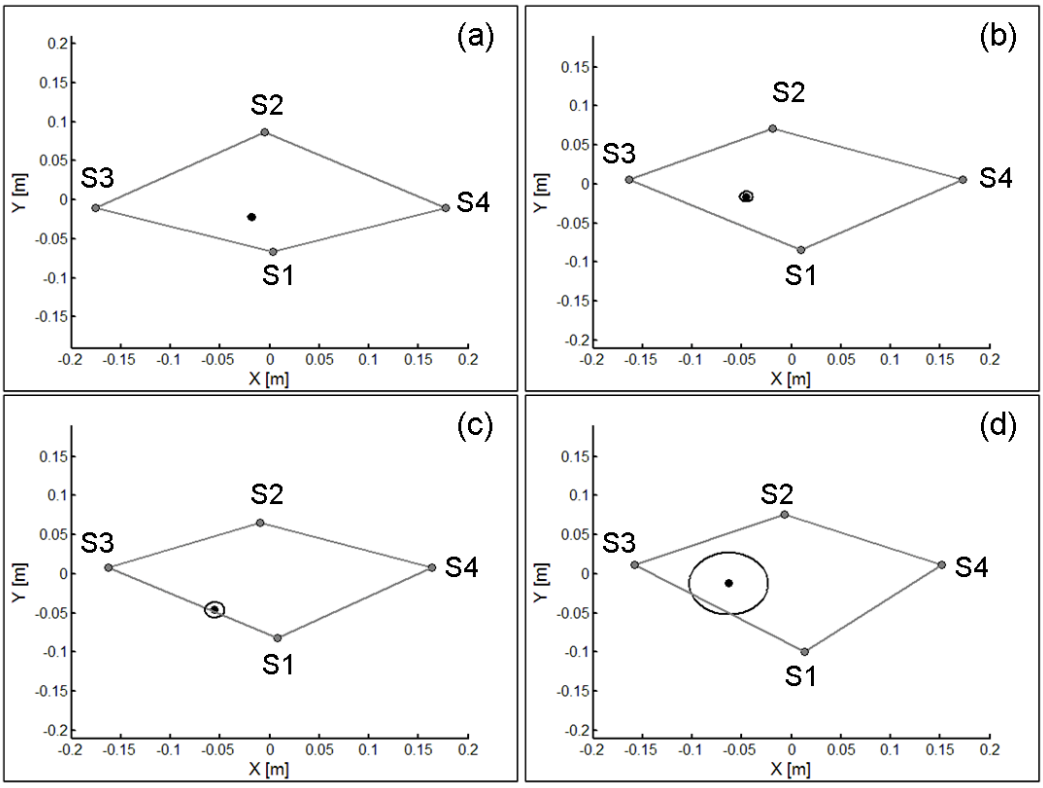

Figure 4-8: Subjects 1 to 5- Intersection of ISA_S with the xy-plane of the local coordinate frame of the shoulders Results given as mean intersection and radius of standard deviation, r_S (computed from trials 1 to 5); (a) Subject 2 (r_S= 0.0036 m), (b) Subject 3 (r_S= 0.0067 m), (c) Subject 4(r_S= 0.0090 m), (d) Subject 5 (r_S= 0.0395 m)

ISA_A: ISA of the left arm relative to the global reference frame

Complete results of Subject 1 are shown in Table 4-17 and Figure 4-9, while mean results of Subjects 1 to 5 are shown in Table 4-18, Table 4-19 and Figure

4-10. Furthermore, complete results of Subjects 2 to 5 are shown in Table A4-29 to Table A4-32 in Appendix 4. For each table of results, the corresponding ISA position plot is provided directly below it.

Table 4-17: Subject 1- ISA_A angular velocity, position, orientation and normalized time at maximum angular velocity. Position computed in the local reference frame of the shoulders, and orientation computed relative to the spine axis and the supination axis of the forearm.

Trial	ω_{max}	Percent	Position			Orientation	
						Spine Axis	Supination Axis
		Downswing	x	y	z		
	[rad/s]	[%]	[m]	[m]	[m]	[deg]	[deg]
1	13.192	100.0	0.076	-0.021	0.000	9.01	45.86
2	18.574	100.0	0.133	-0.008	0.000	9.02	31.92
3	16.844	100.0	0.153	0.028	0.000	11.67	29.98
4	17.435	100.0	0.155	0.018	0.000	5.01	29.74
5	18.332	100.0	0.151	-0.004	0.000	9.62	31.03
Mean	16.875	100.0	0.133	0.003	0.000	8.86	33.71
S	2.173	0.0	0.033	0.020	0.000	2.42	6.85

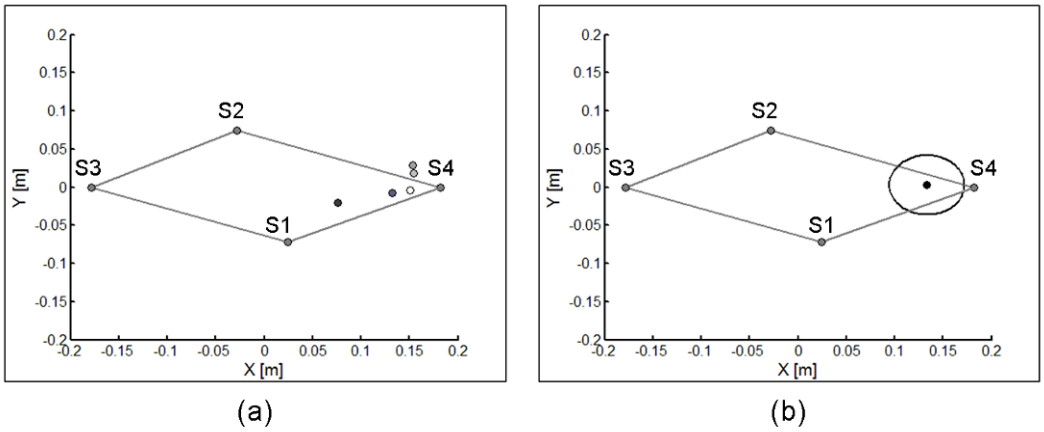

Figure 4-9: Subject 1- Intersection of ISA_A with the xy-plane of the local coordinate frame of the shoulders; (a) intersection point of trials 1 to 5, (b) mean intersection point and radius of standard deviation (r_S= 0.0386 m)

Table 4-18: Subjects 1 to 5- Mean ISA_A angular velocity, position, orientation and normalized time at maximum angular velocity. Position computed in the local reference frame of the shoulders, and orientation computed relative to the spine axis and the supination axis of the forearm.

Subject	ω_{max}	Percent	Position			Orientation	
						Spine	Supination
		Downswing	x	y	z	Axis	Axis
	[rad/s]	[%]	[m]	[m]	[m]	[deg]	[deg]
1	16.875	100.0	0.133	0.003	0.000	8.86	33.71
2	18.104	93.9	0.187	0.010	0.000	9.38	38.47
3	19.828	100.0	0.175	0.039	0.000	21.83	31.14
4	15.735	77.0	-0.007	-0.045	0.000	4.51	83.56
5	15.348	89.6	0.018	-0.029	0.000	15.71	67.17

Table 4-19: Subjects 1 to 5- Standard deviation of ISA_A angular velocity, position, orientation and normalized time at maximum angular velocity. Position computed in the local reference frame of the shoulders, and orientation computed relative to the spine axis and the supination axis of the forearm.

Subject	ω_{max}	Percent	Position			Orientation	
						Spine	Supination
		Downswing	x	y	z	Axis	Axis
	[rad/s]	[%]	[m]	[m]	[m]	[deg]	[deg]
1	2.173	0.0	0.033	0.020	0.000	2.42	6.85
2	0.654	13.6	0.086	0.040	0.000	1.44	27.49
3	1.083	0.0	0.071	0.057	0.000	3.59	7.03
4	0.267	4.0	0.004	0.006	0.000	0.79	3.09
5	1.860	9.5	0.043	0.036	0.000	2.26	18.49

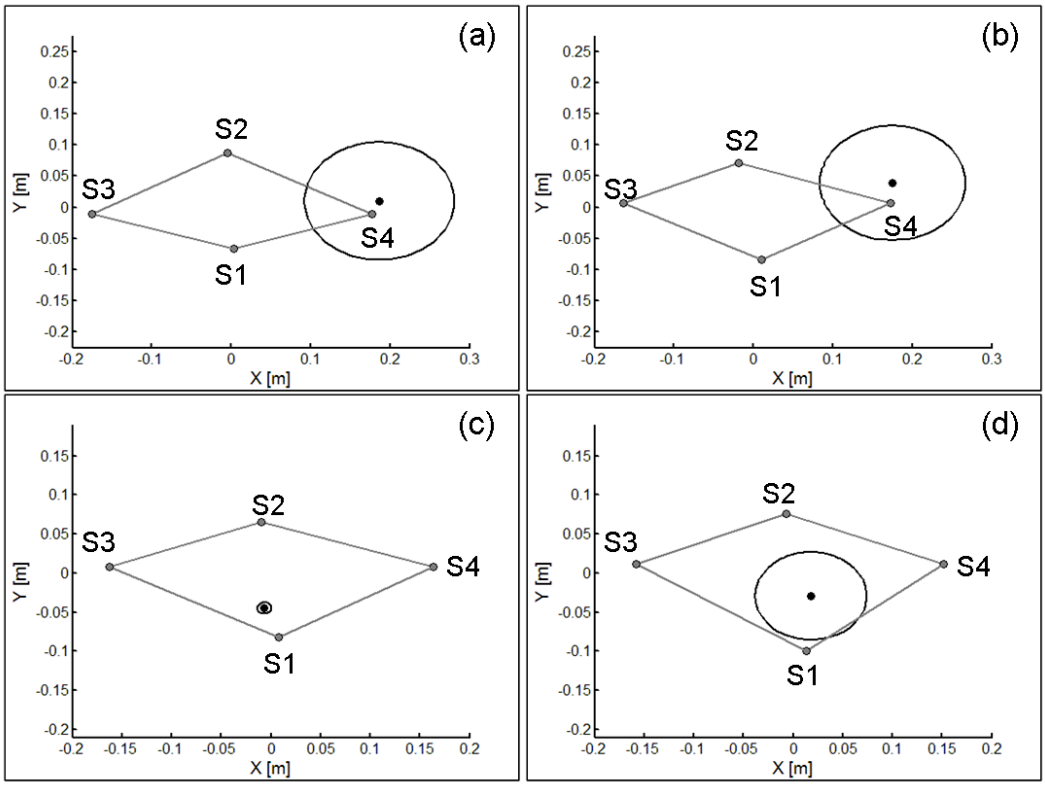

Figure 4-10: Subjects 2 to 5- Intersection of ISA_A with the xy-plane of the local coordinate frame of the shoulders. Results given as mean intersection and radius of standard deviation, r_S (computed from trials 1 to 5); (a) Subject 2 (r_S= 0.0948 m), (b) Subject 3 (r_S= 0.0910 m), (c) Subject 4(r_S= 0.0072 m), (d) Subject 5 (r_S= 0.0561 m)

ISA_C: ISA of the golf club relative to the global reference frame

Complete results of Subject 1 are shown in Table 4-20, while mean results of Subjects 1 to 5 are shown in Table 4-21, Table 4-22. Furthermore, complete results of Subjects 2 to 5 are shown in Table A4-33 to Table A4-36 in Appendix 4.

Table 4-20: Subject 1- ISA_C angular velocity, position, orientation and normalized time at maximum angular velocity. Position computed as the distance from the centroid of the wrist, and orientation computed relative to the supination axis of the forearm.

Trial	ω_{max} [rad/s]	Percent Downswing [%]	Distance [m]	Orientation [deg]
1	22.031	97.0	0.104	42.88
2	22.573	94.0	0.099	48.38
3	21.412	94.5	0.086	47.24
4	22.533	92.0	0.090	49.46
5	22.699	94.5	0.084	48.66
Mean	22.250	94.4	0.093	47.32
S	0.533	1.8	0.009	2.61

Table 4-21: Subjects 1 to 5- Mean ISA_C angular velocity, position, orientation and normalized time at maximum angular velocity. Position computed as the distance from the centroid of the wrist, and orientation computed relative to the supination axis of the forearm.

Subject	ω_{max} [rad/s]	Percent Downswing [%]	Distance [m]	Orientation [deg]
1	22.250	94.4	0.093	47.32
2	509.896	73.4	0.390	54.80
3	1037.169	73.3	0.226	59.11
4	139.438	87.2	0.447	52.17
5	33.943	74.7	0.247	64.60

Table 4-22: Subjects 1 to 5- Standard deviation of ISA_C angular velocity, position, orientation and normalized time at maximum angular velocity. Position computed as the distance from the centroid of the wrist, and orientation computed relative to the supination axis of the forearm.

Subject	ω_{max} [rad/s]	Percent Downswing [%]	Distance [m]	Orientation [deg]
1	0.533	1.8	0.009	2.61
2	339.469	10.0	0.162	4.19
3	967.627	2.6	0.575	17.83
4	88.891	8.3	0.182	13.78
5	6.591	14.2	0.084	10.16

4.3.2.2 Maximum Angular velocity about ISAr

The four variables computed at maximum angular velocity (ω_{max}, percent downswing corresponding to ω_{max}, ISA position and ISA orientation) are given for each ISAr and subject. For each ISA, complete results are given for Subject 1 and mean results are provided for all 5 subjects.

$ISAr_P$: ISA of the relative motion of the pelvis to the left leg

Complete results of Subject 1 are shown in Table 4-23 and Figure 4-11, while mean results of Subjects 1 to 5 are shown in Table 4-24, Table 4-25 and Figure 4-12. Furthermore, complete results of Subjects 2 to 5 are shown in Table A4-37 to Table A4-40 in Appendix 4. For each table of results, the corresponding ISA position plot is provided directly below it.

Table 4-23: Subject 1- $ISAr_P$ angular velocity, position, orientation and normalized time at maximum angular velocity. Position computed in the local reference frame of the pelvis, and orientation computed relative to the spine axis and axis of the left leg.

Trial	ω_{max}	Percent	Position			Orientation	
						Spine	Left Leg
		Downswing	x	y	z	Axis	Axis
	[rad/s]	[%]	[m]	[m]	[m]	[deg]	[deg]
1	4.381	73.0	0.147	0.052	0.000	15.33	23.52
2	4.495	65.0	0.158	0.040	0.000	22.37	28.24
3	3.808	70.5	0.117	0.062	0.000	8.46	24.50
4	4.630	67.5	0.148	0.040	0.000	18.35	26.51
5	4.434	60.5	0.161	0.043	0.000	18.96	25.17
Mean	4.350	67.3	0.146	0.048	0.000	16.70	25.59
S	0.317	4.9	0.017	0.010	0.000	5.24	1.84

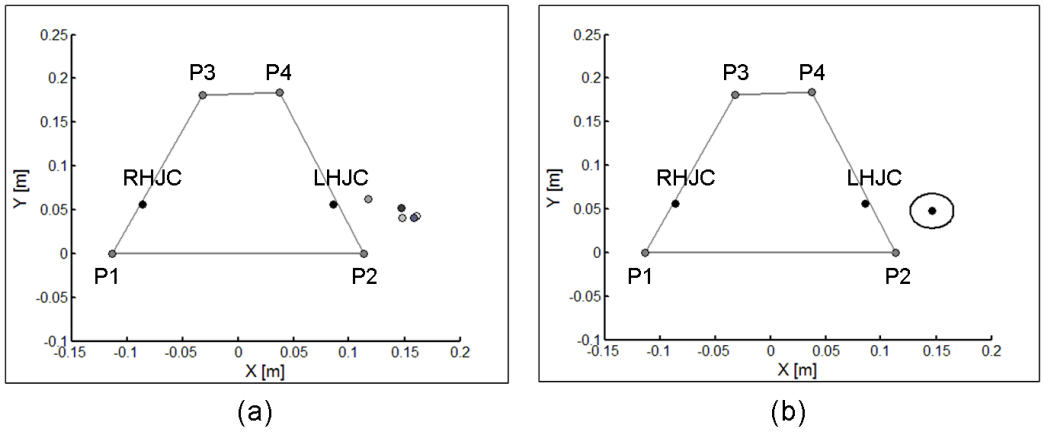

Figure 4-11: Subject 1- Intersection of $ISAr_P$ with the xy-plane of the local coordinate frame of the pelvis; (a) intersection point of trials 1 to 5, (b) mean intersection point and radius of standard deviation (r_S= 0.0197 m)

Table 4-24: Subjects 1to 5- Mean $ISAr_P$ angular velocity, position, orientation and normalized time at maximum angular velocity. Position computed in the local reference frame of the pelvis, and orientation computed relative to the spine axis and axis of the left leg.

Subject	ω_{max}	Percent	Position			Orientation	
		Downswing	x	y	z	Spine Axis	Left Leg Axis
	[rad/s]	[%]	[m]	[m]	[m]	[deg]	[deg]
1	4.350	67.3	0.146	0.048	0.000	16.70	25.59
2	5.825	77.8	-0.041	0.027	0.000	34.90	75.15
3	5.739	65.9	0.070	-0.008	0.000	17.74	56.27
4	7.840	73.5	0.069	0.047	0.000	20.05	48.21
5	6.453	87.7	-0.022	-0.051	0.000	36.94	66.51

Table 4-25: Subjects 1to 5- Standard deviation of $ISAr_P$ angular velocity, position, orientation and normalized time at maximum angular velocity. Position computed in the local reference frame of the pelvis, and orientation computed relative to the spine axis and axis of the left leg.

Subject	ω_{max}	Percent	Position			Orientation	
		Downswing	x	y	z	Spine Axis	Left Leg Axis
	[rad/s]	[%]	[m]	[m]	[m]	[deg]	[deg]
1	0.317	4.9	0.017	0.010	0.000	5.24	1.84
2	0.835	7.5	0.047	0.053	0.000	10.46	4.21
3	0.193	11.7	0.060	0.030	0.000	11.77	10.71
4	0.202	2.7	0.006	0.009	0.000	3.18	1.78
5	0.165	0.9	0.029	0.021	0.000	5.58	5.83

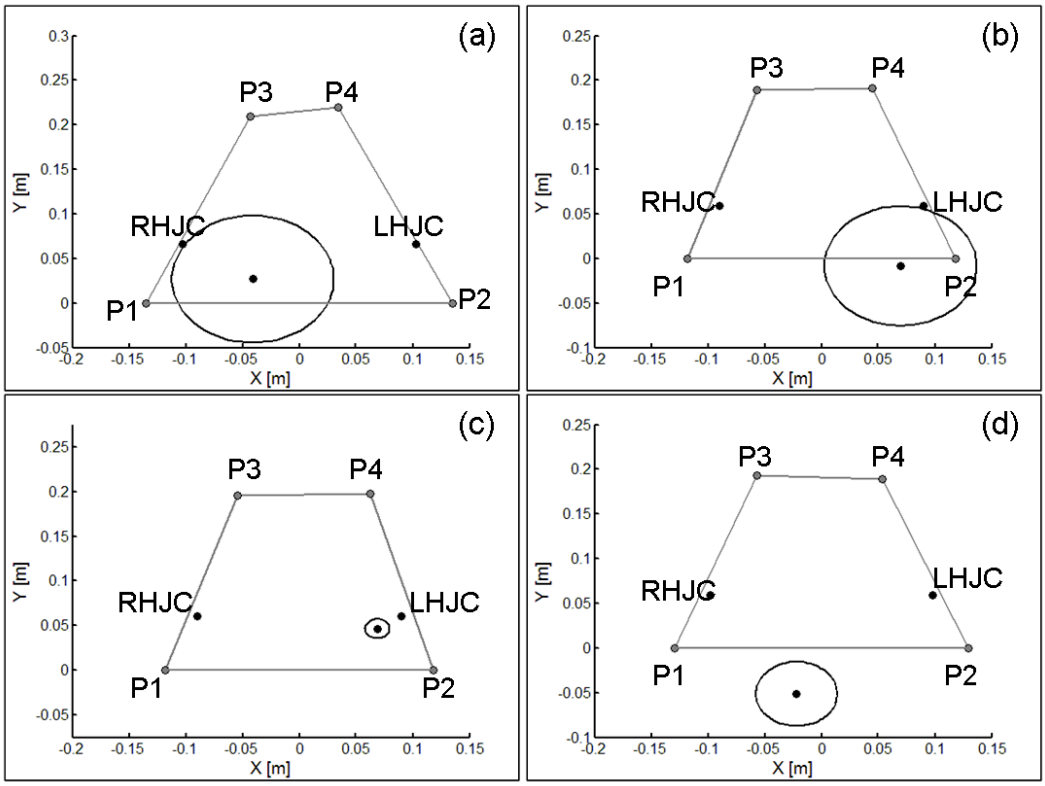

Figure 4-12: Subjects 2 to 5- Intersection of $ISAr_P$ with the xy-plane of the local coordinate frame of the pelvis. Results given as mean intersection and radius of standard deviation, r_S (computed from trials 1 to 5); (a) Subject 2 (r_S= 0.0708 m), (b) Subject 3 (r_S= 0.0671 m), (c) Subject 4(r_S= 0.0108 m), (d) Subject 5 (r_S= 0.0358 m)

$ISAr_S$: ISA of the relative motion of the shoulders to the pelvis

Complete results of Subject 1 are shown in Table 4-26 and Figure 4-13, while mean results of Subjects 1 to 5 are shown in Table 4-27, Table 4-28 and Figure 4-14. Furthermore, complete results of Subjects 2 to 5 are shown in Table A4-41 to Table A4-44 in Appendix 4. For each table of results, the corresponding ISA position plot is provided directly below it. It must be noted that mean and standard deviation values for $ISAr_S$ of Subject 4 was computed from Trials 1, 2, 3 and 5. This analysis omits Trial 4, as a discontinuity occurred that caused a shift in the percent downswing coinciding with the maximum angular velocity, as shown in Figure A4-27 of Appendix 4.

Table 4-26: Subject 1- $ISAr_S$ angular velocity, position, orientation and normalized time at maximum angular velocity. Position computed in the local reference frame of the shoulders, and orientation computed relative to the spine axis.

Trial	ω_{max}	Percent Downswing	Position			Orientation
			x	y	z	
	[rad/s]	[%]	[m]	[m]	[m]	[deg]
1	4.594	81.0	0.033	-0.141	0.000	24.42
2	4.648	100.0	-0.019	-0.014	0.000	18.68
3	4.377	100.0	-0.045	-0.074	0.000	29.88
4	3.486	100.0	-0.012	-0.091	0.000	20.48
5	4.667	77.5	0.038	-0.140	0.000	24.85
Mean	4.354	91.7	-0.001	-0.092	0.000	23.66
S	0.499	11.4	0.035	0.053	0.000	4.35

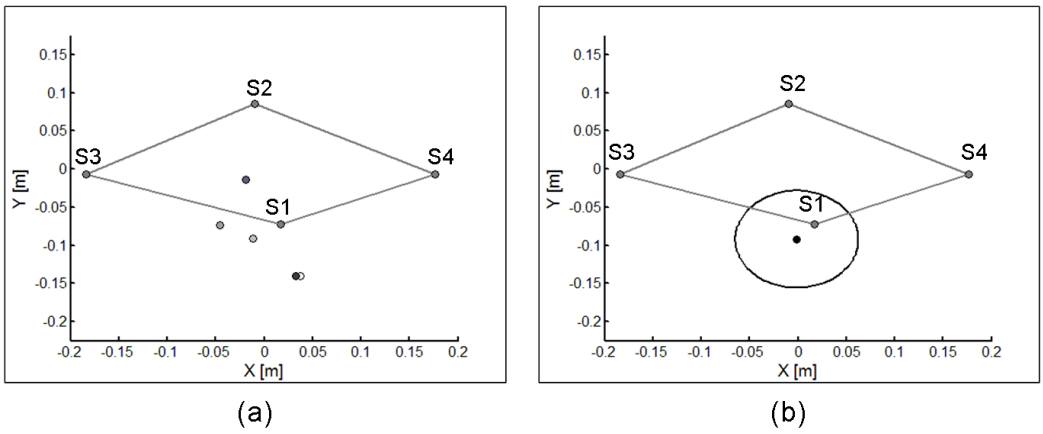

Figure 4-13: Subject 1- Intersection of $ISAr_S$ with the xy-plane of the local coordinate frame of the shoulders; (a) intersection point of trials 1 to 5, (b) mean intersection point and radius of standard deviation (r_S= 0.0635 m)

Table 4-27: Subjects 1 to 5- Mean $ISAr_S$ angular velocity, position, orientation and normalized time at maximum angular velocity. Position computed in the local reference frame of the shoulders, and orientation computed relative to the spine axis.

Subject	ω_{max}	Percent Downswing	Position			Orientation
			x	y	z	
	[rad/s]	[%]	[m]	[m]	[m]	[deg]
1	4.354	91.7	-0.001	-0.092	0.000	23.66
2	4.304	58.7	0.032	-0.174	0.000	36.39
3	6.559	60.8	0.268	-0.153	0.000	48.47
4	5.586	79.9	0.024	-0.072	0.000	25.43
5	4.885	58.5	0.099	-0.169	0.000	31.93

Table 4-28: Subjects 1 to 5- Standard deviation of $ISAr_S$ angular velocity, position, orientation and normalized time at maximum angular velocity. Position computed in the local reference frame of the shoulders, and orientation computed relative to the spine axis.

Subject	ω_{max}	Percent Downswing	Position			Orientation
			x	y	z	
	[rad/s]	[%]	[m]	[m]	[m]	[deg]
1	0.499	11.4	0.035	0.053	0.000	4.35
2	0.394	3.9	0.010	0.045	0.000	3.53
3	0.634	2.6	0.037	0.056	0.000	1.80
4	1.076	16.6	0.068	0.023	0.000	6.27
5	0.083	0.8	0.032	0.043	0.000	5.96

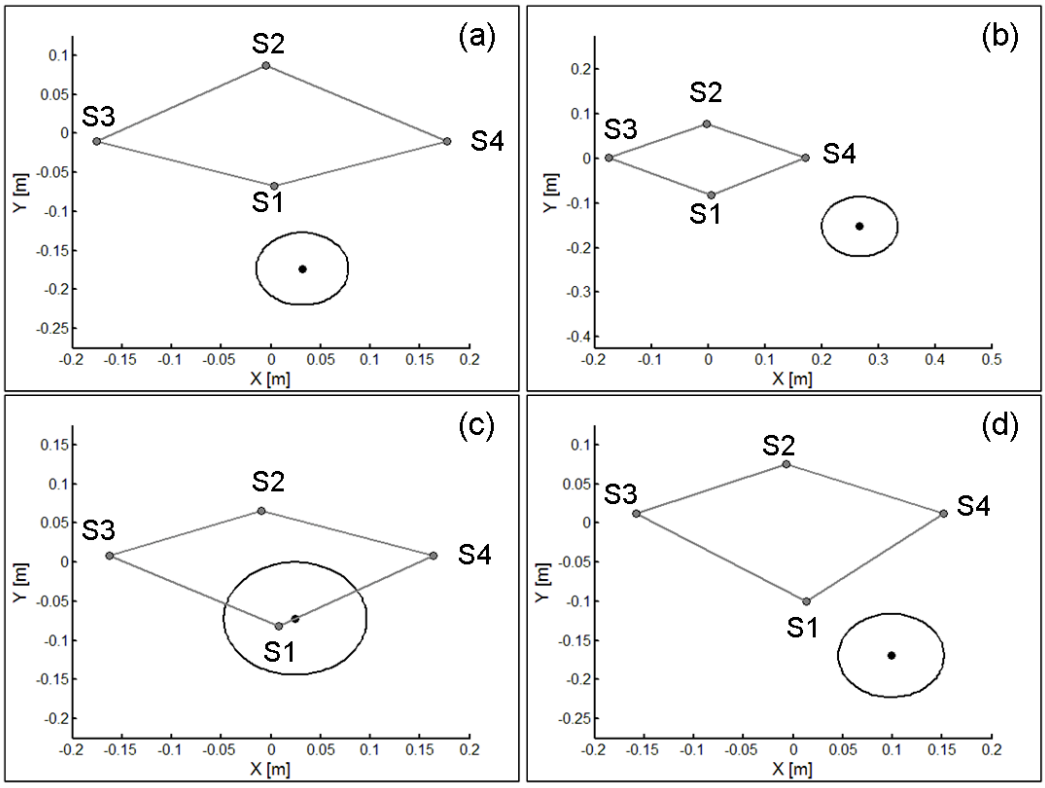

Figure 4-14: Subjects 2 to 5- Intersection of $ISAr_S$ with the xy-plane of the local coordinate frame of the shoulders. Results given as mean intersection and radius of standard deviation, r_S (computed from trials 1 to 5); (a) Subject 2 (r_S= 0.0461 m), (b) Subject 3 (r_S= 0.0672 m), (c) Subject 4(r_S= 0.0718 m), (d) Subject 5 (r_S= 0.0536 m)

$ISAr_A$: ISA of the relative motion of the arm to the shoulders

Complete results of Subject 1 are shown in Table 4-29 and Figure 4-15, while mean results of Subjects 1 to 5 are shown in Table 4-30, Table 4-31 and Figure

4-16. Furthermore, complete results of Subjects 2 to 5 are shown in Table A4-45 to Table A4-48 in Appendix 4. For each table of results, the corresponding ISA position plot is provided directly below it.

Table 4-29: Subject 1- $ISAr_A$ angular velocity, position, orientation and normalized time at maximum angular velocity. Position computed in the local reference frame of the shoulders, and orientation computed relative to the spine axis and the supination axis of the forearm.

Trial	ω_{max}	Percent	Position			Orientation	
		Downswing	x	y	z	Spine Axis	Supination Axis
	[rad/s]	[%]	[m]	[m]	[m]	[deg]	[deg]
1	6.604	100.0	0.178	-0.029	0.000	17.61	30.75
2	10.087	100.0	0.338	0.200	0.000	18.68	9.89
3	5.242	89.0	0.140	-0.058	0.000	30.20	52.28
4	6.081	100.0	0.050	-0.071	0.000	20.48	46.01
5	7.596	95.0	0.209	-0.011	0.000	14.22	30.71
Mean	7.122	96.8	0.183	0.006	0.000	20.24	33.93
S	1.864	4.9	0.105	0.111	0.000	6.02	16.44

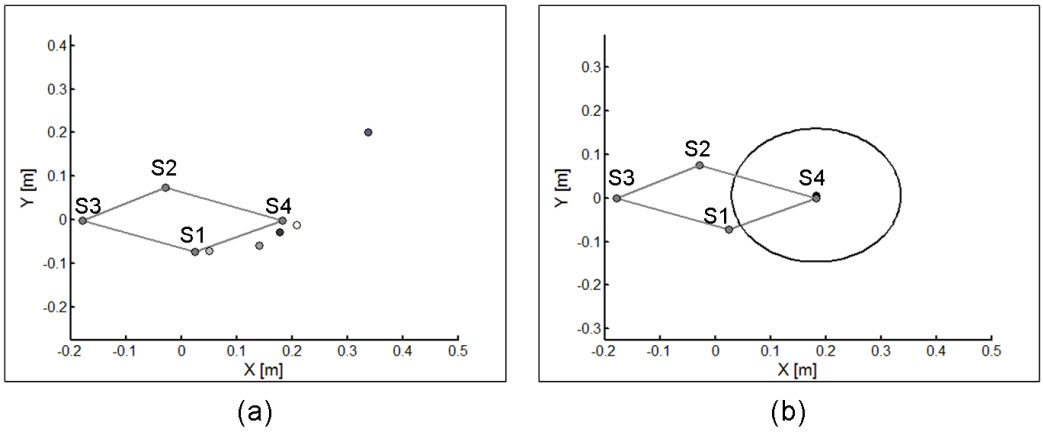

Figure 4-15: Subject 1- Intersection of $ISAr_A$ with the xy-plane of the local coordinate frame of the shoulders; (a) intersection point of trials 1 to 5, (b) mean intersection point and radius of standard deviation (r_S= 0.1528 m)

Table 4-30: Subjects 1 to 5- Mean $ISAr_A$ angular velocity, position, orientation and normalized time at maximum angular velocity. Position computed in the local reference frame of the shoulders, and orientation computed relative to the spine axis and the supination axis of the forearm.

Subject	ω_{max}	Percent	Position			Orientation	
		Downswing	x	y	z	Spine Axis	Supination Axis
	[rad/s]	[%]	[m]	[m]	[m]	[deg]	[deg]
1	7.122	96.8	0.183	0.006	0.000	20.24	33.93
2	15.216	100.0	1.141	0.626	0.000	29.76	12.94
3	19.579	100.0	1.413	1.415	0.000	12.77	9.66
4	9.834	99.8	1.009	0.321	0.000	27.66	22.36
5	9.256	96.6	0.415	0.115	0.000	46.07	31.98

Table 4-31: Subjects 1 to 5- Standard deviation of $ISAr_A$ angular velocity, position, orientation and normalized time at maximum angular velocity. Position computed in the local reference frame of the shoulders, and orientation computed relative to the spine axis and the supination axis of the forearm.

Subject	ω_{max}	Percent	Position			Orientation	
		Downswing	x	y	z	Spine Axis	Supination Axis
	[rad/s]	[%]	[m]	[m]	[m]	[deg]	[deg]
1	1.864	4.9	0.105	0.111	0.000	6.02	16.44
2	1.138	0.0	0.351	0.262	0.000	11.12	2.39
3	1.439	0.0	0.626	0.874	0.000	10.43	2.75
4	0.638	0.4	4.714	1.789	0.000	7.27	7.33
5	2.989	5.1	0.163	0.118	0.000	4.20	20.30

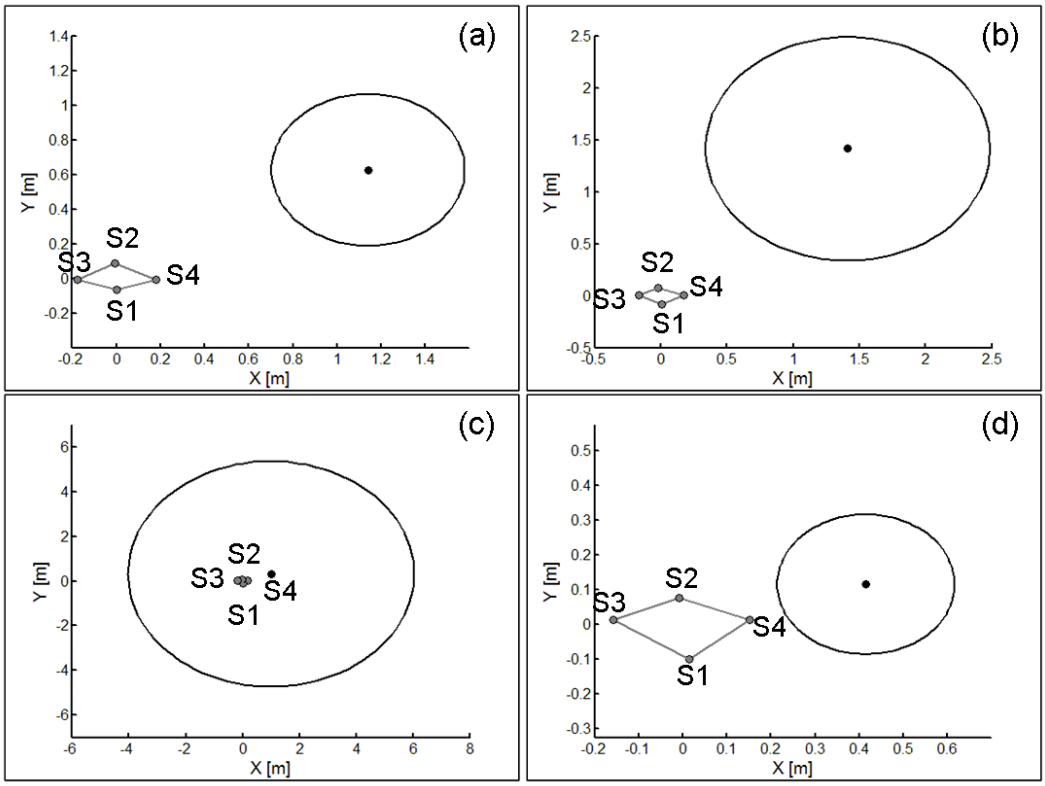

Figure 4-16: Subject 2 to 5- Intersection of $ISAr_A$ with the xy-plane of the local coordinate frame of the shoulders. Results given as mean intersection and radius of standard deviation, r_S (computed from trials 1 to 5); (a) Subject 2 (r_S= 0.4380 m), (b) Subject 3 (r_S= 1.0751 m), (c) Subject 4(r_S= 5.0420 m), (d) Subject 5 (r_S= 0.2012 m)

$ISAr_C$: ISA of the relative motion of the golf club relative to the left arm

Complete results of Subject 1 are shown in Table 4-32, while mean results of Subjects 1 to 5 are shown in Table 4-33 and Table 4-34. Furthermore, complete results of Subjects 2 to 5 are shown in Table A4-49 to Table A4-52 in Appendix 4.

Table 4-32: Subject 1-ISAr$_C$ angular velocity, position, orientation and normalized time at maximum angular velocity. Position computed as the distance from the centroid of the wrist, and orientation computed relative to the supination axis of the forearm.

Trial	ω_{max} [rad/s]	Percent Downswing [%]	Distance [m]	Orientation [deg]
1	9.602	99.0	0.049	29.85
2	6.223	84.5	0.152	73.25
3	87.630	100.0	0.537	61.55
4	14.798	94.5	0.296	55.11
5	56.649	94.5	0.626	60.31
Mean	34.980	94.5	0.332	56.01
S	35.777	6.1	0.246	16.06

Table 4-33: Subjects 1to 5- Mean ISAr$_C$ angular velocity, position, orientation and normalized time at maximum angular velocity. Position computed as the distance from the centroid of the wrist, and orientation computed relative to the supination axis of the forearm.

Subject	ω_{max} [rad/s]	Percent Downswing [%]	Distance [m]	Orientation [deg]
1	34.980	94.5	0.332	56.01
2	362.160	92.9	0.461	49.15
3	644.642	88.0	0.470	56.66
4	68.143	88.7	0.291	53.07
5	41.585	82.2	0.485	46.45

Table 4-34: Subjects 1 to 5- Standard deviation of ISAr$_C$ angular velocity, position, orientation and normalized time at maximum angular velocity. Position computed as the distance from the centroid of the wrist, and orientation computed relative to the supination axis of the forearm.

Subject	ω_{max} [rad/s]	Percent Downswing [%]	Distance [m]	Orientation [deg]
1	35.777	6.1	0.246	16.06
2	154.662	2.6	0.039	3.29
3	360.267	9.4	0.109	14.58
4	47.319	17.6	0.296	20.56
5	40.332	10.0	0.182	7.29

4.3.3 Golf Club Head Velocity

The velocity of the golf club head was determined from the displacement of marker C4, affixed to the golf club head (see Section 3.4). This velocity provides a quantifiable measure of the end result of the downswing sequence, and a comparison point between subjects. Averaged club head velocity of Subjects 1 to 5 is shown in Table 4-35. Furthermore, complete results of Subjects 1 to 5 are shown in Table A4-53 of Appendix 4.

Table 4-35: Subjects 1to 5- Mean and standard deviation (S) of golf club head velocity at impact. Results computed from the 5 trials of each subject.

Subject	Club Head Velocity	
	Mean [m/s]	S [m/s]
1	26.236	0.883
2	33.363	0.393
3	34.500	0.800
4	33.980	0.280
5	31.969	0.478

Chapter 5 Discussion

The following chapter discusses the golf swing model results presented in Chapter 4, and is divided into 4 sections. The first section, Applied Error in Marker Displacement, discusses the amount of error introduced on marker position, from the applied error compensation techniques, and on marker velocity, from relative ISA computation. The second section, Marker Velocity about ISA and ISAr, examines the component of marker velocity about each segment of the golf swing model. The third section, ISA Angular Velocity, discusses the magnitude of angular velocity about each segment's ISA, the ISA relative to the global reference frame, and ISAr, the ISA computed from the relative motion between two physiologically linked segments.

5.1 Applied Error on Marker Displacement

The error compensation techniques introduced in Sections 3.3.3 and 3.3.4 produce marker displacement consistent with rigid body motion from stereophotogrammetric measurements. While these methodologies allow rigid body kinematics to be conducted, they introduce error on the measured marker displacements. Furthermore, error between measured marker velocity, from numerical differentiation of measured displacement, and velocity from movement about a relative ISA is also present. Marker velocity error results from the assumption that physiologically linked segments are rigidly connected.

The amount of error introduced on marker position, from error compensation techniques, and marker velocity, from relative ISA computation, was shown in Section 4.1.1. As the extent of error introduced during analysis has been measured, it can now be compared to known sources of marker displacement error.

5.1.1 RMSE on Marker Position

The RMSE computed between measured and computed marker displacements of the three markers used in ISA computation, for each segment, is shown in Table 4-2. When averaging the results over the 5 subjects, the RMSE introduced on marker positions varied from 1.09 mm to 9.24 mm. For all subjects, the minimum RMSE was measured for left leg markers, ranging from 0.73mm (Subject 1) to 1.39mm (Subject 3). Conversely, the maximum RMSE for all subjects was measured for markers placed on the shoulders, ranging from 5.47mm (Subject 2) to 14.49mm (Subject 3). This last value, of 14.49mm, represents the largest mean RMSE introduced on the marker displacements of a given segment. The measured and solidified displacements of marker S4 used in ISA computation of the shoulders are shown in Figure 5-1, to illustrate the maximum error introduced on marker displacement. The shoulder displacement shown is from Trial 3 of Subject 3, which produced the highest RMSE of all measured trials.

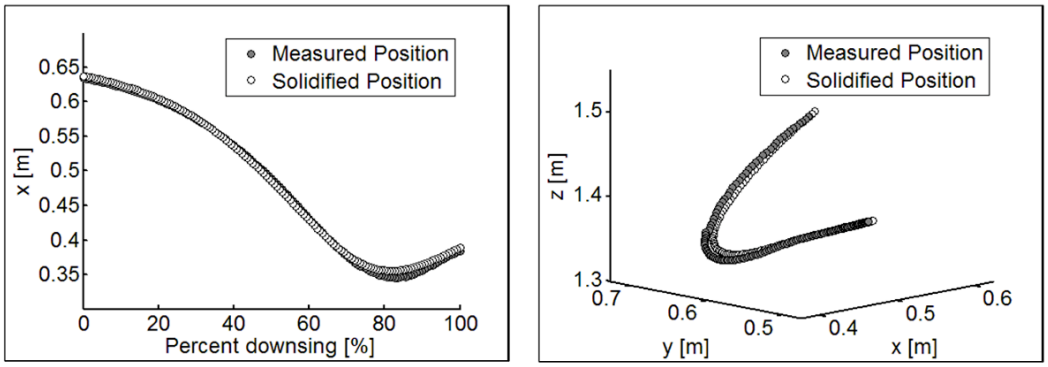

Figure 5-1: Measured and solidified displacement of marker S4 used in ISA computation; (a) x-component as a function of percent downswing, (b) marker trajectory

For all subjects, the minimum RMSE was measured for the three markers affixed to the left leg. At first glance this is an unexpected result, as a considerable amount of soft tissue artifact can be expected from the left thigh, which would affect the displacement of marker L3. However, of all analyzed segments, the left leg undergoes the least amount of motion during the downswing, which would

limit the extent of soft tissue artifact. Furthermore, marker L3 was affixed to a wrapped area of the left thigh, using hypoallergenic surgical tape, which may have further reduced the extent of soft tissue artifact. Conversely, the maximum RMSE was measured on the position of markers affixed to the shoulders, which was consistent for all subjects. This was an expected result, as the 4 markers chosen to measure the displacement of the shoulders do not belong to a single rigid segment. The markers placed on the jugular notch and C7 vertebra, S1 and S2 respectively, form the left or right shoulder girdle when paired with the marker placed on the left (S3) or right (S4) acromion, respectively. Each shoulder girdle is comprised of the right or left clavicle and the corresponding scapula [Moore and Dalley (2006)], where these two rigid segments are connected by the acromioclavicular joint and the entire complex is free to move about the sternoclavicular joint [Moore and Dalley (2006)]. Each shoulder girdle is a combination of two rigid segments, where relative motion between segments is possible. Therefore, the displacements of any combination of three markers affixed to the shoulders may include large relative displacements resulting from non-rigidity from either or both shoulder girdles. This explains why RMSE was highest for marker displacements of the shoulders, as the solidification procedure must eliminate these relative displacements.

The maximum RMSE between measured and computed marker displacements was 14.49 mm, the mean value for displacements of the shoulder for Subject 3. Although this RMSE is more than double the error measured for any other analyzed segment, its magnitude is inferior to the two sources of error coming from the interface between the marker and the underlying bone structure: marker placement error [Della Croce et al. (2005)] and soft tissue artifact [Leardini et al. (2005)]. As discussed in Section 3.3.1.1, Della Croce et al. [Della Croce et al. (1999)] determined that inter-examiner variability caused a RMSE of 21.18 mm in the position of pelvic markers, when averaging the results over markers P1 to P4. Furthermore, many authors have quantified the amplitude of soft tissue artifact of the lower limbs [Leardini et al. (2005)], as described in Section 2.3.2.3.

The amplitude of soft tissue artifact has produced translational errors of up to 40 mm have been measured in the thigh [Cappozzo et al. (1996)], while others have measured RMSE from 16.8mm to 17.1mm for the lateral and medial regions of the thigh, respectively [Sati et al. (1996)]. This indicates that the RMSE introduced on marker position, from the application of the error compensation techniques of Sections 3.3.3 and 3.3.4, is within the uncertainty measure of stereophotogrammetric measurements.

5.1.2 RMSE on Marker Velocity

To quantify the error introduced from the assumption of rigidly connected segments in relative ISA computation and from instances approaching an undefined ISA, RMSE between measured marker velocity and marker velocity computed from the motion about a relative ISA was calculated.

5.1.2.1 RMSE on Marker Velocity about ISA

The RMSE computed between measured and computed marker velocity of the three markers used in ISA computation, for each segment, is shown in Table 4-4. When averaging the results over the 5 subjects, the RMSE introduced on marker velocity varied from 0.00229 m/s, for ISA_L computation, to 2.40120 m/s, for ISA_C computation. For four subjects, other than Subject 1, the minimum RMSE was measured for the computation of ISA_L, which for all subjects ranged from 0.00069 m/s (Subject 1) to 0.00404 m/s (Subject 5). For all subjects, the maximum RMSE was measured for the computation of ISA_C, ranging from 0.04544 m/s (Subject 1) to 6.92356 m/s (Sub 3). In order to represent these errors on a relative scale, the velocity RMSE values were divided by mean marker velocity, of the three markers used in ISA computation, and expressed in percent. These results are labeled percent mean velocity and are shown in Table 5-1.

Table 5-1: Percent mean velocity, computed as the ratio of velocity RMSE and mean marker velocity. Mean marker velocity was calculated as the mean velocity of the three markers used in ISA computation.

Subject	Percent Mean Velocity				
	ISA_L [%]	ISA_P [%]	ISA_S [%]	ISA_A [%]	ISA_C [%]
1	0.120	0.137	0.399	0.333	0.880
2	0.224	0.504	1.050	0.830	54.531
3	0.300	1.097	0.664	1.123	107.401
4	0.253	0.563	1.526	0.528	14.661
5	0.363	0.671	0.447	0.434	3.940
Mean	0.252	0.594	0.817	0.650	36.283

When averaging the results over the 5 subjects, the percent mean velocity varies from 0.252 percent, for ISA_L computation, to 36.283 percent, for ISA_C computation. For ISA computation of the leg, pelvis, shoulders and left arm, the percent mean velocity error is less than 5 percent for all subjects. This indicates that the RMSE introduced from ISA_L, ISA_P, ISA_S and ISA_A computation is negligible. However, the error introduced by ISA_C computation is not negligible, ranging from small values of 0.880 percent and 3.940 percent, for Subjects 1 and 5, to 14.661 percent to 107.401 percent, for Subjects 3 and 4. The computation of ISA_C displayed a number of discontinuities, where the magnitude of angular velocity about ISA_C was not continuous throughout the downswing. This becomes apparent when plotting the angular velocity as a function of percent downswing, which was presented in Section 4.2.1. Although this was not the case for all subjects, as the data of Subjects 1 and 5 did not display any discontinuities, the discontinuities encountered in the data of Subject 2, 3 and 4 are thought to originate from instances approaching an undefined ISA, as discussed in Section 3.2.2. This became apparent as the computation of ISA_C, for instances where discontinuities occurred, was sensitive to the diagnostic constants $ISA_{Diagnostic\ 2}$ and $ISA_{Diagnostic\ 3}$, which were discussed in Section 3.2.2. The velocity profile of marker C1 of the golf club is shown in Figure 5-2, from numerical differentiation (measured) and movement about ISA_C (computed). This indicates that the RMSE

introduced from ISA_C computation considerably affects the velocity of marker C1 and does not fully represent its displacement.

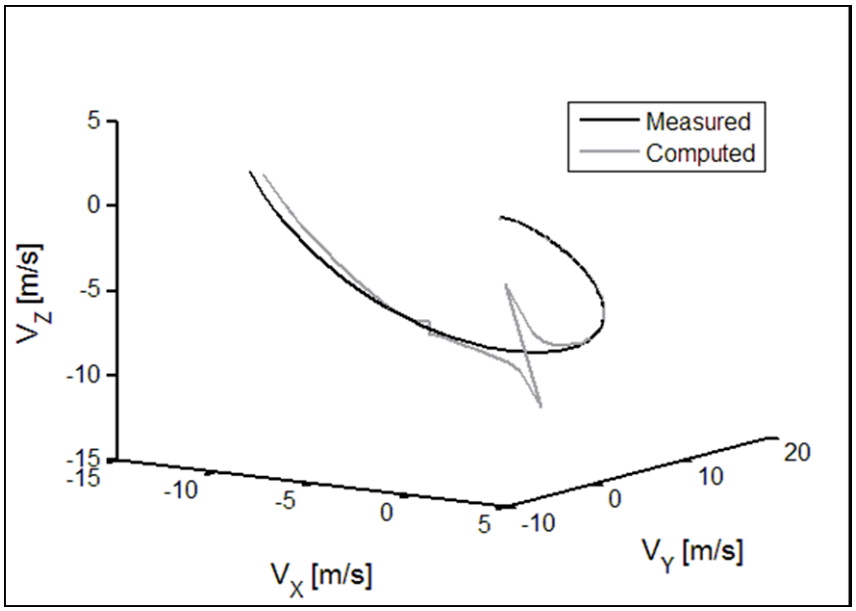

Figure 5-2: Subject 2- Velocity Trajectory of marker C1 of the golf club. Measured marker velocity, from numerical differentiation, and Computed marker velocity from motion about ISA_C.

This said, complete analysis of ISA_C was still conducted and is shown in Section 4.3.2. However, it is important to consider that these computations are not free of computational error, and will therefore be discussed accordingly.

5.1.2.2 RMSE on Marker Velocity about ISAr

The RMSE computed between measured and computed marker velocity of the three markers used in ISAr computation is shown in Table 4-6. When averaging the results over the 5 subjects, the RMSE introduced on relative marker velocity varied from 0.01028 m/s, for $ISAr_P$ computation, to 0.91145 m/s, for $ISAr_C$ computation. For all subjects, the minimum RMSE was measured for the computation of $ISAr_P$, ranging from 0.00103 m/s (Subject 1) to 0.01871 m/s (Subject 4). This was an expected result as the left leg and pelvis form the most rigid connection between two segments analyzed in the golf swing model. Furthermore, these two segments had the smallest RMSE introduced on marker

position, limiting spurious relative motions between them. Conversely, the maximum RMSE for all subjects was measured for the computation of $ISAr_C$, ranging from 0.09800 m/s (Subject 1) to 2.13647 m/s (Subject 2). In order to represent these errors on a relative scale, the velocity RMSE values were divided by mean relative marker velocity, of the three markers used in ISAr computation, and expressed in percent. These results are labeled percent mean relative velocity and are shown in Table 5-2.

Table 5-2: Percent mean relative velocity, computed as the ratio of velocity RMSE and mean relative marker velocity. Mean relative marker velocity was calculated as the mean velocity of the three markers, used in ISAr computation, relative to the preceding segment.

Subject	Percent Mean Relative Velocity			
	$ISAr_P$ [%]	$ISAr_S$ [%]	$ISAr_A$ [%]	$ISAr_C$ [%]
1	0.237	0.751	0.770	8.395
2	1.681	2.219	3.335	55.082
3	1.795	1.824	2.343	96.999
4	1.856	3.860	2.237	20.517
5	0.579	0.656	2.485	17.233
Mean	1.230	1.862	2.234	39.645

When averaging the results over the 5 subjects, the percent mean relative velocity varied from 1.230 percent, for $ISAr_P$ computation, to 39.645 percent, for $ISAr_C$ computation. For ISAr computation of the pelvis, shoulders and left arm, the percent mean relative velocity error is less than 5 percent for all subjects. This indicates that the RMSE introduced from $ISAr_P$, $ISAr_S$ and $ISAr_A$ computation is negligible. However, the error introduced by $ISAr_C$ computation ranged from values of 8.395 percent and 17.233 percent, for Subjects 1 and 5, to 55.082 percent to 96.999 percent, for Subjects 2 and 3. It is believed that this RMSE on relative marker velocity draws from two sources: discontinuities in $ISAr_C$ computation and non-rigidity between the left arm and golf club. As was the case with ISA_C computation, the computation of $ISAr_C$ displayed a number of discontinuities, where the magnitude of angular velocity about $ISAr_C$ was not continuous throughout the downswing. These discontinuities are thought to originate from instances approaching an undefined ISA, as the computation of

ISArC was also sensitive to the diagnostic constants $ISA_{Diagnostic\ 2}$ and $ISA_{Diagnostic\ 3}$, discussed in Section 3.2.2. Furthermore, any non-rigidity between the left-arm and the golf club would manifest itself as error between the measured and computed relative marker velocities. Therefore, another possible source of error explaining the high RMSE associated with $ISAr_C$ may have been non-rigidity between the two segments, as movement at the golf club grip (interface between the hands and golf club) is possible. The relative marker velocity profile of marker C1 of the golf club is shown in Figure 5-3, from numerical differentiation (measured) and movement about $ISAr_C$ (computed). This indicates that the RMSE introduced from $ISAr_C$ computation considerably affects the velocity of marker C1 and does not fully represent its displacement.

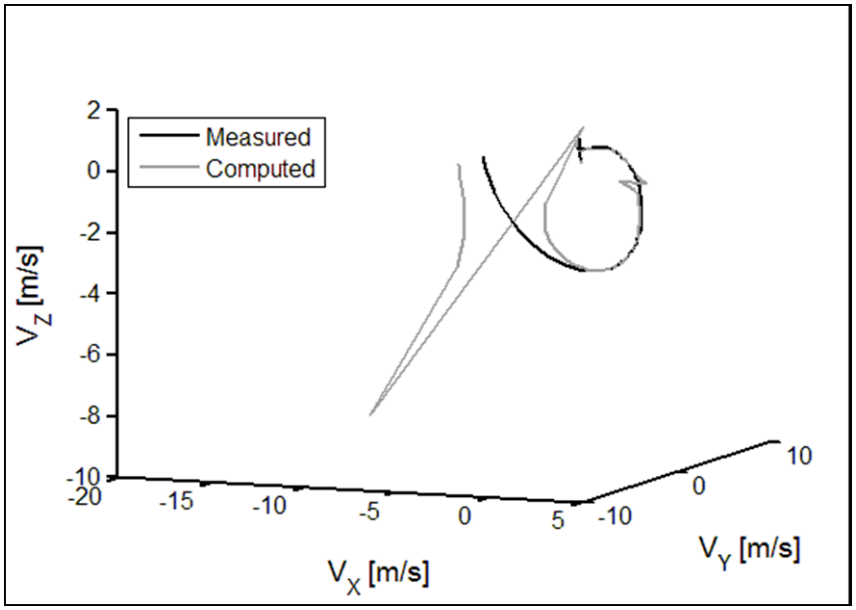

Figure 5-3: Subject 2- Velocity Trajectory of marker C1 of the golf club. Measured marker velocity, from numerical differentiation, and Computed marker velocity from motion about $ISAr_C$.

This being said, complete analysis of $ISAr_C$ was still conducted and is shown in Section 4.3.2. However, as was the case for ISA_C results, it is important to consider that these computations are not free of computational error, and will therefore be discussed accordingly.

5.2 Marker Velocity about ISA and ISAr

When the displacement of a rigid body is expressed in terms of an ISA, marker displacement is divided into two components: parallel velocity, from translation along the ISA, and perpendicular velocity, from a rotation on ISA direction [Eberharter and Ravani (2006)]. The golf swing model assumes that the magnitude of the perpendicular component of marker velocity will far exceed the parallel component of marker velocity and therefore the majority of marker displacement is through a rotation about ISA (see Section 3.4). To verify this assumption, the magnitude of parallel marker velocity was compared to the magnitude of total marker velocity by way of a velocity ratio, as shown in Section 4.2.

5.2.1 Marker Velocity Ratio about ISA

The velocity ratio was computed between parallel and total marker velocity, relative to the global reference frame, of the markers used in the computation of the five ISA of the golf swing model. These results were averaged for the five trials of each subject and are shown in Table 4-8. When averaging the results for the 5 subjects, the velocity ratio for ISA_L indicates that the parallel velocity, along the ISA, constitutes 35 percent of the total velocity of marker affixed to the left leg. This is not unexpected, as the motion of the left leg is not a pure rotation, but rather a combination of flexion/extension and internal/external rotation about the left knee joint [Gatt et al. (1998)], producing a combination of rotation and translation. As for the body segments of interest, the velocity ratios computed from ISA_P, ISA_S and ISA_A were 18.9 percent, 13.1 percent and 13.5 percent, respectively. The results indicate that for all subjects and for the three ISA of interest, at least 73 percent of marker velocity is a result of rotation about their respective ISA. This confirms that for motion about ISA_P, ISA_S and ISA_A, motion is primarily rotational and supports the assumption of the golf swing model. As for the motion of the golf club, the velocity ratio associated with ISA_C was 14.0 percent, ranging from 2 percent to 22.6 percent. This indicates that motion about

ISA_C is also primarily rotation, however is it difficult to determine the effect, if any, of the discontinuities in the computation of ISA_C on the velocity ratio.

5.2.2 Marker Velocity Ratio about ISAr

The velocity ratio was computed between parallel and total marker velocity, relative to the preceding segment, of the markers used in the computation of the four ISAr of the golf swing model. These results were averaged for the five trials of each subject and are shown in Table 4-10. When averaging the results for the 5 subjects, the velocity ratios computed from $ISAr_P$, $ISAr_S$ and $ISAr_A$ were 15.0 percent, 17.3 percent and 14.1 percent, respectively. The results indicate that for all subjects and for the three ISAr of interest, at least 75 percent of marker velocity is a result of rotation about their respective ISAr. As was the case above, this confirms that for motion about $ISAr_P$, $ISAr_S$ and $ISAr_A$, motion is primarily rotational and supports the assumption of the golf swing model. This assumption does not hold for motion about $ISAr_C$, as the velocity ratio associated with $ISAr_C$ was 42.8 percent, ranging from 22 percent to 58.5 percent for all subjects. This indicates that motion about $ISAr_C$ varies from primarily rotational to an equal combination of translation and rotation. Therefore, a study solely based on the angular velocity about $ISAr_C$ does not appropriately assess the relative motion of that segment. Furthermore, it is again difficult to determine the effect, if any, of the computation discontinuities in the velocity ratio of $ISAr_C$.

5.3 ISA Angular Velocity

The kinematic sequence of the golf swing was studied as a chain of ISAs, where the angular velocity of each segment relative to their respective ISA was measured. The angular velocity of each segment provides insight into the sequence of rotations that constitutes the golf swing, and is discussed in the following section.

5.3.1 Time Varying Angular Velocity

The magnitude of the angular velocity of each analyzed segment, about their respective ISA, was determined as a function of percent downswing. The results were divided into two sections: angular velocity about ISA, where total segment displacement was expressed relative to the global reference frame, and angular velocity about ISAr, were relative segment displacement was expressed as a relative ISA. As the computation of ISA_C and $ISAr_C$ displayed a number of discontinuities, plotting the angular velocity as a function of percent downswing did not provide insight into the magnitude of angular velocity and will therefore not be discussed in this section.

5.3.1.1 Angular Velocity about ISA

The magnitude of the angular velocity about each ISA, computed relative to the global reference frame, was plotted as a function of percent downswing. Three characteristics are used to compare the angular velocity of the five subjects: profile of the angular velocity curve, relative magnitude and sequence of maximum angular velocity between segments.

Profile of Angular Velocity

For Subjects 1, 2, 3 and 4, the angular velocities about ISA_P and ISA_S, as a function of percent downswing, appear as near bell curves. The slope remains positive until their respective maximum is reached, after which the slope becomes negative and angular velocity decreases. As for Subject 5, the profile of the angular velocity about ISA_P is also a near bell curve, sharing the characteristics of the other subjects, while the angular velocity about ISA_S increased up to a maximum value and was nearly maintained until impact. The near bell shaped curves experienced in all but one case of the angular velocity about ISA_P and ISA_S were expected. The rotations about the pelvis and shoulders are expected to increase steadily, until attaining a maximum value, and to decrease before impact. As the pelvis and shoulders are distal segments in the kinematic chain of the golf

swing, their angular velocities are expected to slow down before impact and in the process transmitted their momentum to the more proximal segments. The observed results are in line with the summation of speeds principle described by Bunn (1972), where the most distal segments decelerate before impact and impart their velocity to the more proximal segments. Conversely, the angular velocity about ISA_A displays more variability in profile when comparing all subjects. For Subjects 1 and 5, the angular velocity about ISA_A increases until impact, maintaining a positive slope throughout the downswing. For Subjects 2 and 3, the angular velocity about ISA_A has a near bell shape profile followed by an increase until impact, occurring at approximately 85 to 90 percent downswing. This same behavior is seen for Subject 4, although the final increase in angular velocity is smaller in amplitude compared to Subjects 2 and 3. This angular velocity profile was also shown by Cheetham et al. [Cheetham et al. (2008)] for Amateur 1, although the increase occurred after impact. The motion of the left arm is thought to have two components: rotation about the left glenohumeral joint (shoulder joint) and supination of the left wrist. To satisfy the summation of speeds principle [Bunn (1972)], it is expected that the rotation about the left shoulder decrease in velocity before impact, while wrist supination increase in velocity into impact. It is postulated that the profiles of Subjects 2, 3 and 4 show this distinction: the first portion of the curve, near bell shaped, denotes rotation about only the left shoulder joint while the second portion, increasing until impact, denotes the added contribution of wrist supination. The angle of ISA_A relative to the spine axis and supination axis, averaged for the 5 trials of Subject 2, is shown in Figure 5-4. The angle relative to the spine axis reaches approximately 10 degrees at the first maximum of the angular velocity curve, at the top of the bell shaped profile, and then undergoes a slight increase until impact. Conversely, the angle relative to the supination axis decreases after this first maximum and continues to decrease as the angular velocity begins to increase for a second instance. It should be noted that this decrease in relative angle between ISA_A and the supination axis is in large part due to the motion of the left arm, rather than purely from a change in direction in ISA_A.

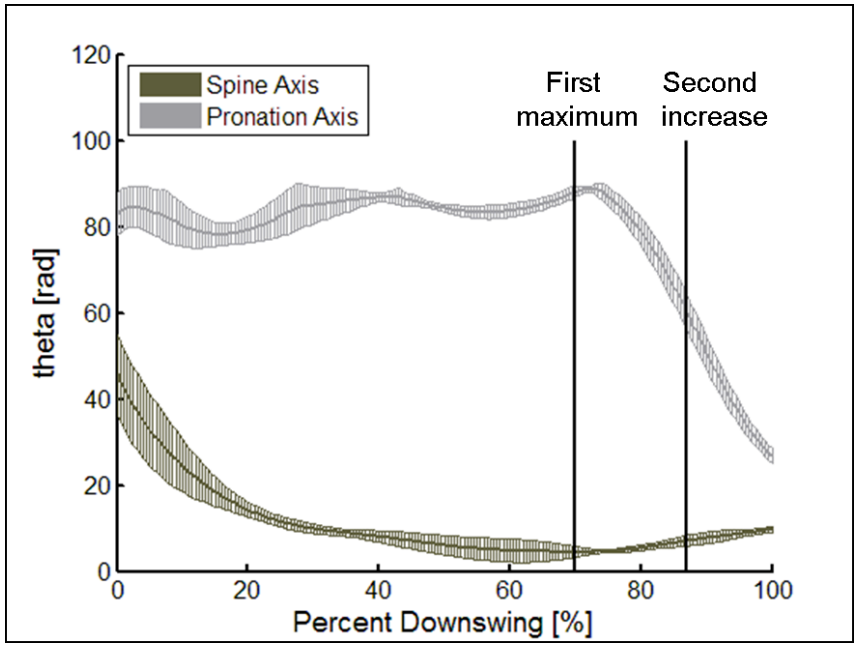

Figure 5-4: Subject 2- Relative angle of ISA_A to the spine axis and supination axis. First maximum denotes the maximum of the bell shaped portion of the angular velocity curve, while Second increase denotes the portion of the curve that undergoes a second increase later in the downswing.

Relative Magnitude and Sequence of Maximum Angular Velocities

For all subjects, the magnitude of each maximum angular velocity, ω_{max}, about each segment ISA, adheres to the following order:

$$(\omega_{\max})_{ISA_P} < (\omega_{\max})_{ISA_S} < (\omega_{\max})_{ISA_A}$$

where ω_{max} increases from the most distal segment, pelvis, to the most proximal segment, left arm. This is an expected result, as the angular velocity should increase from the most proximal segment to the most distal, as the velocity increases from the contribution of each segment in the kinematic chain. This follows the summation of speed principle [Bunn (1972)], the magnitude of segment velocity increases from proximal to distal. However, the sequence at which the maximum angular velocities occur is not the same for all subjects. For Subject 1, the sequence at which each ISA achieves its maximum angular velocities is as follows: pelvis, shoulders and left arm. This sequence shows the

desired progression from the most proximal segment, the pelvis, to the most distal segment, the left arm. Furthermore, it is consistent with the sequence computed by Cheetham et al. [Cheetham et al. (2008)] for one of the professional golfers of the study. For Subjects 3 and 4, the sequence of maximum angular velocities is similar, where proximal segments achieve their maximum before the most distal segment. However, the maximum angular velocity about the pelvis and shoulders appears to occur at approximately the same percent downswing. For Subjects 2 and 5, the sequence at which each ISA achieves its maximum angular velocities is as follows: shoulders, pelvis and left arm. Although the angular velocity about the left arm achieves its maximum the last, the angular velocity about the shoulders max out before the angular velocity about the pelvis. This does not follow the desired sequence of angular velocities, and will be discussed further in Section 5.3.2.

5.3.1.2 Angular Velocity about ISAr

The magnitude of the angular velocity about each ISAr, computed from the relative displacement between physiologically linked segments, was plotted as a function of percent downswing. As in the previous section, three characteristics are used to compare the angular velocity of the five subjects: profile of the angular velocity curve, relative magnitude and sequence of maximum angular velocity between segments.

Profile of Angular Velocity

The angular velocity curves about $ISAr_P$, for all subjects, follow two profiles. First, the curves corresponding to Subjects 1, 4 and 5 display characteristics of a bell shape. The slope remains positive until a distinct maximum is reached, after which the slope becomes negative and angular velocity decreases into impact. For Subjects 1 and 4, the increase in magnitude occurs in one step, whereas the angular velocity increases in two increments. Second, the curves corresponding to Subjects 2 and 3 are similar in nature to the curves described above; they display

characteristics of a bell shape, but maintain their maximum amplitude over a longer period, forming a near plateau. For all subjects, the following general conclusions can be drawn: angular velocity about $ISAr_P$ appears as a near bell curve and increases to a maximum occurring before impact. Therefore, the rotation purely about the pelvis achieves its maximum before impact and is transmitted to the more proximal segments.

The angular velocity about $ISAr_S$, for all subjects, also follows two profiles. First, the magnitude of angular velocity of Subjects 2, 3 and 5 displays a bell curve to a distinct maximum, followed by either an increase in magnitude occurring at 80 to 90 percent downswing, or a constant magnitude into impact. Second, the curves corresponding to Subjects 1 and 4 displayed an increase in magnitude up to 60 to 80 percent downswing, and then maintained a relatively constant magnitude to impact. For all subjects, the magnitude of angular velocity about $ISAr_S$ increased up to a maximum, occurring before impact, followed by either a decrease and corresponding increase until impact or maintained a relatively constant magnitude until impact. Therefore, like in the case of the pelvis, the rotation purely about the shoulders achieves its maximum before impact and is transmitted to the more proximal segments.

For all subjects, the magnitude of angular velocity about $ISAr_A$ increased for the duration of the downswing. Although a positive slope was not always maintained, as the magnitude assumed a plateau at some portions of the downswing, a negative slope was not observed. Furthermore, the magnitude of angular velocity increased rapidly at 80 to 90 percent downswing until impact. Therefore, rotation purely about the left arm increases throughout the downswing and reaches its maximum at impact.

It is important to note that some of the angular velocity curves display sharp, short lived, changes in magnitude which appear as small spikes. These discontinuities are thought to originate from instances approaching an undefined ISA, as they are

sensitive to the magnitude of the diagnostics of Section 3.2.2. However, unlike the case for the angular velocity about ISA_C and $ISAr_C$, these discontinuities are of small magnitude and do not exceed the maximum angular velocity of $ISAr_P$, $ISAr_S$ and $ISAr_A$ computations. One exception to this statement did occur, for the computation of $ISAr_S$ for Trial 4 of Subject 4, as the discontinuity exceeded the actual maximum angular velocity. For that single case, Trial 4 was omitted from the mean computations.

Relative Magnitude and Sequence of Maximum Angular Velocities

For all subjects, the maximum angular velocity, ω_{max}, about the left arm ISAr, $ISAr_A$, is the highest angular velocity of the kinematic chain. This is not unexpected, as the motion of the left arm includes both a rotation about the left shoulder and wrist supination, as discussed above. Furthermore, the order of magnitude of the angular velocities about $ISAr_P$ and $ISAr_S$ are not consistent from all subjects. For Subjects 1, 2 and 3, the magnitude of ω_{max} is approximately equal for angular velocities about $ISAr_P$ and $ISAr_S$, indicating that the rotation purely about the pelvis and shoulders are of similar magnitudes. For Subjects 4 and 5, ω_{max} about the $ISAr_P$ is higher than about $ISAr_S$, indicating that the rotation purely about the pelvis is higher than that about the shoulders.

For all subjects, the sequence at which the maximum angular velocities occur about each ISAr is the same as the sequence of angular velocities about each ISA. For Subject 1, the sequence at which each ISA achieves its maximum angular velocities is as follows: pelvis, shoulders and left arm. This sequence, again, follows the summation of speed principle [Bunn (1972)] as it shows the desired progression from the most proximal segment, the pelvis, to the most distal segment, the left arm. For Subjects 3 and 4, the sequence of maximum angular velocities is similar, where proximal segments achieve their maximum before the most distal segment. However, the maximum angular velocity about the pelvis and shoulders appears to occur at approximately the same percent downswing. Finally, the sequence of maximum angular velocities for Subjects 2 and 5 is as

follows: shoulders, pelvis and left arm. These results indicate that the relative movement between segments either determines or contributes to the sequence of gross segment rotations, about each ISA.

5.3.2 Instances of Maximum Angular Velocity

The kinematic sequence of the golf swing was determined by studying the angular velocity of each segment relative to their ISA. The instance where each angular velocity is at its maximum is of particular interest, as the order in which segments sequentially achieves their respective maximum yields the kinematic sequence. The following results were computed, in Section 4.3.2, at the instant were each ISA and ISAr achieved its respective maximum: magnitude of angular velocity, ω_{max}, the percent downswing corresponding to that instant, ISA position and ISA orientation. Magnitude of angular velocity, ω_{max}, given as mean angular velocity plus or minus one standard deviation.

5.3.2.1 Maximum Angular Velocity about ISA

The four variables computed at maximum angular velocity (ω_{max}, percent downswing corresponding to ω_{max}, ISA position and ISA orientation) were determined for each ISA and subject and are shown in Section 4.3.2.1. These four variables will be discussed for each corresponding ISA.

ISA_P: ISA of the pelvis relative to the global reference frame

The maximum angular velocity, ω_{max}, about ISA_P ranged from 5.719 ± 0.349 rad/s, for Subject 1, to 9.563 ± 0.336 rad/s, for Subject 4. The standard deviation on ω_{max} ranged from 0.249 rad/s, for Subject 5, to 0.465 rad/s, for Subject 2, which represents relative values of 3.4 percent and 6.6 percent relative to their corresponding ω_{max}, respectively. This reveals that the magnitude of ω_{max} is consistent within all subjects, as the standard deviation represents less than 10 percent of the mean value. The maximum angular velocities about ISA_P are

consistent with the pelvic angular velocity determined by Cheetham et al. [Cheetham et al. (2008)], who reported values of 6.89 ± 1.19 rad/s for amateurs and 8.33 ± 0.93 rad/s for professionals. Of all subjects, only the angular velocity of Subject 4 was not contained within the one standard deviation of these two means. Furthermore, the computed maximum angular velocities of the pelvis are also consistent with the results from Myers et al. [Myers et al. (2008)], who reported the maximum rate of change of a pelvis angle to be 6.241 ± 1.018 rad/s for low ball speed players and 7.568 ± 1.274 rad/s for high ball speed players. It is important to note that the results published by Myers et al. [Myers et al. (2008)] do not represent the angular velocity of the pelvis, but an approximation given by the rate of change of a two-dimensional line connecting the left and right anterior superior iliac crests (see Table 3-29 and Figure 3-38) and the line of play.

The instant corresponding to the ω_{max} of each subject varied from 68.2 ± 3.2 percent downswing, for Subject 3, to 83.7 ± 2.3 percent downswing, for Subject 5. This indicates that for all subjects the maximum angular velocity occurs in the last 2/3 of the downswing. The standard deviation of the corresponding instances ranged from 1.6 percent downswing, for Subject 1, to 3.2 percent downswing, for Subject 3. These results are slightly above those published by Cheetham al. [Cheetham et al. (2008)] for professional golfers. Although results were not explicitly given, the instance of maximum pelvis angular velocity was determined from interpolation of the given angular velocity plot, of a professional golfer, and from the given downswing duration. From these procedures, an approximate percent downswing value of 60 percent was computed, which was 8.2 percent lower than the lowest mean value computed in this study. These results indicate that the professional golfer from Cheetham et al. [Cheetham et al. (2008)] fired his hips earlier in the downswing, perhaps in an attempt to create greater separation between the pelvis and hips, as this has been shown to be one of the swing variables with the highest correlation to club head velocity [McLaughlin and Best (1994)].

For all subjects, the intersection of ISA_P with the xy-plane of the local coordinate frame of the pelvis is located near the centerline of the pelvis, corresponding to the y-axis. The largest deviation from the y-axis was measured for Subject 1 and measured 16.0 mm (x-coordinate). The y-coordinate of the intersection displays two characteristics between all subjects. For Subjects 2 and 4, the intersection is approximately in-line with the hip joint centers, while for Subjects 1, 3 and 5 the intersection is in a more posterior region of the pelvis, closer to markers P3 and P4 then to the hip joint centers. This may be a consequence of a lateral displacement of the pelvis in Subjects 1, 3 and 5. For the case of a cylinder rotating without slip, when a lateral displacement is added to the rotation about the centroidal axis of the cylinder, the ISA coincides with the line of contact between the cylinder and the surface [Page et al. (2006)]. Therefore, the ISA changes from the centroidal axis to the line of contact, resulting in a shift in ISA position perpendicular to the lateral displacement of the cylinder. In the case of the pelvis during the downswing, the lateral shift of the pelvis in the direction of play, resulting from the weight transfer from the right side of the body to the left side of the body [Burden et al. (1998)], could cause the ISA to shift from a more centered position in the pelvis (in line with the hip joint centers) to a more posterior position as seen in Subjects 1, 3 and 5.

The orientation of ISA_P was compared to two anatomical axes: the spine axis and the axis of the left leg. For all subjects, the angle relative to the spine axis varied from 8.05 degrees, for Subject 5, to 16.71 degrees, for Subject 2. This indicates that the orientation of ISA_P approaches, for all subjects, the orientation of the spine axis. The standard deviation on this angle varied from 0.89 degrees to 2.23 degrees, indicating consistency of ISA_P orientation relative to the spine axis within subjects. Furthermore, the angle relative to the left leg axis ranged from 13.16 degrees, for Subject 1, to 43.59 degrees, for Subject 2. The standard deviation on this angle varied from 1.12 degrees to 2.35 degrees. Although this result indicates, for all subjects, consistency of ISA_P orientation relative to the axis of the left leg, only Subjects 1 and 3 displayed proximity to this axis. For

these two subjects, the angles of ISA_P relative to the spine axis and relative to the axis of the left leg are within 10 degrees of each other. The difference between the two relative angles of Subject 1, relative to the spine axis and to the axis of the left leg, is 2.0 degrees, while the difference for Subject 3 is 8.84 degrees. It is hypothesized that this small difference in angles indicates that pelvic rotation for these two subjects may be a combination of rotation about the spine and rotation about the left leg. The orientation of ISA_P, as well as the orientation of the spine axis and the left leg axis are shown in Figure 5-5 for Subject 1 at the instance of maximum angular velocity about ISA_P. This shows that the orientation of ISA_P is approximately midway between the spine axis and the axis of the left leg, supporting the hypothesis of a combination of motions about these two axes.

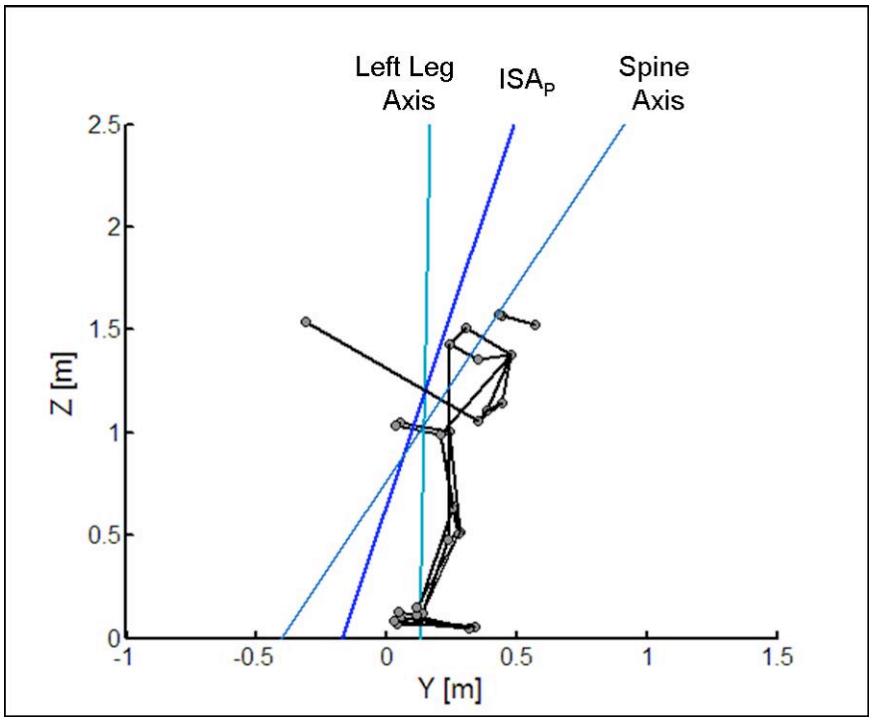

Figure 5-5: Subject 1-Rear view of the golf swing, along the negative x-axis, at percent downswing corresponding to ω_{max} about ISA_P.

ISA_S: ISA of the shoulders relative to the global reference frame

The maximum angular velocity, ω_{max}, about ISA_S ranged from 8.408 ± 0.224 rad/s, for Subject 1, to 13.514 ± 0.443 rad/s, for Subject 4. The standard deviation on ω_{max} ranged from 0.224rad/s, for Subject 1, to 0.470 rad/s, for Subject 3, which represents relative values of 2.7 percent and 4.5 percent relative to their corresponding ω_{max}, respectively. This reveals that the magnitude of ω_{max} is consistent within all subjects, as the standard deviation represents less than 5 percent of the mean value. The maximum angular velocities about ISA_S are consistent with the thorax angular velocity determined by Cheetham et al. [Cheetham et al. (2008)], who reported values of 10.18 ± 1.47 rad/s for amateurs and 12.69 ± 1.06 rad/s for professionals. Of all subjects, only the mean angular velocity of Subject 1 was not contained within the one standard deviation of these two means. Furthermore, the computed maximum angular velocities of the pelvis are also consistent with the results from Myers et al. [Myers et al. (2008)], who reported the maximum rate of change of a torso angle to be 10.318 ± 1.166 rad/s for low ball speed players and 13.380 ± 1.274 rad/s for high ball speed players. It is important to note that the results published by Myers et al. [Myers et al. (2008)] do not represent the angular velocity of the torso, but an approximation given by the rate of change of a 2 dimensional line connecting the left acromion and right acromion of the shoulders (see Table 3-29 and Figure 3-38) and the line of play.

The instant corresponding to the ω_{max} of each subject varied from 66.9 ± 2.5 percent downswing, for Subject 2, to 85.2 ± 16.1 percent downswing, for Subject 5. This indicates that for all subjects the maximum angular velocity occurs in the last 1/3 of the downswing. The standard deviation of the corresponding instances ranged from 1.7 percent downswing, for Subject 3, to 16.1 percent downswing, for Subject 5. These results approach those published by Cheetham al. [Cheetham et al. (2008)] for professional golfers. Although results were not explicitly given, the instance of maximum thorax angular velocity was determined from interpolation of the given angular velocity plot, of a professional golfer, and from the given downswing duration. From these procedures, an approximate percent

downswing value of 70 percent was computed, which is contained within the subject values of this study. The percent downswings of Subjects 2, 3 and 4 were all within 7 percent of the professional data of Cheetham et al. [Cheetham et al. (2008)], while Subjects 1 and 5 differed by 15.2 and 12.4 percent, respectively. Although Subject 1 differed by 15.2 percent, a difference of 11.8 percent was maintained between the maximum angular velocities of the pelvis and shoulders, which resembles the differential of Cheetham et al. [Cheetham et al. (2008)].

For all subjects, the intersection of ISA_S with the xy-plane of the shoulders local coordinate frame is located between the origin and the right acromion, marker S3 (see Section 3.4). This shift from the y-axis varied from 18 ± 3 mm, for Subject 2, and 63 ± 34 mm, for Subject 5. The y-coordinate of the intersection displayed similar characteristics for all subjects: either assumed a small value and was nearly aligned with the x-axis, as Subject 1, or assumed a negative value and was located in the anterior portion of the shoulders, as Subjects 2, 3, 4 and 5. For Subject 1, the y-coordinate measured 3 ± 6 mm, nearly aligned with line joining the left and right acromion markers, while the y-coordinate for the other subjects varied from 12 ± 20 mm, for Subject 5, to 46 ± 6 mm, for Subject 4.

The orientation of ISA_S was compared to the anatomical axis of the spine, computed as the line joining the pelvic and shoulder centroids. For all subjects, the angle relative to the spine axis varied from 4.29 ± 0.91 degrees, for Subject 4, to 12.22 ± 5.68 degrees, for Subject 5. This indicates that the orientation of ISA_S approaches, for all subjects, the orientation of the spine axis. The standard deviation on this angle varied from 0.91 degrees to 5.68 degrees, indicating consistency of ISA_S orientation relative to the spine axis within subjects. It is shown in Figure 5-6 that the position of ISA_S is consistent with the spine axis, shown along and perpendicular to the line of play.

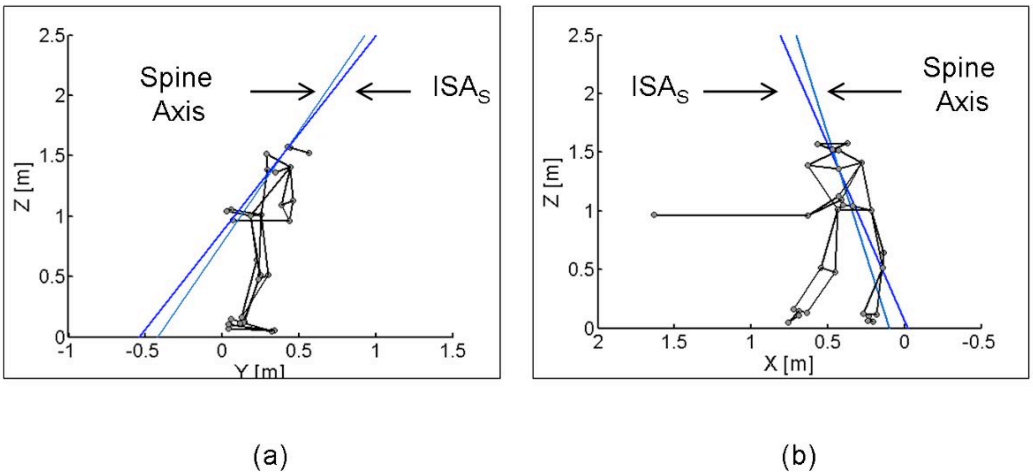

Figure 5-6: Subject 1-Position and orientation of ISA_S at percent downswing corresponding to ω_{max}: (a) Rear view of the golf swing (view along the line of play) (b) Front view of the golf swing (view perpendicular to the line of play)

ISA_A: ISA of the left arm relative to the global reference frame

The maximum angular velocity, ω_{max}, about ISA_A ranged from 15.438 ± 1.860 rad/s, for Subject 5, to 19.828 ± 1.083 rad/s, for Subject 3. The standard deviation on ω_{max} ranged from 0.267 rad/s, for Subject 4, to 2.173 rad/s, for Subject 1, which represents relative values of 1.7 percent and 12.9 percent relative to their corresponding ω_{max}, respectively. This reveals that the magnitude of ω_{max} about the left arm is more variable than about the pelvis and shoulders, as the standard deviation for some subjects represents more than 10 percent of the mean value. The maximum angular velocities about ISA_A are higher in magnitude than the arm angular velocity determined by Cheetham et al. [Cheetham et al. (2008)], who reported values of 13.32 ± 1.66 rad/s for amateurs and 17.10 ± 1.19 rad/s for professionals. The angular velocity of all subjects exceeded the angular velocity of the amateur group, which was not unanticipated as the subjects of the current study are all of low handicap. However, it was unexpected that the angular velocity of Subjects 2 and 3 exceeded the magnitude of the professionals. Cheetham et al. [Cheetham et al. (2008)] reported only one component of left arm angular velocity, perpendicular to the instantaneous swing plane defined by the position of the left arm and golf club shaft. Therefore it is not unexpected the angular velocities of this study are of higher magnitude.

The instant corresponding to the ω_{max} of each subject varied from 77.0 ± 24.0 percent downswing, for Subject 4, to 100.0 ± 0.0 percent downswing, for Subjects 1 and 3. This indicates that for all subjects the maximum angular velocity occurs in the last 1/3 of the downswing, and for Subjects 1 and 3 the angular velocity continued to increase into impact. The standard deviation of the corresponding instances ranged from 0.0 percent downswing, for Subjects 1 and 3, to 13.6 percent downswing, for Subject 2. Only the results of Subject 4 approach those published by Cheetham al. [Cheetham et al. (2008)] for a single professional golfer. Although results were not explicitly given, the instance of maximum thorax angular velocity was determined from interpolation of the given angular velocity plot, of a professional golfer, and from the given downswing duration. From these procedures, an approximate percent downswing value of 75 percent was computed, which approaches the value of Subject 4, of 77 percent downswing. As the angular velocity values published by Cheetham al. [Cheetham et al. (2008)] were computed perpendicular to the swing plane, arm motion from wrist supination was not included in the results. Furthermore, it would appear that the ISA_A of Subject 4 displayed the least amount of similarity with the supination axis, which will be discussed below. Therefore, it is suggested that the angular velocity about ISA_A reflects the rotation of the left arm about the left glenohumeral joint (shoulder joint), which would explain the proximity to the results of Cheetham al. [Cheetham et al. (2008)], while the angular velocity of Subjects 1 and 3 reflects a combination of shoulder rotation and wrist supination.

The intersection of ISA_A with the xy-plane of the shoulders local coordinate frame displayed two tendencies. For Subjects 1, 2 and 3, the mean intersection was located in proximity to the left glenohumeral joint, represented by marker S4 (see Section 3.4). This would indicate that the left arm is rotating relative to the shoulders, possibly as a combination of a rotation about the shoulder joint and wrist supination. For Subjects 4 and 5, the mean intersection was located closer to the centroid of the shoulders, represented by the origin of the local coordinate frame (see Section 4.3.2). For these two subjects, the intersection of ISA_A

resembles the intersection of ISA_S, indicating that the motion of the left arm may be primarily due to a rotation of the shoulders. This is further supported by the proximity in time of the maximum angular velocities of the shoulders and left arm, as the difference between these two maximums was 0.6 percent downswing and 7.2 percent downswing for Subjects 4 and 5, respectively. For all subjects other than Subject 4, the intersection of ISA_A and the local coordinate frame of the shoulders not as consistent as the position of ISA_P and ISA_S. Excluding Subject 4, the radius of standard deviation varied from 38.6 mm, for Subject 1, to 94.8 mm, for Subject 2. This variability in ISA position was not unexpected, as the computation of ISA_A assumes that the entire left arm, from the left acromion (marker S4) to the left wrist (markers A3 and A4), acts as a rigid link. However, some motion does occur at the left elbow, as not all subjects in this study kept their left arm stiff throughout the golf swing. Therefore, any motion at the left elbow would result in added variability in the position of the ISA_A. This is considered one of the main sources of variability for computations of the left arm and may indicate that alternate marker configurations may need to be explored.

The orientation of ISA_A was compared to the anatomical axis of the spine and the supination axis of the left arm, joining the centroids of the elbow and wrist. For all subjects, the angle relative to the spine axis varied from 4.51 ± 0.79 degrees, for Subject 4, to 21.83 ± 3.59 degrees, for Subject 3. Furthermore, the standard deviation on this angle varied from 0.79 degrees to 3.59 degrees, indicating consistency of ISA_A orientation relative to the spine axis within subjects. For all subjects, the orientation of ISA_A was closer to that of the spine axis than the supination axis of the left arm. This indicates that the orientation of ISA_A was more consistent with the orientation of the spine than the orientation of the left arm. The relative angle between ISA_A and the supination axis showed considerable variability for Subjects 2 and 5, as the standard deviation of these two subjects was 27.49 degrees and 18.49 degrees, respectively. This high variability could be a result of variability in the orientation of the left arm, from motion about the left elbow, as the standard deviation of the ISA_A relative to the

spine axis of these two subjects varied by only 1.44 degrees and 2.26 degrees. This high variability in left arm orientation makes it difficult to discuss any similarities between ISA_A and the supination axis. As for the other subjects, the standard deviation of the relative angle to the supination axis varied from 3.09 degrees, for Subject 4, to 7.03 degree, for Subject 3. Of these three subjects, the relative angle measured 33.71 ± 6.85 degrees for Subject 1, 31.14 ± 7.03 degrees for Subject 3 and 83.56 ± 3.09 degrees for Subject 4. The relative angle is approximately the same for Subjects 1 and 3, which are the two subjects that display the least difference between the two reference angles. The position of ISA_A of Subject 1 is shown in Figure 5-7 at the instance of impact, indicting proximity to the spine axis while showing a slight deviation towards the supination axis. This may be a result of the combination of motion about both the left shoulder and supination of the forearm, as these same subjects achieved their maximum angular velocity at impact, which was thought to be a result of wrist supination. However, it cannot be ruled out that this closeness in angle may also be a result of relative position of the left arm. Furthermore, Subject 4 displayed the largest relative angle to the supination axis, measuring near 90 degrees. Along with the location of ISA_A and the percent downswing of the maximum angular velocity, this supports the notion that the motion of the left arm, for this subject, may be primarily due to a rotation of the shoulders.

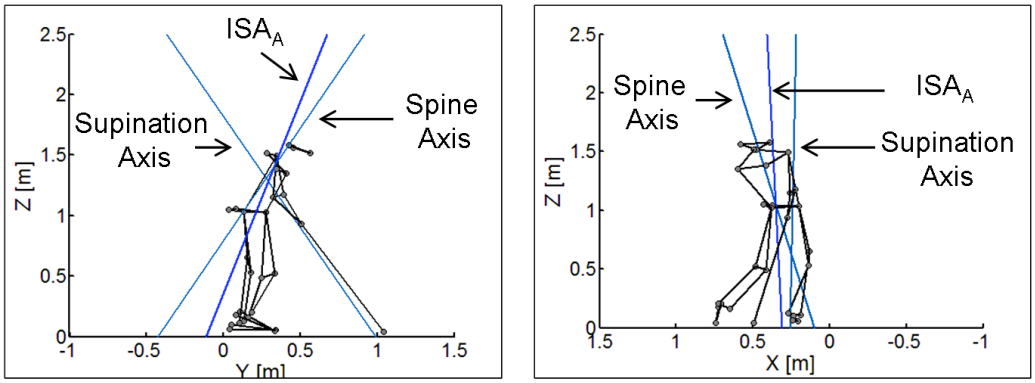

Figure 5-7: Subject 1-Position and orientation of ISA_A at percent downswing corresponding to ω_{max}: (a) Rear view of the golf swing (view along the line of play) (b) Front view of the golf swing (view perpendicular to the line of play)

ISA_C: ISA of the golf club relative to the global reference frame

As previously discussed, the computation of ISA_C was not free of computational error. Other than for Subjects 1 and 5, large discontinuities occurred causing shifts in the magnitude and percent downswing of the maximum angular velocities. These computational errors become evident when studying the maximum angular velocities, as the maximum angular velocities of Subjects 2, 3 and 4 are all above 100 rad/s, more than 3 times the magnitude published by other studies [Cheetham et al. (2008), Nesbit (2005), Teu et al. (2006)]. Therefore, only results from Subjects 1 and 5 will be discussed in detail, as computational errors do not permit an accurate description of the golf club motion of Subjects 2, 3 and 4.

The maximum angular velocity, ω_{max}, about ISA_C measured 22.250 ± 0.533 rad/s, for Subject 1 and 33.943 ± 6.591 rad/s for Subject 5. The maximum angular velocity of subjects 5 is comparable in magnitude than the golf club angular velocity determined by Cheetham et al. [Cheetham et al. (2008)], who reported values of 31.24 ± 1.94 rad/s for amateurs and 39.34 ± 6.59 rad/s for professionals. The angular velocity of Subject 1 is well below the data provided for amateur, by approximately 30 percent, while the mean angular velocity of Subject 5 is located between the amateur and professional data. It should be noted that Cheetham et al. [Cheetham et al. (2008)] reported only one component of golf club angular velocity, perpendicular to the instantaneous swing plane defined by the position of the left arm and golf club shaft. Nesbit [Nesbit (2005)] computed the angular velocity of the golf club head by way of a full body multi-linked solid model, and reported a maximum angular velocity of 30.94 ± 2.41 rad/s. The angular velocity reported by Nesbit is comparable to the magnitude of Subject 5, and is consistent with the findings of Cheetham et al. [Cheetham et al. (2005)] for amateur golfers. Teu et al. [Teu et al. (2006)] computed the angular velocity of the golf club head by studied the kinematic chain using dual Euler angles. The angular velocity reported by Teu et al. [Teu et al. (2006)], for a single 1-handicap subject, measured 38.8 rad/s at impact. This result is comparable to that reported by Cheetham et al. [Cheetham et al. (2005)] for professional golfers, both of which

were higher than the results of Subject 1 and 5. It is important to note that these last two studies computed the angular velocity of the golf club head, which differs from the computation of the shaft angular velocity of the current study. If it is assumed that the golf shaft has little effect on angular velocity, essentially acts as a rigid link, then theses findings can serve as a comparison to this study. This assumption can certainly be debated, and lead to disparities between the current study and the two studies mentioned above, but was followed for comparison purposes.

The instant corresponding to the ω_{max} for Subject 1 was 94.4 ± 1.8 percent downswing and 74.7 ± 14.2 percent downswing for Subject 5. This indicates that for all subjects the maximum angular velocity occurs in the last 1/4 of the downswing. Only the results of Subject 1 approach those published by Cheetham al. [Cheetham et al. (2008)] for professional golfers. Although results were not explicitly given, the instance of maximum golf club angular velocity was determined to coincide with impact and therefore coincides with a percent downswing value of 100. As Cheetham et al. [Cheetham et al. (2008)] reported only one component of golf club angular velocity, it is possible all components do not achieve their respective maximum at impact and may have caused disparities between studies. The results published by Teu et al. [Teu et al. (2006)] also indicate that the angular velocity of the golf club did not attain its maximum value at impact, but rather shortly before impact.

The position of ISA_C was expressed as the shortest distance between ISA_C and the centroid of the left wrist joint. This provided an approximate distance between ISA_C and the expected joint center. The distance between ISA_C and the left wrist centroid measured 0.093 ± 0.009 m for Subject 1 and 0.247 ± 0.084 m for Subject 5. This indicates that the ISA_C of Subject 1 is within 10 cm of the position of the left wrist, reflecting some closeness to the expected joint center, while the ISA_C of Subject 5 does not support this hypothesis. Possible reasons for this discrepancy include non-rigidity between the left-arm and the golf club, and significant

rotation of the left arm throughout impact. If the left arm remains fairly still just prior to impact, allowing the golf club to swing in front of the body at impact, then the motion of the golf club near impact should be concentrated about the left wrist. However, if the left arm does not allow the golf club to "catch up" at impact, then the motion of the left arm would cause a shift in the expected position of ISA_C, as shown by the results of Subject 5.

The orientation of the golf club ISA was computed as the angle between ISA_C and the supination axis of the left forearm, which was expected to be the orientation of the main components of golf club rotation relative to the left arm. The angle between ISA_C and the supination axis of the left arm measured 47.32 ± 2.61 degrees for Subject 1 and 64.60 ± 10.16 degrees for Subject 5. For both subjects, the relative angle does not provided any indication of closeness between the orientation of ISA_C and the supination axis of the left arm. It was hypothesized that most of the relative motion between the golf club and the left arm would be concentrated at the left wrist, from wrist supination. However, it has been shown that ulnar/radial abduction and hand flexion/extension also play an important role in the motion of the golf club [Teu et al. (2006)], the later having a larger effect on golf club head velocity. Therefore, the motion of the golf club relative to the left arm is more likely to be a combination of the three movements of the wrist, than simply wrist supination, which in turn would account for the large relative angle measured.

Summary: Motion about ISA (from total segment motion)

For all subjects, the summation of speeds principles was found, as the magnitude of maximum angular velocities increased from the most proximal segment to the most distal segment. Furthermore, Subjects 1, 3 and 4 achieved their maximum angular velocities in the desired kinematic sequence, where the maximum angular velocities are achieved first by the proximal segments and followed by the more distal segments of the sequence. For Subjects 1, 3 and 4, the first maximum angular velocity is reached by the pelvis, which confirms the start of the

downswing with the motion of the pelvis. The ISA of the pelvis was located along the anterior/posterior axis of the pelvis and either aligned or slightly posterior to the hip joint centers, which could be affected by the lateral displacement of the pelvis during the downswing. For most subjects ISA pelvis orientation is consistent with the spine axis, and in some cases is located between the spine axis and the axis of the left leg, indicating a possible rotation about the left leg. For most subjects (1, 3 and 4) the second maximum angular velocity is about the ISA of the shoulders. This indicates that the shoulders follow the motion of the pelvis and continue the kinematic chain of the downswing. The ISA of the shoulders was located near the centroid of the shoulders, origin of the local coordinate frame, to slightly anterior and towards the left acromion. As was the case for the pelvis, the orientation of ISA was consistent with the spine axis, as expected. For all subjects, the final maximum angular velocity was achieved by the left arm. In some cases, this angular velocity increased until impact, possibly due to wrist supination, and in others cases achieved a distinct maximum before impact. For three out of the five subjects, the left arm ISA was consistent in position with the left glenohumeral joint, indicating relative motion about the left shoulder, while the others subjects produced an ISA closer to the shoulder centroid, indicating little relative motion between the shoulder and left arm. Of all segments, the variability in ISA position was highest for the left arm, which was believed to originate from inconsistent motion about the left elbow joint. The orientation of the left arm ISA was most consistent with the orientation of the spine axis, indicating that the largest component of left arm motion was from rotation about the shoulders. The ISA of the golf club could only be discussed for two subjects, as computational discontinuities did occur for most subjects. This indicates that further analysis into instances approaching an indeterminate ISA and alternate marker configurations should be investigated in order to accurately describe the motion of the golf club using ISA theory.

5.3.2.2 Maximum Angular Velocity about ISAr

The four variables computed at maximum angular velocity (ω_{max}, percent downswing corresponding to ω_{max}, ISA position and ISA orientation) were determined for each of the four ISAr that comprise the golf swing model and are shown in Section 4.3.2.2. These four variables will be discussed for each corresponding ISAr.

$ISAr_P$: ISA of the motion of the pelvis relative to the left leg

The maximum angular velocity, ω_{max}, about $ISAr_P$ ranged from 4.350 ± 0.317 rad/s, for Subject 1, to 7.840 ± 0.202 rad/s, for Subject 4. The standard deviation on ω_{max} ranged from 0.165 rad/s, for Subject 5, to 0.835 rad/s, for Subject 2, which represents relative values of 2.6 percent and 14.3 percent relative to their corresponding ω_{max}, respectively. This reveals that the magnitude of ω_{max} about $ISAr_P$ is not as consistent as ω_{max} about ISA_P, as the standard deviation was less than 10 percent of the mean value for motion about ISA_P. As expected, the magnitude of ω_{max} about $ISAr_P$ is smaller than about ISA_P, which ranged from 5.719 ± 0.349 rad/s, for Subject 1, to 9.563 ± 0.336 rad/s, for Subject 4. As the motion about $ISAr_P$ is one component of the full motion of the pelvis, it is expected that the magnitude of its angular velocity be lesser than that of the full motion. Robinson [Robinson (1994)] reported the relative angular velocity of the hips at the midpoint of the downswing, when the left forearm is parallel to the ground. Unfortunately details on the computation were not provided, although it was labeled the relative angular velocity of segments. Therefore, it will be used as a comparison for the angular velocity about $ISAr_P$. Robinson [Robinson (1994)] reported hip angular velocities of 4.18 rad/s for amateur golfers and 5.37 rad/s for professionals. The magnitudes are slightly lower than those measured in the current study, especially when considering that the professional data of Robinson [Robinson (1994)] is lower in magnitude than 4 out of the 5 subject of this study. It is hypothesized that the data provided by Robinson [Robinson (1994)] represents a single component of segment relative angular velocity.

The instant corresponding to the ω_{max} of each subject varied from 65.9 ± 11.7 percent downswing, for Subject 3, to 87.7 ± 0.9 percent downswing, for Subject 5, which indicates that for all subjects the maximum angular velocity occurs in the last 2/3 of the downswing. The standard deviation of the corresponding instances ranged from 0.9 percent downswing, for Subject 5, to 11.7 percent downswing, for Subject 3. Large variability is observed with the percent downswing of Subject 3 and is also observed in the position and orientation of $ISAr_P$, as they are all connected to one another, and will be discussed shortly. The percent downswing corresponding to ω_{max} was comparable to those determined for motion about ISA_P, which ranged from 68.2 ± 3.2 percent downswing to 83.7 ± 2.3 percent downswing. This confirms that the relative motion of the pelvis, uniquely from motion about the pelvis, determined the instance of maximum angular velocity. As was the case for motion about ISA_P, the results of this study differ from those published by Cheetham al. [Cheetham et al. (2008)] for professional golfers, from which an approximate percent downswing value of 60 percent was computed. These results indicate that the professional golfer from Cheetham et al. [Cheetham et al. (2008)] fired his hips earlier in the downswing, perhaps in an attempt to create greater separation between the pelvis and hips, as this has been shown to be one of the swing variables with the highest correlation to club head velocity [McLaughlin and Best (1994)].

The intersection of $ISAr_P$ with the xy-plane of the pelvis local coordinate frame displayed two tendencies. For Subjects 1, 3 and 4, the mean intersection was located in the left hand portion of the pelvis, in proximity to the left hip joint centre, represented by marker P2 (see Section 3.4). Although there is large variability in the position of Subject 3, with a standard deviation radius of 0.0671m, these results would indicate that the pelvis is rotating relative to the left hip joint. This supports the instructional technique where by golfers are suggested to, following weight transfer from their right side to their left side, rotate their pelvis about a firm left leg [Harmon (2001)]. As for Subjects 2 and 5, the mean intersection was located closer to the origin of the pelvic local coordinate frame,

which is located halfway between the markers P1 and P2 (see Section 3.4). This could possibly indicate that these subjects have not fully transferred their weight to their left side, and consequently rotate their pelvis about a more central position. In both cases, the position of ISA_P differs from the position of $ISAr_P$, which becomes especially evident when observing the position of both ISA as a function of time. The intersection of these two ISA with the xy-plane of the pelvis local coordinate frame is shown in Figure 5-8 for 6 instances in the downswing, ranging from 0 to 100 percent downswing. This shows that the position of ISA_P is far from the pelvis at the beginning of the downswing and approaches the pelvis as the downswing progresses. The reason for this distance between the two at the beginning of the downswing is the lateral displacement of the pelvis. As ISA_P expresses the entire motion of the pelvis as a single rotation, the translation of the pelvis causes ISA_P to distance itself from the pelvis, as shown in Figure 5-8. Conversely, the position of $ISAr_P$ is in close proximity to the pelvis for the duration of the downswing, as the translational component of the pelvis motion has been removed from the computation through the motion of the left leg.

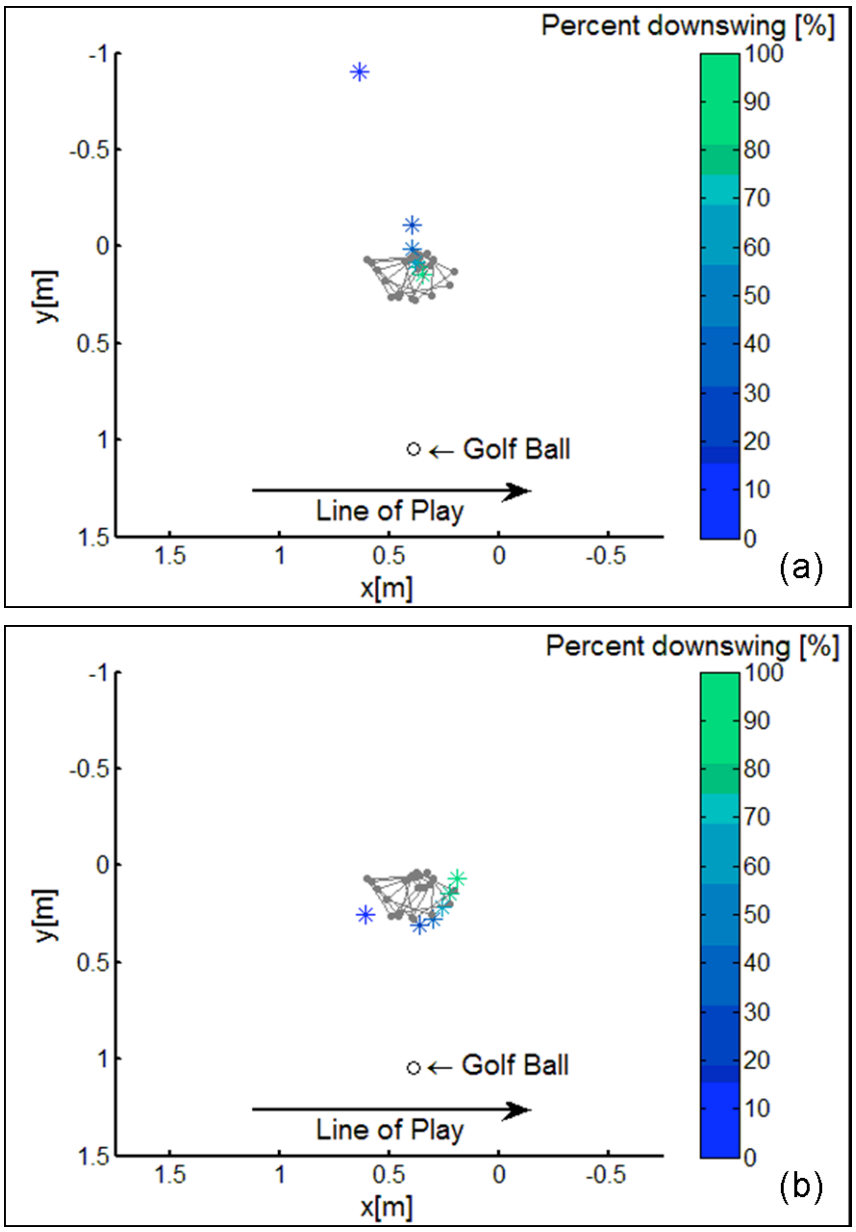

Figure 5-8: Intersection between ISA of the pelvis and the xy-plane of the pelvic local coordinate frame as a function of percent downswing: (a) ISA_P intersection (b) $ISAr_P$ intersection

The orientation of $ISAr_P$ was compared to two anatomical axes: the spine axis and the axis of the left leg. For all subjects, the angle relative to the spine axis varied from 16.70 ± 5.24 degrees, for Subject 1, to 36.94 ± 5.58 degrees, for Subject 5. For all subjects, the angle relative to the spine axis either remained relatively constant (increase less than 2 degrees) for Subjects 1 and 3, or increased by large amounts (from 9.0 degrees to 28.9 degrees) for Subjects 2, 3 and 4, relative to the

orientation of ISA_P. This would indicate the $ISAr_P$ is either maintained the orientation of ISA_P relative to the spine axis, or has distanced itself from the spine axis. Therefore, the relative rotation of the pelvis is less consistent with the orientation of the spine. Furthermore, for all subjects, the angle relative to the axis of the left leg varied from 25.59 ± 1.84 degrees, for Subject 1, to 75.15 ± 4.21 degrees, for Subject 2. For all subjects, the angle relative to the axis of the left leg increased when compared to the angle formed with ISA_P. This increase in relative angle ranged from 12.4 degrees to 35.0 degrees for Subjects 1 and 5, respectively. This indicates that the relative rotation of the pelvis is less consistent with the orientation of the left leg.

If it is assumed that the complete motion of the pelvis consists of a combination of movements about the left leg, consisting of a translation and rotation, and a rotation about the spine, then the orientation of $ISAr_P$ would be expected to be more consistent with the spine axis then the axis of the left leg. This is expected as the motion of the left leg imparted onto the pelvis is removed during computation of $ISAr_P$, and the remaining motion dictates the position and orientation of $ISAr_P$. The position and orientation of $ISAr_P$ is shown in Figure 5-9 for Trial 1 of Subject 1. It is shown in Figure 5-9 (a) that the projection of $ISAr_P$ in the yz-plane (perpendicular to the line of play) is consistent with the spine axis. However, the projection in the xz-plane (parallel to the line of play), shown in Figure 5-9 (b), illustrates the reported difference in orientation between $ISAr_P$ and the spine axis. Therefore, although agreement between the two axes has been found in the yz-plane, the difference in orientation in the xz-plane must be noted.

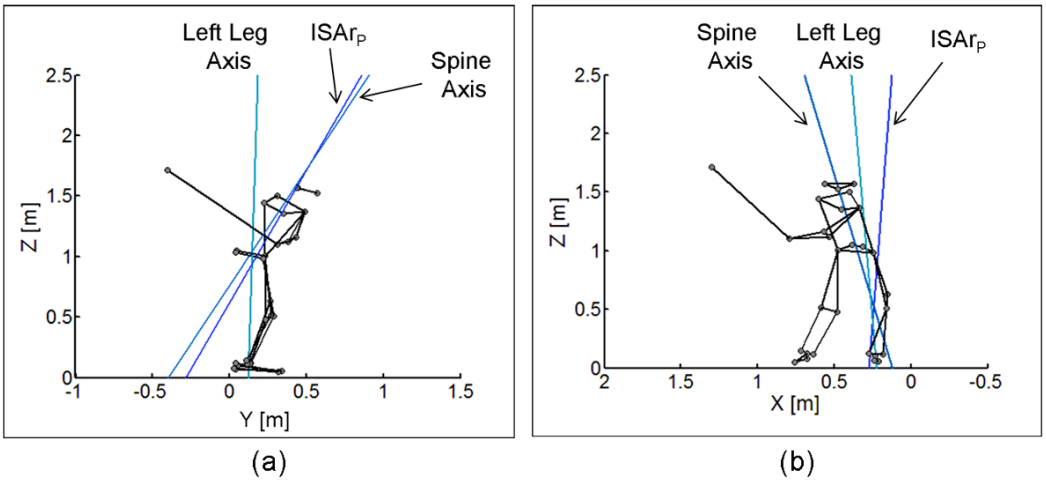

Figure 5-9: Subject 1-Position and orientation of $ISAr_P$ at percent downswing corresponding to ω_{max}: (a) Rear view of the golf swing (view along the line of play) (b) Front view of the golf swing (view perpendicular to the line of play)

$ISAr_S$: ISA of the motion of the shoulders relative to the pelvis

The maximum angular velocity, ω_{max}, about $ISAr_S$ ranged from 4.304 ± 0.394 rad/s, for Subject 2, to 6.559 ± 0.634 rad/s, for Subject 3. The standard deviation on ω_{max} ranged from 0.083 rad/s, for Subject 5, to 1.076 rad/s, for Subject 4, which represents relative values of 1.7 percent and 19.3 percent relative to their corresponding ω_{max}, respectively. This reveals that the magnitude of ω_{max} about $ISAr_S$ is not as consistent as ω_{max} about ISA_S, as the standard deviation was less than 10 percent of the mean value for motion about ISA_S. As expected, the magnitude of ω_{max} about $ISAr_S$ is smaller than about ISA_S, which ranged from 8.408 ± 0.224 rad/s to 13.514 ± 0.443 rad/s. As the motion about $ISAr_S$ is one component of the full motion of the shoulders, it is expected that the magnitude of its angular velocity be lesser than that of the full motion. Myers et al. [Myers et al. (2008)] computed the angle between 2 two-dimensional lines representing the position of the pelvis and of the shoulders. Differentiation of this angle, labeled torso-pelvic separation velocity, provides an approximation for the relative angular velocity between the shoulders and pelvis. Myers et al. [Myers et al. (2008)] reported torso-pelvic separation velocities of 4.854 ± 0.813 rad/s, for low ball velocity players, and of 6.800 ± 0.970 rad/s, for high ball velocity players.

These values are in agreement with those presented in the current study, as the angular velocity of the low ball velocity players is close to the magnitude of Subject 2 and the angular velocity of the high ball velocity players is close to the magnitude of Subject 3.

The instant corresponding to the ω_{max} of each subject varied from 58.5 ± 0.8 percent downswing, for Subject 5, to 91.7 ± 11.4 percent downswing, for Subject 1. This indicates that, other than Subject 1, the maximum angular velocity occurs in the last 1/3 of the downswing. The standard deviation of the corresponding instances ranged from 0.8 percent downswing, for Subject 5, to 16.6 percent downswing, for Subject 4. For most subjects the percent downswing corresponding to ω_{max} was comparable to those determined for motion about ISA_S. However, in the case of Subjects 3 and 5, their percent downswing decreased by 12.0 and 23.9 percent when compared to the data about ISA_S, respectively. For these subjects it would seem that the relative motion of the shoulders relative to the pelvis achieves its peek in magnitude before that of the pelvis. Cheetham al. [Cheetham et al. (2008)] determined an approximate percent downswing value of 60 percent was computed for the complete motion of the shoulders. These results indicate that the professional golfer from Cheetham et al. [Cheetham et al. (2008)] rotated his hips earlier in the downswing, perhaps in an attempt to create greater separation between the pelvis and hips, as this has been shown to be one of the swing variables with the highest correlation to club head velocity [McLaughlin and Best (1994)].

The intersection of $ISAr_S$ with the xy-plane of the shoulder local coordinate frame displayed two variations from the centroid (origin of the local coordinate frame). First, the intersection is anterior to the shoulder centroid, closer to marker S1. Second, some subjects displayed a shift from the anterior/posterior axis of the shoulders, from marker S1 to S2, and the intersection are closer to the left side of the shoulders. For Subjects 1 and 4, the intersection of $ISAr_S$ is in close proximity to the jugular notch (marker S1), which is slightly anterior to the shoulder

centroid. This anterior shift from the shoulder centroid measures 0.092 m to 0.072 m for Subjects 1 and 4, respectively. For both subjects, $ISAr_S$ is approximately aligned with the anterior/posterior axis of the shoulders (y-axis of the local coordinate frame) as expected. The results of Subject 2 displayed similar characteristics to those of Subjects 1 and 4, as the intersection of $ISAr_S$ was nearly aligned with the y-axis and also displayed an anterior shift relative to the shoulder centroid. However, the anterior shift was of larger magnitude, measuring 0.174 m. For Subjects 3 and 5, the two variations from the shoulder centroid discussed above were displayed. An anterior shift similar in magnitude to Subject 3 was noted, measuring 0.153 m to 0.169 m, and the intersection of $ISAr_S$ was closer to the left side of the shoulders, shifting 0.099 m to 0.268 m to the left of the centroid. The anterior position of $ISAr_S$ relative to the shoulder centroid, occurring for all subjects, may be the result of the lateral shift of the pelvis during the downswing. During the weight transfer from the right side of the body to the left side of the body during the downswing, the pelvis undergoes a lateral translation along the line of play. As a result the shoulders also undergo a lateral shift during the downswing. However, the lateral shift of the shoulders may not necessarily be of the same magnitude, causing a lateral flexion of the spine referred to as "side bending" as reported by McTeigue et al. [McTeigue et al. (1994)]. This lateral flexion of the spine can be seen in Figure 5-9 (b), where the spine axis is tilted from the vertical position and away from the line of play. When $ISAr_S$ is computed, the complete motion of the shoulders about the pelvis ISA, ISA_P, is removed from the total motion of the shoulders, and in the process compensating for the lateral shift of the pelvis. This lateral translation removed from the motion of the shoulders is equal to adding a lateral translation away from the line of play. Similar to the motion of the pelvis, where ISA_P is shifted perpendicular to the line of play due to the translation of the pelvis, the position of $ISAr_S$ would also be shifted perpendicular to the line of play. This would cause the intersection of $ISAr_S$ to undergo a shift from near the centroid of the pelvis, as seen in the position of ISA_S, to a more anterior portion of the shoulders.

The orientation of $ISAr_S$ was compared to the anatomical axis of the spine, computed as the line joining the pelvic and shoulder centroids. For all subjects, the angle relative to the spine axis varied from 23.66 ± 4.35 degrees, for Subject 1, to 48.47 ± 1.80 degrees, for Subject 3. This indicates that the orientation of $ISAr_S$ is less consistent with the orientation of the spine axis when compared to ISA_S, which formed an angle of 4.29 ± 0.91 degrees to 12.22 ± 5.68 degrees relative to the spine axis. The standard deviation on this angle varied from 1.80 degrees to 6.27 degrees, indicating consistency of $ISAr_S$ orientation relative to the spine axis within subjects. The position and orientation of $ISAr_S$ is shown in Figure 5-10 for Trial 1 of Subject 1. It is shown in Figure 5-10 (a) that the projection of $ISAr_S$ in the yz-plane (perpendicular to the line of play) is not perfectly aligned with the spine axis, while the projection in the xz-plane (parallel to the line of play) shown in Figure 5-10 (b), is consistent with the spine axis. From visual inspection, it would appear that the orientation of $ISAr_S$ is more consistent to the z-axis of the shoulder local coordinate frame then the spine axis (see Section 4.3.2).

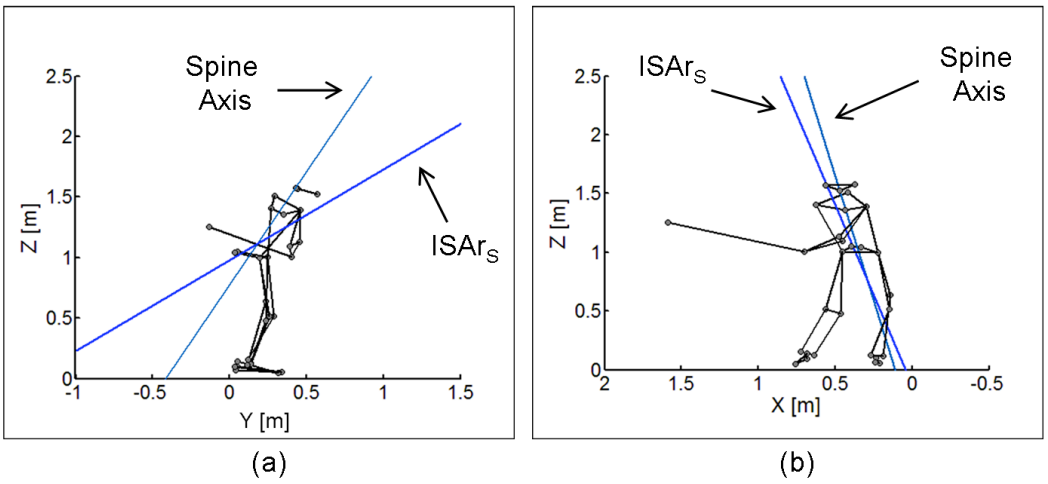

Figure 5-10: Subject 1-Position and orientation of $ISAr_S$ at percent downswing corresponding to ω_{max}: (a) Rear view of the golf swing (view along the line of play) (b) Front view of the golf swing (view perpendicular to the line of play)

It is of interest to note that the maximum angular velocity about $ISAr_S$ did not always occur within the downswing, but in some cases occurred in the follow

through (after impact). The position and orientation of $ISAr_S$ is shown in Figure 5-11 for Trial 1 of Subject 1 at the instant of maximum angular of the entire golf swing. It can be seen that the orientation of ISArS is more consistent with the spine axis then in the case of Figure 5-10. This would seem to indicate that the orientation of $ISAr_S$ is in fact consistent with the spine axis at the instant of maximum angular velocity, and that analysis of this ISA during the follow through could be of interest.

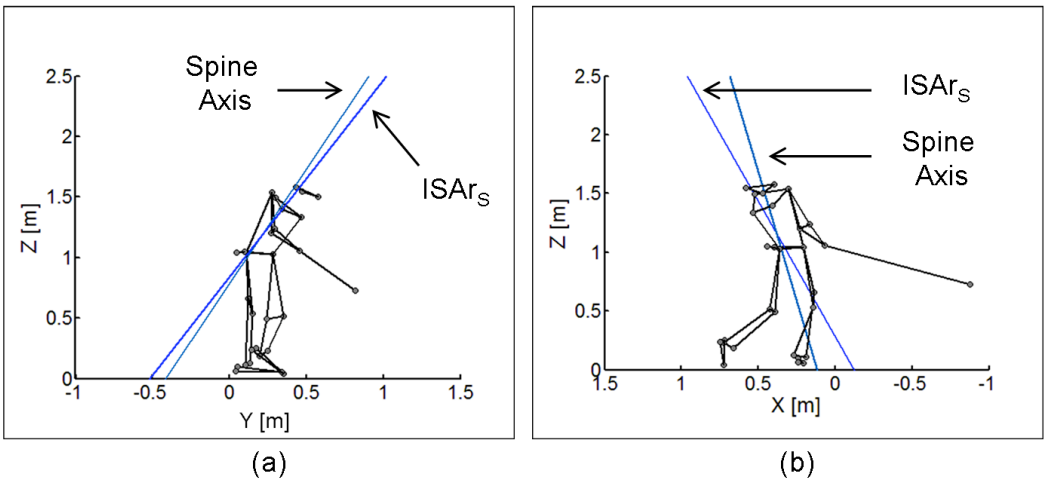

Figure 5-11: Subject 1-Position and orientation of $ISAr_S$ at percent downswing corresponding to ω_{max} of the entire golf swing (including the follow through): (a) Rear view of the golf swing (view along the line of play) (b) Front view of the golf swing (view perpendicular to the line of play)

$ISAr_A$: ISA of the motion of the left arm relative to the shoulders

Of the four variables used to describe each ISA of the golf swing model, the position and orientation of ISA provide the most visual insight into the behavior of the analyzed segment. Although the angular velocity about the ISA is essential to determine the sequence of motion, the position of ISA locates the non-rigid spherical joints of the golf swing model. When observing Figure 4-16, it becomes apparent that for Subjects 2, 3 and 4 the position of $ISAr_A$ is not consistent with motion about the left glenohumeral joint, as expected. Rather, the mean intersection of $ISAr_A$ with the xy-plane of the local coordinate frame of the shoulders is not within 0.5 m of the expected joint position and the radius of

standard deviation is of large magnitude, ranging from 0.4380 m to 5.0420 m. This large variability can be the result of non-rigidity of the left shoulder joint and primarily non-rigidity of the left arm. The computation of $ISAr_A$ assumes that the entire left arm, from the left acromion (marker S4) to the left wrist (markers A3 and A4), acts as a rigid link. Therefore, any motion at the left elbow would result in variability in the position of the $ISAr_A$. That said, it becomes difficult to discuss the motion about $ISAr_A$ for Subject 2, 3 and 4 as the location of the joint is not consistent with anatomical landmarks of the body, and therefore a function joint cannot be determined. These results further indicate that the current marker configuration, along with assuming the entire left arm acts as a rigid-link, may introduce a large amount of variability, making $ISAr_A$ computation difficult for some subjects. Consequently, only the motion about $ISAr_A$ for Subjects 1 and 5 will be discussed. In order to assess the motion of all subjects, it could be of interest to reduce some of the relative motion at the shoulder joint and motion at the left elbow joint during the downswing. This could be accomplished by imposing the use of marker S4 (located above the left glenohumeral joint) for computation of shoulder and left arm ISA, although this would introduce a bias in ISA computation of the left arm by eliminating a degree of freedom.

The maximum angular velocity, ω_{max}, about $ISAr_A$ measured 7.122 ± 1.864 rad/s for Subject 1 and 9.256 ± 2.989 rad/s for Subject 5. The standard deviation for Subjects 1 and 5 represent relative values of 26.2 percent and 32.3 percent relative to their corresponding ω_{max}, respectively. These relative values are higher than those measured for motion about ISA_A for the same two subjects, which measured 12.9 percent and 12.1 percent. This would seem to indicate that the variability is higher for motion about $ISAr_A$ compared to ISA_A. Robinson [Robinson (1994)] reported the time derivative of the relative angle between the left arm and the shoulders at impact, providing an approximation of the relative angular velocity between the left arm and the shoulders. Robinson [Robinson (1994)] reported angular velocities of 7.93 rad/s for amateur golfers and 9.44 rad/s for professionals. These angular velocities are comparable to those of the current

study, although it was expected that the professional data provided by Robinson [Robinson (1994)] be of larger magnitude. However, as these comparative results represent the time derivative of a single, two-dimensional angle, it is not surprising that the results be lower than expected.

The instant corresponding to the ω_{max} measured 96.8 ± 4.9 percent downswing for Subject 1 and 96.6 ± 5.1 percent downswing for Subject 5. This indicates that for Subjects 1 and 5 the maximum angular velocity occurred just prior to impact, within the last 10 percent of the downswing. The values are comparable to those determined for motion about ISA_A, which measured 100 ± 0.0 percent for Subject 1 and 89.6 ± 9.5 for Subject 5. These values differ from those published by Cheetham al. [Cheetham et al. (2008)] who determined a percent downswing of 75 percent for the maximum angular velocity of the left arm of a professional golfer. As previously mentioned, the angular velocity values published by Cheetham al. [Cheetham et al. (2008)] were computed perpendicular to the swing plane, and therefore arm motion from wrist supination was not included in the results. As wrist supination can constitute one of the major components of arm motion relative to the shoulders, it may explain the disparities between the instances of maximum angular velocity of arm motion from the current study and those published by Cheetham al. [Cheetham et al. (2008)].

The mean intersection of $ISAr_A$ of Subject 1 with the xy-plane of the shoulder local coordinate frame was nearly coincident with the position of marker S4 placed on the left acromion, which is located above the left glenohumeral joint. This indicates that the motion of the left arm relative to the shoulders of Subject 1 is located near the left glenohumeral joint as expected. For Subject 5, the closest anatomical landmark to the mean intersection of $ISAr_A$ is marker S4. However, unlike the case of Subject 1, the mean intersection is not located in close proximity to the left glenohumeral joint, as some deviation can be seen in Figure 4-16. The intersection of $ISAr_A$ is to the left of marker S4, approximately 0.25m to the left (in the x-axis direction), as well as more posterior to marker S4,

approximately 0.12m (in the negative y-axis direction). The reasons for these deviations from the expected $ISAr_A$ location include non-rigidity of the left glenohumeral joint and primarily motion at the left elbow. If wrist supination was an important component of the arm motion of Subject 5 and elbow flexion/extension occurred during the downswing, then the supination axis of the forearm would not be aligned with the left glenohumeral joint. Consequently, the position of $ISAr_A$ would deviate from the left glenohumeral joint. Therefore these results indicate that motion at the left elbow may

The orientation of $ISAr_A$ was compared to the anatomical axis of the spine and the supination axis of the left arm, joining the centroids of the elbow and wrist. For Subject 1, the angle relative to the spine axis measured 20.24 ± 6.02 degrees while the angle relative to the supination axis measured 33.93 ± 16.44 degrees. When compared to the relative angles formed by ISA_A of Subject 1, the angle relative to the supination axis remained relatively unchanged (33.71 ± 6.85 degrees) while the angle relative to the spine axis increase by 11.38 degrees (from 8.86 ± 2.42 degrees). This would seem to indicate that the relative motion of the left arm has become more a combination of shoulder rotation and wrist supination, as opposed to being primarily consistent with the spine axis. For Subject 5, the angle relative to the spine axis measured 46.02 ± 4.20 degrees while the angle relative to the supination axis measured 31.98 ± 20.30 degrees. When compared to the relative angles formed by ISA_A of Subject 5, the angle relative to the supination axis decreased by 35.19 degrees (from 67.17 ± 18.49 degrees) while the angle relative to the spine axis increased by 30.36 degrees (from 15.71 ± 2.26 degrees). This indicates a clear shift from consistency with the spine axis, for the full motion of the left arm, to an orientation approximately half way between the spine axis and the supination axis. This is an expected result, as the rotation about the shoulders (consistent with the spine axis) has been removed from the total motion of the left arm during computation of $ISAr_A$. Consequently, the motion of the left arm relative to the shoulders should distance itself from the spine axis and approach the supination axis.

$ISAr_C$: ISA of the motion of the golf club relative to the left arm

As previously discussed, the computation of ISA_C was not free of computational error, which in turn affected the computation of $ISAr_C$. Other than for Subjects 1 and 5, large discontinuities occurred causing shifts in the magnitude and percent downswing of the maximum angular velocities. These computational errors become evident when studying the maximum angular velocities, as ω_{max} reached values of up to 362.160 ± 154.662 rad/s for Subject 2. These values indicate that the current computation of ISA_C and $ISAr_C$ does not provide an accurate description of golf club motion and should be re-evaluated. Therefore, only results from Subjects 1 and 5 will be discussed in detail.

The maximum angular velocity, ω_{max}, about $ISAr_C$ measured 34.980 ± 35.777 rad/s, for Subject 1 and 41.585 ± 40.332 rad/s for Subject 5. Theses values are both highly variable, as the standard deviation for both subjects is approximately equal to the corresponding mean value of ω_{max}. Furthermore, the magnitude of these angular velocities is larger than the angular velocity about ISA_C for the same subjects, which was an unexpected result. Unfortunately, to the knowledge of the current investigators, no studies were found that have quantified the relative angular velocity between the golf club and the left arm. Therefore, no comparison could be made with other reported values. However, given the high variability of the angular velocity about $ISAr_C$, it would be difficult to determine agreement with other studies.

The instant corresponding to the ω_{max} for Subject 1 was 94.5 ± 6.1 percent downswing and 82.2 ± 10.0 percent downswing for Subject 5. This indicates that the maximum angular velocity was achieved in the last 20 percent of the downswing. Only the results of Subject 1 approach those published by Cheetham al. [Cheetham et al. (2008)], where a percent downswing of 100 was determined for the instance of ω_{max} for a professional golfer. Although the instance of ω_{max} for Subject 1 did not occur at impact (100 percent downswing), results published by

Teu et al. [Teu et al. (2006)] also indicate that the angular velocity of the golf club did not attain its maximum value at impact, but rather shortly before impact.

The position of $ISAr_C$ was expressed as the shortest distance between $ISAr_C$ and the centroid of the left wrist joint. This provided an approximate distance between $ISAr_C$ and the expected joint center. The distance between $ISAr_C$ and the left wrist centroid measured 0.332 ± 0.246 m for Subject 1 and 0.485 ± 0.182 m for Subject 5. Theses distances are larger and less consistent then those determined from the position of ISA_C, which measured 0.093 ± 0.009 m for Subject 1 and 0.247 ± 0.084 m for Subject 5. This indicates that the $ISAr_C$ of Subjects 1 and 5 do not reflect closeness to the expected joint center.

The orientation of the golf club ISA was computed as the angle between $ISAr_C$ and the supination axis of the left forearm, which was expected to be the orientation of the main components of golf club rotation relative to the left arm. The angle between $ISAr_C$ and the supination axis of the left arm measured 56.01 ± 16.06 degrees for Subject 1 and 46.45 ± 7.29 degrees for Subject 5. For both subjects, the relative angle does not provided any indication of closeness between the orientation of $ISAr_C$ and the supination axis of the left arm. It was hypothesized that most of the relative motion between the golf club and the left arm would be concentrated at the left wrist, from wrist supination. However, as was is discussed previously, Teu et al. [Teu et al. (2006)] has shown that ulnar/radial abduction and hand flexion/extension also play an important role in the motion of the golf club, the later having a larger effect on golf club head velocity. Therefore, the motion of the golf club relative to the left arm is more likely to be a combination of the three movements of the wrist, than simply wrist supination, which in turn would account for the large relative angle measured.

For the analysis of $ISAr_C$ of Subjects 1 and 5, large disparities between measured and expected results were noted for each of the four variables discussed. It is hypothesized that these disparities may be the result of non-rigidity between the

left-arm and the golf club, as well as computational errors. Although distinct discontinuities may not have been observed for Subjects 1 and 5, the velocity RMSE for the computation of $ISAr_C$, as shown in Table 4-10, was still an order of magnitude larger than all other computations for these subjects. The results of the current section support the findings of Section 4.1.2.2, confirming that the motion about $ISAr_C$ does not accurately describe the relative displacement between the golf club and the left arm.

Summary: Motion about ISAr (from relative segment motion)

For all subjects, the angular velocity of the left arm, relative to the shoulders, has the highest magnitude in the kinematic chain. For most subjects, the angular velocities occurring strictly about the pelvis and shoulders are approximately of the same magnitude. For Subjects 1, 3 and 4, the first maximum angular velocity reached in the kinematic chain occurred for relative pelvis motion. This confirms that, for most subjects, the motion of the pelvis initiates the downswing. For three of the five subjects, the intersection of $ISAr_P$ was located in proximity to the left hip joint center, indicating motion about the left side of the pelvis. For the other subjects, $ISAr_P$ was located near the pelvis centroid, which may be a result of lesser weight transfer when compared to the previous subjects. The orientation of $ISAr_P$ is less consistent with the orientation of the spine, when compared to ISA_P, and more consistent with the orientation of the left leg. For most subjects, three of five, the second maximum angular velocity is about $ISAr_S$, indicating that the shoulders follow the motion of the pelvis. For the other two subjects, the relative motion of the shoulders commences the downswing, not respecting the proximal to distal kinematic chain. The intersection of $ISAr_S$ was located anterior to the centroid of the shoulders, in proximity of the jugular notch, which may be a result of lateral displacement during the downswing. In some cases, the intersection of $ISAr_S$ was also located slightly towards the right portion of the shoulders. The orientation of this axis was less consistent with the spine axis, when compared to the orientation of ISA_S, and appears more consistent with the z-axis of the shoulder locate coordinate frame. For all subjects, the last maximum angular

velocity occurred from the relative motion of the left arm to the shoulders. For Subjects 1 and 5, the intersection of $ISAr_A$ was near the left glenohumeral joint, as expected. However, the position of $ISAr_A$ for Subjects 2, 3 and 4 was not representative of arm motion, as the intersection of this axis was at a considerable distance from the body segment. It is hypothesized that these disparities are the result of non-rigidities in the left shoulder joint and primarily from motion at the left elbow. This indicates that the assumption of the left arm acting as a rigid segment during the downswing does not hold for all subjects and that the use of an alternate marker configuration may be necessary. As was the case when studying the full motion of the golf club, the ISA of relative golf club motion could only be discussed for two subjects, as computational discontinuities did occur for most subjects. This indicates that further analysis into instances approaching an indeterminate ISA and alternate marker configurations should be investigated in order to accurately describe the relative motion of the golf club to the left arm using ISA theory.

5.4 Golf Club Head Velocity

The velocity of the golf club head was determined from the displacement of marker C4, affixed to the golf club head (see Section 3.4). This velocity, shown in Table 4-35, provides a quantifiable measure of the end result of the downswing sequence, and a comparison point between subjects. It is of particular interest to compare the magnitude and sequence of the maximum angular velocities to club head velocity at impact. The maximum angular velocity about the pelvis, ISA_P, shoulders, ISA_S, and left arm, ISA_A, are shown in Figure 5-12 for each subject. Furthermore, the instant corresponding to these maximum angular velocities is shown in Figure 5-13.

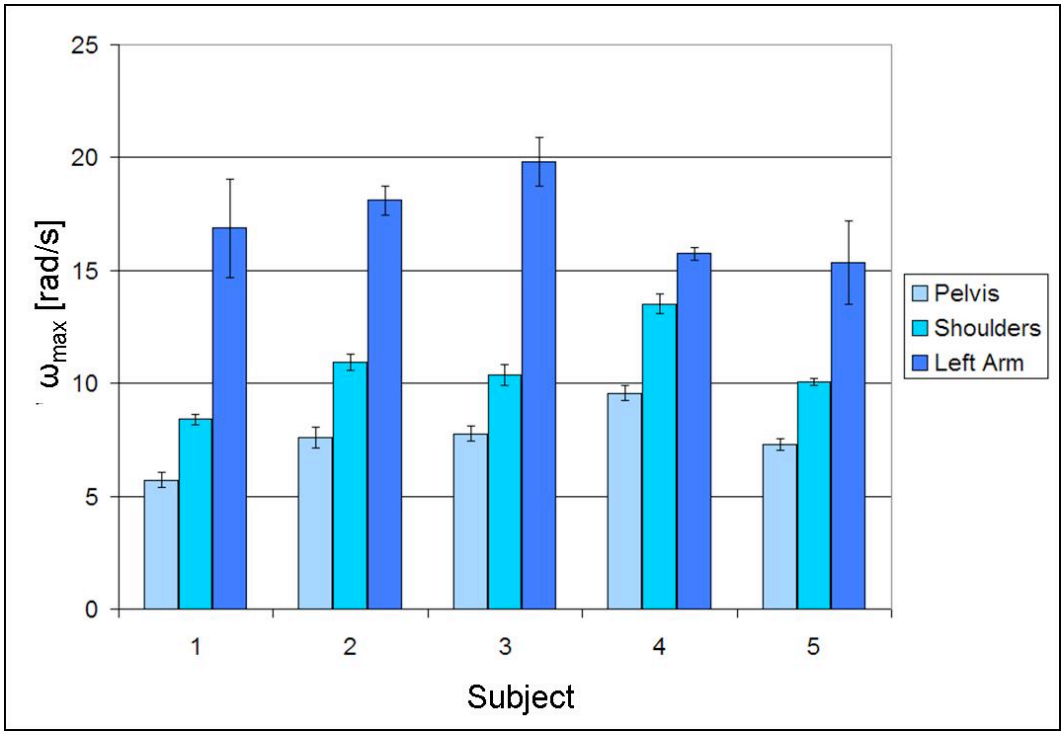

Figure 5-12: Subjects 1 to 5- Mean ω_{max}, with standard deviation error bars, about the pelvis (ISA_P), the shoulders (ISA_S) and the left arm (ISA_A)

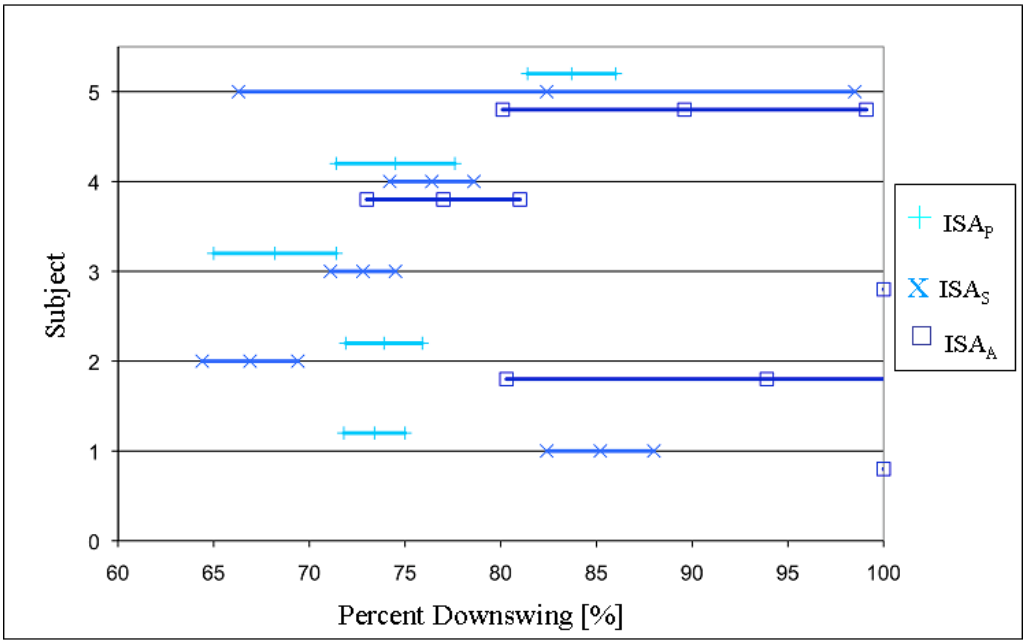

Figure 5-13: Subjects 1 to 5- Instances corresponding to ω_{max} about the pelvis (ISA_P), the shoulders (ISA_S) and the left arm (ISA_A). Data shown as horizontal bars spanning the percent downswing of each ω_{max}, with three tick marks: mean percent downswing minus 1 standard deviation, mean percent downswing and mean percent downswing plus 1 standard deviation. Subject data has been stratified for each segment from proximal (pelvis) to distal (left arm).

As previously discussed in Section 5.3.1, it is shown in Figure 5-12 that, for all subjects, the magnitude of ω_{max} increases from the most proximal segment, pelvis, to the most distal segment, left arm. This is an expected result, as the angular velocity should increase from the most distal segment to the most proximal, as the velocity increases from the contribution of each segment in the kinematic chain. This follows the summation of speed principle [Bunn (1972)], where the magnitude of segment velocity increases from proximal to distal. Furthermore, it is shown in Figure 5-13 that the body segments of Subject 1 achieved maximum angular velocities in a sequence starting from the most proximal segment, the pelvis, end ending with the most distal segment, the left arm. This sequence was also noted for Subjects 3 and 4, although the elapsed time between events was of smaller magnitude. Cheetham et al. [Cheetham et al. (2008)] reported the kinematic sequence of one professional golfer, where the angular velocity of the shoulders, thorax and left arm was given as a function of time. Although results were not explicitly given, the instances of maximum angular velocity were determined from interpolation of the given angular velocity plot and downswing duration. From these procedures, approximate percent downswing values of 60, 70 and 75 percent downswing were determined for the pelvis, thorax and left arm, respectively. This kinematic sequence is consistent with the results of Subjects 1, 3 and 4 of the current study. As the arm angular velocity reported by Cheetham et al. [Cheetham et al. (2008)] was computed perpendicular to an instantaneous swing plane, comparisons within this section will focus on motion of the pelvis and shoulders. Of Subjects 1, 2 and 3, Subject 3 has the lowest amount of difference with the data published by Cheetham et al. [Cheetham et al. (2008)], displaying errors of 11.7 and 3.4 percent downswing compared to the pelvis and thorax values, respectively. However, the difference in percent downswing between the instances of maximum angular velocities of the pelvis and shoulders of Subject 1 more closely resembles the data published by Cheetham et al. [Cheetham et al. (2008)], as the difference of 11.8 percent of Subject 1 resembles the difference of 12.89 for the professional golfer.

It is of interest to determine the effect of proper kinematic sequencing, as shown by Cheetham et al. [Cheetham et al. (2008)] and Subjects 1, 3 and 4, when compared to the kinematic sequence of Subjects 2 and 5, which do not follows a proximal to distal sequence. In order to make an appropriate comparison, subjects with similar physical attributes and maximum angular velocities, but varying kinematics sequences were compared. The two subjects that best satisfy these criteria are subjects 2 and 3, as the magnitude of angular velocities are comparable, as shown in Figure 5-12, while their kinematic sequences have different characteristics, as shown in Figure 5-13. A summary of the body segment maximum angular velocities and club head velocity of Subjects 2 and 3 is given in Table 5-3, as well as the percent difference between the two. The results of Table 5-3 indicate that ω_{max} about ISA_P is approximately the same for both subjects (Subject 3 larger by 2.1 percent of the mean value of Subject 2), while the value of ω_{max} about ISA_S for Subject 2 is 5.5 percent larger than the value of Subject 3. Even though the angular velocity of the shoulders for Subject 3 is slightly lower than that of Subject 2, the value of ω_{max} about ISA_A is 9.5 percent larger than the value of Subject 2 and the resulting club head velocity is also slightly larger than that of Subject 2 (larger by 3.4 percent). It is hypothesized that the following two reasons could be responsible for the larger angular velocity of the left arm and club head velocity of Subject 3, given that the angular velocity about its shoulders was smaller than that of Subject 2. First, it is possible that Subject 3 simply rotated their left arm at a higher velocity than Subject 2, by adding to the motion of the shoulders, while Subject 2 allowed the shoulders to drive the left arm. Second, as the kinematic sequence of Subject 3 is consistent with the summation of speeds principle [Bunn (1972)], whereby the most proximal segments decelerate before impact and impart their velocity to the more distal segments, it is possible that the momentum of the pelvis and shoulders summed together to propel the left arm at a higher velocity and consequently producing a higher club head velocity. Although the higher angular velocity about the shoulders and club head velocity of Subject 3 is not significantly larger in magnitude when compared to Subject 2, as the difference in both cases is below

10 percent of the mean value of Subject 2, it still supports the hypothesis that a proximal to distal kinematic sequence can increase club head velocity.

Table 5-3: Subjects 2 and 3- Comparison of body segment maximum angular velocity and club head velocity at impact. Percent difference computed as magnitude of Subject 3 minus the magnitude of Subject 2, divided by the magnitude of Subject 2 and expressed in percent.

Subject	ω_{max}			
	ISA_P [rad/s]	ISA_S [rad/s]	ISA_A [rad/s]	Club Head Velocity [m/s]
2	7.602	10.918	18.104	33.363
3	7.762	10.318	19.828	34.500
Percent Difference	2.1	-5.5	9.5	3.4

The club head velocity at impact for Subjects 2 to 4 ranged from 31.969 ± 0.478 m/s to 34.500 ± 0.800 m/s, the magnitude of Subject 1 measured 26.236 ± 0.883 m/s. This clearly shows that the club head velocity of Subject 1 was noticeably lower in magnitude when compared to the other subjects. During data collection, it was clear that Subject 1 was focused on making smooth, controlled golf swings as opposed to placing sole emphasis on club head velocity. Given that Subject 1 provided the clearest example of the summation of speeds principle, as shown in Figure 5-13, this may be a reflection of the controlled, lesser velocity golf swings of this subject.

Chapter 6 Conclusions and Future Work

There were three main objectives for the current study to achieve a better understanding of the rotational components of the golf swing. The first objective was to identify the location and orientation of ISAs of the major body segments involved in the golf swing motion. This represents the first study to provide an in depth investigation into the origins of the rotational components of the golf swing and in the process provides considerable insight into the assumptions of previous kinematic models. Mainly, this analysis could provide a basis for the selection of the position and displacement of the central hub, in planar double- and triple-link models, and the location and orientation of the segment local coordinates frames for three-dimensional kinematic models based on Euler/Cardan angle convention. These represent very important contributions to the field of golf biomechanics for the use of current kinematic models, as well as presenting an alternative analysis method. The second objective was to compute segment angular velocity relative to that segment's ISA. This angular velocity would provide the best estimate of a segment's gross rotation and represents one of the most important contributions of this study. The third objective was to verify that the amplitude and sequence of the maximum angular velocity of body segments follows the expected proximal to distal sequence brought forth by Cochran and Stobbs [Cochran and Stobbs (1968)]. This analysis could impart considerable insight into the kinematic sequence of events of the downswing, which is of considerable interest in the study of golf swing kinematics. The purpose of the following section is to discuss the main conclusions that can be drawn from this thesis and how they have met the objectives outlined above. It has been divided into three sections: Applicability of ISA Theory in the Study of Golf Biomechanics, Kinematic Sequence of the Golf Swing and Future Work.

6.1 Applicability of ISA Theory in the Study of Golf Biomechanics

As this study is the first to apply ISA theory to study the motion of the golf swing, to the knowledge of the current investigators, it is of interest to determine to what extent the applied methodologies accurately represent body motion. The computational techniques of Sections 3.3.3 and 3.3.4 produced rigid body motion from stereophotogrammetric measurements of body features. In the golf swing model, some body segments were assumed to act as rigid bodies even though noticeable relative motion between markers exists, such as the shoulders (from the left acromion to the right acromion) and the left arm (from the left acromion to the left wrist). Even in the case of these two segments, the magnitude of applied RMSE on marker position was smaller than the RMSE resulting from soft tissue artifact and marker placement error. This confirms that the applied error on marker position is smaller than the measurement error inherent to stereophotogrammetric systems, and therefore justifies these computational techniques. ISA computational errors were observed in this study, and it was hypothesized that these errors originated from instances approaching an undefined ISA and from non-rigidities between physiologically linked segments. These errors became apparent as differences between measured marker velocity, from numerical differentiation, and computed marker velocity, from motion about the segment's ISA. For ISA computation of complete segment motion, these errors only occurred for the motion of the golf club (ISA_C) and for three of the five subjects. The magnitude of these velocity errors represented an average of 36.28 percent of the magnitude of mean marker velocity. This indicates that the motion about ISA_C did not accurately describe golf club motion for all subjects. To counter these errors, perhaps a refinement of the diagnostic techniques, such as non-constant values of $ISA_{Diagnostic\,2}$ and $ISA_{Diagnostic\,3}$, or the use of an alternate marker configuration could help to reduced computational errors. That said, ISA computation of complete segment motion of the left leg, pelvis, shoulders and left arm produced negligible velocity errors representing less than an average of 1

percent of the magnitude of mean marker velocity. This confirms that the first objective of the study was met, as the location of ISA of the major body segments involved in the golf swing was established and motion about each ISA accurately represents body motion. For ISA computation of relative segment motion, computational errors only occurred for the motion of the golf club relative to the left arm ($ISAr_C$). The magnitude of these velocity errors represented an average of 39.65 percent of the magnitude of mean marker velocity. Again, it is assumed that two sources contributed to these errors: instances of an undefined ISA and non-rigidities between physiologically linked segments. To eliminate non-rigidities between linked segments, it is suggested to impose the use of a same marker for two consecutives ISAs. This procedure would impose ISA position, as the repeating marker would have no relative velocity, and the computation would determine the "best-fit" segment rotation about an axis passing through this marker. This would introduce a bias on ISA computation, eliminating a degree of freedom, but could become necessary for computations between the left arm and of golf club. That said, ISA computation of relative segment motion of the pelvis, shoulders and left arm produced negligible velocity errors representing less than an average of 2.5 percent of the magnitude of mean relative marker velocity. This confirms that the first objective of the study was met, as the location of ISA of the relative motion between the major body segments involved in the golf swing was established and motion about each ISAr accurately represents relative body motion.

One of the main assumptions of the golf swing model states that the motion of body segments in the downswing is primarily rotational and therefore most of segment motion would be represented by a rotation about its ISA. To verify this assumption, the ratio of parallel marker velocity, from segment translation, to total marker velocity was studied. For ISA computation of complete pelvis, shoulder, left arm and golf club segment motion, approximately 80 percent of marker velocity originated from rotation about each ISA, confirming the assumption of primarily rotational motion. For ISA computation of relative pelvis,

shoulder, left arm segment motion, approximately 75 percent of marker velocity originated from rotation about each ISAr, confirming the assumption for these segments. As the assumption of primarily rotational motion about the ISA of body segments was confirmed, for both complete and relative displacements, this validates the use of ISA theory in the golf swing model to study the rotation of the major body segments of the golf swing motion. This is a significant result, as it confirms that ISA theory can be applied in golf swing analysis and that pelvis, shoulder and left arm rotation can be effectively studied with the golf swing model. This is an important finding for the field of golf biomechanics, confirming that ISA theory can not only provide a new analysis method to study the extent and sequence of segment rotation, but can also be used to confirm or negate assumptions of previous kinematic models. Furthermore, this confirms the second objective of this study, as the angular velocity about a segment's ISA provides an important estimate of gross rotation. However, the motion of the golf club relative to the left arm did not verify this assumption, as an average of 42.8 percent of segment motion, for all subjects, consisted of a translation along each $ISAr_C$. As this does not confirm the assumption of relative motion from rotation about $ISAr_C$, it is needed to revise the analysis of relative motion between these two segments. Perhaps imposing the use of a repeating marker for the two segments, such as the displacement of the wrist centroid, would provide a good approximation of the relative rotation between the golf club and left arm.

6.2 Kinematic Sequence of the Golf Swing

The kinematic sequence of the golf swing was analyzed by computing the ISA of each major body segment involved in the motion. Perpendicular segment motion was then isolated to determine the angular velocity of each segment relative to their ISA. This marks the first study to quantify segment rotation about a non-stationary axis, resulting in the closest approximation to a segment's pure rotation and providing considerable insight into the rotational sequence of the golf swing. The ISA was first computed for each segment's complete motion, expressed

relative to the global reference frame. For all subjects, the magnitude of maximum angular velocities increased from the most proximal segment (the pelvis) to the most distal segment (the left arm), in accordance with the summation of speeds principle. This is a significant result, as this confirms that a segment's angular velocity about its ISA increases along the kinematic chain, producing the desired increase in velocity. This fulfills the third objective of the study for complete segment motion, as it is the first time that the sequence of angular velocities has been established from segment rotation about an ISA, consistent with gross segment rotation. Although the increase in magnitude was consistent for all subjects, the sequence at which these maximum angular velocities were reached varied. Three of the five subjects achieved their maximum angular velocities in the desired kinematic sequence, where the first maximum was achieved by the most proximal segment and followed by the more distal segments in the chain. This represents the first analysis where the proximal to distal sequence has been confirmed for motion about an ISA. This is a very exciting result for the analysis of the golf swing, as the current model not only provides a quantifiable measure of the kinematic sequence, that is when maximum angular velocities occur, but each maximum can occur about a non-fixed axis, which indicates where the maximum angular velocity occurs. For three subjects mentioned above, the first maximum angular velocity was reached by the pelvis, which confirms that the start of the downswing coincided with the motion of the pelvis. The ISA of the pelvis was located along the anterior/posterior axis of the pelvis and either aligned or slightly posterior to the hip joint centers, which could be affected by the lateral displacement of the pelvis during the downswing. For most subjects the orientation of ISA of the pelvis was consistent with the spine axis, and in some cases was located between the spine axis and the axis of the left leg, indicating a possible rotational component about the left leg. These results indicate that placing a local coordinate system aligned with the anterior/posterior axis of the pelvis, and either aligned or slightly posterior to the hip joint centers, provides the most appropriate coordinate system to represent pelvic rotation. Furthermore, incorporating an orthogonal axis parallel to the spine axis would provide an

effective reference axis. This is an important recommendation for future studies, based on the Euler/Cardan angle convention, for constructing a local coordinate frame of the pelvis. For these same three subjects, the second maximum angular velocity achieved was about the ISA of the shoulders. For these subjects, the shoulders followed the motion of the pelvis and continued the kinematic chain of the downswing. For the other two subjects of the study, the shoulders achieved their maximum angular velocity first, followed by the pelvis. This succession did not follow the desired proximal to distal sequence, not allowing for a proper summation of momentum. The ISA of the shoulders was located near the centroid of the shoulders, origin of the local coordinate frame, or slightly anterior and towards the left acromion. As was the case for the pelvis, the orientation of ISA was consistent with the spine axis, as expected. This confirms that, when studying the complete motion of the shoulders, the most appropriate position for the central hub (for planar rigid-linked models) or for the local coordinate system of the shoulders (for models based on Euler/Cardan conventions) would be consistent with the shoulder centroid and that an axis placed parallel to the spine axis would be most effective. This represents an important recommendation for current models that begin studying the kinematic sequence at the shoulder level, not incorporating the motion of the lower body. The final maximum angular velocity was achieved by the left arm, achieving either slightly before or coinciding with impact. For three out of the five subjects, the left arm ISA was consistent in position with the left glenohumeral joint, indicating relative motion about the left shoulder, while the other subjects produced an ISA closer to the shoulder centroid. The orientation of the left arm ISA was most consistent with the orientation of the spine axis, indicating that the largest component of left arm motion was from rotation about the shoulders. These results indicate two tendencies for ISA location: for two subjects the location is near the shoulder centroid, which would support the choice of a single upper link in the double-pendulum models, while for the three other subjects, the location is near the left shoulder joint, supporting the use of two-separate upper links consistent with triple-link models. Therefore, neither model can be said to be more consistent

with the results of the current study based on ISA position. However, the results do indicate that left arm ISA position can provide insight into which model to apply and, given a larger sampling population, could determine which of the two is most effective in representing left arm rotation.

Once the ISA was computed for each segment's complete motion, the relative motion between body segments was expressed in terms of a relative ISA. This provided insight into the individual contribution of each segment in the kinematic chain. This represents the first study to analyze the magnitude and sequence of the relative motion between segments in terms of angular velocity about an ISA. These results are of particular interest for fixed link models, such as the double- and triple-link planar models, as ISAr location and orientation can confirm or negate the need of placing a joint between segments. For all subjects, the angular velocity of the left arm, relative to the shoulders, had the highest magnitude of angular velocity. For most subjects, the angular velocities occurring strictly about the pelvis, relative to the left leg, and shoulders, relative to the pelvis, were approximately of the same magnitude. For three of the five subjects, the first maximum angular velocity reached in the kinematic chain occurred for pelvis motion. This confirmed for these subjects that the motion strictly about the pelvis initiated the downswing. For three of the five subjects, the ISA of relative pelvic motion was located in proximity to the left hip joint center, indicating motion about the left side of the pelvis. For the other subjects, this ISA was located near the pelvis centroid, which may have been a result of lesser weight transfer. These results indicate that the pelvis centroid might not be the most appropriate location to place a local coordinate system if trying to establish a kinematic chain with the segments of the lower body and could possibly be placed closer to the left hip joint centre. This is a very exciting finding, as it demonstrates that relative pelvic rotation may not occur about the centroid, but in some cases reflects the lateral shift towards the left leg. Furthermore, this is a very important recommendation for future models that which to incorporate the motion of the lower body with those of the upper body, which has yet to be seen. The orientation of ISA of

relative pelvis motion was less consistent with the orientation of the spine, when compared to ISA of complete pelvic motion, and more consistent with the orientation of the left leg. For these same three subjects, the second maximum angular velocity was achieved for the relative motion of the shoulders, indicating that motion purely about the shoulders follows the motion initiated by the pelvis. For the other two subjects, the relative motion of the shoulders commenced the downswing, not respecting the proximal to distal sequence. The intersection of ISA of relative shoulder motion was located anterior to the centroid of the shoulders, in proximity of the jugular notch, which may be a result of the difference in lateral displacement between the pelvis and shoulders during the downswing. Therefore, when analyzing the motion of the shoulders relative to the pelvis, the central hub or local coordinate frame consistent with the jugular notch would be most effective to characterize relation rotation. This represents a very important recommendation for future models that wish to incorporate the motion of the pelvis with those of the upper body, as the most effective location of the central hub would no longer be the shoulder centroid, used in current models, but rather the jugular notch. The orientation of this axis was less consistent with the spine axis, when compared to the orientation of ISA of complete shoulder motion, and appears more consistent with the z-axis of the shoulder local coordinate frame. As was the case for complete segment motion, the last maximum angular velocity for all subjects occurred from the motion of the left arm relative to the shoulders. For two of the five subjects, the position of the ISA of relative arm motion was near the left glenohumeral joint, as expected. However, for the other three subjects, the position of this ISA was not representative of arm motion, as the intersection of this axis was at a considerable distance from the body segment. It is hypothesized that these disparities are the result of non-rigidities in the left shoulder joint and motion about the left elbow. This indicates that the assumption of the left arm acting as a rigid segment during the downswing does not hold for all subjects and that alternate marker configurations should be investigated. However, from the two subjects indicating proximity to the left shoulder joint, it would seem that the location of the second joint for triple-link planar models and

of the local coordinate of the left shoulder should be consistent with the left shoulder joint.

6.3 Future Work

One of the main issues encountered during this study was the computation of the ISA of golf club motion. For three of the five subjects, discontinuities occurred in the computational process believed to originate from instances nearing an undefined ISA and non-rigidities between linked segments. As these discontinuities were sensitive to the computational diagnostic $ISA_{Diagnostic\,2}$ and $ISA_{Diagnostic\,3}$, it would be of interest to further investigate these instances and perhaps determine alternate compensation procedures. For example, when discontinuities occur, it could be of interest to determine an iterative procedure by which data points surrounding the discontinuity are removed until the RMSE between measured and computed marker velocity is reduced. Furthermore, it could be of interest to experiment with alternate marker configurations and study the possible effect.

One aspect of the golf swing model that could benefit from further analysis is the computation of an ISA from the relative motion between segments. This is of particular interest for segments that are not linked with rigid joints, such as the shoulders and left arm, and the left arm with the golf club. When considerable non-rigidities are present, the resulting ISA may be difficult to interpret, as was the case for most subjects when analyzing the relative motion between the shoulders and the left arm. As previously mentioned, the use of the same marker for two continuous segments would remove any non-rigidities between segments, while imposing ISA position. Although this imposes a bias on the computation, it could provide very interesting results for the motion of the left arm. For example, the use of a marker placed on the left acromion for both shoulder and left arm computation would produce an ISA consistent with the left acromion (near the left glenohumeral joint). For the ISA between the left arm and golf club, a marker representing the wrist centroid could be used in both computations. To ensure

than an ISA could be computed when a marker is used for two consecutive segments, one would have to ensure that the position of this marker would be maintained following the solidification procedure. Incorporating these procedures could eliminate the non-rigidities between linked segments and reduce the variability of results for the left-arm and golf club. This would result in a golf swing model where the relative motion between non-rigidly connected segments could be more easily interpreted, using a fixed axis position, while maintaining the variable orientation of the ISA method. This is an exiting prospect for both representing relative motion between non-rigidly connected segments and for establishing comparisons with other three-dimensional kinematic models.

References

Adams LP & Spirakis A (1997). Stereo photogrammetry. In J F Orr & J C Shelton (Eds.) *Optimal Measurement Methods In Biomechanics* (pp.17-38). London: Chapman & Hall.

Alonso FJ, Pintado P, Del Castillo JM (2005). Filtering of kinematic signals using the Hodrick-Prescott filter. *Journal of Applied Biomechanics*, 21(3), 271-285.

Andriacchi TP, Alexander EJ, Toney MK, Dyrby C & Sum J (1998). A point cluster method for in vivo motion analysis: applied to a study of knee kinematics. *Journal of Biomechanical Engineering*, 120(6), 743-749.

ASTM International (2008). Standard Practice for Use of the Terms Precision and Bias n ASMT Test Methods. Designation E 177 -08.

Bell AL, Pedersen DR & Brand RA (1990). A comparison of the accuracy of several hip center location prediction methods. *Journal of Biomechanics*, 23(6), 617-621.

Blankevoort L, Huiskes R & de Lange A (1990). Helical axes of passive knee joint motions. *Journal of Biomechanics*, 23(12), 1219-1229.

Bryant JT, Wevers HW & Lowe PJ (1984). One parameter model for error in instantaneous centre of rotation measurements. *Journal of Biomechanics*, 12(5), 317-323.

Bunn JW (1972). *Scientific Principles of Coaching*. New Jersey: Prentice-Hall.

Burden AM, Grimshaw PN & Wallace ES (1998). Hip and shoulder rotations during the golf swing of sub-10 handicap players, *Journal of Sports Sciences*, 16(2), 165-176.

Cappello A, La Palombara PF & Leardini A (1996). Optimization and smoothing techniques in movement analysis. *International Journal of Biomedical Computing*, 41(3), 137-151.

Cappozzo A, Catani F, Della Croce U & Leardini A (1995). Position and orientation in space of bones during movement: Anatomical frame definition and determination. *Clinical Biomechanics*, 10(4), 171-178.

Cappozzo A, Catani F, Leardini A, Benedetti MG & Croce UD (1996). Position and orientation in space of bones during movement: experimental artefacts. *Clinical Biomechanics*, 11(2), 90-100.

Cappozzo A, Della Croce U, Leardini A & Chiari L (2005). Human movement analysis using stereophotogrammetry. Part 1: theoretical background. *Gait & Posture*, 21(2), 186-196.

Cheetham PJ, Rose GA, Hinrichs RN, Neal RJ, Mottram RE, Hurrion, PD & Vint PF (2008). Comparison of Kinematic Sequence Parameters between Amateur and Professional Golfers. In D Crews & R Lutz (Eds.), Science and Golf V: Proceedings of the World Scientific Congress of Golf. Phoenix, Arizona.

Chèze L, Fregly BJ & Dimnet J (1995). A solidification procedure to facilitate kinematic analyses based on video system data. *Journal of Biomechanics*, 28(7), 879-884.

Chèze L, Fregly BJ & Dimnet J (1998). Determination of joint functional axes from noisy marker data using the finite helical axis. *Human Movement Science*, 17(1), 1-15.

Chiari L, Della Croce U, Leardini A & Cappozzo A (2005). Human movement analysis using stereophotogrammetry. Part 2: instrumental errors. *Gait & Posture*, 21(2), 197-211.

Cochran A & Stobbs J (1968). *The Search for the Perfect Swing*. New York: J. B. Lippincott Company

Craig JJ (2005). Jacobians: velocities and static forces. In A Dworkin, DA George, J Buckley & G Dulles (Eds.) *Introduction to Robotics: Mechanics and Control 3rd Edition* (pp.135-164). New Jersey: Pearson Prentice Hall.

Desjardins P, Plamondon A, Nadeau S & Delisle A (2002). Handling missing marker coordinates in 3D analysis. *Medical Engineering & Physics*, 24(6), 437-440.

Della Croce U, Cappozzo A & Kerrigan DC (1999). Pelvis and lower limb anatomical landmark calibration precision and its propagation to bone geometry and joint angles. *Medical & Biological Engineering & Computing*, 37(2), 155-161.

Della Croce U, Leardini A, Chiari L, Cappozzo A (2005). Human movement analysis using stereophotogrammetry. Part 4: assessment of anatomical landmark misplacement and its effects on joint kinematics. *Gait & Posture*, 21(2), 226-237.

Eberharter JK & Ravani B (2006). Kinematic registration in 3D using the 2D Reuleaux method. *Journal of Mechanical Design*, 128(2), 349-355.

Ehara Y, Fujimoto H, Miyazaki S, Mochimaru M, Tanaka S, Yamamoto S (1997). Comparison of the performance of 3D camera systems II. *Gait & Posture*, 5(3), 251-255.

Ehrig RM, Taylor WR, Duda GN & Heller MO (2007). A survey of formal methods for determining functional joint axes. *Journal of Biomechanics*, 40(10), 2150-2157.

Everaert DG, Spaepen AJ, Wouters MJ, Stappaerts KH & Oostendorp RA (1999). Measuring small linear displacements with a three-dimensional video motion analysis system: determining its accuracy and precision. *Archives of physical medicine and rehabilitation*, 80(9), 1082-1089.

Fuller J, Liu L-J, Murphy MC & Mann RW (1997). A comparison of lower-extremity skeletal kinematics measured using skin-and pin-mounted markers. Human Movement Science, 16(2), 219-242.

Gatt Jr CJ, Pavol MJ, Parker RD & Grabiner MD (1998). Three-dimensional knee joint kinetics during a golf swing: Influences of skill level and footwear. *The American Journal of Sports Medicine*, 26(2), 285-294.

Gazzani F (1993). Comparative assessment of two algorithms for calibrating stereophotogrammetric systems. *Journal of Biomechanics*, 26(12), 1449-1454.

Giakas G & Baltzopoulos V (1997). Optimal digital filtering requires a different cut-off frequency strategy for the determination of the higher derivatives. *Journal of Biomechanics*, 30(8), 851-855.

Giakas G, Stergioulas LK & Vourdas A (2000). Time-frequency analysis and filtering of kinematic signals with impacts using the Wigner function: accurate estimation of the second derivative. *Journal of Biomechanics*, 33(5), 567-574.

Gill HS, Morris J, Biden E & O'Connor JJ (1997). Optometric methods in biomechanical gait analysis. In JF Orr & JC Shelton (Eds.) *Optimal Measurement Methods In Biomechanics* (pp.125-153). London: Chapman & Hall.

Harmon B (2001). Butch's basics: Eight secrets I taught Tiger. *Golf Digest*, August 2001.

Herda L, Fua P, Plänkers R, Boulic R & Thalmann D (2001). Using skeleton-based tracking to increase the reliability of optical motion capture. *Human Movement Science*, 20(3), 313-341.

Holden JP, Orsini JA, Siegel KL, Kepple TM, Gerber LH & Stanhope SJ (1997). Surface movement errors in shank kinematics and knee kinetics during gait. *Gait & Posture*, 5(3), 217-227.

Holman JP (1984). Analysis of Experimental Data. In HK Rodger & S Hazlett (Eds.) *Experimental Methods for Engineers* (pp.46-99). New York: McGraw-Hill.

Jonsson H & Kärrholm J (1994). Three-dimensional knee joint movements during a step-up: evaluation after anterior cruciate ligament rupture. *Journal of Orthopedic Research*, 12(6), 769-779.

Jorgensen T (1970). On the Dynamics of the Swing of a Golf Club. *American Journal of Physics*, 38(5), 644-651.

Jorgensen TP (1994). *The Physics of Golf 1st Edition*. New York: Springer.

Kaneko Y & Sato F (2000). The Adaptation of golf swing inertia property of golf club. In AJ Subic & S Haake (Eds.), *The Engineering of Sport: Research, Development and Innovation* (pp. 469-476). London: Blackwell Science

Klein PJ & DeHaven JJ (1995). Accuracy of three-dimensional linear and angular estimates obtained with the Ariel Performance Analysis System. *Archives of Physical Medicine and Rehabilitation*, 76(2), 183-189.

Kreyszig E (1999a). Data Analysis. Probability Theory. In B Holland, S Malinowski (Eds.), *Advanced Engineering Mathematics 8th Edition* (pp.1050-1103). New York: John Wiley & Sons, Inc.

Kreyszig E (1999b). Fourier Analysis and Partial Differential Equations. In B Holland, S Malinowski (Eds.), *Advanced Engineering Mathematics 8th Edition* (pp.526-581). New York: John Wiley & Sons, Inc.

Kreyszig E (1999c). Vector Differential Calculus. In B Holland, S Malinowski (Eds.), *Advanced Engineering Mathematics 8th Edition* (pp.400-463). New York: John Wiley & Sons, Inc.

Kreyszig E (1999d). Numerical Methods in General. In B Holland, S Malinowski (Eds.), *Advanced Engineering Mathematics 8th Edition* (pp.830-885). New York: John Wiley & Sons, Inc.

Leardini A, Cappozzo A, Catani F, Toksvig-Larsen S, Petitto A, Sforza V, Cassanelli G & Giannini S (1999). Validation of a functional method for the estimation of hip joint centre location. *Journal of Biomechanics*, 32(1), 99-103.

Leardini A, Chiari L, Della Croce U, Cappozzo A (2005). Human movement analysis using stereophotogrammetry. Part 3. Soft tissue artifact assessment and compensation. *Gait & Posture*, 21(2), 212-225.

Leigh JR (1992). Discrete-time Signals; Idealized Approximation; Frequency Spectrum; Reconstruction. In *Applied Digital Control: Theory, Design and Implementation 2nd Edition* (pp.6-22). London: prentice Hall International.

Lewis JL & Lew WD (1978). A method for locating an optimal 'fixed' axis of rotation for the human knee joint. *Journal of Biomechanical Engineering*, 100, 187-193.

Lucchetti L, Cappozzo A, Cappello A & Della Croce U (1998). Skin movement artefact assessment and compensation in the estimation of knee-joint kinematics. *Journal of Biomechanics*, 31 (11), 977-984.

Maletsky LP, Sun J & Morton NA (2007). Accuracy of an optical active-marker system to track the relative motion of rigid bodies. *Journal of Biomechanics*, 40(3), 682-685.

McLaughlin PA & Best RJ (1994). Three-dimensional kinematic analysis of the golf swing. In AJ Cochran & MR Farrally (Eds.), Science and Golf II: Proceedings of the World Scientific Congress of Golf. University of St Andrews, Scotland.

McTeigue M, Lamb SR, Mottram R & Pirozzolo F (1994). Spine and hip motion analysis during the golf swing. In AJ Cochran & MR Farrally (Eds.), Science and Golf II: Proceedings of the World Scientific Congress of Golf. University of St Andrews, Scotland.

Motion Analysis (2006). Chapter 8: Calibration Panel. In EVaRT 5.0 (REV 2) User's Manual. Santa Rosa: Motion Analysis Corporation.

Moore KL & Dalley F (2006). *Clinically Oriented Anatomy 5th Edition*. Baltimore: Lippincott Williams & Wilkins.

Muijtjens AM, Roos JM, Arts T, Hasman A & Reneman RS (1997). Tracking markers with missing data by lower rank approximation. *Journal of Biomechanics*, 30(1), 95-98.

Miura K (2001). Parametric acceleration- the effect of inward pull of the golf club at impact stage. Sports Engineering, 4(4), 75-86.

Myers J, Lephart S, Tsai Y-S, Sell T, Smoliga J & Jolly J (2008). The role of upper torso and pelvis rotation in driving performance during the golf swing. *Journal of Sports Sciences*, 26(2), 181-188.

Nesbit SM (2005). A three dimensional kinematic and kinetic study of the golf swing. *Journal of Sports Science & Medicine*, 4(4), 499-519.

Nicholson WK (2003). Vector Geometry. In C Koop, D Hick, M Henderson & E Franks (Eds.), *Linear Algebra with Applications* 4th Edition (pp.143-184). Toronto: McGraw-Hill Ryerson Limited.

Page A, Candelas P, Belmar F & De Rosario H (2007). Analysis of 3D rigid-body motion using photogrammetry: A simple model based on a mechanical analogy. *American Journal of Physics*, 75(1), 56-61.

Panjabi MM (1979). Centers and angles of rotation of body joints: a study of errors and optimization. *Journal of Biomechanics*, 12(12), 911-920.

Penner AR (2003). The physics of golf. *Reports on Progress in Physics*, 66(2), 131-171.

Piazza SJ, Chou L-S, Denniston NL, McMulkin ML, Quigley EJ, Richards JG & Schwartz MS (2007). A proposed standard for assessing the marker-location accuracy of video-based motion analysis systems. In proceedings of the 12th Annual Gait and Clinical Movement Analysis Society, Springfield.

Pickering WM & Vickers GT (1999). On the double pendulum model of the golf swing. *Sports Engineering*, 2 (4), 161-172.

Polk JD, Psutka SP & Demes B (2005). Sampling frequencies and measurement error for linear and temporal gait parameters in primate locomotion. *Journal of Human Evolution*, 49(6), 665-679.

Reinschmidth C, van den Bogent AJ & Lundberg A (1999). Finite helical axes of the tibiofemoral joint during locomotion. In proceedings of the 17th Congress of the International Society of Biomechanics. Calgary, Canada.

Reuleaux F (1963). The Kinematics of Machinery: outline of a Theory of Machines. New York: Dover Publications.

Richards JG (1999). The measurement of human motion: A comparison of commercially available systems. *Human Movement Science*, 18(5), 589-602.

Robinson RL (1994). A study of the correlation between swing characteristics and club head velocity. In AJ Cochran & MR Farrally (Eds.), Science and Golf II: Proceedings of the World Scientific Congress of Golf. University of St Andrews, Scotland.

Ross SM (1987). Elements of Probability. In *Introduction to Probability and Statistics for Engineers and Scientists* (pp.1-23). New York: John Wiley & Sons.

Sati M, De Guise JA, Larouche S & Drouin G (1996). Quantitative assessment of skin-bone movement at the knee. *The knee*, 3(3), 121-138.

Schenck H (1979). Graphical and Statistical Analysis: Data of Low Precision (pp.227-254). In RW Larson & L Lackenbach (Eds.) *Theories of Engineering Experimentation*. New York: McGraw-Hill.

Shikin EV & Plis AI (1995). Spline functions of one variable. *In Handbook on Splines for the User* (pp.11-46). Boca Raton: CRC Press.

Söderkvist I & Wedin P-A (1993). Determining the movements of the skeleton using well-configured markers. *Journal of Biomechanics*, 26(12), 1473-1477.

Sprigings EJ & Neal RJ (2000). An Insight Into the Importance of Wrist Torque in Driving the Golfball: A Simulation Study. *Journal of Applied Biomechanics*, 16(4), 356-366.

Stokdijk M, Meskers CG, Veeger HE, de Boer Y A, Rozing PM (1999). Determination of the optimal elbow axis for evaluation of placement of prostheses. *Clinical Biomechanics*, 14(3), 177-184.

Stokdijk M, Nagels J, Rozing PM (2000). The glenohumeral joint rotation centre in vivo. *Journal of Biomechanics*, 33(12), 1629-1636.

Taylor JR (1982a). Statistical Analysis of Random Uncertainties. In ED Commins (Ed.) *An Introduction to Error Analysis: The Study of Uncertainties in Physical Measurements* (pp.81-98). Mill Valley: University Science Books.

Taylor JR (1982b). Preliminary Description of Error Analysis. In ED Commins (Ed.) *An Introduction to Error Analysis: The Study of Uncertainties in Physical Measurements* (pp.3-13). Mill Valley: University Science Books.

Taylor JR (1982c). Rejection of Data. In ED Commins (Ed.) *An Introduction to Error Analysis: The Study of Uncertainties in Physical Measurements* (pp.141-146). Mill Valley: University Science Books.

Taylor JR (1982d). How to Report and Use Uncertainties. In ED Commins (Ed.) *An Introduction to Error Analysis: The Study of Uncertainties in Physical Measurements* (pp.141-146). Mill Valley: University Science Books.

Teu KK, Kim W, Fuss FK & Tan J (2006). The analysis of golf swing as a kinematic chain using dual Euler angle algorithm. *Journal of Biomechanics*, 39(7), 1227-1238.

Turner AB & Hills NJ (1998). A Three-Link Mathematical Model of the Golf Swing. In M R Farrally & A J Cochran (Eds.), Science and Golf III: Proceedings of the World Scientific Congress of Golf. University of St Andrews, Scotland.

Veeger HEJ, Yu B & An KN (1996). Orientation of axes in the elbow and forearm for biomechanical modeling. In proceedings of the First Conference of the International Shoulder Group. Delft University, Delft.

Veldpaus FE, Woltring HJ & Dortmans LJ (1988). A least-squares algorithm for the equiform transformation from spatial marker co-ordinates. *Journal of Biomechanics*, 21(1), 45-54.

Watanabe K & Hokari M (2006). Measurement of 3-D loci and attitudes of the golf driver head while swinging. *IEEE transactions on systems, man and cybernetics. Part A. Systems and humans*, 36(6), 1161-1169.

Winter DA (2004). Kinematics. In Biomechanics and Motor Control of Human Movement 3rd edition (pp.13-58). New Jersey: John Wiley & Sons Inc.

Woltring HJ, Huiskes R, de Lange A & Veldpaus FE (1985). Finite centroid and helical axis estimation from noisy landmark measurements in the study of human joint kinematics. *Journal of Biomechanics*, 18(5), 379-389.

Woltring HJ (1994a). 3-D attitude representation of human joints: a standardization proposal. *Journal of Biomechanics*, 27(12), 1399-1414.

Woltring HJ, Long K, Osterbauer PJ & Fuhr AW (1994b). Instantaneous helical axis estimation from 3-D video data in neck kinematics for whiplash diagnostics. *Journal of Biomechanics*, 27(12), 1415-1432.

Woltring HJ (1995). Smoothing and Differentiation Techniques Applied to 3-D Data. In P Allard, IAF Stokes & J-P Blanchi (Eds.) *Three-Dimensional Analysis of Human Movement* (pp.57-78). Illinois: Human Kinetics.

Wu G, van der Helm FC, Veeger HE, Makhsous M, Van Roy P, Anglin C, Nagels J, Karduna AR, McQuade K, Wang X, Werner FW & Buchholz B (2005). ISB recommendation on definitions of joint coordinate systems of various joints for the reporting of human joint motion--Part II: shoulder, elbow, wrist and hand. *Journal of Biomechanics*, 38(5), 981-992.

Appendix 1 Stereophotogrammetric system calibration

Calibration of stereophotogrammetric system

Before data can be collected, the stereophotogrammetric system must go through a two-step calibration process. First, a static calibration is conducted by placing the *seed* at the origin of the calibration volume (Figure A1-1a). The *seed* is an L-shaped bar fitted with 4 reflective spherical markers, which determines the direction of the X-Y axes, from which the Z-axis can be located. Once this step is completed, the cameras are said to be "seeded", which means that they have been located relative to the coordinate system. Second, a dynamic calibration is done by waving the *wand* within the desired volume of capture (Figure A1-1b). The *wand* is a T-shaped bar fitted with three reflective spherical markers, where the two end markers are at a calibrated distance of 500mm. While the *wand* is circulating within the volume, the system measures the distance between markers and adjusts the settings of its cameras. The calibration is complete when the measurements are within a prescribed tolerance of the reference length, chosen as 0.5mm.

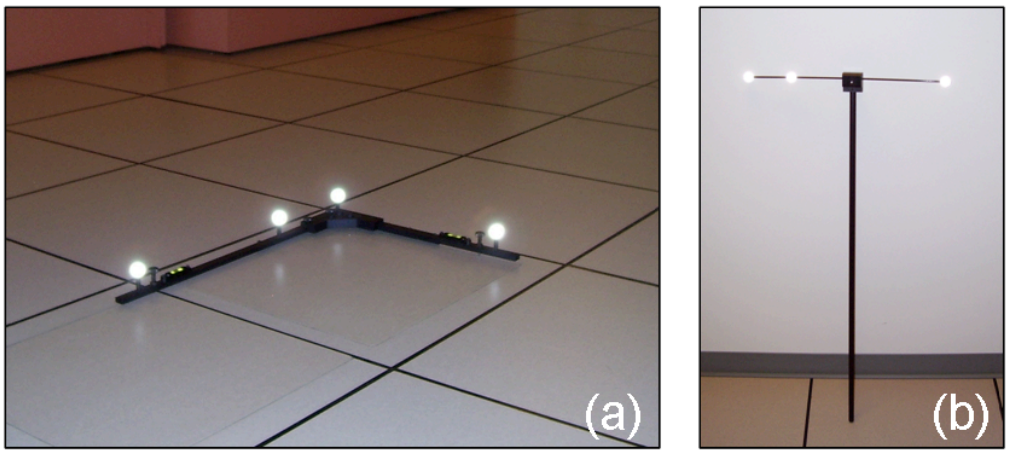

Figure A1-1: Stereophotogrammetric system calibration; (a) Static calibration seed, (b) Dynamic calibration wand

Appendix 2 Measurement Accuracy Study

A2.1 CMM Calibration of the Experimental Apparatus

Rotational Apparatus

The references distances of the rotational apparatus, *Length 1* and *Length 2*, were calibrated by CMM measurement of maker coordinates. The coordinates of the centroid of *Markers 1*, *2* and *3*, are given in Table A2-1, while the inter-marker distances are given in Table A2-2.

Table A2-1: Rotational Apparatus; Marker Coordinates

Marker	Coordinate	Trial No. 1 [mm]	Trial No. 2 [mm]	Trial No. 3 [mm]	Mean [mm]
1	x	193.271	193.261	193.288	193.273
	y	-222.872	-222.86	-222.848	-222.860
	z	-225.771	-225.855	-225.922	-225.849
2	x	211.814	211.819	211.884	211.839
	y	-96.851	-96.963	-96.899	-96.904
	z	-228.239	-228.054	-227.948	-228.080
3	x	173.804	173.814	173.856	173.825
	y	-97.071	-97.102	-96.961	-97.045
	z	-228.125	-228.057	-228.201	-228.128

Table A2-2: Rotational Apparatus; Reference Lengths

Reference Length	Vector components v_x [mm]	v_y [mm]	v_z [mm]	Distance [mm]
1	-18.566	-125.956	2.231	127.336
2	38.014	0.140	0.047	38.015

Translational Apparatus

The inter-maker displacements of the translational apparatus were determined by CMM measurement of marker centroids. The coordinates of the *Stationary* and *Translating* markers were measured for all micrometer positions and the resulting displacements were calculated, given in Table A2-3.

Table A2-3: CMM Calibration of the Translational Apparatus

Trial No.	Marker	Micrometer position	Coordinates			Position vector (to *Stationary* marker)			Displacement vector			Displacement	
			x	y	z	x	y	z	x	y	z		Mean
		[in]	[mm]	[mm]	[mm]	[mm]	[mm]	[mm]	[mm]	[mm]	[mm]	[mm]	[mm]
1	Stationary	N/A	271.308	-369.525	-301.164								
	Translating	0.000	222.352	-368.835	-301.504	-48.956	0.69	-0.34					
		0.025	222.984	-368.751	-301.578	-48.324	0.774	-0.414	0.632	0.084	-0.074	0.642	
		0.050	223.661	-368.862	-301.545	-47.647	0.663	-0.381	1.309	-0.027	-0.041	1.310	
		0.100	225.01	-368.787	-301.298	-46.298	0.738	-0.134	2.658	0.048	0.206	2.666	
		0.250	228.76	-368.794	-301.637	-42.548	0.731	-0.473	6.408	0.041	-0.133	6.410	
		0.400	232.52	-368.757	-301.739	-38.788	0.768	-0.575	10.168	0.078	-0.235	10.171	
2	Stationary	N/A	271.432	-369.47	-301.679								
	Translating	0.000	222.465	-368.777	-301.681	-48.967	0.693	-0.002					
		0.025	223.069	-368.809	-301.744	-48.363	0.661	-0.065	0.604	-0.032	-0.063	0.608	0.646
		0.050	223.637	-368.843	-301.557	-47.795	0.627	0.122	1.172	-0.066	0.124	1.180	1.257
		0.100	224.882	-368.799	-301.31	-46.55	0.671	0.369	2.417	-0.022	0.371	2.445	2.571
		0.250	228.719	-368.878	-301.62	-42.713	0.592	0.059	6.254	-0.101	0.061	6.255	6.350
		0.400	232.47	-368.8	-301.653	-38.962	0.67	0.026	10.005	-0.023	0.028	10.005	10.117
3	Stationary	N/A	271.4	-369.58	-301.275								
	Translating	0.000	222.342	-368.879	-301.678	-49.058	0.701	-0.403					
		0.025	223.001	-368.915	-301.488	-48.399	0.665	-0.213	0.659	-0.036	0.19	0.687	
		0.050	223.62	-368.784	-301.657	-47.78	0.796	-0.382	1.278	0.095	0.021	1.282	
		0.100	224.942	-368.826	-301.687	-46.458	0.754	-0.412	2.6	0.053	-0.009	2.601	
		0.250	228.725	-368.86	-301.471	-42.675	0.72	-0.196	6.383	0.019	0.207	6.386	
		0.400	232.515	-368.83	-301.513	-38.885	0.75	-0.238	10.173	0.049	0.165	10.174	

A2.2 Results

A2.2.1 Rotational Accuracy

The results of the Rotational Accuracy section of the Measurement Accuracy Study are given in Table A2-4 to Table A2-11. This outlines the accuracy of measuring reference *Length 1* and *Length 2* of the rotational apparatus. Furthermore, statistical variance was analyzed for measurements taken at different sampling rates and different settings within the measurement volume.

Length 1 Measurement

Measurement bias and precision of reference *Length 1* are given in Table A2-4 and Table A2-5, respectively, while statistical variance tests and student t-tests on the measurement populations of *Length 1* are given in Table A2-6 and Table A2-7, respectively.

Table A2-4: Rotational Accuracy- Length 1 Measurement Bias as a function of Position, Height and Speed (S1 to S5)

Position	Height	Sampling Rate [Hz]	Length 1 Measurement Bias S1 [mm]	S2 [mm]	S3 [mm]	S4 [mm]	S5 [mm]	Maximum Bias Bias [mm]	Speed
1	1	60	0.017	0.0278	0.4761	0.1247	0.2888	0.4761	3
		125	0.0534	0.0288	0.0766	0.0021	0.2755	0.2755	5
		250	0.1958	0.3262	0.2164	0.2438	0.4195	0.4195	5
		500	0.2498	0.5281	0.3242	0.2992	0.2034	0.5281	2
	2	60	0.5037	0.9963	1.2891	1.0521	1.016	1.2891	3
		125	0.76	1.0326	1.0057	1.1933	1.0911	1.1933	4
		250	0.6463	0.748	0.5417	0.9066	0.8185	0.9066	4
		500	0.3735	0.4509	0.4855	0.116	0.1397	0.4855	3
2	1	60	0.1038	0.1396	0.0525	0.0891	0.0869	0.1396	2
		125	0.0545	0.1507	0.1078	0.1367	0.0962	0.1507	2
		250	0.1813	0.2613	0.2678	0.1628	0.1124	0.2678	3
		500	0.2475	0.3022	0.068	0.1079	0.1461	0.3022	2
	2	60	0.8475	0.7234	0.8336	0.759	0.7397	0.8475	1
		125	0.823	0.9653	0.8457	0.6903	0.7915	0.9653	2
		250	0.9209	0.8307	0.896	0.9784	0.9282	0.9784	4
		500	0.8023	0.8994	0.928	0.5014	0.5491	0.928	3
3	1	60	0.0568	0.1718	0.1055	0.173	0.0729	0.173	4
		125	0.0321	0.0187	0.1589	0.0801	0.1047	0.1589	3
		250	0.1689	0.3152	0.1202	0.1072	0.0537	0.3152	2
		500	0.4326	0.2394	0.3946	0.1587	0.1919	0.4326	1
	2	60	0.2389	0.1786	0.1196	0.3348	0.367	0.367	5
		125	0.0833	0.3501	0.2027	0.2827	0.2575	0.3501	2
		250	0.3248	0.329	0.5019	0.5062	0.343	0.5062	4
		500	0.3659	0.4457	0.439	0.4248	0.6268	0.6268	5

Table A2-5: Rotational Accuracy- Length 1 Measurement Precision (S) as a function of Position, Height and Speed (S1 to S5)

Position	Height	Sampling Rate [Hz]	Length 1 Measurement Precision S1 [mm]	S2 [mm]	S3 [mm]	S4 [mm]	S5 [mm]	Max Precision (S) Max S [mm]	Speed
1	1	60	0.1604	0.1741	0.3001	0.2392	0.237	0.3001	3
		125	0.0608	0.0645	0.1631	0.1281	0.2028	0.2028	5
		250	0.1252	0.0545	0.1306	0.3623	0.2257	0.3623	4
		500	0.0627	0.1472	0.1278	0.1185	0.0233	0.1472	2
	2	60	0.194	0.4949	0.2409	0.0678	0.3384	0.4949	2
		125	0.2502	0.3896	0.372	0.2653	0.098	0.3896	2
		250	0.2128	0.2522	0.144	0.7447	0.6582	0.7447	4
		500	0.1925	0.1625	0.2135	0.1001	0.3589	0.3589	5
2	1	60	0.0795	0.0051	0.0426	0.0965	0.0552	0.0965	4
		125	0.0704	0.0325	0.0399	0.0553	0.0759	0.0759	5
		250	0.0498	0.154	0.0879	0.0872	0.0623	0.154	2
		500	0.0429	0.0243	0.1344	0.1456	0.1311	0.1456	4
	2	60	0.2246	0.0606	0.0771	0.0932	0.2111	0.2246	1
		125	0.2487	0.2006	0.1681	0.187	0.0765	0.2487	1
		250	0.1439	0.2521	0.1499	0.2908	0.33	0.33	5
		500	0.8139	0.2393	0.1231	0.3989	0.2056	0.8139	1
3	1	60	0.1707	0.0151	0.1551	0.3114	0.1069	0.3114	4
		125	0.1106	0.3366	0.1711	0.1225	0.3299	0.3366	2
		250	0.096	0.5033	0.0646	0.2665	0.1933	0.5033	2
		500	0.2053	0.1037	0.605	0.1338	0.192	0.605	3
	2	60	0.212	0.024	0.0551	0.1655	0.0677	0.212	1
		125	0.1228	0.2507	0.1428	0.1163	0.1869	0.2507	2
		250	0.0984	0.0385	0.1184	0.248	0.0508	0.248	4
		500	0.0464	0.0729	0.0733	0.0843	0.0756	0.0843	4

Table A2-6: Rotational Accuracy- Length 1 Variance Test for each Position (Pos.), Height (H.) and Speed population

Pos.	H.	Population (x vs. y)	Length 1 Variance Test									
			Speed 1		Speed 2		Speed 3		Speed 4		Speed 5	
			h	S_x/S_y	h	S_x/S_y	h	S_x/S_y	h	S_x/S_y	h	S_x/S_y
1	1	1 vs. 2	1	2.6394	1	2.7003	0	1.8399	0	1.8672	0	1.1688
		1 vs. 3	0	1.2812	1	3.1912	1	2.299	0	1.5147	0	1.0498
		1 vs. 4	1	2.5589	0	1.1823	1	2.3478	1	2.0183	1	10.187
		2 vs. 3	1	2.0602	0	1.1818	0	1.2495	1	2.8282	0	1.1133
		2 vs. 4	0	1.0315	1	2.284	0	1.2761	0	1.0809	1	8.7163
		3 vs. 4	0	1.9973	1	2.6993	0	1.0212	1	3.0571	1	9.7043
	2	1 vs. 2	0	1.2902	0	1.2703	0	1.544	1	3.9138	1	3.4535
		1 vs. 3	0	1.0971	0	1.9621	0	1.6734	1	10.987	0	1.9448
		1 vs. 4	0	1.0074	1	3.0459	0	1.1283	0	1.4766	0	1.0605
		2 vs. 3	0	1.1761	0	1.5445	1	2.5838	1	2.8072	1	6.7162
		2 vs. 4	0	1.2997	1	2.3978	0	1.7422	1	2.6506	1	3.6625
		3 vs. 4	0	1.1051	0	1.5524	0	1.4831	1	7.4407	0	1.8338
2	1	1 vs. 2	0	1.1299	1	6.3318	0	1.0672	0	1.7456	0	1.3734
		1 vs. 3	0	1.5982	1	30.011	1	2.0642	0	1.1057	0	1.1286
		1 vs. 4	0	1.8524	1	4.7437	1	3.1541	0	1.51	1	2.3739
		2 vs. 3	0	1.4145	1	4.7397	1	2.2029	0	1.5788	0	1.2168
		2 vs. 4	0	1.6395	0	1.3348	1	3.3661	1	2.636	0	1.7285
		3 vs. 4	0	1.1591	1	6.3265	0	1.528	0	1.6696	1	2.1033
	2	1 vs. 2	0	1.1073	1	3.3125	1	2.18	1	2.0064	1	2.7601
		1 vs. 3	0	1.561	1	4.1625	0	1.9432	1	3.1193	0	1.5635
		1 vs. 4	1	3.6243	1	3.951	0	1.5958	1	4.2792	0	1.0267
		2 vs. 3	0	1.7285	0	1.2566	0	1.1219	0	1.5547	1	4.3155
		2 vs. 4	1	3.2731	0	1.1928	0	1.3661	1	2.1328	1	2.6882
		3 vs. 4	1	5.6574	0	1.0535	0	1.2177	0	1.3719	0	1.6053
3	1	1 vs. 2	0	1.5437	1	22.3411	0	1.1031	1	2.5416	1	3.0857
		1 vs. 3	0	1.7775	1	33.4029	1	2.4017	0	1.1687	0	1.8082
		1 vs. 4	0	1.203	1	6.8826	1	3.9008	1	2.3272	0	1.7964
		2 vs. 3	0	1.1514	0	1.4951	1	2.6494	1	2.1747	0	1.7065
		2 vs. 4	0	1.8571	1	3.246	1	3.5361	0	1.0921	0	1.7177
		3 vs. 4	1	2.1384	1	4.8532	1	9.3686	0	1.9913	0	1.0066
	2	1 vs. 2	0	1.7262	1	10.4595	1	2.592	0	1.4232	1	2.7591
		1 vs. 3	1	2.1542	0	1.6076	1	2.1495	0	1.4988	0	1.3337
		1 vs. 4	1	4.5668	1	3.0425	0	1.3304	0	1.9635	0	1.1161
		2 vs. 3	0	1.2479	1	6.5063	0	1.2059	1	2.1331	1	3.6798
		2 vs. 4	1	2.6455	1	3.4378	0	1.9483	0	1.3796	1	2.4722
		3 vs. 4	1	2.1199	0	1.8926	0	1.6157	1	2.943	0	1.4885
Σh_1			11		23		15		18		15	

Table A2-7: Rotational Accuracy- Length 1 Student T-Test for each Position (Pos.), Height (H.) and Speed population

Pos.	H.	Population	Length 1 Student T-Test									
		(x vs. y)	Speed 1		Speed 2		Speed 3		Speed 4		Speed 5	
			h	p-value	h	p-value	h	p-value	h	p-value	h	p-value
1	1	1 vs. 2	0	0.5164	0	0.6252	1	0.0487	0	0.4777	0	0.9446
		1 vs. 3	0	0.1442	1	0.0283	0	0.2413	0	0.6596	0	0.5272
		1 vs. 4	0	0.055	1	0.0134	0	0.4654	0	0.321	0	0.5677
		2 vs. 3	0	0.1509	1	0.0037	0	0.0721	0	0.3373	0	0.4572
		2 vs. 4	1	0.0176	1	0.0058	1	0.0286	1	0.0421	0	0.5733
		3 vs. 4	0	0.5402	0	0.0899	0	0.3643	0	0.8138	0	0.1743
	2	1 vs. 2	0	0.2335	0	0.9251	0	0.3302	0	0.4222	0	0.7309
		1 vs. 3	0	0.4393	0	0.482	1	0.0099	0	0.753	0	0.6679
		1 vs. 4	0	0.4558	0	0.1439	1	0.0124	1	0.0002	1	0.037
		2 vs. 3	0	0.5812	0	0.3479	0	0.1141	0	0.564	0	0.5172
		2 vs. 4	0	0.1013	0	0.0754	0	0.1036	1	0.0028	1	0.0114
		3 vs. 4	0	0.175	0	0.1614	0	0.7251	0	0.1425	0	0.1919
2	1	1 vs. 2	0	0.4668	0	0.5922	0	0.1766	0	0.5002	0	0.8718
		1 vs. 3	0	0.2257	0	0.2434	1	0.0188	0	0.382	0	0.6238
		1 vs. 4	0	0.0511	1	0.0003	0	0.8584	0	0.8616	0	0.5111
		2 vs. 3	0	0.0635	0	0.2905	1	0.0454	0	0.6833	0	0.7892
		2 vs. 4	1	0.0154	1	0.003	0	0.649	0	0.7651	0	0.5991
		3 vs. 4	0	0.156	0	0.6732	0	0.0974	0	0.605	0	0.7085
	2	1 vs. 2	0	0.9054	0	0.1163	0	0.9151	0	0.5996	0	0.7097
		1 vs. 3	0	0.6585	0	0.5132	0	0.5563	0	0.2812	0	0.4513
		1 vs. 4	0	0.9306	0	0.2847	0	0.3231	0	0.3374	0	0.3253
		2 vs. 3	0	0.5869	0	0.5096	0	0.7187	0	0.2224	0	0.5229
		2 vs. 4	0	0.9684	0	0.7333	0	0.5314	0	0.499	0	0.1281
		3 vs. 4	0	0.816	0	0.7496	0	0.789	0	0.1695	0	0.1665
3	1	1 vs. 2	0	0.844	0	0.3829	0	0.7093	0	0.6558	0	0.4252
		1 vs. 3	0	0.3773	0	0.6478	0	0.0805	0	0.3019	0	0.3772
		1 vs. 4	0	0.0714	0	0.3266	0	0.2377	0	0.945	0	0.1052
		2 vs. 3	0	0.1809	0	0.3937	0	0.0574	0	0.3306	0	0.8285
		2 vs. 4	1	0.041	0	0.2732	0	0.202	0	0.4951	0	0.7124
		3 vs. 4	0	0.1142	0	0.8111	0	0.4784	0	0.1974	0	0.4291
	2	1 vs. 2	0	0.333	0	0.3037	0	0.3999	0	0.6782	0	0.3939
		1 vs. 3	0	0.5592	1	0.0046	1	0.0071	0	0.3759	0	0.6485
		1 vs. 4	0	0.3682	1	0.0038	1	0.0038	0	0.4484	1	0.0114
		2 vs. 3	0	0.0565	0	0.8923	1	0.0491	0	0.2305	0	0.4871
		2 vs. 4	1	0.0203	0	0.5604	0	0.0633	0	0.1616	1	0.0338
		3 vs. 4	0	0.5485	0	0.0704	0	0.4778	0	0.6193	1	0.0057

Length 2 Measurement

Measurement bias and precision of reference *Length 2* are given in Table A2-8 and Table A2-9, respectively, while statistical variance tests and student t-tests on the measurement populations of *Length 2* are given in Table A2-10 and Table A2-11, respectively.

Table A2-8: Rotational Accuracy- Length 2 Measurement Bias as a function of Position, Height and Speed (S1 to S5)

Position	Height	Sampling Rate [Hz]	Length 2 Measurement Bias S1 [mm]	S2 [mm]	S3 [mm]	S4 [mm]	S5 [mm]	Maximum Bias Max Bias [mm]	Speed
1	1	60	0.0896	0.1241	0.6713	0.5402	0.2895	0.6713	3
		125	0.0908	0.2591	0.4359	0.5474	0.5053	0.5474	4
		250	0.0949	0.1569	0.1133	0.3316	0.2418	0.3316	4
		500	0.1143	0.1045	0.0409	0.0034	0.145	0.145	5
	2	60	0.7866	0.2932	0.578	0.2639	0.7348	0.7866	1
		125	0.3559	0.1481	0.9036	0.2915	0.6069	0.9036	3
		250	0.1824	0.2668	0.2164	0.6163	0.3608	0.6163	4
		500	0.1442	0.0732	0.0431	0.2413	0.1735	0.2413	4
2	1	60	0.1299	0.1084	0.0711	0.0786	0.0247	0.1299	1
		125	0.1314	0.1305	0.1146	0.119	0.0556	0.1314	1
		250	0.1788	0.0513	0.0248	0.0444	0.0127	0.1788	1
		500	0.1971	0.0963	0.077	0.0231	0.0159	0.1971	1
	2	60	0.1827	0.2578	0.2594	0.2852	0.0067	0.2852	4
		125	0.4593	0.2155	0.0659	0.2515	0.1779	0.4593	1
		250	0.4139	0.0732	0.204	0.3622	0.0762	0.4139	1
		500	0.4244	0.3441	0.4332	0.0569	0.0089	0.4332	3
3	1	60	0.0881	0.0112	0.1663	0.1984	0.2162	0.2162	5
		125	0.1134	0.0708	0.1221	0.0119	0.1597	0.1597	5
		250	0.099	0.2706	0.1964	0.2799	0.0864	0.2799	4
		500	0.0997	0.0613	0.2492	0.0732	0.1683	0.2492	3
	2	60	0.1434	0.207	0.252	0.3198	0.0903	0.3198	4
		125	0.3151	0.3397	0.3124	0.2834	0.1809	0.3397	2
		250	0.2863	0.2822	0.3806	0.1447	0.0969	0.3806	3
		500	0.1017	0.2784	0.1937	0.1629	0.2691	0.2784	2

Table A2-9: Rotational Accuracy- Length 2 Measurement Precision (S) as a function of Position, Height and Speed (S1 to S5)

Position	Height	Sampling Rate [Hz]	Length 2 Measurement Standard Deviation S1 [mm]	S2 [mm]	S3 [mm]	S4 [mm]	S5 [mm]	Max Precision (S) Max S [mm]	Speed
1	1	60	0.0784	0.1415	0.5959	0.4001	0.3744	0.5959	3
		125	0.2668	0.1717	0.2757	0.1862	0.2379	0.2757	3
		250	0.0851	0.2332	0.1515	0.1552	0.2626	0.2626	5
		500	0.0861	0.0312	0.0311	0.1398	0.0321	0.1398	4
	2	60	0.2222	0.1718	0.4265	0.6191	0.36	0.6191	4
		125	0.2688	0.1977	0.2312	0.3462	0.0738	0.3462	4
		250	0.8134	0.6143	0.1071	0.9829	0.1067	0.9829	4
		500	0.0833	0.0528	0.3402	0.2349	0.1945	0.3402	3
2	1	60	0.079	0.0407	0.0316	0.0378	0.0429	0.079	1
		125	0.037	0.0231	0.0387	0.0362	0.0823	0.0823	5
		250	0.0449	0.068	0.0188	0.0576	0.0554	0.068	2
		500	0.1219	0.119	0.0245	0.0758	0.0134	0.1219	1
	2	60	0.0633	0.0177	0.2599	0.2773	0.1896	0.2773	4
		125	0.3566	0.0518	0.2149	0.3058	0.0682	0.3566	1
		250	0.0555	0.2422	0.1295	0.1688	0.1646	0.2422	2
		500	0.3509	0.0774	0.2669	0.1857	0.0128	0.3509	1
3	1	60	0.0665	0.1527	0.1287	0.0435	0.29	0.29	5
		125	0.1832	0.202	0.2361	0.1643	0.186	0.2361	3
		250	0.0948	0.3234	0.2493	0.3544	0.1383	0.3544	4
		500	0.2098	0.0552	0.0562	0.2731	0.2866	0.2866	5
	2	60	0.143	0.163	0.1017	0.0777	0.0348	0.163	2
		125	0.1601	0.2165	0.162	0.1129	0.0555	0.2165	2
		250	0.0953	0.0323	0.0568	0.0513	0.1233	0.1233	5
		500	0.0702	0.1363	0.0969	0.1088	0.1419	0.1419	5

Table A2-10: Rotational Accuracy- Length 2 Variance Test for each Position (Pos.), Height (H.) and Speed population

Pos.	H.	Population (x vs. y)	Length 2 Variance Test									
			Speed 1		Speed 2		Speed 3		Speed 4		Speed 5	
			h	S_x/S_y	h	S_x/S_y	h	S_x/S_y	h	S_x/S_y	h	S_x/S_y
1	1	1 vs. 2	1	3.4015	0	1.2131	1	2.1611	1	2.1493	0	1.5741
		1 vs. 3	0	1.0854	0	1.6475	1	3.9343	1	2.5772	0	1.426
		1 vs. 4	0	1.0983	1	4.5336	1	19.1698	1	2.8622	1	11.664
		2 vs. 3	1	3.1338	0	1.3581	0	1.8205	0	1.1991	0	1.1038
		2 vs. 4	1	3.097	1	5.4996	1	8.8705	0	1.3317	1	7.4102
		3 vs. 4	0	1.0119	1	7.4691	1	4.8725	0	1.1106	1	8.1794
	2	1 vs. 2	0	1.2096	0	1.1511	0	1.8443	0	1.7886	1	4.8799
		1 vs. 3	1	3.6606	1	3.5761	1	3.9809	0	1.5874	1	3.3753
		1 vs. 4	1	2.6666	1	3.2505	0	1.2535	1	2.6359	0	1.8506
		2 vs. 3	1	3.0263	1	3.1067	1	2.1585	1	2.8392	0	1.4458
		2 vs. 4	1	3.2256	1	3.7417	0	1.4714	0	1.4738	1	2.6369
		3 vs. 4	1	9.7616	1	11.6241	1	3.1759	1	4.1843	0	1.8238
2	1	1 vs. 2	1	2.1373	0	1.7675	0	1.2234	0	1.0418	0	1.919
		1 vs. 3	0	1.7598	0	1.67	0	1.6801	0	1.5268	0	1.2902
		1 vs. 4	0	1.5424	1	2.9207	0	1.2903	1	2.0077	1	3.1948
		2 vs. 3	0	1.2145	1	2.9516	1	2.0555	0	1.5907	0	1.4873
		2 vs. 4	1	3.2966	1	5.1623	0	1.5786	1	2.0917	1	6.1307
		3 vs. 4	1	2.7144	0	1.749	0	1.3021	0	1.315	1	4.1219
	2	1 vs. 2	1	5.6335	1	2.9244	0	1.2092	0	1.1029	1	2.7785
		1 vs. 3	0	1.1406	1	13.6823	1	2.0061	0	1.6432	0	1.1521
		1 vs. 4	1	5.5442	1	4.3709	0	1.0269	0	1.4934	1	14.773
		2 vs. 3	1	6.4255	1	4.6786	0	1.659	0	1.8123	1	2.4117
		2 vs. 4	0	1.0161	0	1.4946	0	1.2417	0	1.6471	1	5.3172
		3 vs. 4	1	6.3236	1	3.1303	1	2.06	0	1.1003	1	12.823
3	1	1 vs. 2	1	2.7563	0	1.3221	0	1.8349	1	3.7726	0	1.5593
		1 vs. 3	0	1.4259	1	2.1173	0	1.9377	1	8.1388	1	2.0964
		1 vs. 4	1	3.1562	1	2.7652	1	2.2909	1	6.2725	0	1.0119
		2 vs. 3	0	1.933	0	1.6014	0	1.056	1	2.1573	0	1.3444
		2 vs. 4	0	1.1451	1	3.656	1	4.2035	0	1.6626	0	1.5411
		3 vs. 4	1	2.2134	1	5.8549	1	4.4391	0	1.2975	1	2.0718
	2	1 vs. 2	0	1.1193	0	1.3277	0	1.5927	0	1.4527	0	1.5948
		1 vs. 3	0	1.5016	1	5.0533	0	1.7896	0	1.5149	1	3.5473
		1 vs. 4	1	2.0382	0	1.196	0	1.0499	0	1.3998	1	4.0806
		2 vs. 3	0	1.6808	1	6.7093	1	2.8503	1	2.2008	1	2.2243
		2 vs. 4	1	2.2814	0	1.588	0	1.6721	0	1.0378	1	2.5587
		3 vs. 4	0	1.3573	1	4.2251	0	1.7046	1	2.1206	0	1.1503
Σh_1			20		23		15		14		20	

Table A2-11: Rotational Accuracy- Length 2 Student T-Test for each Position (Pos.), Height (H.) and Speed population

Pos.	H.	Population	Length 2 Student T-Test									
		(x vs. y)	Speed 1		Speed 2		Speed 3		Speed 4		Speed 5	
			h	p-value	h	p-value	h	p-value	h	p-value	h	p-value
1	1	1 vs. 2	0	0.9946	0	0.3524	0	0.5682	0	0.9787	0	0.4469
		1 vs. 3	0	0.0508	0	0.8452	0	0.1911	0	0.4473	0	0.8652
		1 vs. 4	1	0.0387	0	0.0523	0	0.1076	0	0.0933	0	0.1157
		2 vs. 3	0	0.3147	0	0.5739	0	0.1504	0	0.1979	0	0.2671
		2 vs. 4	0	0.2738	1	0.0226	1	0.0409	1	0.0155	1	0.0094
		3 vs. 4	0	0.7951	0	0.1266	0	0.1592	0	0.053	0	0.0645
	2	1 vs. 2	0	0.2335	0	0.9251	0	0.3302	0	0.4222	0	0.7309
		1 vs. 3	0	0.4393	0	0.482	1	0.0099	0	0.753	0	0.6679
		1 vs. 4	0	0.4558	0	0.1439	1	0.0124	1	0.0002	1	0.037
		2 vs. 3	0	0.5812	0	0.3479	0	0.1141	0	0.564	0	0.5172
		2 vs. 4	0	0.1013	0	0.0754	0	0.1036	1	0.0028	1	0.0114
		3 vs. 4	0	0.175	0	0.1614	0	0.7251	0	0.1425	0	0.1919
2	1	1 vs. 2	0	0.4668	0	0.5922	0	0.1766	0	0.5002	0	0.8718
		1 vs. 3	0	0.2257	0	0.2434	1	0.0188	0	0.382	0	0.6238
		1 vs. 4	0	0.0511	1	0.0003	0	0.8584	0	0.8616	0	0.5111
		2 vs. 3	0	0.0635	0	0.2905	1	0.0454	0	0.6833	0	0.7892
		2 vs. 4	1	0.0154	1	0.003	0	0.649	0	0.7651	0	0.5991
		3 vs. 4	0	0.156	0	0.6732	0	0.0974	0	0.605	0	0.7085
	2	1 vs. 2	0	0.9054	0	0.1163	0	0.9151	0	0.5996	0	0.7097
		1 vs. 3	0	0.6585	0	0.5132	0	0.5563	0	0.2812	0	0.4513
		1 vs. 4	0	0.9306	0	0.2847	0	0.3231	0	0.3374	0	0.3253
		2 vs. 3	0	0.5869	0	0.5096	0	0.7187	0	0.2224	0	0.5229
		2 vs. 4	0	0.9684	0	0.7333	0	0.5314	0	0.499	0	0.1281
		3 vs. 4	0	0.816	0	0.7496	0	0.789	0	0.1695	0	0.1665
3	1	1 vs. 2	0	0.844	0	0.3829	0	0.7093	0	0.6558	0	0.4252
		1 vs. 3	0	0.3773	0	0.6478	0	0.0805	0	0.3019	0	0.3772
		1 vs. 4	0	0.0714	0	0.3266	0	0.2377	0	0.945	0	0.1052
		2 vs. 3	0	0.1809	0	0.3937	0	0.0574	0	0.3306	0	0.8285
		2 vs. 4	1	0.041	0	0.2732	0	0.202	0	0.4951	0	0.7124
		3 vs. 4	0	0.1142	0	0.8111	0	0.4784	0	0.1974	0	0.4291
	2	1 vs. 2	0	0.333	0	0.3037	0	0.3999	0	0.6782	0	0.3939
		1 vs. 3	0	0.5592	1	0.0046	1	0.0071	0	0.3759	0	0.6485
		1 vs. 4	0	0.3682	1	0.0038	1	0.0038	0	0.4484	1	0.0114
		2 vs. 3	0	0.0565	0	0.8923	1	0.0491	0	0.2305	0	0.4871
		2 vs. 4	1	0.0203	0	0.5604	0	0.0633	0	0.1616	1	0.0338
		3 vs. 4	0	0.5485	0	0.0704	0	0.4778	0	0.6193	1	0.0057

A2.2.2 Linear Accuracy

The results of the Linear Accuracy section of the Measurement Accuracy Study are given in Table A2-12 to Table A2-15. This outlines the accuracy of measuring reference displacements 1 through 5 and *Length 2* of the translational apparatus. Furthermore, statistical variance was analyzed for measurements taken at different sampling rates and different settings within the measurement volume.

Measurement bias and precision of reference displacements 1 through 5 are given in Table A2-12 and Table A2-13, respectively, while statistical variance tests and student t-tests of the different measurement populations are given in Table A2-14 and Table A2-15, respectively.

Table A2-12: Linear Accuracy- Displacement Bias

Position	Sampling	Displacement Bias					Maximum Bias	
	Rate	Disp. 1	Disp. 2	Disp. 3	Disp. 4	Disp. 5	Bias	Disp.
	[Hz]	[mm]	[mm]	[mm]	[mm]	[mm]	[mm]	
1	60	0.242	0.3576	0.2548	0.1599	0.2025	0.3576	2
	125	0.1448	0.2316	0.2935	0.1193	0.1902	0.2935	3
	250	0.148	0.387	0.212	0.1697	0.0661	0.387	2
	500	0.1265	0.2193	0.0864	0.3629	0.0899	0.3629	4
2	60	0.1347	0.2256	0.153	0.1645	0.1786	0.2256	2
	125	0.085	0.0947	0.0772	0.0589	0.1037	0.1037	5
	250	0.148	0.1457	0.1374	0.1198	0.1969	0.1969	5
	500	0.0966	0.1344	0.0958	0.0898	0.1657	0.1657	5
3	60	0.1391	0.2423	0.1875	0.2737	0.4784	0.4784	5
	125	0.1788	0.2349	0.2255	0.5033	0.7044	0.7044	5
	250	0.132	0.2275	0.264	0.2367	0.5285	0.5285	5
	500	0.106	0.3356	0.3077	0.3255	0.4992	0.4992	5

Table A2-13: Linear Accuracy- Displacement Precision

Position	Sampling Rate [Hz]	Displacement Standard Deviation Disp. 1 [mm]	Disp. 2 [mm]	Disp. 3 [mm]	Disp. 4 [mm]	Disp. 5 [mm]	Max Precision Precision [mm]	Disp.
1	60	0.3722	0.5924	0.311	0.2439	0.3228	0.5924	2
	125	0.1217	0.257	0.3106	0.1327	0.2755	0.3106	3
	250	0.1368	0.4149	0.2236	0.2117	0.0753	0.4149	2
	500	0.1878	0.2319	0.099	0.4766	0.1279	0.4766	4
2	60	0.1715	0.3219	0.2162	0.2288	0.2643	0.3219	2
	125	0.1005	0.138	0.0991	0.074	0.1034	0.138	2
	250	0.1932	0.1841	0.1561	0.1332	0.2038	0.2038	5
	500	0.1282	0.1643	0.119	0.1332	0.2202	0.2202	5
3	60	0.1806	0.2896	0.2322	0.3504	0.3634	0.3634	5
	125	0.2167	0.2797	0.2977	0.8013	1.0071	1.0071	5
	250	0.184	0.2669	0.4115	0.3694	0.5983	0.5983	5
	500	0.1497	0.3793	0.3659	0.3621	0.4477	0.4477	5

Table A2-14: Linear Accuracy- Variance Test

Position	Populations (x vs. y)	Variance Test Disp. 1		Disp.2		Disp. 3		Disp. 4		Disp. 5	
		h	S_x/S_y	h	S_x/S_y	h	S_x/S_y	h	S_x/S_y	h	S_x/S_y
1	1 vs. 2	1	3.0587	1	2.3053	0	1.0014	0	1.8373	0	1.1719
	1 vs. 3	1	2.7217	0	1.4278	0	1.391	0	1.152	1	4.2848
	1 vs. 4	0	1.9816	1	2.5538	1	3.1402	0	1.9545	1	2.5243
	2 vs. 3	0	1.1238	0	1.6146	0	1.3891	0	1.5949	1	3.6562
	2 vs. 4	0	1.5435	0	1.1078	1	3.1359	1	3.5911	1	2.154
	3 vs. 4	0	1.3735	0	1.7887	1	2.2575	1	2.2516	0	1.6974
2	1 vs. 2	0	1.7067	1	2.3323	1	2.1829	1	3.092	1	2.5564
	1 vs. 3	0	1.1265	0	1.7481	0	1.385	0	1.7178	0	1.2966
	1 vs. 4	0	1.3379	0	1.959	0	1.8164	0	1.7184	0	1.2003
	2 vs. 3	0	1.9225	0	1.3342	0	1.5762	0	1.7999	0	1.9716
	2 vs. 4	0	1.2756	0	1.1905	0	1.2018	0	1.7993	1	2.1299
	3 vs. 4	0	1.5071	0	1.1207	0	1.3115	0	1.0003	0	1.0803
3	1 vs. 2	0	1.2001	0	1.0355	0	1.2819	1	2.2868	1	2.7713
	1 vs. 3	0	1.0189	0	1.0849	0	1.7718	0	1.0541	0	1.6464
	1 vs. 4	0	1.2063	0	1.31	0	1.5758	0	1.0333	0	1.2319
	2 vs. 3	0	1.1779	0	1.0477	0	1.3822	1	2.1695	0	1.6833
	2 vs. 4	0	1.4478	0	1.3564	0	1.2292	1	2.2131	1	2.2495
	3 vs. 4	0	1.2291	0	1.4211	0	1.1244	0	1.0201	0	1.3364
Σh_1		2		3		4		6		8	

Table A2-15: Linear Accuracy- Student T-Test

Position	Populations (x vs. y)	Student t-test									
		Disp.1		Disp.2		Disp. 3		Disp. 4		Disp. 5	
		h	p-value	h	p-value	h	p-value	h	p-value	h	p-value
1	1 vs. 2	0	0.8221	0	0.401	0	0.7467	0	0.7329	0	0.6486
	1 vs. 3	0	0.5139	0	0.5536	0	0.7643	0	0.2521	0	0.7348
	1 vs. 4	0	0.4479	0	0.1425	0	0.5568	0	0.2562	0	0.8191
	2 vs. 3	0	0.3527	0	0.8097	0	0.9433	0	0.2672	0	0.2917
	2 vs. 4	0	0.3095	0	0.2383	0	0.8766	0	0.1612	0	0.3739
	3 vs. 4	0	0.8006	0	0.2697	0	0.7506	0	0.0696	0	0.824
2	1 vs. 2	0	0.9422	0	0.794	0	0.2442	0	0.5632	0	0.8622
	1 vs. 3	0	0.9168	0	0.9863	0	0.2948	0	0.9256	0	0.9007
	1 vs. 4	0	0.848	0	0.7687	0	0.595	0	0.7188	0	0.271
	2 vs. 3	0	0.9539	0	0.6713	0	0.9945	0	0.4543	0	0.9734
	2 vs. 4	0	0.8701	0	0.3626	0	0.3358	0	0.7718	0	0.1787
	3 vs. 4	0	0.9516	0	0.6859	0	0.4414	0	0.7076	0	0.2607
3	1 vs. 2	0	0.9852	0	0.7884	0	0.2664	0	0.1428	0	0.8224
	1 vs. 3	0	0.7363	0	0.7383	0	0.876	0	0.8553	0	0.5878
	1 vs. 4	0	0.3321	0	0.1656	0	0.6675	0	0.5414	0	0.6206
	2 vs. 3	0	0.774	0	0.9512	0	0.3305	0	0.1216	0	0.9737
	2 vs. 4	0	0.3969	0	0.1076	0	0.6104	0	0.0769	0	0.9322
	3 vs. 4	0	0.5461	0	0.0935	0	0.6374	0	0.6761	0	0.8919
Σh_1		0		0		0		0		0	

Appendix 3 Soft Tissue Artifact Compensation

The continuous noise model of Section 3.3.3.3 was used to add soft tissue artifact to the displacements of markers M1, M2 and M3 of the analytical model. Three variables are required to fully define the continuous noise model: signal amplitude A, signal angular velocity ω and signal phase angle θ. Noise amplitude A was selected to represent the measured displacement of a marker placed on the lower extremity due to soft tissue artifact, while the phase angle θ was determined to ensure constant amplitude of the total noise signal (see Section 3.3.3.3). The choice of signal angular velocity ω, associated with signal frequency, is debatable, as it is difficult to determine the frequency of soft tissue artifact movement. Therefore a series of sampling frequencies from 1 to 2 Hz (in increments of 0.25 Hz) were investigated, containing the frequency of the base signal, which is approximately 1.2 Hz (7.5 [rad/s] / 2π [rad/cycle]). A continuous noise model for each sampling frequency was added to the displacements of the analytical model, and ISA error parameters were computed, the results of which are shown in Table A3-1.

Table A3-1: ISA error resulting from soft tissue artifact calculated from the disturbed displacement and solidified displacement. The maximum value of each ISA error parameter is given, as well as the corresponding frequency. * Reference value 0.9m/s; ** reference value 7.5 rad/s.

Noise	ISA Error			
Frequency	ε_o	ε_p	ε_v [m/s]	ε_w [rad/s]
[Hz]	[rad]	[m]	(% relative error)*	(% relative error)**
1.00	4.623E-02	1.245E-02	6.576E-02 (7.31E+00)	8.501E-01 (1.13E+01)
1.25	5.982E-02	1.426E-02	8.536E-02 (9.48E+00)	9.871E-01 (1.32E+01)
1.50	6.849E-02	1.588E-02	9.784E-02 (1.09E+01)	1.110E+00 (1.48E+01)
1.75	8.462E-02	1.763E-02	1.203E-01 (1.34E+01)	1.206E+00 (1.61E+01)
2.00	9.385E-02	1.917E-02	1.333E-01 (1.48E+01)	1.326E+00 (1.77E+01)
Max Error	9.385E-02	1.917E-02	1.333E-01 (1.48E+01)	1.326E+00 (1.77E+01)
Frequency	2.00	2.00	2.00	2.00

It was determined that the magnitude of ISA error parameters were all proportional to the sampling frequency. Therefore, to recreate the largest expected errors within the given frequency interval, a frequency of 2 Hz was selected, resulting in an angular velocity ω_N of 4π rad/s.

Appendix 4 Swing Model Complete Results

A4.1 Applied Error on Marker Displacement

The error compensation techniques of Sections 3.3.3 and 3.3.4 produce marker displacement consistent with rigid body motion from stereophotogrammetric measurements. These techniques replace occluded data points, reduce the effects of random and systematic instrument error and eliminate inter-marker variability. These methodologies introduce error on the measured marker displacements. Furthermore, from marker position and velocity, the relative displacement between linked segments was modeled as the movement about a relative ISA. This computation assumes that two segments are rigidly connected and, when the assumption does not hold, produces an approximation of the motion between them. This manifests itself as error between measured velocity, from numerical differentiation of measured displacement, and marker velocity from movement about the relative ISA. Further errors between measured and computed marker velocity are caused by instances approaching an undefined ISA and have not been fully attenuated by the applied diagnostics.

The amount of error introduced on marker position, from error compensation techniques, and marker velocity, from relative ISA computation, was measured. This quantifies the extent of error introduced during analysis, which can then be compared to known sources of marker displacement error.

A4.1.1 RMSE on Marker Position

To quantify the error introduced on marker displacement from the compensation technique of Sections 3.3.3 and 3.3.4, the RMSE between measured marker displacements and the computed rigid body marker displacements was calculated. Specifically, RMSE was computed between measured and computed marker displacements of the three markers used in ISA computation for each segment and

trial. Results are shown in Table A4-1 to Table A4-4 for Subjects 2 to 5, respectively

Table A4-1: Subject 2-RMSE on marker position. Error computed between measured marker position and solidified marker position, for the three markers of each segment used in the computation of ISA.

Trial	Position RMSE				
	Left Leg [m]	Pelvis [m]	Shoulders [m]	Left Arm [m]	Club [m]
1	0.00061	0.00273	0.00697	0.00481	0.00430
2	0.00072	0.00297	0.00587	0.00541	0.00536
3	0.00060	0.00400	0.00356	0.00196	0.00576
4	0.00062	0.00265	0.00721	0.00477	0.00498
5	0.00064	0.00293	0.00374	0.00466	0.00332
Mean	0.00064	0.00306	0.00547	0.00432	0.00474

Table A4-2: Subject 3-RMSE on marker position. Error computed between measured marker position and solidified marker position, for the three markers of each segment used in the computation of ISA.

Trial	Position RMSE				
	Left Leg [m]	Pelvis [m]	Shoulders [m]	Left Arm [m]	Club [m]
1	0.00117	0.00152	0.01321	0.00516	0.00561
2	0.00140	0.00279	0.01310	0.00449	0.00607
3	0.00124	0.00171	0.01661	0.00451	0.00624
4	0.00157	0.00263	0.01515	0.00460	0.00644
5	0.00157	0.00289	0.01435	0.00512	0.00758
Mean	0.00139	0.00231	0.01449	0.00478	0.00639

Table A4-3: Subject 4-RMSE on marker position. Error computed between measured marker position and solidified marker position, for the three markers of each segment used in the computation of ISA.

Trial	Position RMSE				
	Left Leg [m]	Pelvis [m]	Shoulders [m]	Left Arm [m]	Club [m]
1	0.00145	0.00319	0.00377	0.00424	0.00556
2	0.00127	0.00399	0.01154	0.00388	0.00490
3	0.00129	0.00406	0.01109	0.00429	0.00571
4	0.00132	0.00355	0.01054	0.00428	0.00581
5	0.00130	0.00298	0.01139	0.00308	0.00604
Mean	0.00133	0.00355	0.00967	0.00396	0.00560

Table A4-4: Subject 5-RMSE on marker position. Error computed between measured marker position and solidified marker position, for the three markers of each segment used in the computation of ISA.

Trial	Position RMSE				
	Left Leg [m]	Pelvis [m]	Shoulders [m]	Left Arm [m]	Club [m]
1	0.00121	0.00182	0.00724	0.00520	0.00202
2	0.00147	0.00207	0.00664	0.00366	0.00273
3	0.00146	0.00216	0.00620	0.00384	0.00244
4	0.00139	0.00196	0.00634	0.00509	0.00247
5	0.00124	0.00247	0.00642	0.00357	0.00173
Mean	0.00135	0.00210	0.00657	0.00427	0.00228

A4.1.2 RMSE on Marker Velocity

To quantify the error introduced from the assumption of rigidly connected segments in relative ISA computation and from instances approaching an undefined ISA, RMSE between measured marker velocity and marker velocity computed from the motion about a relative ISA was calculated. Specifically, RMSE was computed between measured and computed marker velocity of the three markers used in relative ISA computation for each segment and trial.

A4.1.2.1 RMSE on Marker Velocity about ISA

RMSE was computed between measured and computed marker velocity of the three markers used in ISA computation for each segment and trial. These results were then averaged for the 5 trials of each subject. Results are shown for the five ISA of the golf swing model, computed relative to the global reference frame. Results are shown in Table A4-5 to Table A4-8 for Subjects 2 to 5, respectively.

Table A4-5: Subject 2-RMSE on marker velocity. Error computed between measured marker velocity from numerical differentiation, of solidified marker position, and from movement about the ISA. Results shown for the RMSE on the three markers of each segment used in the computation of ISA.

Trial	Velocity RMSE				
	ISA_L [m/s]	ISA_P [m/s]	ISA_S [m/s]	ISA_A [m/s]	ISA_C [m/s]
1	0.00121	0.00319	0.00779	0.02866	4.22096
2	0.00234	0.00607	0.01319	0.03443	3.33810
3	0.00187	0.00393	0.01165	0.03051	7.13186
4	0.00145	0.00348	0.01082	0.03088	3.89523
5	0.00147	0.00341	0.01151	0.03334	0.21534
Mean	0.00167	0.00402	0.01099	0.03156	3.76030

Table A4-6: Subject 3-RMSE on marker velocity. Error computed between measured marker velocity from numerical differentiation, of solidified marker position, and from movement about the ISA. Results shown for the RMSE on the three markers of each segment used in the computation of ISA.

Trial	Velocity RMSE				
	ISA_L [m/s]	ISA_P [m/s]	ISA_S [m/s]	ISA_A [m/s]	ISA_C [m/s]
1	0.00189	0.00757	0.00524	0.02346	3.06044
2	0.00236	0.00555	0.00541	0.02866	15.44418
3	0.00432	0.00581	0.00666	0.03961	4.00572
4	0.00245	0.00740	0.00720	0.03832	10.38254
5	0.00233	0.00906	0.00595	0.04064	1.72491
Mean	0.00267	0.00708	0.00609	0.03414	6.92356

Table A4-7: Subject 4-RMSE on marker velocity. Error computed between measured marker velocity from numerical differentiation, of solidified marker position, and from movement about the ISA. Results shown for the RMSE on the three markers of each segment used in the computation of ISA.

Trial	Velocity RMSE				
	ISA_L [m/s]	ISA_P [m/s]	ISA_S [m/s]	ISA_A [m/s]	ISA_C [m/s]
1	0.00084	0.00077	0.00249	0.00524	0.03852
2	0.00217	0.00463	0.02168	0.01600	0.53723
3	0.00265	0.00694	0.03190	0.02028	2.06949
4	0.00331	0.00628	0.01680	0.01674	1.04712
5	0.00286	0.00689	0.02321	0.01661	1.23728
Mean	0.00237	0.00510	0.01922	0.01497	0.98593

Table A4-8: Subject 5-RMSE on marker velocity. Error computed between measured marker velocity from numerical differentiation, of solidified marker position, and from movement about the ISA. Results shown for the RMSE on the three markers of each segment used in the computation of ISA.

Trial	Velocity RMSE				
	ISA_L [m/s]	ISA_P [m/s]	ISA_S [m/s]	ISA_A [m/s]	ISA_C [m/s]
1	0.00421	0.00300	0.00338	0.01039	0.24514
2	0.00433	0.00445	0.00258	0.01472	0.28079
3	0.00441	0.00734	0.00393	0.01742	0.35395
4	0.00395	0.00611	0.00601	0.01077	0.37511
5	0.00329	0.00392	0.00413	0.00769	0.19891
Mean	0.00404	0.00496	0.00401	0.01220	0.29078

A4.1.2.2 RMSE on Marker Velocity about ISAr

RMSE was computed between measured and computed marker velocity of the three markers used in ISAr computation for each segment and trial. These results were then averaged for the 5 trials of each subject. Results are shown for the four ISAr of the golf swing model, computed from the relative movement to the preceding segment. Results are shown in Table A4-9 to Table A4-12 for Subjects 2 to 5, respectively.

Table A4-9: Subject 2-RMSE on marker velocity. Error computed between measured marker velocity from numerical differentiation, of solidified marker position, and from movement about the ISAr. Results shown for the RMSE on the three markers of each segment used in the computation of ISAr.

Trial	Velocity RMSE			
	$ISAr_P$ [m/s]	$ISAr_S$ [m/s]	$ISAr_A$ [m/s]	$ISAr_C$ [m/s]
1	0.01445	0.01075	0.05877	1.10902
2	0.01508	0.01793	0.04544	2.86552
3	0.01224	0.02609	0.04314	0.96178
4	0.00959	0.01342	0.04094	1.53187
5	0.01494	0.02029	0.04247	0.51167
Mean	0.01326	0.01770	0.04615	1.39597

Table A4-10: Subject 3-RMSE on marker velocity. Error computed between measured marker velocity from numerical differentiation, of solidified marker position, and from movement about the ISAr. Results shown for the RMSE on the three markers of each segment used in the computation of ISAr.

Trial	Velocity RMSE			
	$ISAr_P$ [m/s]	$ISAr_S$ [m/s]	$ISAr_A$ [m/s]	$ISAr_C$ [m/s]
1	0.01265	0.01532	0.02935	1.72387
2	0.00810	0.01595	0.03685	1.80967
3	0.01458	0.02112	0.03438	1.79719
4	0.01536	0.03594	0.03547	3.94872
5	0.02004	0.02398	0.04279	1.40292
Mean	0.01415	0.02246	0.03577	2.13647

Table A4-11: Subject 4-RMSE on marker velocity. Error computed between measured marker velocity from numerical differentiation, of solidified marker position, and from movement about the ISAr. Results shown for the RMSE on the three markers of each segment used in the computation of ISAr.

Trial	Velocity RMSE			
	$ISAr_P$ [m/s]	$ISAr_S$ [m/s]	$ISAr_A$ [m/s]	$ISAr_C$ [m/s]
1	0.00101	0.00464	0.00548	0.04028
2	0.01018	0.02884	0.02264	0.58508
3	0.01772	0.03259	0.03046	0.88671
4	0.02391	0.05999	0.03580	0.48992
5	0.02826	0.03232	0.03086	0.53774
Mean	0.01621	0.03168	0.02505	0.50794

Table A4-12: Subject 5-RMSE on marker velocity. Error computed between measured marker velocity from numerical differentiation, of solidified marker position, and from movement about the ISAr. Results shown for the RMSE on the three markers of each segment used in the computation of ISAr.

Trial	Velocity RMSE			
	$ISAr_P$ [m/s]	$ISAr_S$ [m/s]	$ISAr_A$ [m/s]	$ISAr_C$ [m/s]
1	0.00226	0.00442	0.02106	0.41528
2	0.00548	0.00525	0.02406	0.57962
3	0.00600	0.00599	0.04381	0.17190
4	0.00437	0.00635	0.02251	0.55650
5	0.00317	0.00529	0.01322	0.08982
Mean	0.00426	0.00546	0.02493	0.36262

A4.2 Marker Velocity about ISA and ISAr

When the displacement of a rigid body is expressed in terms of an ISA, marker displacement is divided into two components: parallel velocity, from translation along the ISA, and perpendicular velocity, from a rotation on ISA direction [Eberharter and Ravani (2006)]. The golf swing model assumes that the magnitude of the perpendicular component of marker velocity will far exceed the parallel component of marker velocity and therefore the majority of marker displacement is through a rotation about ISA (see Section 3.4). To verify this assumption, the magnitude of parallel marker velocity was compared to the magnitude of total marker velocity by way of a velocity ratio. This was computed as the ratio of parallel marker velocity magnitude to total marker velocity magnitude, expressed in percentage. This quantifies the extent of motion that is not fully expressed by a rotation about the ISA.

A4.2.1 Marker Velocity Ratio about ISA

Velocity ratio was computed between parallel and total marker velocity of the three markers used in ISA computation, averaged for these three markers, and shown for each segment and trial. These results were then averaged for the 5 trials of each subject. Results are shown for the five ISA of the golf swing model,

computed relative to the global reference frame. Results are shown in Table A4-13 to Table A4-16 for Subjects 2 to 5, respectively.

Table A4-13: Subject 2-Velocity ratio computed as the ratio between the parallel component of marker velocity, parallel to ISA, and total marker velocity, expressed in percentage. Results shown are the mean velocity ratios of the three markers of each segment used in ISA computation.

Trial	Parallel Velocity / Total Velocity				
	ISA_L [%]	ISA_P [%]	ISA_S [%]	ISA_A [%]	ISA_C [%]
1	25.0	16.2	12.6	11.5	15.8
2	29.0	17.8	12.7	12.7	27.7
3	27.4	15.9	13.2	13.3	32.5
4	28.7	14.4	13.3	12.6	19.6
5	26.5	14.4	16.6	13.0	5.9
Mean	27.3	15.7	13.7	12.6	20.3
STD	1.6	1.4	1.7	0.7	10.4

Table A4-14: Subject 3-Velocity ratio computed as the ratio between the parallel component of marker velocity, parallel to ISA, and total marker velocity, expressed in percentage. Results shown are the mean velocity ratios of the three markers of each segment used in ISA computation.

Trial	Parallel Velocity / Total Velocity				
	ISA_L [%]	ISA_P [%]	ISA_S [%]	ISA_A [%]	ISA_C [%]
1	34.0	19.8	11.8	10.3	25.8
2	38.1	20.3	11.9	12.4	22.6
3	41.6	24.6	15.6	16.0	17.8
4	44.2	21.7	7.7	11.5	26.7
5	43.7	26.0	9.5	10.9	20.3
Mean	40.3	22.5	11.3	12.2	22.6
STD	4.3	2.7	3.0	2.3	3.7

Table A4-15: Subject 4-Velocity ratio computed as the ratio between the parallel component of marker velocity, parallel to ISA, and total marker velocity, expressed in percentage. Results shown are the mean velocity ratios of the three markers of each segment used in ISA computation.

Trial	Parallel Velocity / Total Velocity				
	ISA_L [%]	ISA_P [%]	ISA_S [%]	ISA_A [%]	ISA_C [%]
1	32.4	18.2	15.4	11.7	1.5
2	34.6	24.8	17.0	14.1	26.9
3	36.4	27.9	18.3	15.6	14.4
4	42.3	28.7	16.1	16.4	14.8
5	37.3	31.5	18.0	16.0	17.3
Mean	36.6	26.2	17.0	14.8	15.0
STD	3.7	5.1	1.2	1.9	9.1

Table A4-16: Subject 5-Velocity ratio computed as the ratio between the parallel component of marker velocity, parallel to ISA, and total marker velocity, expressed in percentage. Results shown are the mean velocity ratios of the three markers of each segment used in ISA computation.

Trial	Parallel Velocity / Total Velocity				
	ISA_L [%]	ISA_P [%]	ISA_S [%]	ISA_A [%]	ISA_C [%]
1	35.7	6.0	10.3	11.6	8.6
2	36.7	16.2	7.9	15.4	10.3
3	37.6	16.0	7.7	14.1	11.2
4	40.3	10.7	9.3	32.5	11.1
5	38.1	8.9	10.9	13.6	8.9
Mean	37.7	11.6	9.2	17.5	10.0
STD	1.7	4.5	1.4	8.5	1.2

A4.2.2 Marker Velocity Ratio about ISAr

Velocity ratio was computed between parallel and total marker velocity of the three markers used in ISAr computation, for each segment and trial, and averaged for these three markers. These results were then averaged for the 5 trials of each subject. Results are shown for the four ISAr of the golf swing model, computed from the relative movement to the preceding segment. Results are shown in Table A4-17 to Table A4-20 for Subjects 2 to 5, respectively.

Table A4-17: Subject 2-Velocity ratio computed as the ratio between the parallel component of marker velocity, parallel to ISAr, and total marker velocity, expressed in percentage. Results shown are the mean velocity ratios of the three markers of each segment used in ISAr computation.

Trial	Parallel Velocity / Total Velocity			
	$ISAr_P$ [%]	$ISAr_S$ [%]	$ISAr_A$ [%]	$ISAr_C$ [%]
1	10.0	13.7	19.1	42.9
2	10.4	15.8	14.6	55.1
3	10.9	21.6	19.2	40.1
4	9.7	14.0	16.5	42.6
5	9.6	24.3	16.9	52.9
Mean	10.1	17.9	17.3	46.7
STD	0.5	4.8	1.9	6.8

Table A4-18: Subject 3-Velocity ratio computed as the ratio between the parallel component of marker velocity, parallel to ISAr, and total marker velocity, expressed in percentage. Results shown are the mean velocity ratios of the three markers of each segment used in ISAr computation.

Trial	Parallel Velocity / Total Velocity			
	$ISAr_P$ [%]	$ISAr_S$ [%]	$ISAr_A$ [%]	$ISAr_C$ [%]
1	21.4	14.7	20.5	27.8
2	14.2	16.7	13.4	27.7
3	17.7	16.8	13.4	55.5
4	11.9	14.8	10.9	35.6
5	12.2	17.5	10.6	31.4
Mean	15.5	16.1	13.7	35.6
STD	4.0	1.3	4.0	11.6

Table A4-19: Subject 4-Velocity ratio computed as the ratio between the parallel component of marker velocity, parallel to ISAr, and total marker velocity, expressed in percentage. Results shown are the mean velocity ratios of the three markers of each segment used in ISAr computation.

Trial	Parallel Velocity / Total Velocity			
	$ISAr_P$ [%]	$ISAr_S$ [%]	$ISAr_A$ [%]	$ISAr_C$ [%]
1	26.5	15.8	15.3	21.2
2	16.3	25.0	10.2	62.8
3	18.7	25.4	10.9	68.6
4	11.8	25.4	10.0	69.8
5	11.2	26.0	13.6	70.3
Mean	16.9	23.5	12.0	58.5
STD	6.2	4.3	2.3	21.1

Table A4-20: Subject 5-Velocity ratio computed as the ratio between the parallel component of marker velocity, parallel to ISAr, and total marker velocity, expressed in percentage. Results shown are the mean velocity ratios of the three markers of each segment used in ISAr computation.

Trial	Parallel Velocity / Total Velocity			
	$ISAr_P$ [%]	$ISAr_S$ [%]	$ISAr_A$ [%]	$ISAr_C$ [%]
1	9.1	9.8	13.5	50.1
2	6.5	17.2	20.0	53.8
3	5.6	17.4	15.8	56.7
4	10.0	16.8	9.3	43.2
5	6.8	10.8	16.1	52.0
Mean	7.6	14.4	14.9	51.2
STD	1.9	3.8	3.9	5.1

A4.3 ISA Angular Velocity

A4.3.1 Time Varying Angular velocity about ISA

The purpose of this thesis was to determine the kinematic sequence of the golf swing, a motion which consists primarily of gross rotations of the lower body, upper body and arms. It is of particular interest to determine the sequence of these rotations, which can be accomplished by studying the angular velocity of each

segment relative to their ISA. The magnitude of the angular velocity of each analyzed segment, about their respective ISA, was determined as a function of percent downswing.

A4.3.1.1 Angular Velocity about ISA

The magnitude of the angular velocity about each ISA, computed relative to the global reference frame, was plotted as a function of percent downswing. Each angular velocity, one for each ISA, was plotted as the mean magnitude plus or minus one standard deviation, computed from the 5 measured trials. Results are shown in Figure A4-1 to Figure A4-4 for Subjects 2 to 5, respectively.

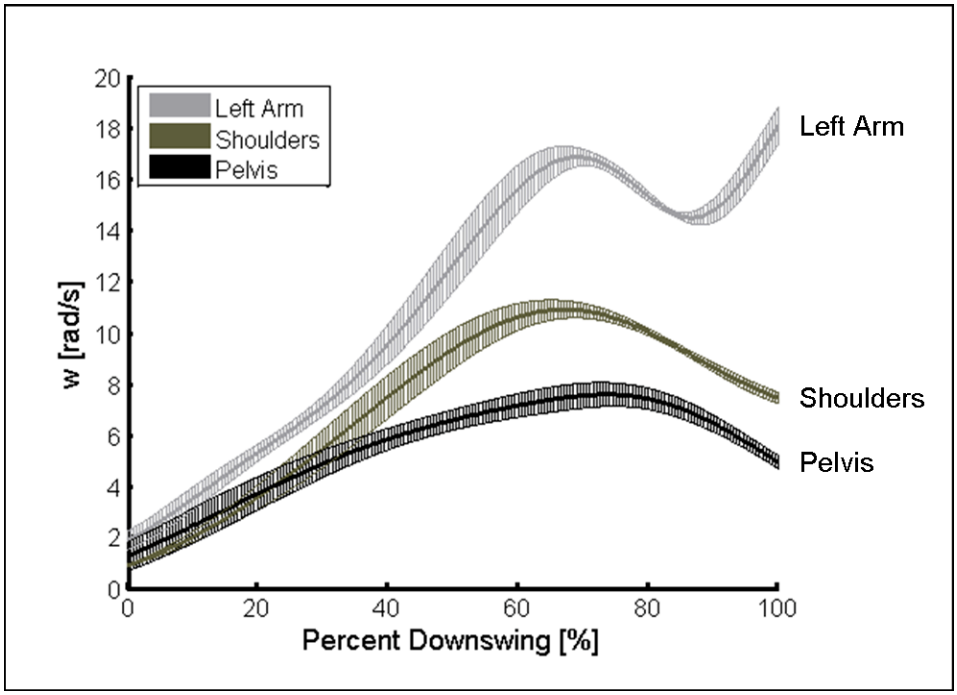

Figure A4-1: Subject 2- Magnitude of segment angular velocity about their ISA, relative to the global reference frame.

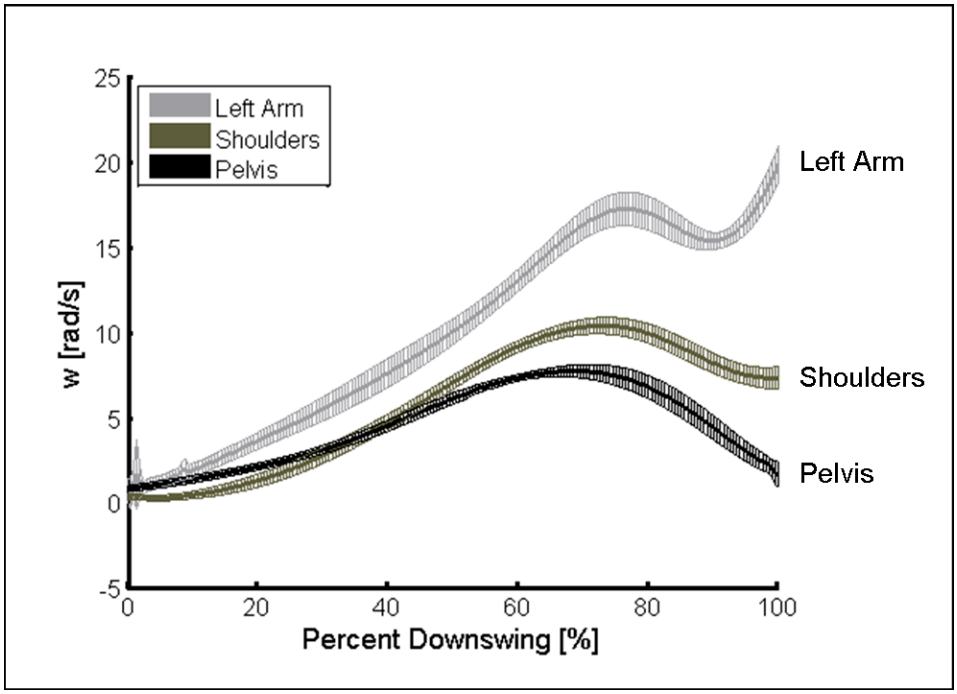

Figure A4-2: Subject 3- Magnitude of segment angular velocity about their ISA, relative to the global reference frame.

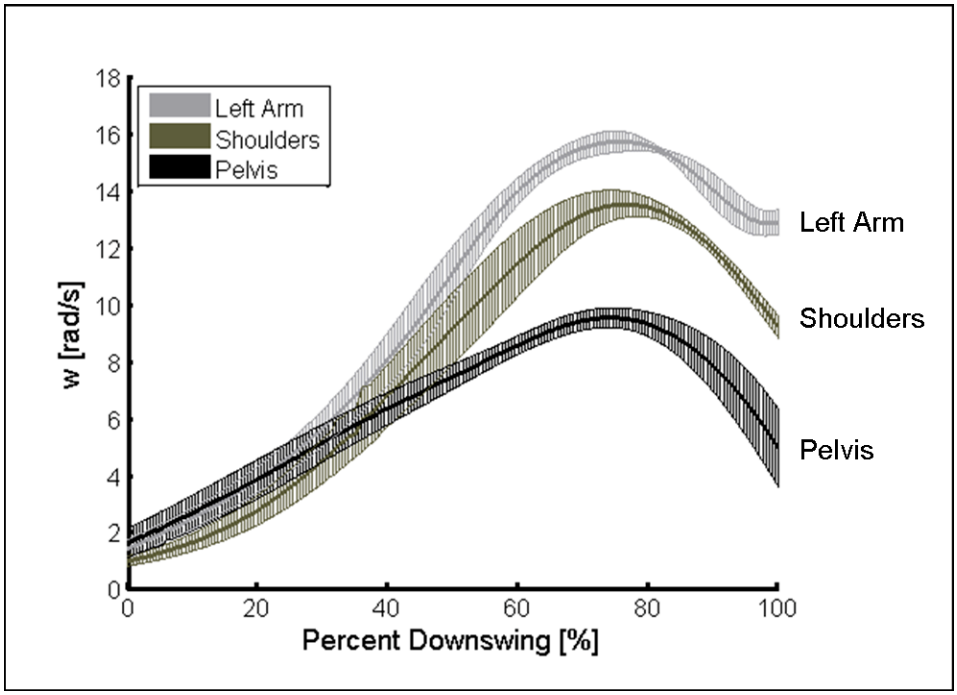

Figure A4-3: Subject 4- Magnitude of segment angular velocity about their ISA, relative to the global reference frame.

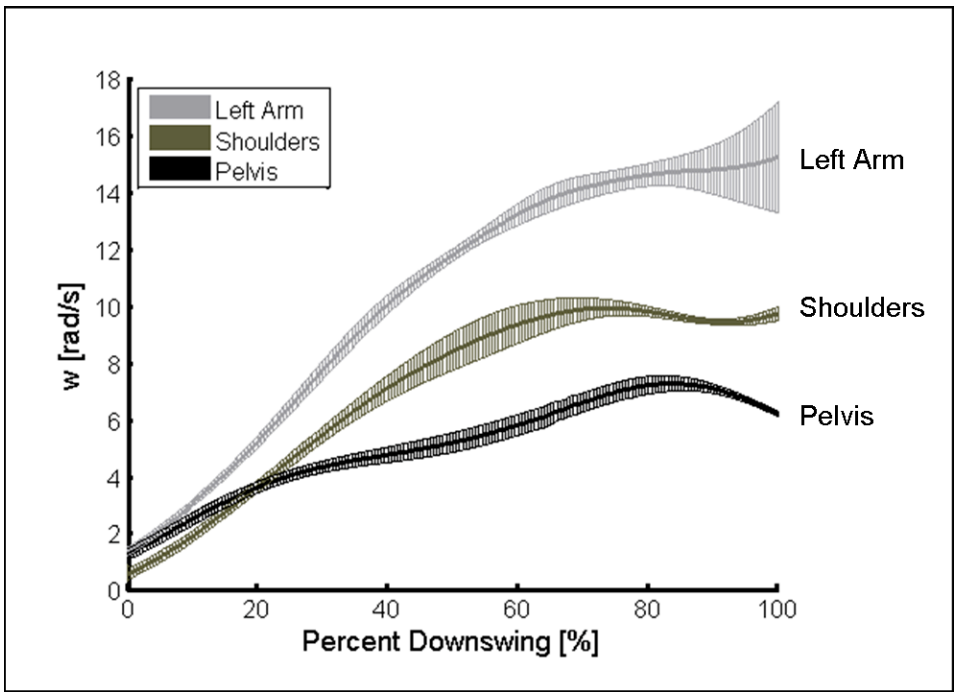

Figure A4-4: Subject 5- Magnitude of segment angular velocity about their ISA, relative to the global reference frame.

A4.3.1.2 Angular velocity about ISAr

The magnitude of the angular velocity about each ISAr, computed relative to the preceding body segment, was plotted as a function of percent downswing. Each angular velocity, one for each ISAr, was plotted as the mean magnitude plus or minus one standard deviation, computed from the 5 measured trials. Results are shown in Figure A4-5 to Figure A4-8 for Subjects 2 to 5, respectively.

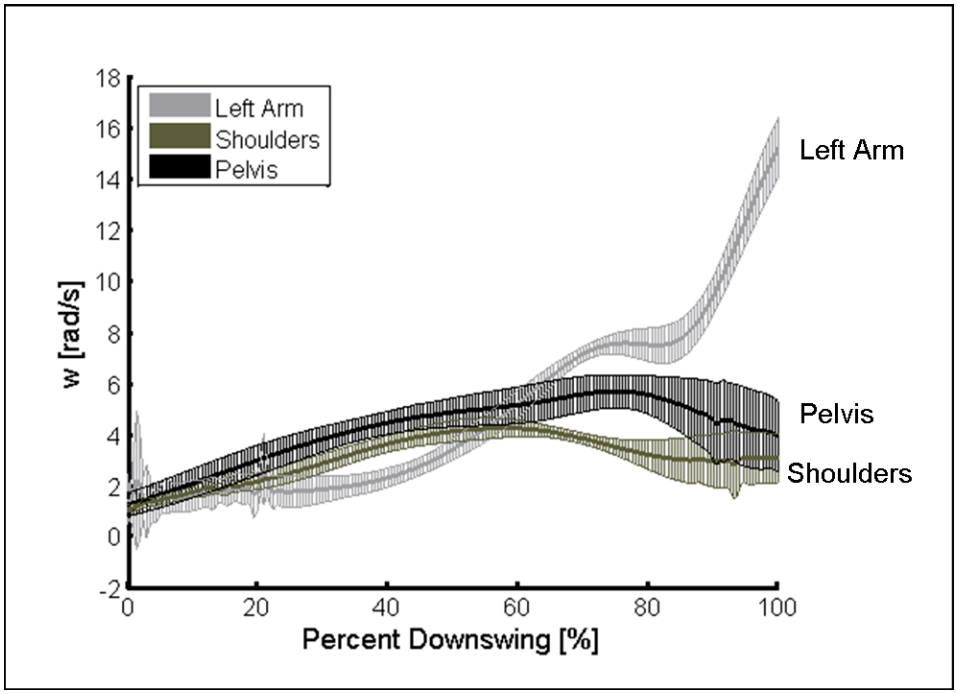

Figure A4-5: Subject 2- Magnitude of segment angular velocity about their ISAr, relative to the preceding body segment.

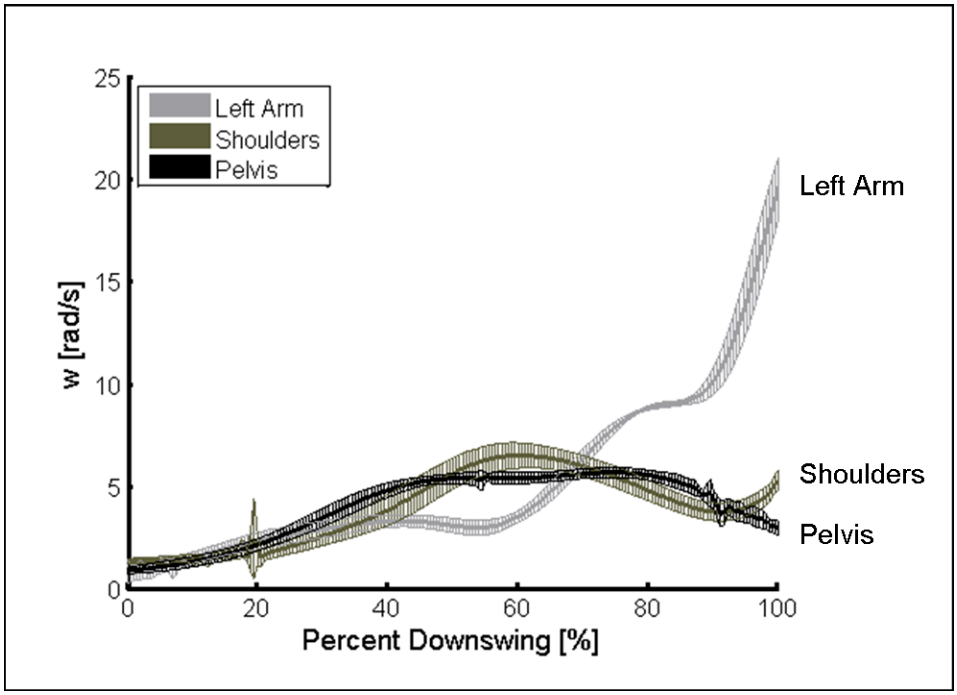

Figure A4-6: Subject 3- Magnitude of segment angular velocity about their ISAr, relative to the preceding body segment.

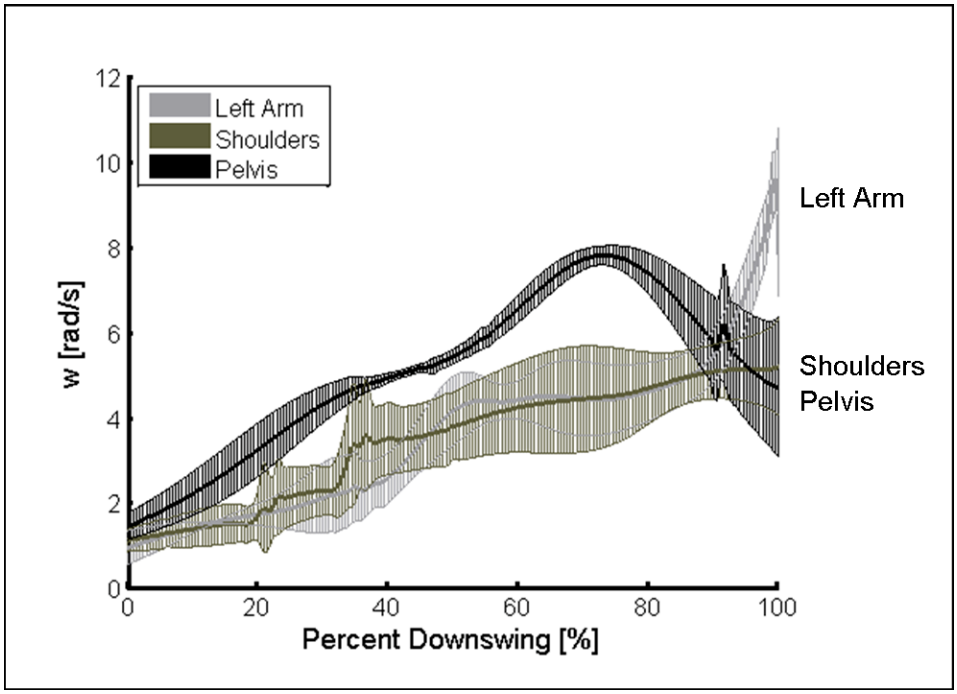

Figure A4-7: Subject 4- Magnitude of segment angular velocity about their ISAr, relative to the preceding body segment.

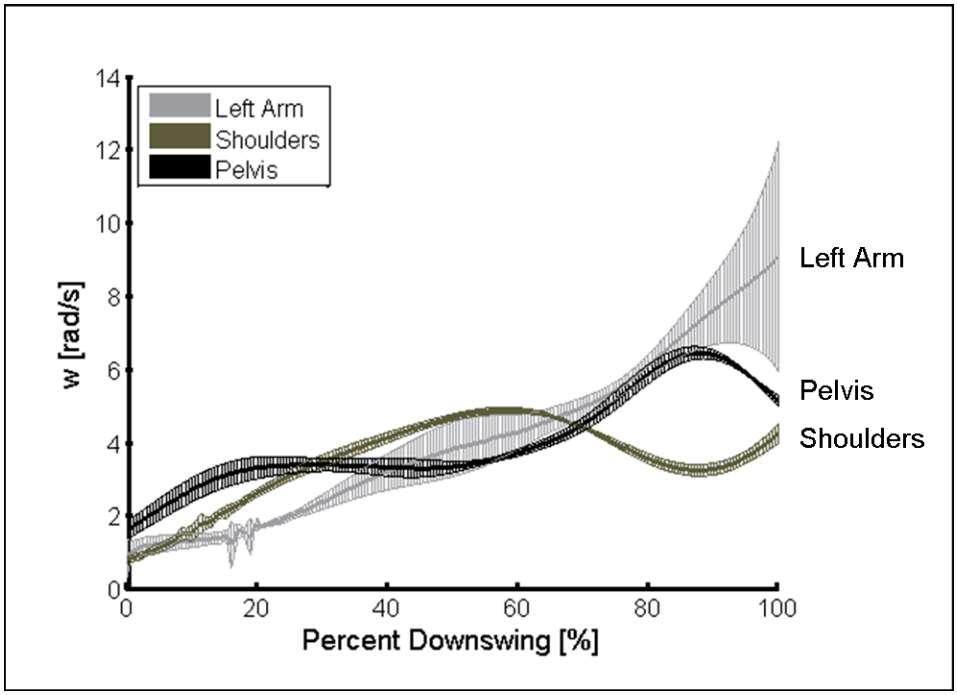

Figure A4-8: Subject 5- Magnitude of segment angular velocity about their ISAr, relative to the preceding body segment.

A4.3.2 Instances of Maximum Angular Velocity

The kinematic sequence of the golf swing can be determined by studying the angular velocity of each segment relative to their ISA. Furthermore, the instance where each angular velocity is at its maximum is of particular interest, as the order in which segments sequentially achieves their respective maximum yields the kinematic sequence. The following results were computed at the instant were each ISA and ISAr achieved its respective maximum: magnitude of angular velocity, ω_{max}, the percent downswing corresponding to that instant, ISA position and ISA orientation. The final two variables, ISA position and orientation, are computed differently for each ISA and chosen to compare the ISA to the expected gross axis of rotation of that segment.

ISA Position at Maximum Angular Velocity

ISA_P and $ISAr_P$

The position of the pelvis ISA was computed from the local coordinate frame of the pelvis, computed from Cappozzo et al. [Cappozzo et al. (1995)]. The position was given as the intersection between the pelvis ISA and the xy-plane of the pelvis local coordinate frame. Results are then shown as a plot of the pelvis markers, P1 to P4, and the intersection point, all within the local coordinate frame of the pelvis. Furthermore, the position of the right and left hip joint centers, labeled RHJC and LHJC and computed from Leardini et al. [Leardini et al. (1999)] (for the x and y components) and Bell et al. [Bell et al. (1990)] (for the z component), and shown in the local coordinate frame of the pelvis. This provides a reference for the position of the joint centers of the segment. The orientation of the pelvis ISA was computed as the angle between the ISA and two reference axes: the spine axis and axis of the left leg, as the expected orientation would be a combination of the two. The spine axis was computed as the line connecting the pelvis and shoulders centroids, where each centroid was computed from the position of the four affixed markers. The axis of the left leg was given as the line connecting the left hip joint centre and the centroid of the left ankle, computed as the center point between marker L4 and L5 affixed to the left ankle.

ISA_S and $ISAr_S$

The position of the shoulders ISA was computed from the local coordinate frame of the shoulders, computed from was computed from the recommendations of Wu et al. [Wu et al. (2005)]; however some changes were made to accommodate the current marker set. The position was given as the intersection between the shoulders ISA and the xy-plane of the shoulders local coordinate frame. Results are then shown as a plot of the shoulder markers, S1 to S4, and the intersection point, all within the local coordinate frame of the shoulders. The orientation of the shoulders ISA was computed as the angle between the ISA and the spine axis, computed as described above. The spine axis represents the expect orientation of shoulder rotation.

ISA_A and $ISAr_A$

The position of the left arm ISA was computed from the local coordinate frame of the shoulders, computed as described above. The position was given as the intersection between the left arm ISA and the xy-plane of the shoulders local coordinate frame. Results are then shown as a plot of the shoulder markers, S1 to S4, and the intersection point, all within the local coordinate frame of the shoulders. The orientation of the left arm ISA was computed as the angle between the ISA and two reference axes: the spine axis and the supination axis of the wrist. These two reference axes were used to locate the ISA as the expected motion of the left arm would be a combination of movement about the left shoulder joint and supination about the left wrist.

The supination axis of the left arm was given as the line connecting the centroid of the wrist, computed as the center point between markers A3 and A4 affixed to the wrist, and the elbow centroid, computed as the center point between markers A1 and A2 affixed to the elbow.

ISA_C and $ISAr_C$

The position of the golf club ISA was computed as the shortest distance between the ISA and the centroid of the wrist joint. This centroid, computed as the

midpoint between markers C3 and C4 placed on the wrist, provides an approximation for the wrist joint center. The orientation of the golf club ISA was computed as the angle between the ISA and the supination axis of the left forearm, computed as described above. The supination axis represents the expect orientation of golf club rotation.

A4.3.2.1 Maximum Angular velocity about ISA

The four variables conducted at maximum angular velocity (ω_{max}, percent downswing corresponding to ω_{max}, ISA position and ISA orientation) are given for each ISA, subject and five computed trials.

ISA_P: ISA of the pelvis relative to the global reference frame

Results are shown in Table A4-21 to Table A4-24 for Subjects 2 to 5, respectively, and the corresponding ISA position plot is given below each table, in Figure A4-9 to Figure A4-12.

Table A4-21: Subject 2- ISA_P angular velocity, position, orientation and normalized time at maximum angular velocity. Position computed in the local reference frame of the pelvis, and orientation computed relative to the spine axis and axis of the left leg.

Trial	W max	Percent	Position			Orientation	
						Spine	Left Leg
		Downswing	x	y	z	Axis	Axis
	[rad/s]	[%]	[m]	[m]	[m]	[deg]	[deg]
1	6.885	75.5	-0.003	0.085	0.000	11.05	41.43
2	7.892	70.5	0.000	0.089	0.000	10.92	42.10
3	8.028	74.0	-0.005	0.093	0.000	9.62	45.71
4	7.395	74.0	-0.009	0.094	0.000	7.53	45.29
5	7.808	75.5	-0.005	0.089	0.000	9.44	43.41
Mean	7.602	73.9	-0.005	0.090	0.000	9.71	43.59
STD	0.465	2.0	0.003	0.004	0.000	1.42	1.89

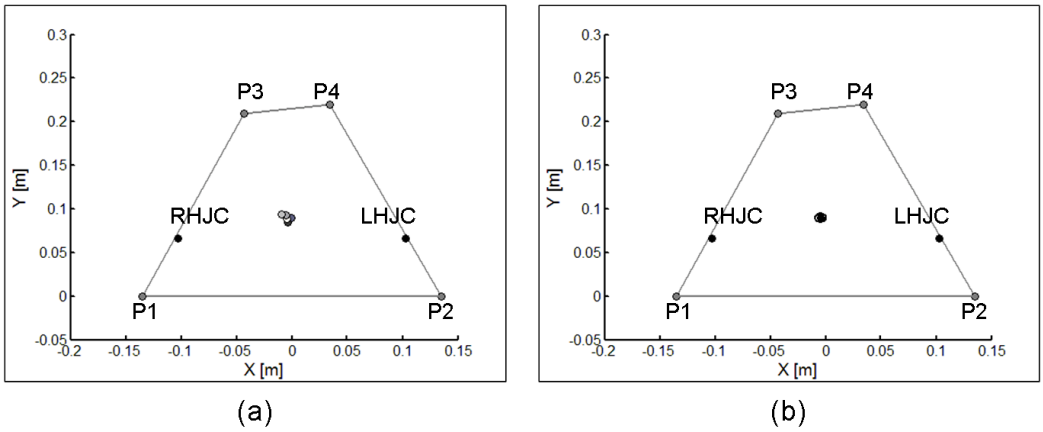

Figure A4-9: Subject 2- Intersection of ISA_P with the xy-plane of the local coordinate frame of the pelvis; (a) intersection point of trials 1 to 5, (b) mean intersection point and radius of standard deviation

Table A4-22: Subject 3- ISA_P angular velocity, position, orientation and normalized time at maximum angular velocity. Position computed in the local reference frame of the pelvis, and orientation computed relative to the spine axis and axis of the left leg.

Trial	W max	Percent	Position			Orientation	
		Downswing	x	y	z	Spine Axis	Left Leg Axis
	[rad/s]	[%]	[m]	[m]	[m]	[deg]	[deg]
1	7.371	66.5	0.008	0.161	0.000	15.14	26.00
2	7.806	70.5	-0.005	0.162	0.000	17.42	24.71
3	7.474	63.5	-0.015	0.164	0.000	18.97	24.22
4	8.133	69.5	-0.002	0.158	0.000	17.48	24.85
5	8.027	71.0	0.001	0.161	0.000	14.51	27.97
Mean	7.762	68.2	-0.003	0.161	0.000	16.71	25.55
STD	0.334	3.2	0.008	0.002	0.000	1.84	1.50

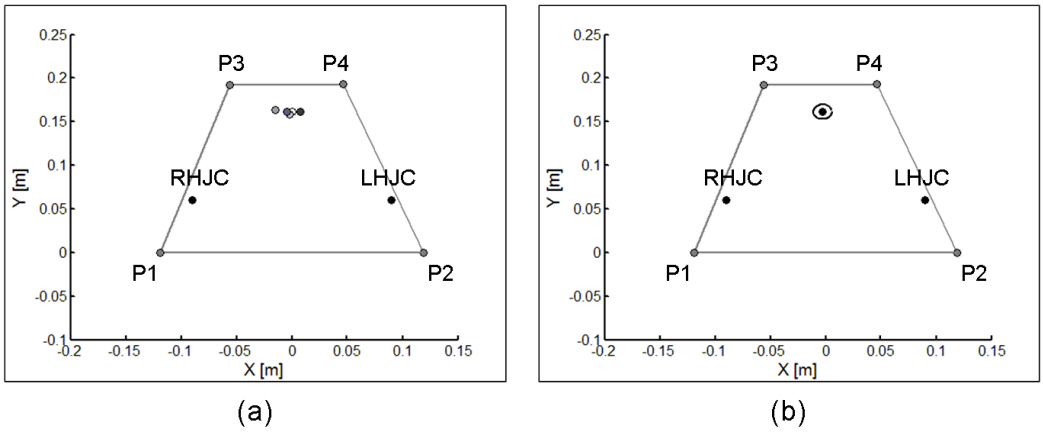

Figure A4-10: Subject 3- Intersection of ISA_P with the xy-plane of the local coordinate frame of the pelvis; (a) intersection point of trials 1 to 5, (b) mean intersection point and radius of standard deviation

Table A4-23: Subject 4- ISA_P angular velocity, position, orientation and normalized time at maximum angular velocity. Position computed in the local reference frame of the pelvis, and orientation computed relative to the spine axis and axis of the left leg.

Trial	W max	Percent	Position			Orientation	
		Downswing	x	y	z	Spine Axis	Left Leg Axis
	[rad/s]	[%]	[m]	[m]	[m]	[deg]	[deg]
1	9.891	73.0	0.007	0.086	0.000	8.34	33.96
2	9.755	79.0	0.004	0.084	0.000	9.28	35.56
3	9.736	74.5	0.009	0.078	0.000	11.28	35.48
4	9.083	75.5	0.005	0.088	0.000	12.86	37.32
5	9.348	70.5	0.007	0.078	0.000	13.52	34.00
Mean	9.563	74.5	0.006	0.083	0.000	11.06	35.26
STD	0.336	3.1	0.002	0.005	0.000	2.23	1.38

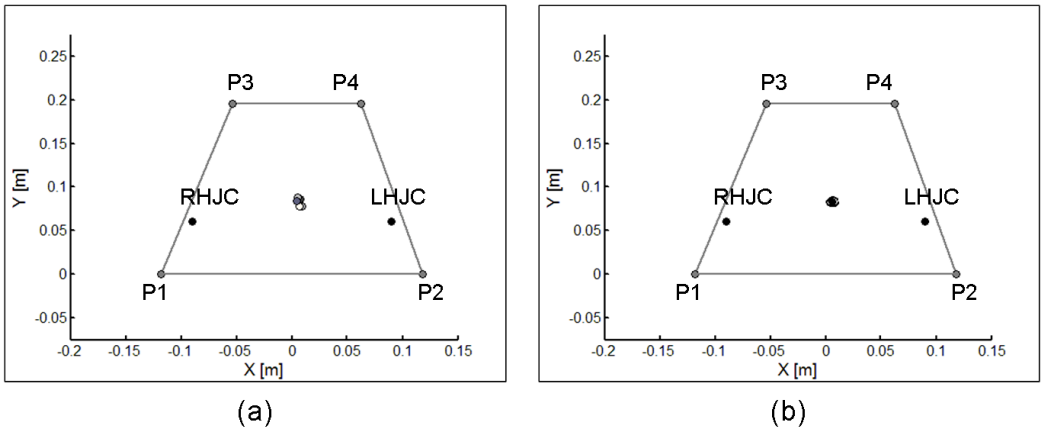

Figure A4-11: Subject 4- Intersection of ISA_P with the xy-plane of the local coordinate frame of the pelvis; (a) intersection point of trials 1 to 5, (b) mean intersection point and radius of standard deviation

Table A4-24: Subject 5- ISA_P angular velocity, position, orientation and normalized time at maximum angular velocity. Position computed in the local reference frame of the pelvis, and orientation computed relative to the spine axis and axis of the left leg.

Trial	W max	Percent	Position			Orientation	
		Downswing	x	y	z	Spine Axis	Left Leg Axis
	[rad/s]	[%]	[m]	[m]	[m]	[deg]	[deg]
1	7.096	82.5	0.012	0.164	0.000	7.95	30.59
2	7.542	82.5	0.008	0.139	0.000	8.13	30.79
3	7.411	82.0	0.008	0.147	0.000	8.66	31.13
4	7.406	84.0	0.001	0.139	0.000	6.60	29.35
5	6.945	87.5	0.033	0.154	0.000	8.90	35.50
Mean	7.280	83.7	0.012	0.149	0.000	8.05	31.47
STD	0.249	2.3	0.012	0.011	0.000	0.90	2.35

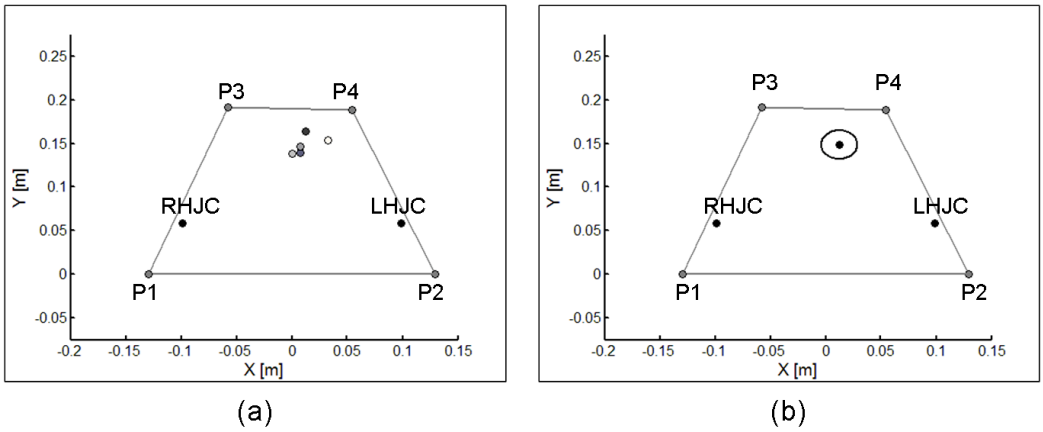

Figure A4-12: Subject 5- Intersection of ISA_P with the xy-plane of the local coordinate frame of the pelvis; (a) intersection point of trials 1 to 5, (b) mean intersection point and radius of standard deviation

ISA_S: ISA of the shoulders relative to the global reference frame

Results are shown in Table A4-25 to Table A4-28 for Subjects 2 to 5, respectively, and the corresponding ISA position plot is given below each table, in Figure A4-13 to Figure A4-16.

Table A4-25: Subject 2- ISA_S angular velocity, position, orientation and normalized time at maximum angular velocity. Position computed in the local reference frame of the shoulders, and orientation computed relative to the spine axis.

Trial	W max	Percent Downswing	Position			Orientation
			x	y	z	
	[rad/s]	[%]	[m]	[m]	[m]	[deg]
1	10.379	69.0	-0.017	-0.024	0.000	3.59
2	11.324	64.0	-0.016	-0.020	0.000	3.04
3	11.155	64.5	-0.017	-0.023	0.000	3.73
4	10.836	68.0	-0.019	-0.023	0.000	3.96
5	10.897	69.0	-0.023	-0.021	0.000	7.18
Mean	10.918	66.9	-0.018	-0.022	0.000	4.30
STD	0.360	2.5	0.003	0.002	0.000	1.65

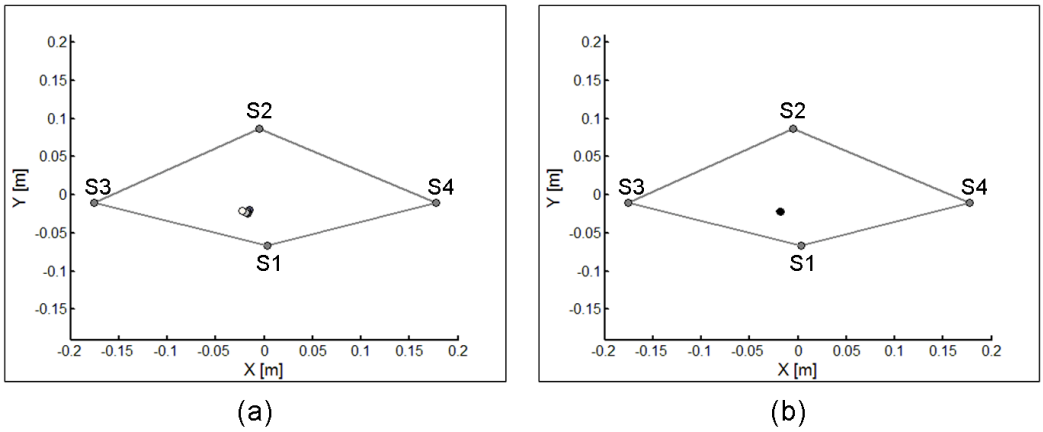

Figure A4-13: Subject 2- Intersection of ISA_S with the xy-plane of the local coordinate frame of the shoulders; (a) intersection point of trials 1 to 5, (b) mean intersection point and radius of standard deviation

Table A4-26: Subject 3- ISA_S angular velocity, position, orientation and normalized time at maximum angular velocity. Position computed in the local reference frame of the shoulders, and orientation computed relative to the spine axis.

Trial	W max	Percent Downswing	Position			Orientation
			x	y	z	
	[rad/s]	[%]	[m]	[m]	[m]	[deg]
1	9.595	70.5	-0.038	-0.012	0.000	11.32
2	10.333	75.0	-0.042	-0.017	0.000	11.16
3	10.536	72.0	-0.046	-0.015	0.000	7.65
4	10.786	73.5	-0.049	-0.015	0.000	9.17
5	10.654	73.0	-0.052	-0.021	0.000	11.26
Mean	10.381	72.8	-0.045	-0.016	0.000	10.11
STD	0.470	1.7	0.006	0.003	0.000	1.64

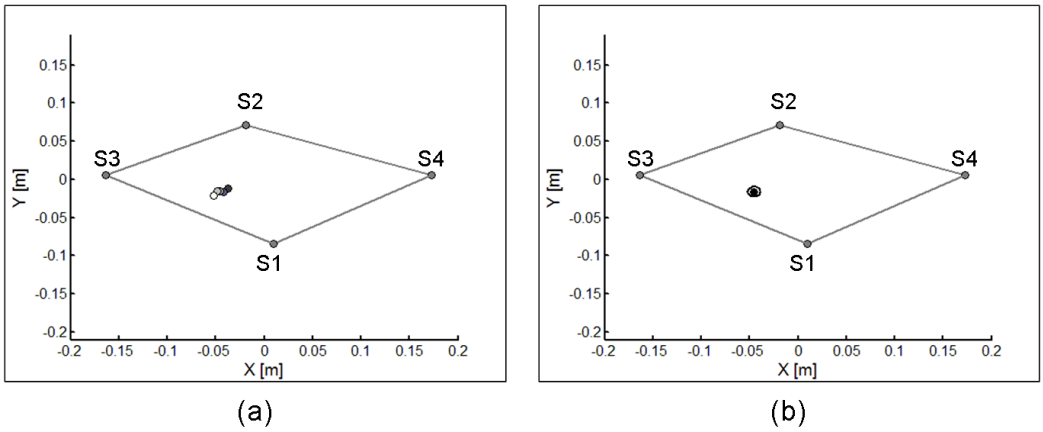

Figure A4-14: Subject 3- Intersection of ISA_S with the xy-plane of the local coordinate frame of the shoulders; (a) intersection point of trials 1 to 5, (b) mean intersection point and radius of standard deviation

Table A4-27: Subject 4- ISA_S angular velocity, position, orientation and normalized time at maximum angular velocity. Position computed in the local reference frame of the shoulders, and orientation computed relative to the spine axis.

Trial	W max	Percent Downswing	Position			Orientation
			x	y	z	
	[rad/s]	[%]	[m]	[m]	[m]	[deg]
1	12.855	79.5	-0.048	-0.048	0.000	3.44
2	13.697	77.5	-0.051	-0.038	0.000	3.34
3	13.843	74.5	-0.058	-0.044	0.000	4.51
4	13.272	76.5	-0.068	-0.047	0.000	4.65
5	13.902	74.0	-0.052	-0.053	0.000	5.51
Mean	13.514	76.4	-0.055	-0.046	0.000	4.29
STD	0.443	2.2	0.008	0.006	0.000	0.91

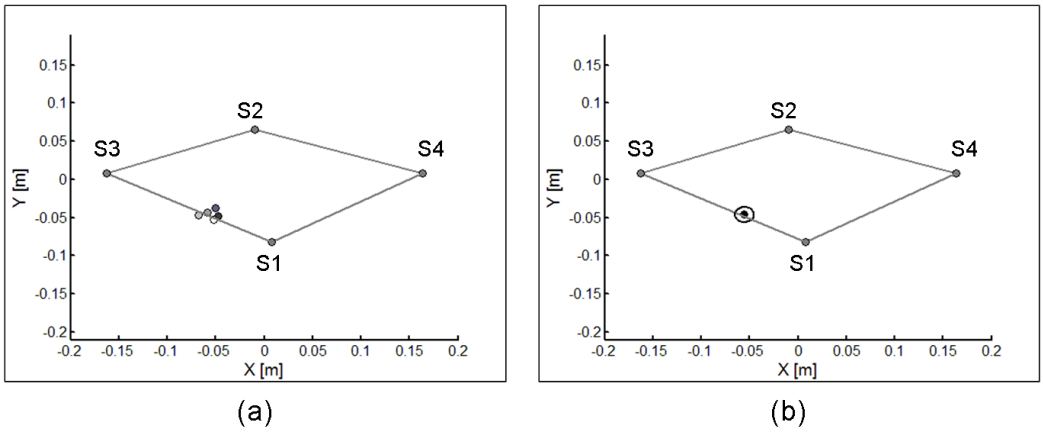

Figure A4-15: Subject 4- Intersection of ISA_S with the xy-plane of the local coordinate frame of the shoulders; (a) intersection point of trials 1 to 5, (b) mean intersection point and radius of standard deviation

Table A4-28: Subject 5- ISA_S angular velocity, position, orientation and normalized time at maximum angular velocity. Position computed in the local reference frame of the shoulders, and orientation computed relative to the spine axis.

Trial	W max	Percent Downswing	Position			Orientation
			x	y	z	
	[rad/s]	[%]	[m]	[m]	[m]	[deg]
1	9.985	73.0	-0.085	0.005	0.000	8.35
2	10.235	69.5	-0.087	0.004	0.000	7.45
3	10.239	69.5	-0.090	-0.002	0.000	8.66
4	9.932	100.0	-0.033	-0.037	0.000	16.86
5	9.918	100.0	-0.020	-0.031	0.000	19.79
Mean	10.062	82.4	-0.063	-0.012	0.000	12.22
STD	0.162	16.1	0.034	0.020	0.000	5.68

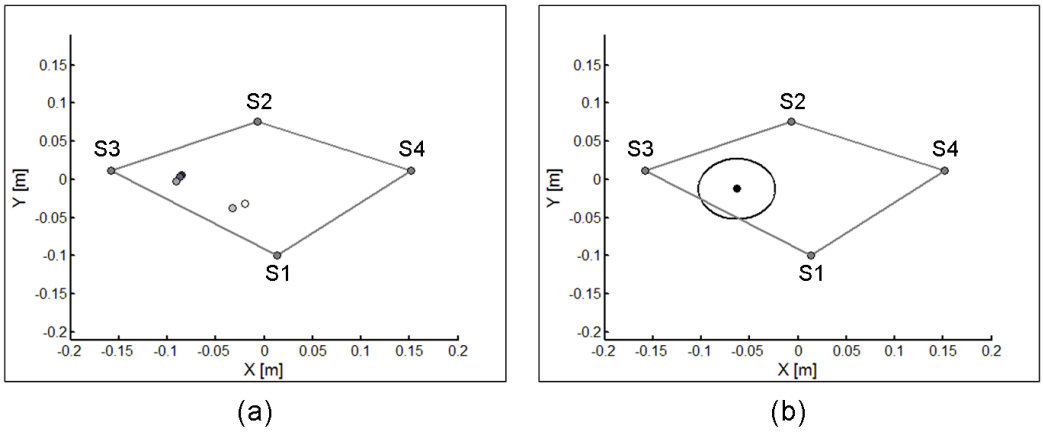

Figure A4-16: Subject 5- Intersection of ISA_S with the xy-plane of the local coordinate frame of the shoulders; (a) intersection point of trials 1 to 5, (b) mean intersection point and radius of standard deviation

ISA_A: ISA of the left arm relative to the global reference frame

Results are shown in Table A4-29 to Table A4-32 for Subjects 2 to 5, respectively, and the corresponding ISA position plot is given below each table, in Figure A4-17 to Figure A4-20.

Table A4-29: Subject 2- ISA_A angular velocity, position, orientation and normalized time at maximum angular velocity. Position computed in the local reference frame of the shoulders, and orientation computed relative to the spine axis and the supination axis of the forearm.

Trial	W max	Percent	Position			Orientation	
		Downswing	x	y	z	Spine Axis	Supination Axis
	[rad/s]	[%]	[m]	[m]	[m]	[deg]	[deg]
1	18.488	100.0	0.220	0.028	0.000	9.22	26.33
2	18.540	100.0	0.229	0.035	0.000	10.27	25.74
3	18.472	100.0	0.215	0.008	0.000	9.98	27.21
4	18.027	100.0	0.234	0.038	0.000	10.47	25.44
5	16.995	69.5	0.034	-0.058	0.000	6.95	87.63
Mean	18.104	93.9	0.187	0.010	0.000	9.38	38.47
STD	0.654	13.6	0.086	0.040	0.000	1.44	27.49

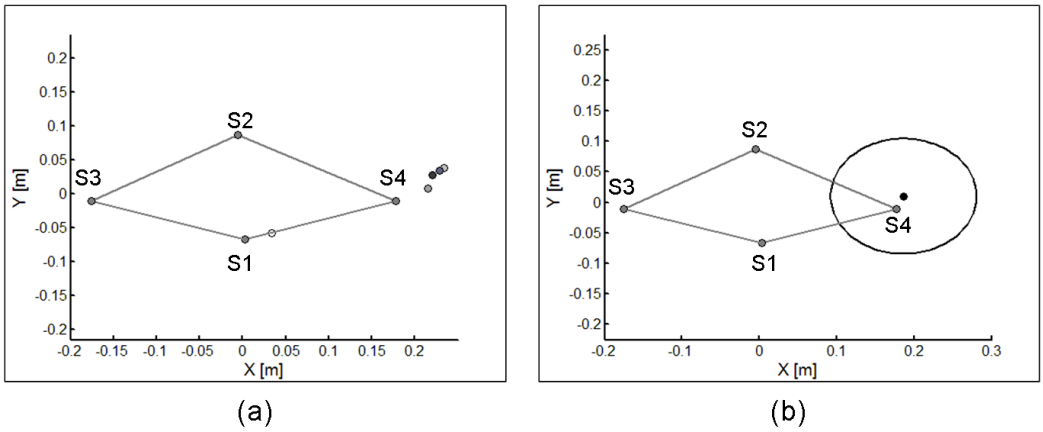

Figure A4-17: Subject 2- Intersection of ISA_A with the xy-plane of the local coordinate frame of the shoulders; (a) intersection point of trials 1 to 5, (b) mean intersection point and radius of standard deviation

Table A4-30: Subject 3- ISA_A angular velocity, position, orientation and normalized time at maximum angular velocity. Position computed in the local reference frame of the shoulders, and orientation computed relative to the spine axis and the supination axis of the forearm.

Trial	W max	Percent	Position			Orientation	
		Downswing	x	y	z	Spine Axis	Supination Axis
	[rad/s]	[%]	[m]	[m]	[m]	[deg]	[deg]
1	19.998	100.0	0.206	0.055	0.000	23.23	25.77
2	18.284	100.0	0.189	0.019	0.000	22.54	32.23
3	19.687	100.0	0.049	-0.051	0.000	26.51	42.92
4	19.842	100.0	0.215	0.080	0.000	19.90	27.98
5	21.330	100.0	0.218	0.092	0.000	16.98	26.80
Mean	19.828	100.0	0.175	0.039	0.000	21.83	31.14
STD	1.083	0.0	0.071	0.057	0.000	3.59	7.03

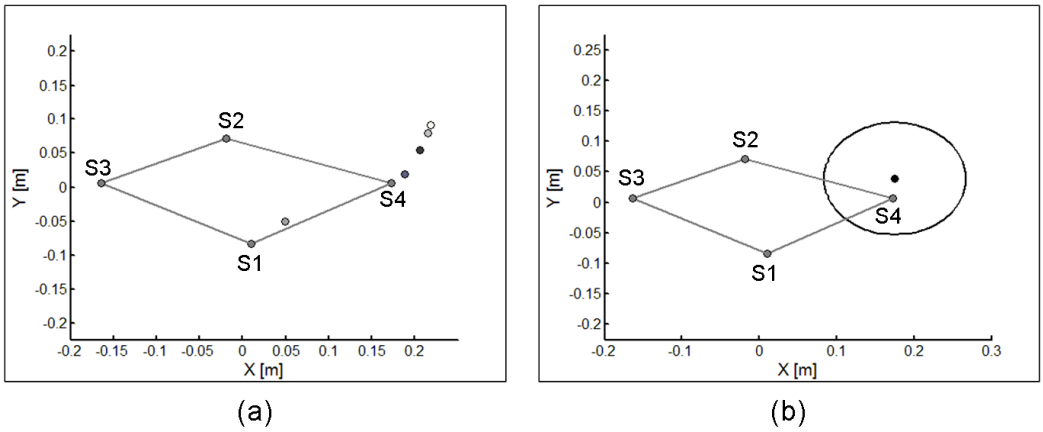

Figure A4-18: Subject 3- Intersection of ISA_A with the xy-plane of the local coordinate frame of the shoulders; (a) intersection point of trials 1 to 5, (b) mean intersection point and radius of standard deviation

Table A4-31: Subject 4- ISA_A angular velocity, position, orientation and normalized time at maximum angular velocity. Position computed in the local reference frame of the shoulders, and orientation computed relative to the spine axis and the supination axis of the forearm.

Trial	W max	Percent	Position			Orientation	
		Downswing	x	y	z	Spine Axis	Supination Axis
	[rad/s]	[%]	[m]	[m]	[m]	[deg]	[deg]
1	15.282	83.5	0.001	-0.052	0.000	4.88	88.21
2	15.703	78.0	-0.009	-0.042	0.000	3.48	82.32
3	15.912	74.0	-0.010	-0.037	0.000	4.42	83.92
4	15.867	75.0	-0.009	-0.047	0.000	4.17	79.71
5	15.911	74.5	-0.006	-0.045	0.000	5.60	83.64
Mean	15.735	77.0	-0.007	-0.045	0.000	4.51	83.56
STD	0.267	4.0	0.004	0.006	0.000	0.79	3.09

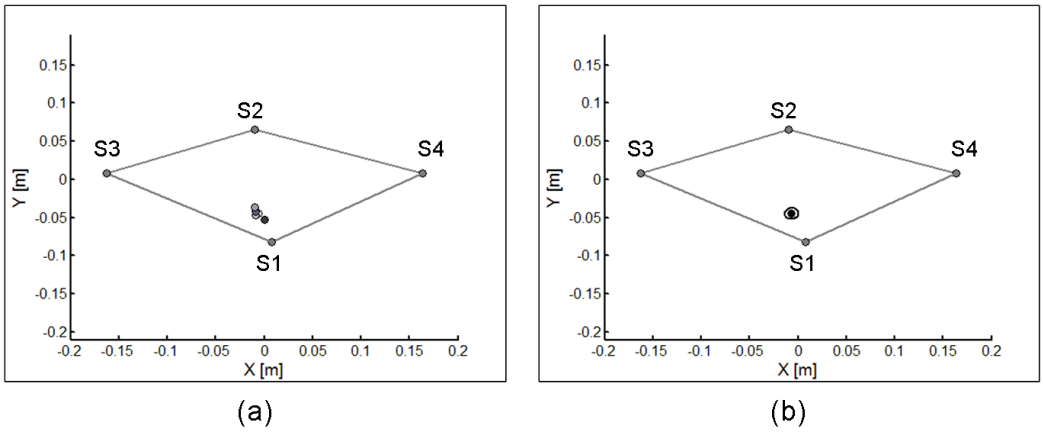

Figure A4-19: Subject 4- Intersection of ISA_A with the xy-plane of the local coordinate frame of the shoulders; (a) intersection point of trials 1 to 5, (b) mean intersection point and radius of standard deviation

Table A4-32: Subject 5- ISA_A angular velocity, position, orientation and normalized time at maximum angular velocity. Position computed in the local reference frame of the shoulders, and orientation computed relative to the spine axis and the supination axis of the forearm.

Trial	W max	Percent	Position			Orientation	
		Downswing	x	y	z	Spine Axis	Supination Axis
	[rad/s]	[%]	[m]	[m]	[m]	[deg]	[deg]
1	14.710	100.0	0.022	-0.004	0.000	17.62	56.16
2	14.746	82.5	-0.009	-0.062	0.000	12.73	80.53
3	18.643	100.0	0.091	0.021	0.000	18.30	39.73
4	14.553	81.5	-0.012	-0.053	0.000	14.67	79.66
5	14.089	84.0	-0.002	-0.048	0.000	15.24	79.76
Mean	15.348	89.6	0.018	-0.029	0.000	15.71	67.17
STD	1.860	9.5	0.043	0.036	0.000	2.26	18.49

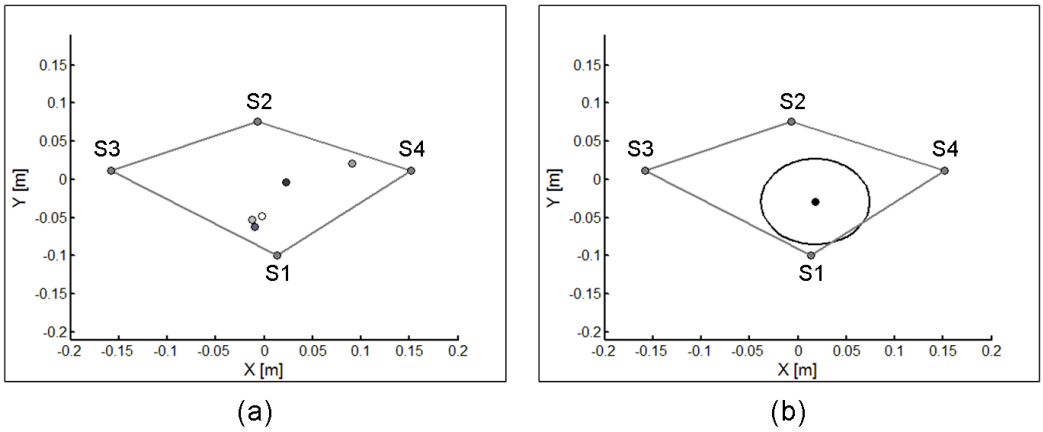

Figure A4-20: Subject 5- Intersection of ISA_A with the xy-plane of the local coordinate frame of the shoulders; (a) intersection point of trials 1 to 5, (b) mean intersection point and radius of standard deviation

ISA_C: ISA of the golf club relative to the global reference frame

Results are shown in Table A4-33 to Table A4-36 for Subjects 2 to 5, respectively.

Table A4-33: Subject 2- ISA_C angular velocity, position, orientation and normalized time at maximum angular velocity. Position computed as the distance from the centroid of the wrist, and orientation computed relative to the supination axis of the forearm.

Trial	W max [rad/s]	Percent Downswing [%]	Distance [m]	Orientation [deg]
1	600.273	75.0	0.476	52.40
2	419.216	65.0	0.437	58.64
3	974.107	65.0	0.465	57.03
4	524.385	72.5	0.468	57.33
5	31.498	89.5	0.102	48.62
Mean	509.896	73.4	0.390	54.80
STD	339.469	10.0	0.162	4.19

Table A4-34: Subject 3- ISA_C angular velocity, position, orientation and normalized time at maximum angular velocity. Position computed as the distance from the centroid of the wrist, and orientation computed relative to the supination axis of the forearm.

Trial	W max [rad/s]	Percent Downswing [%]	Distance [m]	Orientation [deg]
1	316.981	74.0	0.487	67.59
2	2410.359	75.5	0.482	68.43
3	609.057	75.5	0.485	66.13
4	1677.160	72.0	0.477	66.14
5	172.290	69.5	-0.802	27.26
Mean	1037.169	73.3	0.226	59.11
STD	967.627	2.6	0.575	17.83

Table A4-35: Subject 4- ISA_C angular velocity, position, orientation and normalized time at maximum angular velocity. Position computed as the distance from the centroid of the wrist, and orientation computed relative to the supination axis of the forearm.

Trial	W max [rad/s]	Percent Downswing [%]	Distance [m]	Orientation [deg]
1	155.211	73.0	0.448	29.72
2	32.053	94.0	0.139	51.60
3	276.264	89.0	0.488	59.94
4	110.401	88.0	0.574	66.07
5	123.262	92.0	0.587	53.52
Mean	139.438	87.2	0.447	52.17
STD	88.891	8.3	0.182	13.78

Table A4-36: Subject 5- ISA_C angular velocity, position, orientation and normalized time at maximum angular velocity. Position computed as the distance from the centroid of the wrist, and orientation computed relative to the supination axis of the forearm.

Trial	W max [rad/s]	Percent Downswing [%]	Distance [m]	Orientation [deg]
1	30.938	66.5	0.271	66.82
2	30.927	70.5	0.251	74.30
3	38.901	67.0	0.292	69.47
4	42.552	69.5	0.318	64.83
5	26.398	100.0	0.102	47.57
Mean	33.943	74.7	0.247	64.60
STD	6.591	14.2	0.084	10.16

A4.3.2.2 Maximum Angular velocity about ISAr

The four variables computed at maximum angular velocity (ω_{max}, percent downswing corresponding to ω_{max}, ISA position and ISA orientation) are given for each ISAr and subject.

$ISAr_P$: ISA of the relative motion of the pelvis relative to the left leg

Results are shown in Table A4-37 to Table A4-40 for Subjects 2 to 5, respectively, and the corresponding ISA position plot is given below each table, in Figure A4-21 to Figure A4-24.

Table A4-37: Subject 2- $ISAr_P$ angular velocity, position, orientation and normalized time at maximum angular velocity. Position computed in the local reference frame of the pelvis, and orientation computed relative to the spine axis and axis of the left leg.

Trial	W max	Percent	Position			Orientation	
						Spine	Left Leg
		Downswing	x	y	z	Axis	Axis
	[rad/s]	[%]	[m]	[m]	[m]	[deg]	[deg]
1	5.266	76.5	-0.019	0.004	0.000	29.59	71.61
2	6.060	70.5	-0.012	0.004	0.000	28.55	73.24
3	7.175	90.5	-0.124	0.122	0.000	53.35	81.89
4	5.496	74.5	-0.018	-0.007	0.000	29.75	72.47
5	5.126	77.0	-0.031	0.012	0.000	33.26	76.57
Mean	5.825	77.8	-0.041	0.027	0.000	34.90	75.15
STD	0.835	7.5	0.047	0.053	0.000	10.46	4.21

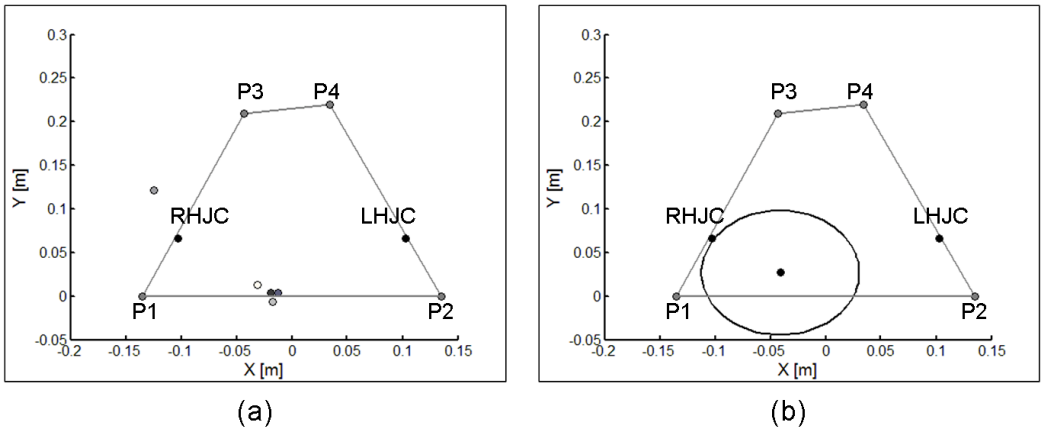

Figure A4-21: Subject 2- Intersection of $ISAr_P$ with the xy-plane of the local coordinate frame of the pelvis; (a) intersection point of trials 1 to 5, (b) mean intersection point and radius of standard deviation

Table A4-38: Subject 3- $ISAr_P$ angular velocity, position, orientation and normalized time at maximum angular velocity. Position computed in the local reference frame of the pelvis, and orientation computed relative to the spine axis and axis of the left leg.

Trial	W max	Percent	Position			Orientation	
		Downswing	x	y	z	Spine Axis	Let Leg Axis
	[rad/s]	[%]	[m]	[m]	[m]	[deg]	[deg]
1	5.801	76.5	0.022	0.027	0.000	27.11	62.79
2	5.485	54.5	0.140	-0.018	0.000	5.75	45.44
3	5.960	72.5	0.023	0.003	0.000	24.93	62.69
4	5.600	52.0	0.130	0.000	0.000	4.05	43.91
5	5.847	74.0	0.033	-0.054	0.000	26.89	66.50
Mean	5.739	65.9	0.070	-0.008	0.000	17.74	56.27
STD	0.193	11.7	0.060	0.030	0.000	11.77	10.71

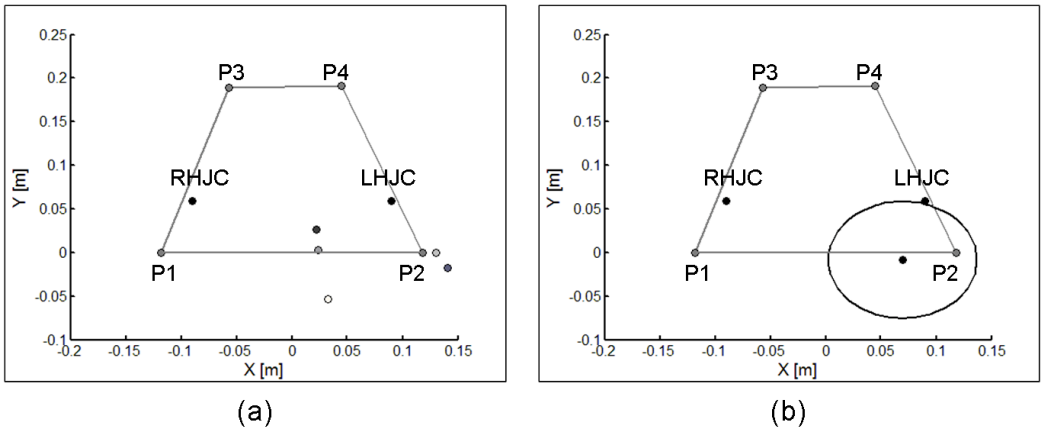

Figure A4-22: Subject 3- Intersection of $ISAr_P$ with the xy-plane of the local coordinate frame of the pelvis; (a) intersection point of trials 1 to 5, (b) mean intersection point and radius of standard deviation

Table A4-39: Subject 4- $ISAr_P$ angular velocity, position, orientation and normalized time at maximum angular velocity. Position computed in the local reference frame of the pelvis, and orientation computed relative to the spine axis and axis of the left leg.

Trial	W max	Percent	Position			Orientation	
		Downswing	x	y	z	Spine Axis	Left Leg Axis
	[rad/s]	[%]	[m]	[m]	[m]	[deg]	[deg]
1	7.702	72.0	0.079	0.032	0.000	15.57	47.20
2	7.874	78.0	0.067	0.048	0.000	19.77	49.96
3	8.159	74.0	0.067	0.049	0.000	18.95	46.83
4	7.830	72.5	0.065	0.057	0.000	23.95	50.34
5	7.636	71.0	0.067	0.047	0.000	21.99	46.73
Mean	7.840	73.5	0.069	0.047	0.000	20.05	48.21
STD	0.202	2.7	0.006	0.009	0.000	3.18	1.78

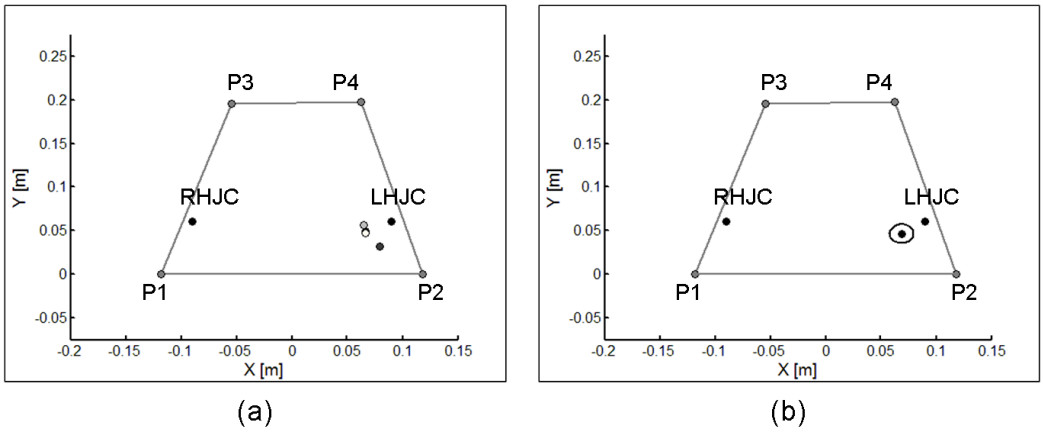

Figure A4-23: Subject 4- Intersection of $ISAr_P$ with the xy-plane of the local coordinate frame of the pelvis; (a) intersection point of trials 1 to 5, (b) mean intersection point and radius of standard deviation

Table A4-40: Subject 5- $ISAr_P$ angular velocity, position, orientation and normalized time at maximum angular velocity. Position computed in the local reference frame of the pelvis, and orientation computed relative to the spine axis and axis of the left leg.

Trial	W max	Percent	Position			Orientation	
		Downswing	x	y	z	Spine Axis	Left Leg Axis
	[rad/s]	[%]	[m]	[m]	[m]	[deg]	[deg]
1	6.280	88.0	-0.011	-0.030	0.000	34.13	64.67
2	6.620	87.5	-0.034	-0.080	0.000	40.49	71.08
3	6.620	86.5	-0.027	-0.065	0.000	39.19	68.19
4	6.446	87.5	0.021	-0.037	0.000	28.57	57.26
5	6.302	89.0	-0.059	-0.045	0.000	42.32	71.33
Mean	6.453	87.7	-0.022	-0.051	0.000	36.94	66.51
STD	0.165	0.9	0.029	0.021	0.000	5.58	5.83

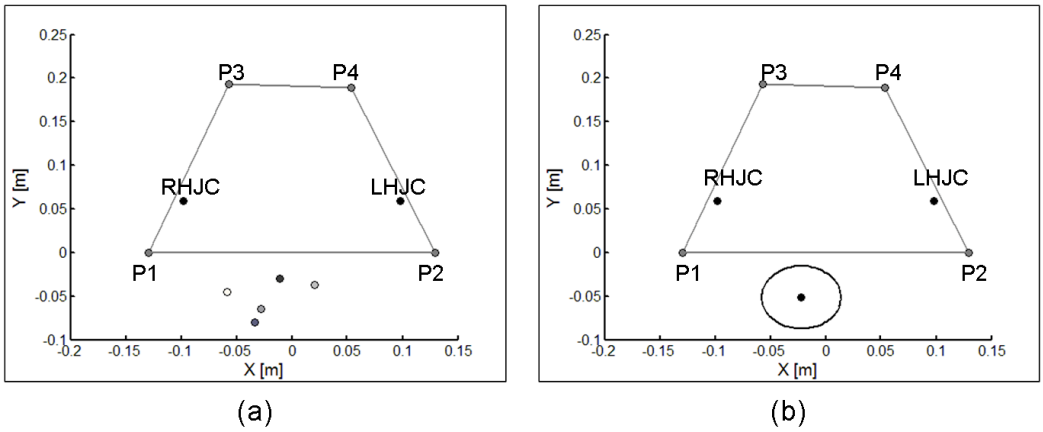

Figure A4-24: Subject 5- Intersection of $ISAr_P$ with the xy-plane of the local coordinate frame of the pelvis; (a) intersection point of trials 1 to 5, (b) mean intersection point and radius of standard deviation

$ISAr_S$: ISA of the relative motion of the shoulders relative to the pelvis

Results are shown in Table A4-41 to Table A4-44 for Subjects 2 to 5, respectively, and the corresponding ISA position plot is given below each table, in Figure A4-25 to Figure A4-28.

Table A4-41: Subject 2- $ISAr_S$ angular velocity, position, orientation and normalized time at maximum angular velocity. Position computed in the local reference frame of the shoulders, and orientation computed relative to the spine axis.

Trial	W max	Percent Downswing	Position			Orientation
			x	y	z	
	[rad/s]	[%]	[m]	[m]	[m]	[deg]
1	4.666	58.0	0.031	-0.223	0.000	35.45
2	4.779	52.5	0.040	-0.217	0.000	34.54
3	3.898	61.0	0.020	-0.137	0.000	40.30
4	4.030	59.5	0.044	-0.168	0.000	31.99
5	4.148	62.5	0.024	-0.123	0.000	39.67
Mean	4.304	58.7	0.032	-0.174	0.000	36.39
STD	0.394	3.9	0.010	0.045	0.000	3.53

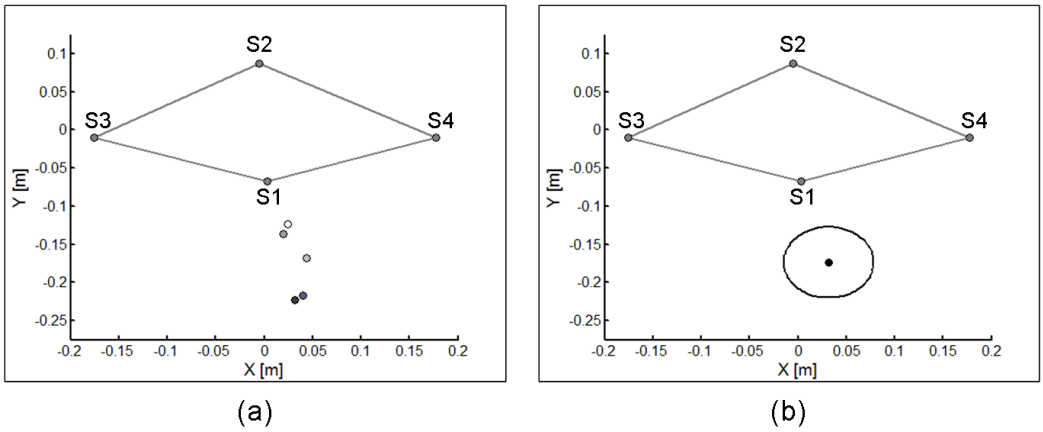

Figure A4-25: Subject 2- Intersection of $ISAr_S$ with the xy-plane of the local coordinate frame of the shoulders; (a) intersection point of trials 1 to 5, (b) mean intersection point and radius of standard deviation

Table A4-42: Subject 3- $ISAr_S$ angular velocity, position, orientation and normalized time at maximum angular velocity. Position computed in the local reference frame of the shoulders, and orientation computed relative to the spine axis.

Trial	W max	Percent Downswing	Position			Orientation
			x	y	z	
	[rad/s]	[%]	[m]	[m]	[m]	[deg]
1	6.476	59.0	0.230	-0.141	0.000	46.79
2	6.890	63.0	0.246	-0.139	0.000	48.34
3	5.912	61.0	0.312	-0.197	0.000	50.16
4	6.054	63.5	0.303	-0.213	0.000	50.44
5	7.463	57.5	0.246	-0.072	0.000	46.63
Mean	6.559	60.8	0.268	-0.153	0.000	48.47
STD	0.634	2.6	0.037	0.056	0.000	1.80

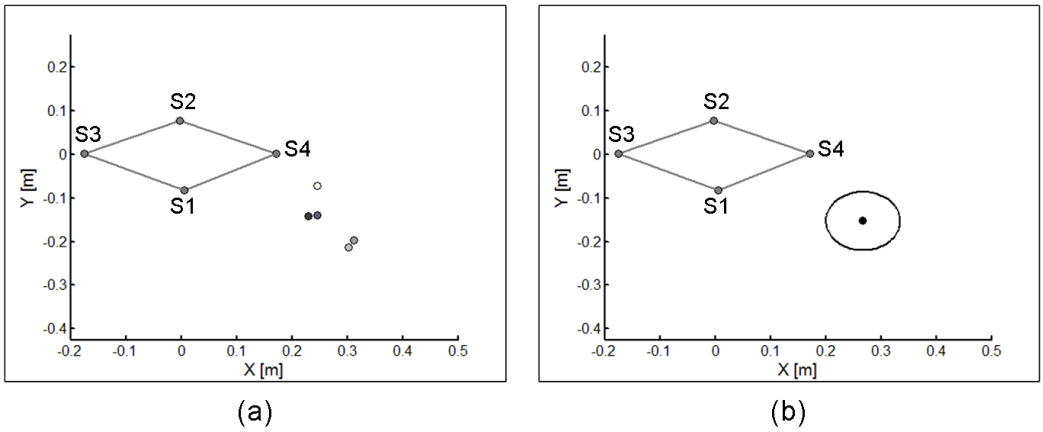

Figure A4-26: Subject 3- Intersection of $ISAr_S$ with the xy-plane of the local coordinate frame of the shoulders; (a) intersection point of trials 1 to 5, (b) mean intersection point and radius of standard deviation

Table A4-43: Subject 4- $ISAr_S$ angular velocity, position, orientation and normalized time at maximum angular velocity. Position computed in the local reference frame of the shoulders, and orientation computed relative to the spine axis.

Trial	W max	Percent Downswing	Position			Orientation
			x	y	z	
	[rad/s]	[%]	[m]	[m]	[m]	[deg]
1	6.977	100.0	-0.024	-0.087	0.000	16.86
2	4.541	69.5	0.075	-0.066	0.000	25.67
3	4.974	63.5	0.091	-0.042	0.000	31.81
5	5.854	86.5	-0.044	-0.093	0.000	27.39
Mean	5.586	79.9	0.024	-0.072	0.000	25.43
STD	1.076	16.6	0.068	0.023	0.000	6.27

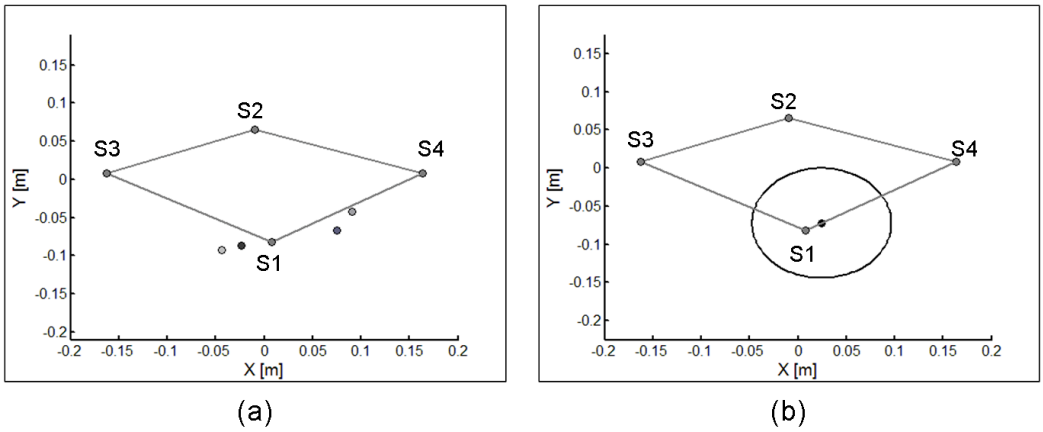

Figure A4-27: Subject 4- Intersection of $ISAr_S$ with the xy-plane of the local coordinate frame of the shoulders; (a) intersection point of trials 1 to 5, (b) mean intersection point and radius of standard deviation

Table A4-44: Subject 5- $ISAr_S$ angular velocity, position, orientation and normalized time at maximum angular velocity. Position computed in the local reference frame of the shoulders, and orientation computed relative to the spine axis.

Trial	W max	Percent Downswing	Position			Orientation
			x	y	z	
	[rad/s]	[%]	[m]	[m]	[m]	[deg]
1	4.931	57.5	0.131	-0.232	0.000	41.97
2	4.921	59.0	0.078	-0.170	0.000	30.61
3	4.971	58.0	0.070	-0.158	0.000	26.12
4	4.764	59.5	0.079	-0.175	0.000	29.55
5	4.838	58.5	0.136	-0.113	0.000	31.37
Mean	4.885	58.5	0.099	-0.169	0.000	31.93
STD	0.083	0.8	0.032	0.043	0.000	5.96

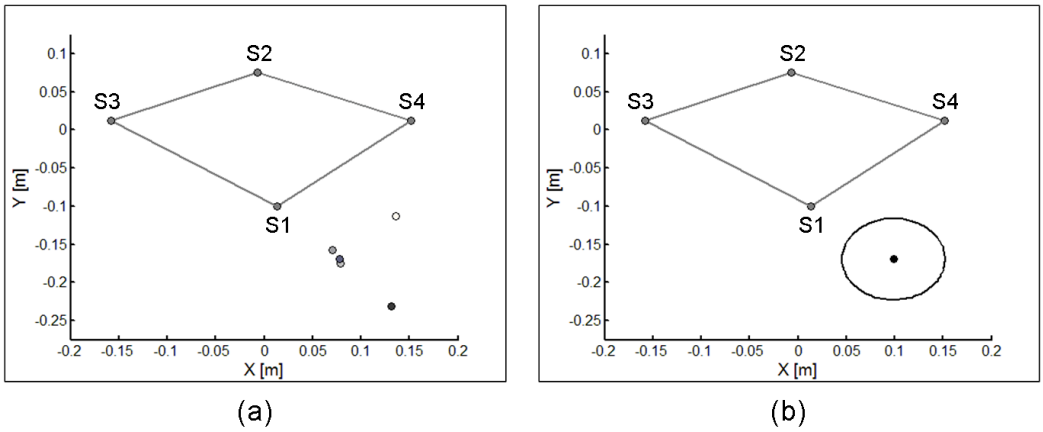

Figure A4-28: Subject 5- Intersection of $ISAr_S$ with the xy-plane of the local coordinate frame of the shoulders; (a) intersection point of trials 1 to 5, (b) mean intersection point and radius of standard deviation

$ISAr_A$: ISA of the relative motion of the arm relative to the shoulders

Results are shown in Table A4-45 to Table A4-48 for Subjects 2 to 5, respectively, and the corresponding ISA position plot is given below each table, in Figure A4-29 to Figure A4-32.

Table A4-45: Subject 2- $ISAr_A$ angular velocity, position, orientation and normalized time at maximum angular velocity. Position computed in the local reference frame of the shoulders, and orientation computed relative to the spine axis and the supination axis of the forearm.

Trial	W max	Percent	Position			Orientation	
		Downswing	x	y	z	Spine Axis	Supination Axis
	[rad/s]	[%]	[m]	[m]	[m]	[deg]	[deg]
1	16.291	100.0	1.143	0.762	0.000	39.27	9.52
2	16.040	100.0	1.223	0.708	0.000	42.19	12.33
3	13.572	100.0	0.552	0.164	0.000	17.45	14.80
4	15.640	100.0	1.316	0.802	0.000	19.87	12.44
5	14.536	100.0	1.471	0.694	0.000	30.04	15.61
Mean	15.216	100.0	1.141	0.626	0.000	29.76	12.94
STD	1.138	0.0	0.351	0.262	0.000	11.12	2.39

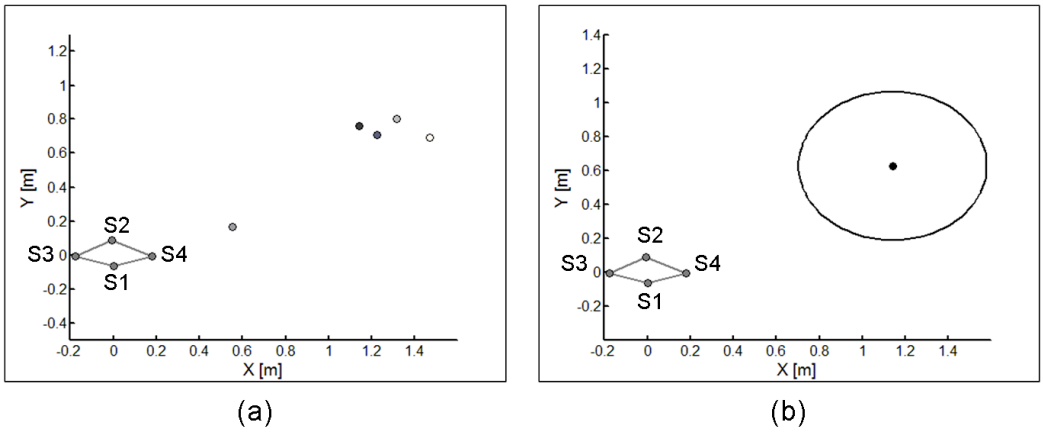

Figure A4-29: Subject 2- Intersection of $ISAr_A$ with the xy-plane of the local coordinate frame of the shoulders; (a) intersection point of trials 1 to 5, (b) mean intersection point and radius of standard deviation

Table A4-46: Subject 3- $ISAr_A$ angular velocity, position, orientation and normalized time at maximum angular velocity. Position computed in the local reference frame of the shoulders, and orientation computed relative to the spine axis and the supination axis of the forearm.

Trial	W max	Percent	Position			Orientation	
	[rad/s]	Downswing [%]	x [m]	y [m]	z [m]	Spine Axis [deg]	Supination Axis [deg]
1	20.387	100.0	0.742	0.723	0.000	3.94	6.64
2	17.560	100.0	1.204	0.955	0.000	7.14	12.78
3	21.375	100.0	2.439	2.915	0.000	27.19	6.89
4	19.003	100.0	1.275	1.080	0.000	20.44	11.29
5	19.571	100.0	1.406	1.400	0.000	5.15	10.68
Mean	19.579	100.0	1.413	1.415	0.000	12.77	9.66
STD	1.439	0.0	0.626	0.874	0.000	10.43	2.75

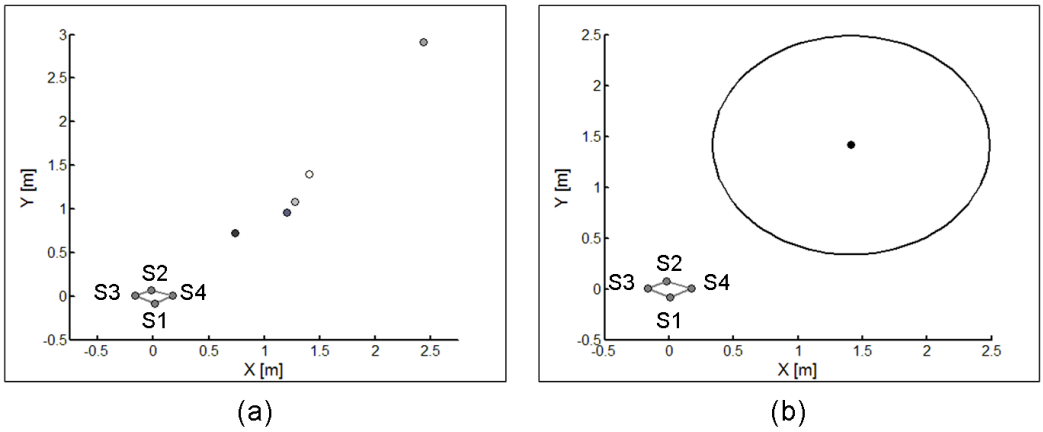

Figure A4-30: Subject 3- Intersection of $ISAr_A$ with the xy-plane of the local coordinate frame of the shoulders; (a) intersection point of trials 1 to 5, (b) mean intersection point and radius of standard deviation

Table A4-47: Subject 4- $ISAr_A$ angular velocity, position, orientation and normalized time at maximum angular velocity. Position computed in the local reference frame of the shoulders, and orientation computed relative to the spine axis and the supination axis of the forearm.

Trial	W max	Percent	Position			Orientation	
		Downswing	x	y	z	Spine Axis	Supination Axis
	[rad/s]	[%]	[m]	[m]	[m]	[deg]	[deg]
1	10.380	100.0	-4.515	-1.453	0.000	16.86	26.65
2	8.951	100.0	1.332	0.028	0.000	35.15	31.32
3	9.602	100.0	7.886	3.042	0.000	30.71	17.78
4	9.710	100.0	-2.017	-0.996	0.000	31.63	23.39
5	10.526	99.0	2.358	0.983	0.000	23.95	12.67
Mean	9.834	99.8	1.009	0.321	0.000	27.66	22.36
STD	0.638	0.4	4.714	1.789	0.000	7.27	7.33

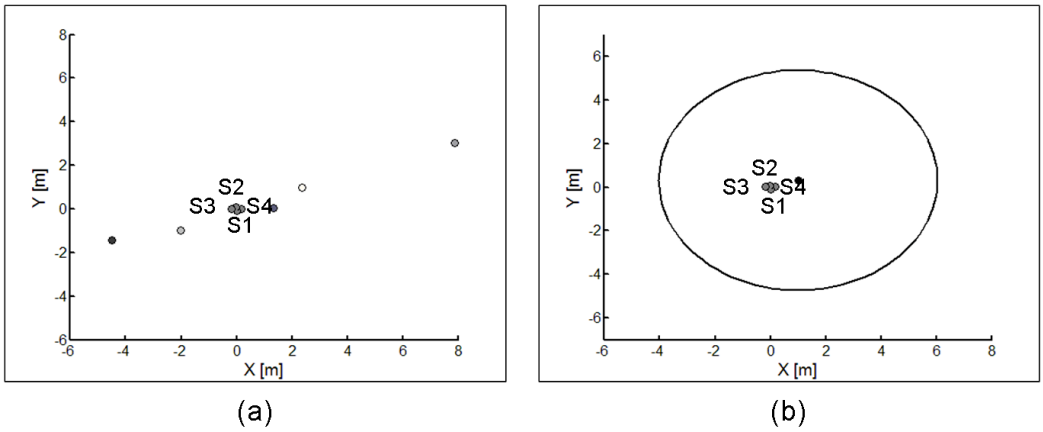

Figure A4-31: Subject 4- Intersection of $ISAr_A$ with the xy-plane of the local coordinate frame of the shoulders; (a) intersection point of trials 1 to 5, (b) mean intersection point and radius of standard deviation

Table A4-48: Subject 5- $ISAr_A$ angular velocity, position, orientation and normalized time at maximum angular velocity. Position computed in the local reference frame of the shoulders, and orientation computed relative to the spine axis and the supination axis of the forearm.

Trial	W max	Percent	Position			Orientation	
		Downswing	x	y	z	Spine Axis	Supination Axis
	[rad/s]	[%]	[m]	[m]	[m]	[deg]	[deg]
1	8.958	100.0	0.619	0.248	0.000	40.20	21.46
2	8.118	100.0	0.423	0.206	0.000	43.57	21.90
3	14.292	100.0	0.324	0.093	0.000	46.83	16.77
4	8.576	94.5	0.511	0.084	0.000	49.77	33.08
5	6.336	88.5	0.198	-0.053	0.000	50.00	66.68
Mean	9.256	96.6	0.415	0.115	0.000	46.07	31.98
STD	2.989	5.1	0.163	0.118	0.000	4.20	20.30

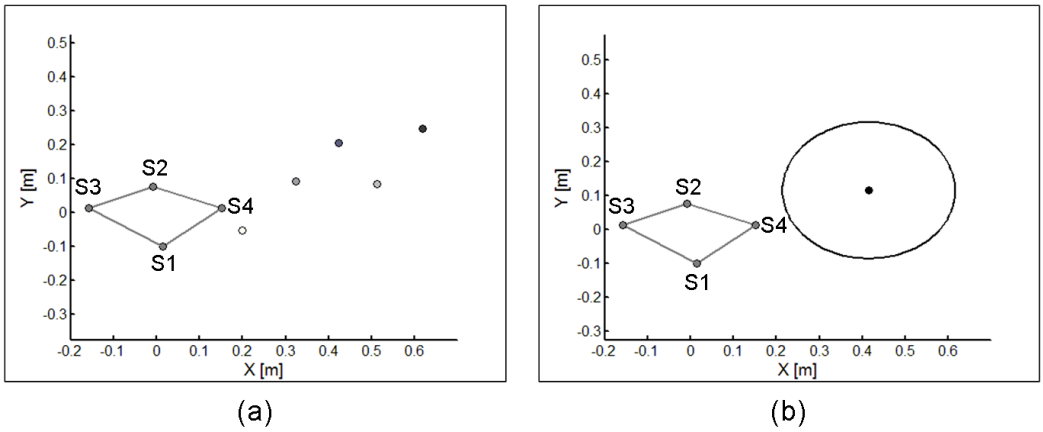

Figure A4-32: Subject 5- Intersection of $ISAr_A$ with the xy-plane of the local coordinate frame of the shoulders; (a) intersection point of trials 1 to 5, (b) mean intersection point and radius of standard deviation

$ISAr_C$: ISA of the relative motion of the golf club relative to the left arm

Results are shown in Table A4-49 to Table A4-52 for Subjects 2 to 5, respectively.

Table A4-49: Subject 2-$ISAr_C$ angular velocity, position, orientation and normalized time at maximum angular velocity. Position computed as the distance from the centroid of the wrist, and orientation computed relative to the supination axis of the forearm.

Trial	W max [rad/s]	Percent Downswing [%]	Distance [m]	Orientation [deg]
1	310.593	94.5	0.428	44.58
2	319.733	91.0	0.445	49.68
3	432.130	89.5	0.512	51.78
4	581.581	93.5	0.429	47.19
5	166.761	96.0	0.493	52.52
Mean	362.160	92.9	0.461	49.15
STD	154.662	2.6	0.039	3.29

Table A4-50: Subject 3-ISAr$_C$ angular velocity, position, orientation and normalized time at maximum angular velocity. Position computed as the distance from the centroid of the wrist, and orientation computed relative to the supination axis of the forearm.

Trial	W max [rad/s]	Percent Downswing [%]	Distance [m]	Orientation [deg]
1	549.038	89.0	0.525	65.38
2	978.654	91.5	0.503	63.66
3	181.024	72.0	0.553	63.16
4	1038.461	90.5	0.489	60.31
5	476.032	97.0	0.279	30.78
Mean	644.642	88.0	0.470	56.66
STD	360.267	9.4	0.109	14.58

Table A4-51: Subject 4-ISAr$_C$ angular velocity, position, orientation and normalized time at maximum angular velocity. Position computed as the distance from the centroid of the wrist, and orientation computed relative to the supination axis of the forearm.

Trial	W max [rad/s]	Percent Downswing [%]	Distance [m]	Orientation [deg]
1	25.533	94.0	0.436	33.82
2	112.567	100.0	0.430	45.13
3	126.219	58.0	0.441	87.93
4	37.480	100.0	0.385	51.74
5	38.914	91.5	-0.236	46.73
Mean	68.143	88.7	0.291	53.07
STD	47.319	17.6	0.296	20.56

Table A4-52: Subject 5-ISAr$_C$ angular velocity, position, orientation and normalized time at maximum angular velocity. Position computed as the distance from the centroid of the wrist, and orientation computed relative to the supination axis of the forearm.

Trial	W max [rad/s]	Percent Downswing [%]	Distance [m]	Orientation [deg]
1	40.639	82.5	0.596	45.29
2	28.048	74.5	0.624	50.08
3	14.026	80.5	0.454	47.29
4	110.976	74.5	0.568	54.60
5	14.234	99.0	0.181	35.01
Mean	41.585	82.2	0.485	46.45
STD	40.332	10.0	0.182	7.29

A4.3.3 Golf Club Head Velocity

The velocity of the golf club head was determined from the displacement of marker C4, affixed to the golf club head (see Section 3.4). This velocity provides a quantifiable measure of the end result of the downswing sequence, and a comparison point between subjects. Results are shown in Table A4-53 for the 5 computed trials of Subjects 1 to 5.

Table A4-53: Subjects 1 to 5- Golf club head velocity at impact.

Trial	Club Head Velocity				
	Subject 1 [m/s]	Subject 2 [m/s]	Subject 3 [m/s]	Subject 4 [m/s]	Subject 5 [m/s]
1	25.579	32.995	33.518	33.517	31.805
2	27.131	33.785	34.234	33.936	31.843
3	24.897	33.792	34.121	34.111	32.526
4	26.720	33.087	35.145	34.094	32.349
5	26.853	33.155	35.483	34.241	31.324
Mean	26.236	34.500	34.500	33.980	31.969
STD	0.954	0.800	0.280	0.280	0.478